An Evaluation of Gallium Arsenide for Detector Applications in X-ray Astronomy

by

Alexander David Thurnall Short

X-ray Astronomy Group
Department of Physics and Astronomy
University of Leicester

UMI Number: U551022

UMI

Dissertation Publishing

UMI U551022

ProQuest

Declaration

I hereby declare that no part of this thesis has been previously submitted to this or any other university as part of the requirements for a higher degree. The work described here was conducted by the undersigned except for the contributions of colleagues indicated in the text.

Alexander Short

September 1997

Acknowledgements

Dedicated to Mum, Dad and Helen.

List of Publications

Some of the results reported in this thesis have been incorporated into the following publications. The chapters to which these papers refer are given in brackets.

1. "Measurement and modelling of the X-ray spectral response of bulk GaAs detectors"

   A.D.T. Short, A.D. Holland

   Proc. SPIE Vol 2808, 1996, 583-594 (chapters 4 and 5)

2. "The X-ray Polarisation Sensitivity of CCDs"

   A.D. Holland, A.D.T. Short, G.W. Fraser, M.J.L. Turner

   Nuclear Instruments and Methods in Physics Research A 355, 1995, 526-531 (appendix A)

3. "X-ray detection using bulk GaAs"

   A.D. Holland, A.D.T. Short, T. Cross

   Nuclear Instruments and Methods in Physics Research A 346, 1994, 366-371 (chapter 4)

4. "Measurement of X-ray Polarisation with Small Pixel CCDs"

   J. Hill, A.D. Holland, C.M. Castelli, A.D.T. Short, M.J.L. Turner, D. Burt

   Proc. SPIE, 1997, in press (appendix A)

ABSTRACT

Forthcoming, imaging X-ray telescopes cannot detect photons with energies above ~10keV due to the limitations of current optics and silicon detectors. However, there are known to be X-ray emissions at higher energies from neutron stars, pulsars, black hole candidates, supernova remnants, active galactic nuclei and galactic clusters. In order that future telescopes may spectroscopically image these emissions, research is being conducted into new optics, and the use of new semiconductors for detector arrays. This thesis covers work to assess gallium arsenide (GaAs) as an X-ray detection medium.

Detector fabrication is discussed and results are presented demonstrating the effect of carrier trapping on spectral resolution. By measuring charge collection efficiency, the activation energy of the dominant electron trap is calculated to be ~0.73eV. This trap may be 'frozen in' at temperatures below -85°C giving a resolution of 2.4keV FWHM at 59.5keV. Trapping is modelled, and a Monte-Carlo simulation is developed. By spectral fitting, the activation energy of the dominant hole trap is calculated to be ~0.2eV. These energy levels are associated with the native EL2 defect. Proton spectra demonstrate that the depletion region width varies linearly with bias at room temperature which is consistent with the existence of a quasi-neutral region.

A series of large scale Liquid Phase Epitaxial (LPE) growth trials was conducted to assess this potential source of high purity material. Layers in excess of 100µm thick were grown, but the resultant devices could not be operated as detectors.

It is concluded that the density of native EL2 defects in bulk GaAs is still too high to allow effective room temperature high resolution spectroscopy, and epitaxial material is difficult and expensive to produce. New sources of material will be sought and other semiconductors such as CdTe will be investigated, as will methods of operating simple high Z detector arrays.

CONTENTS

1. INTRODUCTION

1.1 Motivation (astronomy in the 10 to 100 keV energy range)

X-rays cannot penetrate the earth's atmosphere, and it was therefore not until the capture of German V2 rockets after the second world war, that the X-ray emission from our sun was first detected. It was thought likely that the X-ray luminosity of the sun would be typical of a bright source, and prior to the serendipitous discovery of Sco X-1 in 1962 by Riccardo Giacconi et. al. [Giacconi, R., 1962], it seemed doubtful that any other X-ray sources would be detectable at astronomical distances. Subsequently, it has transpired that the highly energetic thermal and non-thermal processes that generate X-rays occur throughout the universe, and that some of the most interesting and important astronomical objects are powerful X-ray emitters. From the most compact neutron stars, pulsars and black hole candidates to super nova remnants, active galactic nuclei, and on a cosmological scale, even the medium surrounding clusters of galaxies may be studied by their X-ray emission.

Both NASA and ESA now recognise the importance of simultaneously studying the whole electromagnetic spectrum through radio, infra-red, optical, X-ray and γ-ray astronomy. The Advanced X-ray Astrophysics Facility (AXAF) and the X-ray Multiple Mirror (XMM) are therefore component parts of NASA's 'Great Observatories' and ESA's 'Cornerstone Missions' respectively. These integrated programs are intended to provide the principal tools to serve astronomical communities for the next ten years.

Both AXAF and XMM utilise grazing incidence optics and Charge Coupled Device (CCD) detectors to perform imaging spectroscopy. The emphasis is placed on maximising effective area, angular resolution and throughput to achieve good sensitivity to typically low astronomical fluxes, but both will be restricted to X-ray energies below approximately 10keV. This is because of the high energy cut-off imposed by the critical angle of grazing incidence optics, and because of the poor quantum efficiency of silicon CCD detectors above 10keV. Higher energy X-rays may be (and have been) detected using gas proportional counters, and spatial information may be extracted using collimators and coded mask apertures (e.g. the HEAO, SIGMA and GINGA satellites). However, the angular resolution of these instruments is low and the huge advantage in the signal to background noise ratio of focusing optics is lost.

Nevertheless, results obtained using gas proportional counters have demonstrated that there are numerous continuum and line emissions above 10keV. Furthermore, due to their origin, which is principally non-thermal, these X-rays are likely to be polarised.

1.1.1 Hard X-ray emission from galactic sources

The energy associated with accretion onto a compact object such as a neutron star or black hole is of the order of 100MeV per proton. However, the majority of this energy ultimately heats an optically thick plasma which surrounds the compact object in the form of an accretion disc, and the resultant thermal emission is typically at only a few keV. The X-ray spectra from these accretion discs may be observed using grazing incidence optics and silicon CCD detectors as employed on the forthcoming XMM and AXAF observatories. At energies above 10keV, the effective area of these instruments falls dramatically, but evidence from SIGMA [Barret et. al. 1992, Mandrou et. al. 1993] indicates that spectra from both neutron stars and black hole candidates, have a high energy tail. The origin of this emission is unknown, but it is likely to be non-thermal and is therefore probably due to Compton or pair production processes.

The centre of our own galaxy is now known to be a region rich in energetic sources. The X-ray emission from these objects at energies below 10keV is largely obscured by intervening dust and cool matter, but observations made by SIGMA have revealed that some sources which appear quite ordinary at these energies, are emitting violently at higher energies. The luminosity of these objects can be highly variable and characteristic of black hole candidates, but they cannot be properly studied since current hard X-ray telescopes do not have the angular resolution required to distinguish individual sources.

Another galactic source of hard X-rays is cyclotron lines at around 50keV due to the motion of charged particles in the strong magnetic fields associated with neutron stars and pulsars. Also, where a pulsar is associated with a supernova remnant, as is the case in the Crab Nebula, there can be non-thermal continuum radiation. In the absence of a pulsar, these remnants principally emit thermally generated X-rays from the hot gas, with energies below 10keV, although the interaction of the shock front with the interstellar medium should theoretically be a source of non-thermal X-ray emission.

1.1.2 Extragalactic sources

Radio-loud Active Galactic Nuclei (AGN) emit relativistic jets which may be detected (when roughly directed towards us) at energies exceeding 10MeV. These jets generate polarised X-rays by direct synchrotron or synchrotron-self-Compton emission, and a hard X-ray telescope with the capability to measure polarisation, would be able to distinguish X-rays generated by the jet from those generated by nuclear emission. This would be a valuable tool in studying the structure of such systems. The spectra of active galactic nuclei also often contain broad peaks above 10keV due to Compton up-scattering.

Radio-quiet AGN are highly luminous, and emit X-rays across a broad energy band. The mechanism of X-ray production is unclear, but their study is important since it is believed that in the absence of the relativistic jets which largely obscure the nuclear emission of radio-loud AGN, an accreting super-massive black hole may be visible. Compton features associated with the accretion discs of these objects have energies of up to ~100keV, and again, an ability to measure X-ray polarisation would establish whether the up-scattered photons were thermal or non-thermal in origin, since the polarisation state of photons after relativistic Compton scattering is independent of energy. Type 2 Seyfert galaxies have an obscuring molecular torus, and can only be studied at higher energies (>3keV) where this becomes optically thin.

Although spectra from galactic clusters are dominated by the thermal emission of the optically thin intergalactic medium, higher energy X-rays are detected, both from this medium, and from the galaxies themselves.

Consideration is being given to various means of extending the bandwidth of the next generation of imaging X-ray spectrometers up to ~100keV. A number of potential methods were presented at an international workshop held in Leicester last year [Turner, M.J.L., 1997].

1.1.3 Hard X-ray Telescope concepts

Current and forthcoming imaging X-ray telescopes such as ROSAT [Trumper, J., 1990], ASCA [Makishima, K., 1996], AXAF [Weisskopf, M.C., 1988], JET-X [Pounds, K.A., 1990] and XMM [Peacock, A., 1990] are limited to photon energies below approximately 10 keV. This is because at higher energies, the focal length required by Wolter type 1 grazing incidence optics to maintain a reasonable collection area, becomes prohibitive, and the quantum efficiency (QE) of silicon CCD detectors falls dramatically to values which are impractical for detecting the low photon fluxes typical in X-ray Astronomy.

In general, Wolter configuration optics are constrained by the need to reflect X-rays at very shallow angles according to the equations [Ramsey, B.D., 1994, Fraser, G.W., 1993],

$$\theta_c = \left(4\pi r_o \lambda^2 n\right)^{0.5} \qquad \text{giving} \qquad \frac{E_{max}L}{8f} = const \qquad (1\text{-}1)$$

where θ_c is the critical grazing angle below which reflection can occur, r_o is the classical electron radius, n is the electron density, λ is the X-ray wavelength and E_{max} indicates the most energetic X-rays which can be focused by a telescope of focal length f and mirror diameter L. Since the focal length has generally been limited by the maximum length of a telescope which can be placed in orbit, a move to higher X-ray energies has necessitated a reduction in the diameter and hence the collecting

area. To increase the collecting area the latest observatories such as XMM therefore comprise several telescopes in parallel.
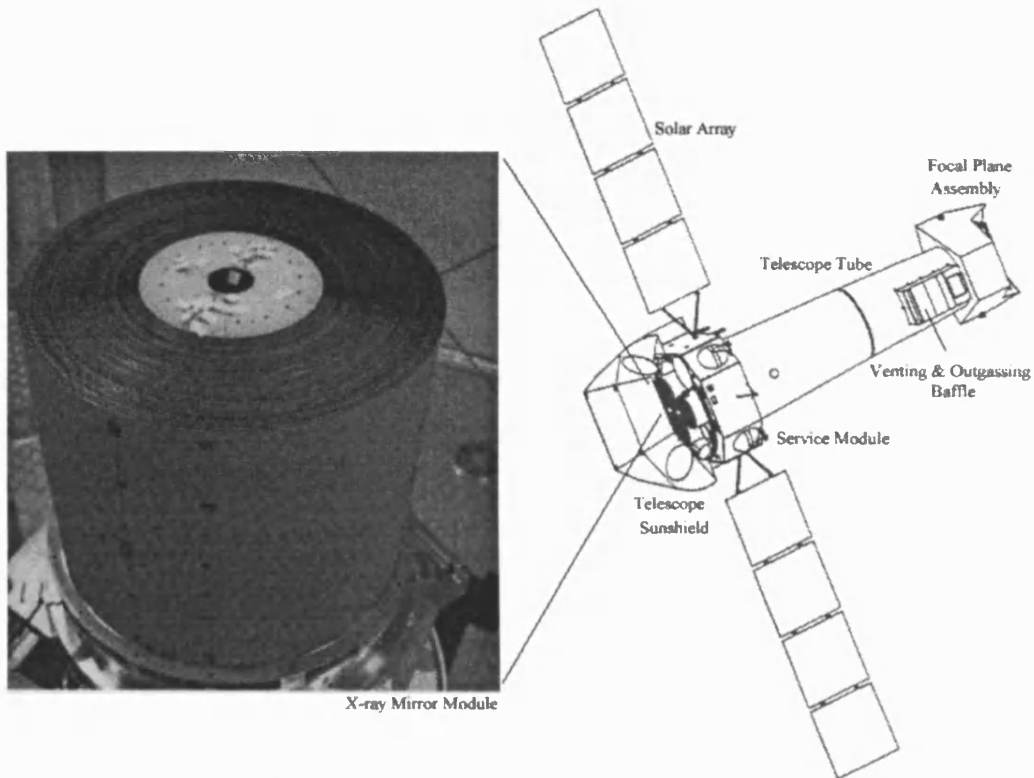
Figure 1-1 A schematic of XMM and a model of one of the three nested concentric mirror modules.

To overcome the constraints of Wolter type 1 optics, the X-ray astronomy group at Leicester University is investigating the use of slumped Micro-Channel-Plate (MCP) optics [Fraser, G.W., 1989] which could focus X-rays onto a high Z detector array, probably of GaAs, CdTe or HgI_2. The Hard X-ray Telescope (HXT) concept was proposed for the ESA M3 mission opportunity in 1993 [Fraser, G.W., 1993].
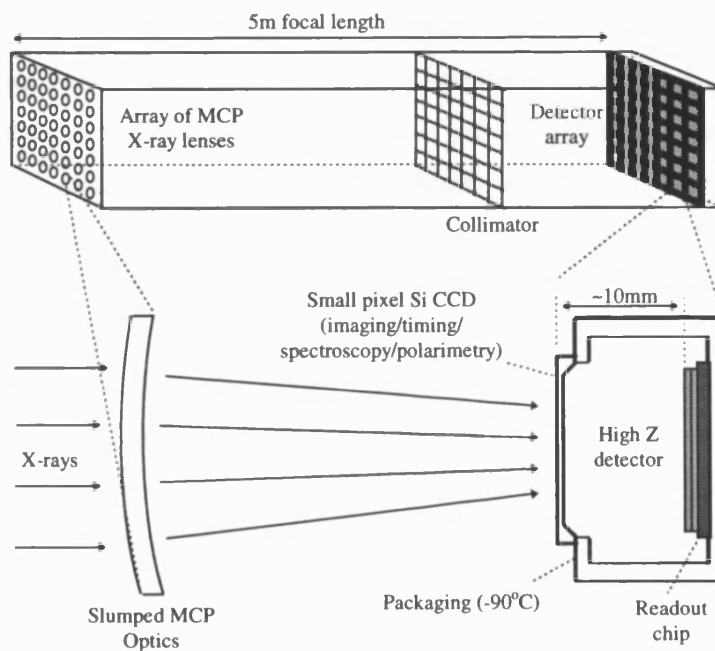
Figure 1-2 A schematic of the proposed Hard X-ray Telescope (HXT).

12

Each MCP element approximates an array of two reflection Wolter configuration X-ray mirrors, but since MCPs can be made smaller than is practical with conventional X-ray mirrors, the incident angles can be reduced (for a given focal length), to values less than the critical angle of higher energy X-rays. The collection area is then maintained by having many such lenses in parallel and HXT would comprise four of the 7x7 element units shown in figure 1-2. This would give a geometric collecting area of ~2500cm^2 and an effective collecting area at 50 keV similar to that of ROSAT at 2 keV. For a 5m focal length, the high energy cut off would be ~100 keV and the telescope's angular resolution would be 1-2 arc minutes. Difficulties associated with the development of MCP lenses, such as achieving sufficiently accurate curvature and channel alignment, have now been largely solved. Progress is also being made in developing radially packed square pore geometries but surface roughness remains a problem. The roughness of the best Wolter configuration mirrors such as those on XMM is ~3 Å rms. MCPs however, still have a roughness of typically 20 Å rms which causes scattering.

Each of HXT's MCP lens elements focuses X-rays onto a corresponding detector element and a simple collimator prevents interference between adjacent X-ray paths and limits "stray light" from off axis sources. The signals from the ~200 detectors are then combined to give a single image. The disadvantage of having N detectors is that the signal to noise ratio will be a factor of √N poorer than if a single such detector could be used for the same collection area.

Another form of high energy optic under investigation by Koujun Yamashita et. al., and discussed in reference [Turner, M.J.L., 1997] is the multi-layer super-mirror. This would resemble a Wolter type 1 mirror but would utilise a multilayer coating to enhance the reflectivity. If the spacing of the layers were constant, then this would give a significantly enhanced reflectivity only over a narrow energy range due to constructive and destructive interference (according to the Bragg condition). However, the multi-layers of the super-mirror would be graded so that higher energy, more penetrating X-rays would be reflected by more closely spaced layers, deeper within the surface. A super-mirror has already been constructed with 8x88Å layers, 11x65Å layers, 16x76Å layers and 35x62Å layers, which demonstrated a reflectivity of >20% at an incident angle of 0.3° over the range 30 to 40keV.

In addition to improving the reflectivity of mirror surfaces, new configurations are being considered to overcome the physical restrictions of placing a telescope with a large focal length and collecting area into orbit. Ideas as simple as launching a number of separate telescopes and co-aligning them to achieve large effective areas have been suggested. Among the proposals to incorporate this multiple vehicle approach is the High Throughput X-ray Spectroscopy (HTXS) mission suggested by Nick White et. al. and discussed in reference [Turner, M.J.L., 1997]. Each satellite would also have an

extending optical bench (figure 1-3), so that after being placed in orbit by a fairly modest launch vehicle (e.g. Delta 2), they could extend to a focal length of 8 to 15m.
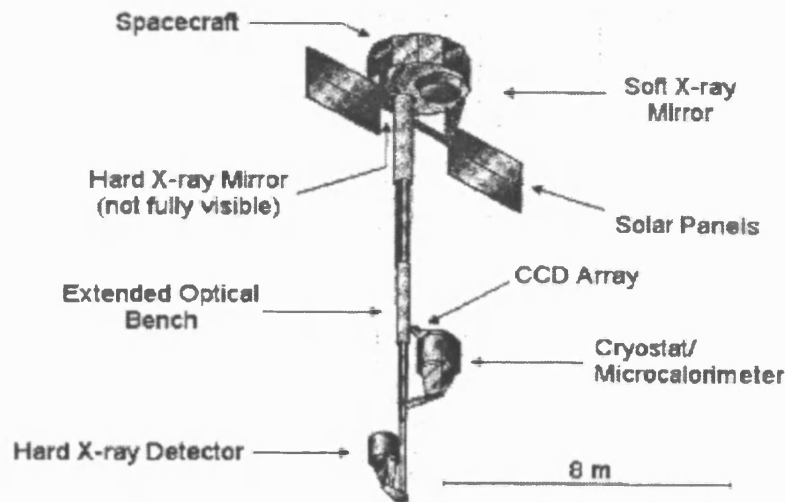
Fig 1-3 Schematic of the proposed HTXS, reproduced from [Turner, M.J.L., 1997].

A group of European astronomers is also considering various ways of placing or assembling a single very large telescope in orbit. Called Xeus [Turner, M.J.L., 1997], it has been suggested that this could incorporate 21 XMM type mirror modules, could be launched in the 18m shroud of an Ariane 5, and could then extend to 25m in orbit, or that it could be even larger if assembled on the infra-structure of the international space station. Whatever the optical configuration of future X-ray telescopes, it is certain that an imaging detector with a high quantum efficiency above 10keV will be required.

The feasibility of measuring the polarisation state of X-rays above approximately 10 keV using a small pixel CCD has been demonstrated experimentally [Buschhorn, G., 1993, Tsunemi, H., 1992, Hill, J.E., 1997] and modelled as part of the work covered by this thesis (see appendix A). The first stage of a high energy detector might therefore be a silicon CCD with pixels as small as 4x4μm, passively cooled in high earth orbit to 170K. These would give near Fano-limited energy resolution and low, but non-zero detection efficiency in the range 5-30 keV. At higher energies, silicon CCDs rapidly become transparent to X-rays so the second stage would be a high Z, hard X-ray detector of moderate (~100μm) pixel size. The material chosen for the hard X-ray detection medium must give high quantum efficiency up to ~100 keV, whilst maintaining spatial resolution (i.e. for planar detector geometries) and should be stable, radiation hard and workable.

1.2 Semiconductor detectors for hard X-ray astronomy

1.2.1 The advantages of semiconductor detectors

One of the principal advantages of semiconductors over gaseous detection media, is the possibility of keeping device dimensions small in order to achieve high spatial resolution for a comparable

quantum efficiency. In spectroscopic applications however, semiconductors have another advantage over even other solid state detectors (such as scintillators), which is that the number of charge carriers generated by the absorption of a photon (or a charged particle) is very high and statistical fluctuations are therefore far less significant. In a scintillation detector, the energy required to generate one information carrier is typically 100eV, whilst in silicon the energy required to generate an electron hole pair is just $\omega \approx 3.65$eV [Bertolini, G., 1968]. Thus a 10keV X-ray will generate $N \approx 100$ charge carriers in a scintillator and $N \approx 2700$ charge carriers in a silicon detector, with (purely statistical) fluctuations in these numbers of $\sqrt{N} = 10$ and 52 (or 10% and 2%) respectively. In fact, since the energy deposited when a photoelectron is scattered is a function of the energy it has remaining, the processes that give rise to the generation of a given electron hole pair are not independent and therefore the fluctuations in the total number of charge carriers generated are not given by simple Poisson statistics, but are substantially smaller. This deviation from Poisson statistics is quantified using the experimentally determined Fano factor, F, so that,

$$\text{observed variance} = F \times \text{Poisson predicted variance} \qquad (1\text{-}2)$$

The Fano factor for silicon is ~0.1 [Palms, J.M., 1969, Zulliger, H.R. 1970, Yamaya, T., 1979], so that the observed fluctuations in 2700 charge carriers are actually more like $\sqrt{(0.1 \times 2700)} = 16$ (0.6%). This property of semiconductor detectors means that they have an ideal best, or 'Fano limited' energy resolution superior to that of any comparable detector type currently in use.

Thanks to the development of integrated circuits by the electronics industry, the technology required to fabricate complex semiconductor devices (particularly using silicon) is relatively mature. They also have the advantage that the first stages of signal amplification can be carried out by Field Effect Transistors defined 'on chip', keeping coupling capacitance to a minimum. One disadvantage however is their relative susceptibility to radiation damage from energetic particles which disrupt the atomic lattice, introducing trapping, generation and recombination centres. The radiation environment, or energetic particle background is always an important operational consideration, and for space borne applications, adequate shielding must be incorporated to prolong detector lifetime.

The current workhorse of imaging X-ray spectrometry is the silicon Charge Coupled Device (CCD) as employed in the AXAF, XMM and JET-X telescopes. These devices are fabricated from single wafers of high resistivity silicon, into the surface of which an electrode structure (normally three phase) is implanted to define an array of pixels. Each pixel is essentially a diode, and will form a potential well in the silicon upon application of bias. Electrons liberated by the absorption of an X-ray are stored in the potential wells and then transferred along columns and rows to an output node by toggling the electrodes in sequence [Lumb, D.H., 1983]. Since the charge generated by an individual photon may be measured, a CCD is a spectrometer and since the first stage of amplification is achieved using a Field Effect Transistor (FET) defined 'on chip' at the output node, the noise can be less than 4 electrons (typical value for an XMM CCD). Pixel dimensions are of the order of 27μm

(AXAF and JET-X) or 40μm (XMM), but can be as small as ~5μm using current technology, and device areas can be as large as an entire silicon wafer (~50cm^2).

In conjunction with suitable X-ray optics, CCDs therefore offer combined imaging and spectroscopy by covering a large focal plane with many thousands of pixel elements and reading out the signals due to individual photons via a single 'on chip' amplifier. To Improve low energy response, the JET-X CCDs incorporate a thin electrode structure and the XMM CCDs have a hole in one electrode, but high energy response is restricted by the photoelectric attenuation coefficient of the silicon and the thickness of the device which is depleted upon application of electrode bias.

1.2.2 Semiconductor options for hard X-ray detection
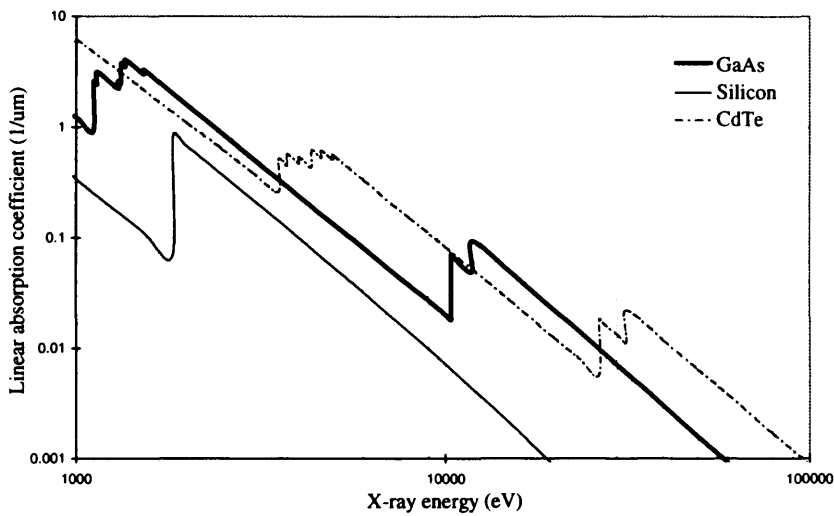
Figure 1-4 Photoelectric absorption coefficient for Si, GaAs and CdTe.

The principal interaction between an incident photon and a semiconductor detection medium, by which the energy of the photon may be measured, is the photoelectric effect (chapter 3). The cross section for this interaction broadly increases with the atomic number of the absorbing medium, and decreases with the energy of the incident photon, and is often quantified in terms of a photoelectric absorption coefficient μ_p, such that the intensity, I, of a beam of initial intensity I_0 after traversing an absorber of thickness t, is

$$I \;=\; I_o \, \exp(-\mu_p t) \tag{1-3}$$

Figure 1-4 shows the photoelectric absorption coefficient for three semiconductors, silicon (Z=14), gallium arsenide (Z≈32), and cadmium telluride (Z≈50), as a function of photon energy. The thickness, t, of an imaging detector is restricted by the need to maintain spatial resolution, and also by the technical problems associated with forming a wide depletion region (active region) in a diode. As will be explained in chapter 3, this requires material of very high resistivity, or near intrinsic purity.

Hence, in order to increase detection efficiency at a given photon energy, and for a given active thickness, it is necessary to select a semiconductor with a higher photoelectric absorption coefficient, μ_p at this energy. This will generally correspond to a material with a higher atomic number, although as shown in figure 1-4, there are energy ranges adjacent to absorption edges, where a material with a lower atomic number may have a higher absorption coefficient.

As shown in figure 1-4, the linear absorption coefficient of silicon at 10keV is ~0.007μm^{-1} and this corresponds to an efficiency of ~30% for a detector thickness of 40μm. This is shown in figure 1-5 which is an approximate theoretical quantum efficiency curve for an XMM EPIC CCD assuming a 40μm depletion depth. The drop off in efficiency at low energies is due to absorption in the electrode structure, and the drop at 1838eV is due to the silicon k absorption edge. At higher energies however, the electrode structure may be neglected and the form of the quantum efficiency curve is due entirely to the drop in linear absorption coefficient.
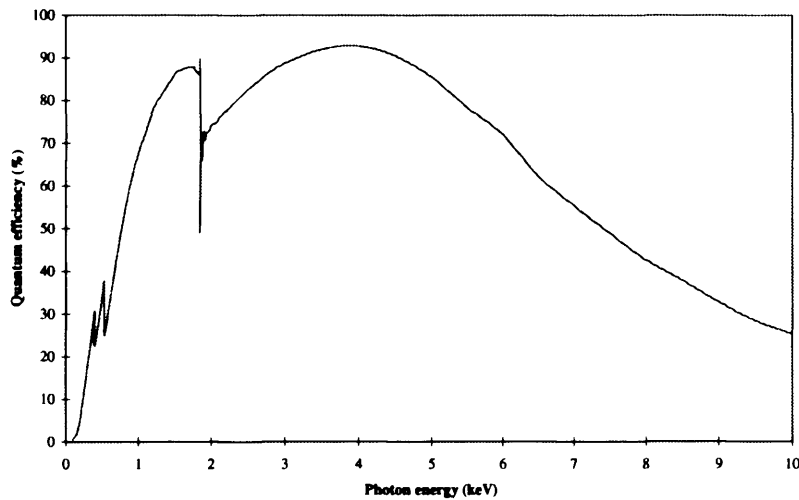
Fig 1-5 Theoretical quantum efficiency of XMM EPIC CCDs (40μm depletion).
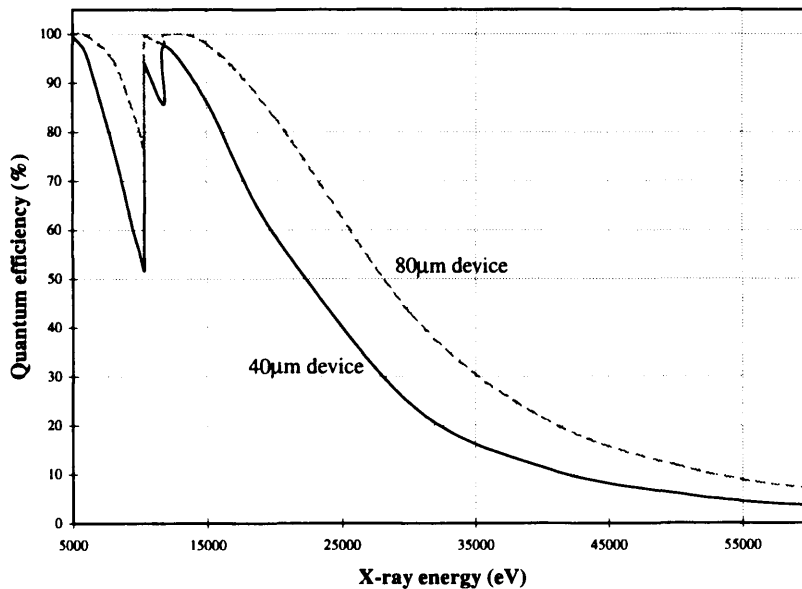
Fig 1-6 Theoretical quantum efficiency of 40 and 80μm thick GaAs detectors.

17

In order to increase the detector efficiency above 10keV it is therefore desirable to use a semiconductor with a higher atomic number than silicon. As shown in figure 1-6, a GaAs detector with an active region 40μm thick would have a quantum efficiency of approximately 40% at 25keV. An 80μm device is also shown, since this is the thickness of the thinnest device considered in this thesis.

Another criterion for selecting a suitable semiconductor for detection of X-rays of any energy, is the width of the energy band-gap. This should be narrow enough so that the number of charge carriers generated by the absorption of an incident photon is high, (and hence $\sqrt{N}/N$ low), but it should be wide enough so that the density of thermally generated charge carriers is not too high at the detector operating temperature, giving rise to leakage current and corresponding shot noise. The equation for the thermally generated charge carrier density in an intrinsic semiconductor (derived in chapter 3), is,

$$ n_i = \frac{2}{h^3} (2\pi m_e^* kT)^{\frac{3}{2}} \exp\left(- \frac{E_C - E_F}{kT}\right) \tag{1-4} $$

$$ = N_C \exp\left(- \frac{E_C - E_F}{kT}\right) \tag{1-5} $$

where E_c-$E_f \approx E_g/2$ (E_g is the width of the band gap). The band gap in silicon is 1.12 eV, and silicon detectors must therefore be cooled to below approximately -50°C for high resolution spectroscopy applications. For room temperature operation, the optimum band gap width is approximately 1.5 eV [Swierkowski, S.P., 1975],[Armantrout, G.A., 1977] and the band gap in GaAs is close to this, at 1.424 eV. Room temperature operation offers attractive practical advantages in dispensing with heat sinks, Peltier coolers, vacuum cryostats etc.

Table 1-1 Some properties of important semiconductors.

	Si	Ge	GaAs	CdTe	HgI₂
atomic numbers	14	32	31,33	48,52	80,53
atomic weight	28.0855	72.61	144.64	240.01	454.4
crystal structure	diamond	diamond	zincbl	zincbl	rhomb
density (g/cm³)	2.328	5.3267	5.32	5.850	6.094
dielectric constant	11.9	16.0	13.1	10.0	
energy gap (eV) @ 300K	1.12	0.66	1.424	1.56	2.13
energy gap (eV) @ 0K	1.17	0.74	1.52		
Direct or Indirect	I	I	D	D	
n_i (cm⁻³)	1.45E10	2.4E13	1.79E6		
int resistivity (Ohm.cm)	2.3E5	47	1E8		
lattice const (angstroms)	5.43095	5.64613	5.6533	6.477	
melting point (°C)	1414	938.35	1238	1121	259
minority carrier lifetime (s)	2.5E-3	1E-3	~1E-8		
electron drift mobility (cm²/V/s)	1500	3900	8500	1050	100
hole drift mobility (cm²/V/s)	450	1900	400	100	4
energy per eh pair (eV)	3.61	2.98	4.27	4.42	4.22
Fano factor	0.1	0.08	0.18		0.2

An ideal semiconductor for photon detection should also have long carrier lifetimes and high carrier mobilities to ensure efficient charge collection. Table 1-1 gives some important parameters of germanium, gallium arsenide, cadmium telluride and mercuric iodide, which all have higher atomic numbers than silicon (also included for comparison).

Germanium has a band gap of just 0.66eV (at 300K) and must therefore be operated at cryogenic temperatures. The other three may be operated at less restrictive temperatures. The technology surrounding mercuric iodide crystal growth and detector fabrication is still very immature, but cadmium telluride (CdTe) and cadmium-zinc-telluride (CZT) detectors are receiving a great deal of attention, notably by Eurorad, Amptek and Sandia National Labs. Many of the problems associated with CdTe and CZT detectors are associated with charge trapping as in GaAs, but because the carrier mobilities are significantly lower and hence the pulse rise-times longer, it has proved possible to apply pulse processing, and correct for charge collection distortions [Lund, J.C., 1995]. This technique has been applied successfully, but a significant proportion of the signal charge is abandoned, degrading the noise performance.
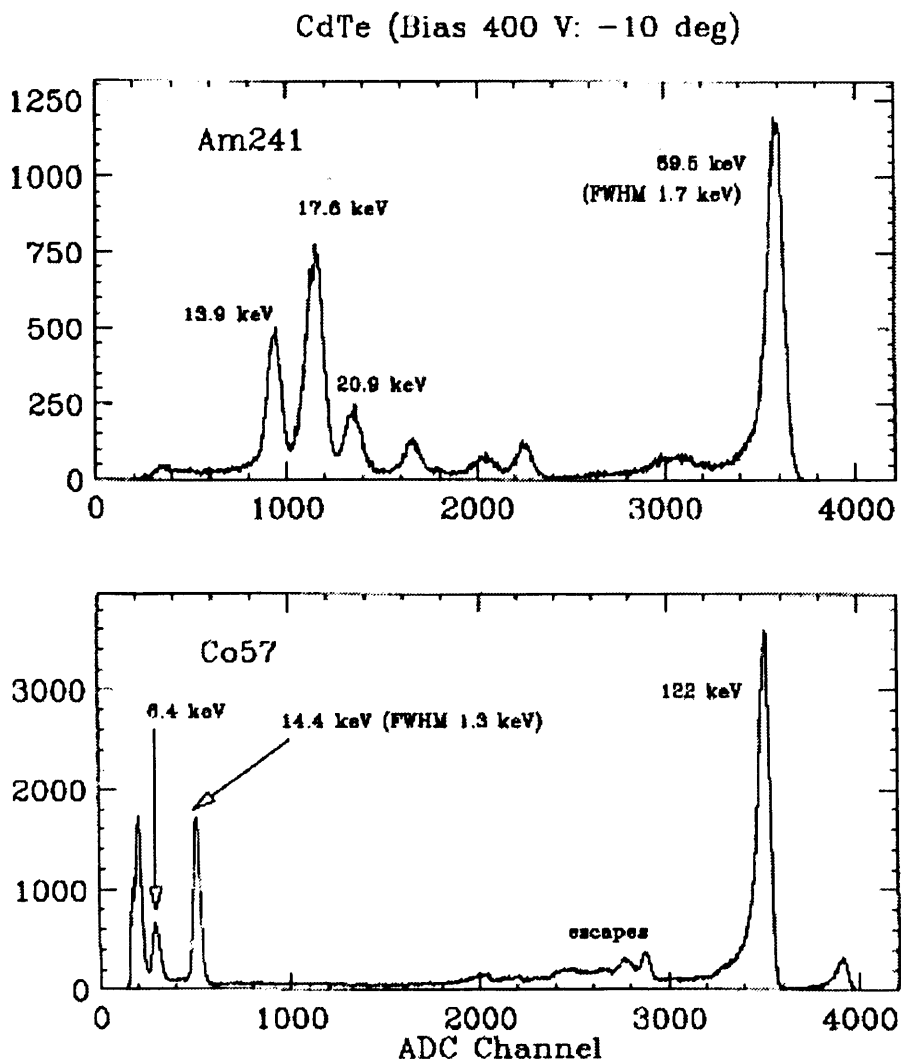
Fig 1-7 Spectra from CdTe detector reproduced from [Matsumoto, C., 1997].

19

Perhaps a better solution which has been demonstrated by Matsumoto et. al. [Matsumoto, C., 1997] is to use an indium Schottky contact on a CdTe diode rather than the usual platinum. This has been shown to reduce hole injection and hence leakage current by at least an order of magnitude, allowing the application of greater bias and hence near complete charge collection. A $2x2x0.5mm^3$ detector under an applied bias of 400V has been shown to give ~0.8nA leakage current at 20°C, and an energy resolution of 1.7keV FWHM at 14keV. At -10°C this improves to ~1.3keV FWHM at 14keV. Americium 241 and Cobalt 57 spectra are shown in figure 1-7. These were obtained without the aid of pulse processing.

In terms of its suitability for the detection of X-rays, gallium arsenide has similar properties to cadmium telluride. It has been developed for high speed electronics applications thanks to its high electron mobility and is also widely used in solar cell production. Contact technology and device fabrication have therefore been studied extensively, and there are many manufacturing facilities world wide (including EEV Ltd. U.K.), capable of producing device structures. However, the development of gallium arsenide as a detector medium has fallen behind that of cadmium telluride, largely because of problems associated with charge collection which hampered development in the early seventies. In the light of improvements in the purity of bulk grown material, and the establishment of very large scale epitaxial growth facilities for solar cell manufacture, GaAs was selected as the material for this initial study which coincides with the technology foresight program IMPACT to develop advanced pixel arrays and CCDs for X-ray applications. At the time of commencing this work, the ATLAS team were also considering gallium arsenide as a potential detector material for the LHC at CERN. To this end, the RD8 collaboration was formed by university research groups in Bologna, Florence, Glasgow, Lancaster, Modena and Sheffield to study amongst other things, basic detector properties [Bertin, R., 1990, Beaumont, S.P., 1992[1], Beaumont, S.P., 1993[1]], charge transport effects [Beaumont, S.P., 1993[2]] and the production of micro-strips [Beaumont S.P., 1992[2]].

1.3 GaAs detectors for X-ray astronomy

GaAs appears to have all of the attributes of a good semiconductor for detecting X-rays at energies above 10keV. These include a high atomic number (32 compared with 14 for silicon), and a band gap wide enough to restrict thermal generation of signal carriers to a minimum at practical operating temperatures. Carrier mobilities are high, although the figure of 8000 $cm^2V^{-1}s^{-1}$ for the electron mobility is deceptive and only applies at low values of electric field. At fields above $3x10^3$ Vcm^{-1}, it decreases due to the transfer of electrons from the direct conduction band valley to a lower mobility valley [Sze, S.M., 1981],[Shur, M., 1987]. The saturation velocity of electrons is therefore close to

that of holes (~ $10^7 cms^{-1}$) and mobility, as a constant, has been rejected throughout this thesis in favour of measured values of the carrier velocity/electric field relationship.

The first GaAs devices to demonstrate good energy resolution [0.64keV FWHM at 59.5keV] were detectors fabricated from liquid phase epitaxial (LPE), high purity material, produced and evaluated by Eberhardt, Ryan and Tavendale in the early seventies [Eberhardt, R.D., 1971]. The LPE layers were grown on n-type, <100> oriented GaAs substrates and ranged in thickness from 60 to 80µm. Subsequently, other LPE GaAs Schottky contact detectors and Vapour phase epitaxy (VPE) detectors have given similar results, but the epitaxial material has been limited to thicknesses of typically ~100µm or less and has proved difficult to reproduce. In order to tackle this problem of reproducibility, part of the work covered by this thesis is an attempt to grow thick epitaxial gallium arsenide on a very large scale and hence to overcome some of the difficulties associated with small scale facilities, and to increase the yield of good detectors once satisfactory growth is achieved. This problem has been tackled by utilising a large scale LPE dipping system at EEV Ltd. which has been developed to grow solar cell layers, and which holds a gallium melt of approximately 3kg. The fabrication of detector structures on the grown layers was also carried out at EEV Ltd, and the evaluation of the material and devices was performed at EEV Ltd, Leicester University, Sheffield University, Loughborough University and the Australian Nuclear Science and Technology Organisation (ANSTO).

Epitaxial GaAs of a purity and thickness suitable for detector fabrication is expensive and extremely difficult to produce. Until recent years, the purity of bulk grown GaAs was inadequate for use as a radiation spectrometer, but demand in the electronics industry for a semiconductor suitable for high speed transistors, quantum well diodes, laser diodes and microwave oscillators has motivated extensive research to improve the material quality of bulk GaAs. High purity bulk material is now readily available from a number of commercial suppliers and has un-surprisingly been the subject of renewed interest as a potential detection medium. The fabrication of detectors using this commercially available bulk GaAs, and their evaluation for suitability in X-ray spectroscopy applications is described in this thesis. The fabrication was conducted at EEV Ltd, and the evaluation at Leicester University.

In the absence of inter-band energy levels i.e. in a pure and well ordered crystal in which band to band recombination were the only means of charge loss, carrier lifetimes in GaAs should be of the order of 0.1ms [Eberhardt, J.E., 1971][Hall, R.N., 1959]. In practice, carrier lifetimes as long as this are never measured, but are usually found to be only a few nanoseconds, a first indication that traps, or inter-band energy levels dominate the material behaviour. These inter-band energy levels impact upon the suitability of GaAs for detector applications in two major ways. Firstly by altering the space charge, and hence the electric field across the depletion region and the depletion region width itself,

21

and secondly by trapping charge carriers directly which makes the charge collection efficiency a function of depth in the depletion region and hence degrades spectral resolution.

Experimental results are presented in this thesis which demonstrate the effect of charge trapping on the resolution and form of X-ray spectral peaks, and which identify the activation energies of the most dominant electron and hole traps. A Monte-Carlo model has been developed which simulates the measured spectra, and this, in conjunction with a series of proton measurements has provided evidence in support of the electric field measurements of Berwick and Brozel [Berwick, K., 1993], and the models of McGregor et. al. [McGregor, D.S., 1994].

1.4 Thesis organisation

In chapter two of this thesis, some of the theory of semiconductor devices and specifically their application to X-ray detection will be presented. This includes fundamental semiconductor properties, X-ray interactions, Schottky barriers, charge transport, pulse formation and detector characteristics. The electric field models of McGregor et. al. are also discussed, but that theory specifically related to the growth of epitaxial material and the modelling of X-ray polarisation measurement with CCDs is covered separately in those chapters.

Chapter three outlines the experimental techniques employed for analysing material (Hall measurements, Deep Level Transient Spectroscopy etc.) and for evaluating devices (IV characteristics, spectroscopic measurements etc.).

The results of measurements carried out on bulk devices are given in chapter four. These include a measurement of the activation energy of the most influential electron trap from the variation of charge collection efficiency with time, proton spectra which reveal the linear dependence of active region width on voltage and 'best' spectra obtained by freezing in the most dominant traps.

A Monte-Carlo model is developed in chapter five and used to fit measured spectra. By fitting spectra acquired at different amplifier shaping times, the de-trapping time and hence the energy of the most dominant hole trap is established. This is analogous to the technique employed in chapter four to establish the electron trap energy level, but here the associated de-trapping times are much shorter.

The theory, experimental set-up, procedure and results of a program to grow thick epitaxial GaAs in conjunction with EEV Solar Power Systems, are presented in chapter six.

Conclusions and future work are discussed in chapter seven, and the thesis has two appendices. The first describes a Monte-Carlo simulation developed early in the course of this work to establish the

feasibility of measuring the polarisation of X-rays using small pixel CCDs. This is an important consideration in the proposal of a hard X-ray telescope. The second appendix contains program listings for the simulations of both X-ray detection in GaAs devices, and the polarisation sensitivity of small pixel CCDs.

2. SEMICONDUCTOR DETECTOR THEORY

Presented here are some of the basic physical principles which govern our understanding of semiconductor materials, X-ray interactions, carrier transport and detector operation, on which much of the work contained in this thesis has been based. The equations derived and quoted in this chapter have been used in the course of this work to quantify and model the effects of carrier trapping on X-ray spectral resolution, but before considering trapping and recombination, the nature of semiconductor material and carrier generation by X-ray interaction will be discussed. Pulse formation and detector characteristics are covered at the end of this chapter.

2.1 The band gap and carrier concentration at thermal equilibrium

In order to appreciate those properties of semiconductors which make them suitable for photon detection, it is necessary first to understand what constitutes a semiconductor. This requires a knowledge of energy bands (from quantum mechanics), electron energy distributions (from statistical thermodynamics) and most specifically, of the band gap in many crystalline solids, the width of which determines the conductive properties of the material.

2.1.1 Energy bands

The existence of allowed energy bands and hence of band gaps in a crystalline solid is a direct consequence of the quantisation of electron energy and momentum states in a bound system. This is the fundamental principle at the heart of early quantum mechanics as proposed by Planck, de Broglie, Bohr etc. and subsequently developed into modern quantum mechanics by the likes of Schrödinger and Born. This section will outline the derivation of energy bands in a periodic system, using as a starting point the very general time independent Schrödinger equation.

Allowed electron states may be described quantum mechanically by a wave function Ψ which is a solution to Schrödinger's wave equation [Eisberg and Resnick, 1985],[Sze, S.M., 1981],[Bar-Lev, A., 1984],

$$\nabla^2\Psi + \frac{2m}{\hbar^2}(E - V)\Psi = 0 \qquad (2\text{-}1)$$

where E is the energy associated with the state and V is the local potential field. Solutions, or eigenfunctions for Ψ give discrete allowed eigenvalues for E, the electron energy, which may only be calculated directly from equation 2-1 in the simplest cases, such as a free electron (V=0) or a single electron confined by a simple potential field (e.g. a hydrogen atom). More complex systems are generally evaluated numerically to give the allowed electron energies or shells associated with large atoms or more complex systems.

GaAs crystals have the zincblende lattice structure which is tetrahedral with each gallium atom surrounded by four equidistant arsenic atoms and vice versa. This forms two interpenetrating face-centred cubic sub-lattices, one of gallium atoms and the other of arsenic atoms. The lattice constant, **a** is 5.6533 Å.
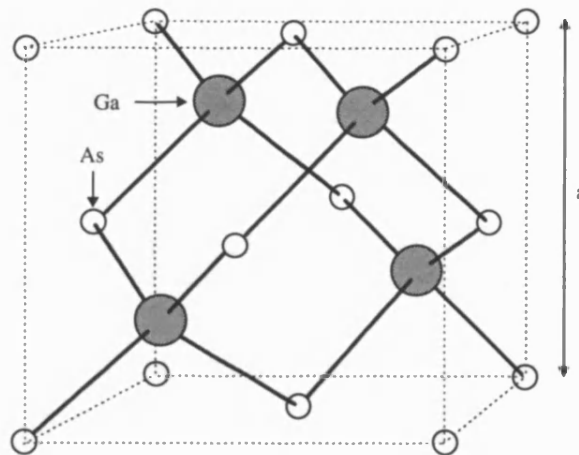
Figure 2-1 The GaAs unit cell. The tetrahedral arrangement is clear and the FCC arrangement of As can be seen. A unit cell could also be drawn to show the FCC arrangement of Ga atoms.

In a crystal lattice, the potentials of the well ordered atoms interact to produce a net potential field which has the same periodicity as the lattice. The Bloch theorem states that the solutions of Schrödinger's equation in this case will also be periodic, and will have the form [Bar-Lev, A., 1984],

$$\Psi_k(r) = e^{ik \cdot r} U_n(k, r) = \text{the Bloch function} \tag{2-2}$$

where $U_n(k,r)$ has the periodicity of the lattice in r, and k is called the wave vector. Several numerical techniques have been developed to obtain solutions to Schrödinger's equation of the form of equation 2-2 for the periodic potentials found in real crystal lattices. For semiconductors, common techniques include the orthogonalized plane-wave method [Allen, L.C., 1955], the pseudopotential method [Philips, J.C., 1958] and the **k.p** method [Smith, R.A., 1979].

It is found that the allowed energy levels for the most tightly bound electrons (n=1,2..) barely differ from the values calculated for the atom if it were in isolation, since the potential field close to the atomic nucleus is little affected by that of neighbouring atoms. Further from the nuclei however, the fields merge and electrons can no longer be said to belong to a particular atom, but to the crystal as a whole. Pauli's exclusion principle must apply to this larger system (that is, no two electrons can occupy the same energy and spin state) so the discrete energy levels must split into many energy levels. Since the number of energy levels required is driven by the number of electrons in the crystal, they become so numerous that they may be considered to constitute continuous bands of allowed energies.
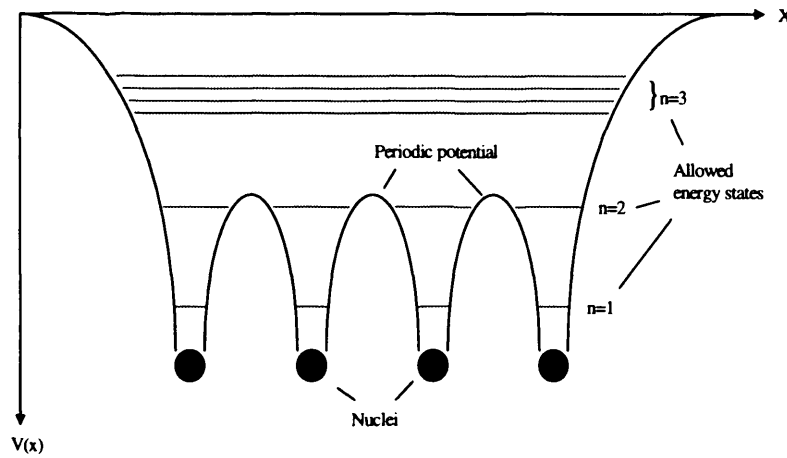
Figure 2-2 Schematic of energy states in a hypothetical crystal of four atoms. Here the n=3 state belongs to the whole crystal and must split to satisfy Pauli's exclusion principle.

In a real, three dimensional crystal, the band structure can become rather complicated since the inter-atomic distance and hence the form of the potential field depend on the direction under consideration. The edges of the allowed energy bands are generally expressed in reciprocal k-space where k is the propagation vector or momentum vector which is related to the associated wavelength of the particle by k=2π/λ. The relationship between the momentum vector k, the energy E, and the momentum p of a particle depends upon the solution of Schrödinger's wave equation e.g. for the case of a constant potential V_o<E, the solution of equation 2-1 will be of the form,

$$\psi(x) = A \exp(jkx) + B \exp(-jkx) \qquad (2e\text{-}1)$$

where

$$k^2 = \frac{2m}{\hbar^2}(E - V_o) \qquad (2e\text{-}2)$$

and if the electron is free, then V_o=0, and

$$E = \frac{\hbar^2 k^2}{2m} = \frac{p^2}{2m} \qquad (2e\text{-}3)$$

so for a free particle i.e. where the energy is kinetic only, the momentum is given by hk/2π. In a diatomic crystalline structure, the relationship between E and k is more complex, but it is generally only necessary to know its form over a particular range of particle (electron) energy, and here it can often be approximated with a simple function.

An important consideration in determining material properties, is whether the allowed energy bands, E(k) overlap or leave forbidden energy gaps (band gaps). Another is whether any gaps are direct (that is the conduction band minimum coincides with the valence band maximum) or indirect. This will determine the probability of direct band to band transitions in accordance with k-selection rules since a lattice vibration or phonon is required to conserve crystal momentum for a transition to take place which requires a change in k.

A semiconductor has an energy band (the valence band) which contains electrons bound to specific atoms, and another (the conduction band) which is almost empty. These are separated by a band gap. Electrons in the conduction band occupy energy levels belonging to the whole crystal and may move through the lattice (conduct). A hole left in the valence band by the absence of an electron may be filled by an electron from a neighbouring atom but this will leave a new hole. It is the convention when considering the valence band to treat the minority holes rather than the electrons as moving from atom to atom and thus through the lattice. Holes clearly drift in the opposite direction to electrons and since they represent a gap where a negative electron should be, they carry a positive charge of equal magnitude to that of an electron.

Semiconductors generally have a forbidden energy gap approximately 1eV wide. If the gap is too narrow then many electrons can readily cross into the conduction band and the material will be a conductor. If the gap is too wide then few electrons may cross into the conduction band and the material will be an insulator. The transitions between conducting, semi-conducting and insulating behaviour are gradual, and depend on factors such as temperature and the presence of electron donor or acceptor impurity atoms (often deliberately introduced as dopants). As well as directly increasing the number of electrons in the conduction band or holes in the valence band, dopants or chemical impurities also disrupt the potential field in their vicinity and introduce localised energy levels into the band gap, as can crystal defects.
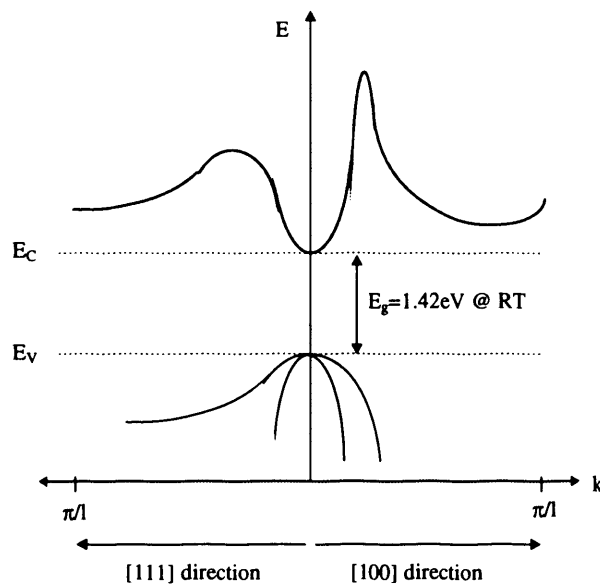
Figure 2-3 Simplified band structure diagram for GaAs. Ev is energy of the top of the valence band. Ec is the energy of the bottom of the conduction band.

GaAs has a direct band gap 1.42eV wide at 300K (1.52eV at 0K). This compares with 1.12eV at 300K for Si in which the gap is indirect. It is this difference in band gap which initially makes GaAs seem more suitable than silicon for detecting photons at room temperature since the density of thermally generated carriers and hence the noise due to statistical fluctuations in this quantity is far

lower. The equations for the densities of thermally generated electrons and holes are perhaps the most fundamental equations specific to semiconductor operation, and their derivation will be covered in the following section.

2.1.2 The density of states and the Fermi-Dirac distribution function

In order to establish the distribution of electrons within the allowed energy bands, it is necessary to know the distribution of allowed states as a function of energy and the probability that each state is occupied.

Since energy bands are formed by the splitting of discrete energy levels so that Pauli's exclusion principle is observed across the entire system (crystal), the distribution of allowed states is expressed as a 'Density of States' $N(E)$ per unit crystal volume. This may be readily calculated if the shape of the energy bands in k space, $E(k)$ is known. In the case of semiconductors where the occupancy of only the very top of the valence band and the very bottom of the conduction band are of great importance, the situation is simplified, since the $E(k)$ relations at the extreme edges of energy bands are approximately parabolic.

$$E = E_C + \frac{\hbar^2 k^2}{2m_e^*}$$

(2-3)

$$E = E_V - \frac{\hbar^2 k^2}{2m_h^*}$$

where E_C is the energy of the bottom of the conduction band and E_V is the energy of the top of the valence band and m^* is the effective mass.

Consider a rectangular box shaped portion of a crystal lattice, N_X atoms by N_Y atoms by N_Z atoms, with lattice constant 'a' and dimensions,

$$L_X = N_X a \qquad L_Y = N_Y a \qquad L_Z = N_Z a$$

(2-4)

In one dimension, the Bloch function (equation 2-2) is,

$$\Psi_k(x) = e^{ikx} U_n(k, x)$$

(2-5)

and for an arbitrary point within the crystal, x=sa where s is not necessarily an integer,

$$\Psi_k(sa) = e^{iksa} U_n(k, sa)$$

(2-6)

Since our rectangular box of atoms represents any such box chosen within the crystal away from edge effects, the boundary conditions must be periodic in x, y and z i.e.

$$\Psi(sa) = \Psi(sa + Na)$$

(2-7)

$$e^{iksa} U_n(sa) = e^{ik(sa + Na)} U_n(sa + Na) \qquad (2\text{-}8)$$

U_n has period, 'a' by definition, so

$$e^{iksa} = e^{ik(sa + Na)} \qquad (2\text{-}9)$$

$$e^{iksa} = e^{iksa} e^{ikNa} \qquad (2\text{-}10)$$

$$e^{ikNa} = 1 \qquad (2\text{-}11)$$

$$kNa = 2n\pi \qquad (2\text{-}12)$$

where n is an integer so that equation 2-12 expresses the quantisation of momentum or k states. Hence in our hypothetical portion of crystal, the length in k space associated with a single energy state is

$$\Delta k_x = \frac{2\pi}{N_x a} \Delta n = \frac{2\pi}{L_x} \qquad (2\text{-}13)$$

And the volume in k space associated with a single energy state is,

$$\Delta k_x \Delta k_y \Delta k_z = \frac{(2\pi)^3}{L_x L_y L_z} \qquad (2\text{-}14)$$

Each energy state can accommodate two electrons with opposite spin, so the volume in k space associated with a single electron state is,

$$\frac{\Delta k_x \Delta k_y \Delta k_z}{2} = \frac{(2\pi)^3}{2 L_x L_y L_z} \qquad (2\text{-}15)$$

Since k is a vector, the volume in k space associated with values in the range k to k+dk is simply the volume of a hollow sphere of radius k and thickness dk, which is $4\pi k^2 dk$. The number of allowed electron states in this range is therefore,

$$\frac{8\pi k^2 dk L_x L_y L_z}{(2\pi)^3} = \left(\frac{k}{\pi}\right)^2 L_x L_y L_z dk \qquad (2\text{-}16)$$

and the number of states dN per unit volume (real space) with wave vector values in the range k to k+dk is,

$$dN = \left(\frac{k}{\pi}\right)^2 dk \qquad (2\text{-}17)$$

From the parabolic approximation to E(k) at the bottom of the conduction band (equation 2-3), we have,

$$k = (E - E_c)^{\frac{1}{2}} \left(\frac{2m_e^*}{\hbar^2}\right)^{\frac{1}{2}} \qquad (2\text{-}18)$$

$$dk = \frac{m_e^*}{\hbar^2 k} dE = \frac{m_e^*}{\hbar^2} (E - E_c)^{-\frac{1}{2}} \left(\frac{2m_e^*}{\hbar^2}\right)^{-\frac{1}{2}} dE \qquad (2\text{-}19)$$

Substituting equations 2-18 and 2-19 into equation 2-17,

$$dN = \frac{4\pi}{h^3} (E - E_c)^{\frac{1}{2}} (2m_e^*)^{\frac{3}{2}} dE = N_c(E)dE \qquad (2\text{-}20)$$

where $N_c(E)$ is the density of electron states near the bottom of the conduction band. Similarly, for holes near the top of the valence band, the density of states is given by,

$$dN = \frac{4\pi}{h^3} (E - E_v)^{\frac{1}{2}} (2m_h^*)^{\frac{3}{2}} dE = N_v(E)dE \qquad (2\text{-}21)$$

To calculate the numbers of electrons and holes in the conduction and valence bands we need not just the density of possible states, but the probability that they are occupied at a given temperature. This probability may be found for any ensemble of particles by considering their number and their total energy to give the probability of finding particles at any particular energy. Electrons are fermions. They have anti-symmetric wave functions, they are indistinguishable and they obey Pauli's exclusion principle which allows only two electrons of opposite spin to occupy the same energy level. From statistical mechanics, the resulting distribution function for such particles is the Fermi-Dirac distribution function,

$$F(E) = \frac{1}{1 + \exp\left(\dfrac{E - E_F}{kT}\right)} \qquad (2\text{-}22)$$

E_F is the Fermi energy level which represents the maximum energy occupied by electrons at T=0K or the highest filled energy level when all possible electron states are filled beginning with the lowest energy and leaving no gaps. The value of E_F clearly depends on the distribution of electron states and the number of electrons that must be accommodated in them, and thus varies from material to material.

2.1.3 Intrinsic semiconductor in thermodynamic equilibrium

An intrinsic semiconductor contains no impurity donor or acceptor atoms so that all free carrier generation is due to electrons crossing the band gap into the conduction band and leaving equal numbers of holes in the valence band. In practice it is not possible to grow crystals which are completely free of impurities, but the term intrinsic is used for material which is not intentionally doped with donors or acceptors, and in which the concentration of carriers due to impurities is less significant than that thermally generated.

The density $dn(E)$ of electrons in the conduction band with energies in the range E to E+dE is simply the product of the density of available states, $N_C(E)$ and the probability of their being occupied, $F(E)$. From equations 2-20 and 2-22 this is,

$$dn(E) = N_C(E)F(E)dE$$

$$= \frac{4\pi}{h^3} (2m_e^*)^{\frac{3}{2}}(E - E_C)^{\frac{1}{2}}\left(1 + \exp\frac{E - E_F}{kT}\right)^{-1} dE \qquad (2\text{-}23)$$

and to obtain the density of electrons in the entire conduction band we may integrate dn(E) from E_C to ∞ since $F(E)$ tends rapidly to zero with E.

$$n_i = \int_{Ec}^{\infty} dn(E) \qquad (2\text{-}24)$$

To further simplify the integration we may also exchange the Fermi-Dirac distribution function for the classical Maxwell-Boltzman distribution function since $E-E_F \gg kT$ across the integration range.

$$n_i = \frac{4\pi(2m_e^*)^{\frac{3}{2}}}{h^3} \int_{Ec}^{\infty} (E - E_C)^{\frac{1}{2}} \exp\left(- \frac{E - E_F}{kT}\right)dE \qquad (2\text{-}25)$$

which can be easily solved to give,

$$n_i = \frac{2}{h^3} (2\pi m_e^* kT)^{\frac{3}{2}} \exp\left(- \frac{E_C - E_F}{kT}\right) \qquad (2\text{-}26)$$

$$= N_C \exp\left(- \frac{E_C - E_F}{kT}\right) \qquad (2\text{-}27)$$

where N_C is called the effective density of states in the conduction band. The density of holes in the valence band is calculated in exactly the same way, using $N_V(E)$ rather than $N_C(E)$ and remembering that the probability that an allowed state is occupied by a hole is just $1-F(E)$, the probability that it is not occupied by an electron. The result is,

$$p_i = \frac{2}{h^3} (2\pi m_h^* kT)^{\frac{3}{2}} \exp\left(- \frac{E_F - E_V}{kT}\right) \qquad (2\text{-}28)$$

$$= N_V \exp\left(- \frac{E_F - E_V}{kT}\right) \qquad (2\text{-}29)$$

To find the value of the Fermi energy level, E_F we equate equations 2-27 and 2-29, since in an intrinsic semiconductor the number of holes in the valence band must be equal to the number of electrons in the conduction band. Re-arranging for E_F, this gives,

$$E_F = \frac{E_C+E_V}{2} + \frac{kT}{2} \ln \frac{N_V}{N_C} = \frac{E_C+E_V}{2} + \frac{3}{4} kT \ln \frac{m_h^*}{m_e^*} \qquad (2\text{-}30)$$

Since the effective masses of electrons and holes, m_e^* and m_h^* are generally of the same order of magnitude, this places E_F close to the centre of the band gap, midway between E_C and E_V.

For ideal intrinsic GaAs,

$$\frac{m_e^*}{m_o} = 0.067 \qquad\qquad \frac{m_h^*}{m_o} = 0.082 \qquad\qquad (2\text{-}31)$$

where m_o is the electron rest mass, and from equation 2-30, this gives,

$$E_F = \frac{E_C + E_V}{2} + 0.004eV \qquad\qquad (2\text{-}32)$$

From equations 2-26 to 2-29 and equation 2-31, the effective densities of states in GaAs are,

$$N_C = 4.7 \times 10^{17} cm^{-3} \qquad\qquad N_V = 7.0 \times 10^{18} cm^{-3} \qquad\qquad (2\text{-}33)$$

and combining equations 2-27, 2-32 and 2-33 the intrinsic carrier concentration at 300K is,

$$n_i = p_i = 1.79 \times 10^6 cm^{-3} \qquad\qquad (2\text{-}34)$$

This represents a lower limit for the thermally generated charge carrier density in ideal intrinsic GaAs at room temperature, and compares with $1.45 \times 10^{10} cm^{-3}$ for Si and $2.4 \times 10^{13} cm^{-3}$ for Ge. Thus the leakage, or dark current in an ideal GaAs detector will be several orders of magnitude less than in an equivalent Si or Ge detector with a corresponding reduction in noise. This makes GaAs appear more attractive for use as a detector at room temperature.

Another important quantity for all semiconductors is the product of n_i and p_i which, since $n_i = p_i$, is equal to, and usually referred to as n_i^2.

$$n_i^2 = N_C N_V \exp\left(-\frac{E_C - E_V}{kT}\right) = AT^3 \exp\left(-\frac{E_g}{kT}\right) \qquad\qquad (2\text{-}35)$$

where A is a material constant and E_g is the band gap width.
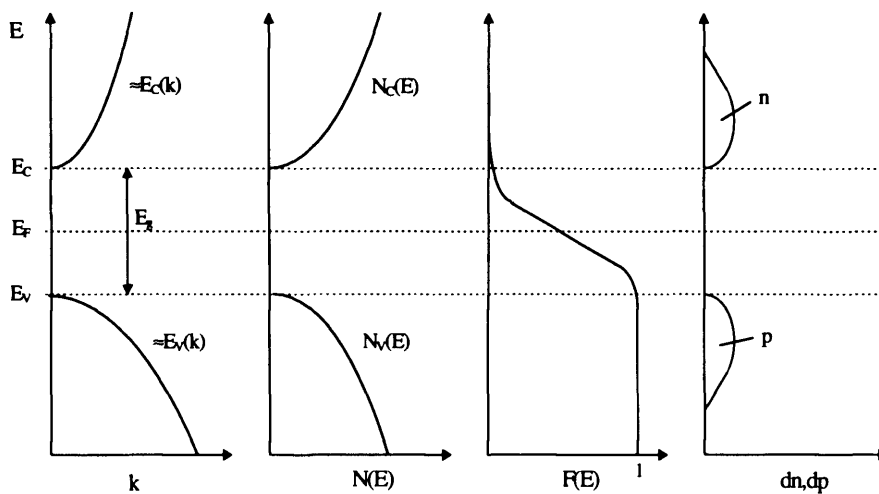
Figure 2-4 A schematic showing the parabolic approximation to E(k), the density of states, the Fermi-Dirac distribution, n and p for an intrinsic semiconductor.

2.1.4 Extrinsic semiconductor in thermal equilibrium

An extrinsic semiconductor is one in which donor or acceptor impurities introduce a significant density of electrons into the conduction band (n type semiconductor) or holes into the valence band (p type semiconductor). Equations 2-27 and 2-29 still give the electron and hole densities but the 'i' is dropped from the notation to indicate that the material is not intrinsic.

$$n = N_C \exp\left(-\frac{E_C - E_F}{kT}\right) \tag{2-36}$$

$$p = N_V \exp\left(-\frac{E_F - E_V}{kT}\right) \tag{2-37}$$

The effect of the doping however, is to move the Fermi energy level by changing the form of the charge neutrality condition from n=p in the intrinsic case to,

$$n + N_A^- = p + N_D^+ \tag{2-38}$$

where N_A^- is the density of ionised acceptors and N_D^+ is the density of ionised donors. The position of the Fermi energy level may be expressed in terms of n and p by dividing equation 2-36 by equation 2-37 and re-arranging to give,

$$E_F = \frac{E_C + E_V}{2} + \frac{kT}{2} \ln \frac{N_V}{N_C} + \frac{kT}{2} \ln \frac{n}{p} = E_i + \frac{kT}{2} \ln \frac{n}{p} \tag{2-39}$$

Where E_i indicates the Fermi level in the intrinsic case. Hence, adding donor impurities will move the Fermi level towards E_C and increase the density of electrons in both the conduction and valence bands. There are no new available states in these bands, so there is a corresponding reduction in the hole density and the product of n and p does not change from its value in the intrinsic case (=n_i^2). That np is independent of E_F may be demonstrated by multiplying equation 2-36 by equation 2-37,

$$np = N_C N_V \exp\left(-\frac{E_g}{kT}\right) = n_i^2 \tag{2-40}$$

The energy levels of significant semiconductor impurities are generally sufficiently close to the band edges (far from the Fermi level), that all the impurity atoms may be considered to be ionised. For a real semiconductor under normal operating conditions it may invariably be assumed that the majority carrier density will be due almost entirely to these ionised impurities. Hence for an n type semiconductor, n≈N_D and since np=n_i^2,

$$p = \frac{n_i^2}{n} \approx \frac{n_i^2}{N_D} \tag{2-41}$$

Substituting this into equation 2-39 gives,

$$E_F = E_i + kT \ln \frac{N_D}{n_i} \tag{2-42}$$

and for a p type semiconductor,

$$E_F = E_i - kT \ln \frac{N_A}{n_i}$$

(2-43)
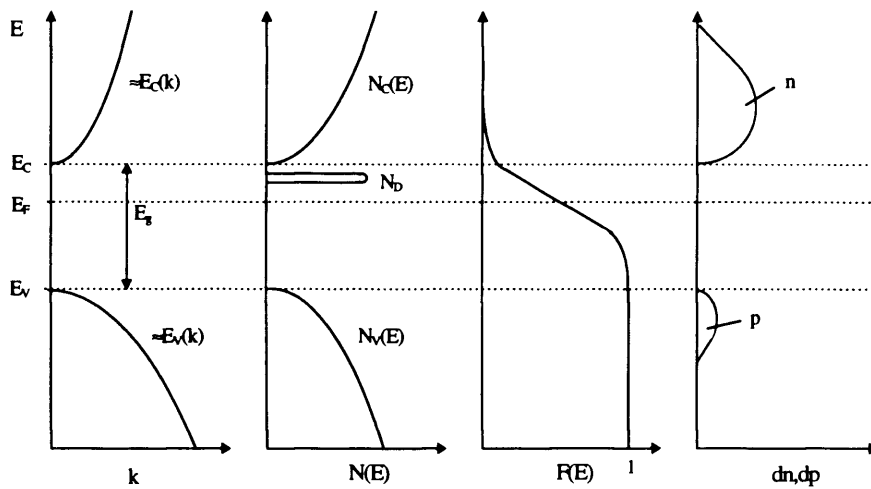
Figure 2-5 A schematic showing the parabolic approximation to E(k), the density of states, the Fermi-Dirac distribution, n and p for an n-type semiconductor.

2.1.5 The effects of deep energy levels

Except for samples of the purest epitaxial material, GaAs contains a significant concentration of impurities whose associated energy levels are close to the middle of the band gap and hence the intrinsic Fermi level. Because of their distance from the band edges, these are referred to as deep levels or deep traps, and their presence drastically alters the material behaviour [Sumner, T.J., 1992, Nava, F., 1994, Bencivelli, W., 1995, Bertin, R., 1990, Beaumont S.P., 1992/1993].

As indicated in figure 2-4 and figure 2-5, the Fermi-Dirac distribution function (equation 2-22) varies rapidly around the Fermi level and only very gradually elsewhere. In the absence of any deep levels, increases in the free electron concentration, n, (due to the introduction of donors for instance), require a corresponding decrease in the free hole concentration, p. These variations in concentration may be small, but since they occur in the conduction and valence bands some distance from the intrinsic Fermi level, where the distribution function is varying very gradually, they represent a large movement in the Fermi level. The concentration of ionised deep levels close to the intrinsic Fermi energy where the distribution function is varying rapidly is, on the other hand, extremely sensitive to small movements in the Fermi level and hence the change in occupancy of these levels required to satisfy the Fermi-Dirac distribution for even a fairly large change in n or p, requires only a very small movement of the Fermi level. The Fermi level is said to be 'pinned' close to the centre of the band gap.

Deep levels also act as traps and recombination/generation centres, accelerating charge loss and reducing carrier lifetime. The high density of deep levels in bulk GaAs places its charge transport behaviour in the realm of relaxation, rather than lifetime materials. These levels also introduce space charge which effects the profile of the electric and potential fields across devices in accordance with Poisson's equation. These characteristics are covered in subsequent sections.

2.2 X-ray interactions in Semiconductor Materials
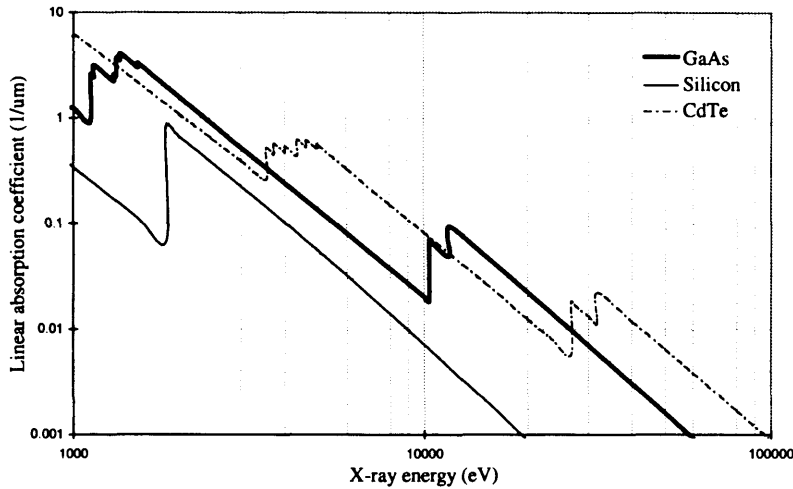
Figure 2-6 The total linear absorption coefficients of GaAs, Silicon and CdTe

There are three principal mechanisms by which X-rays interact with matter; photoelectric absorption, Compton scattering and pair production. Associated with each there is a linear absorption coefficient, and the total linear absorption coefficient is the sum of all three.

$$\mu_t = \mu_{ph} + \mu_{co} + \mu_{pp} \qquad (2\text{-}44)$$

μ_t is the probability per unit path length that a given photon is removed from an incident beam, and the intensity, I, of a beam of initial intensity I_o after traversing an absorber of thickness t, is

$$I = I_o \exp(-\mu t) \qquad (2\text{-}45)$$

The relative probabilities of photo-electric, Compton or pair production interactions are proportional to the relative magnitudes of μ_{ph}, μ_{co} and μ_{pp}. Pair production is only significant at very high incident X-ray energies.

2.2.1 Photoelectric absorption

In the photoelectric absorption process, a photon's energy is completely transferred to an absorber atom which then ejects an energetic photoelectron from one of its bound shells. In a diatomic crystal such as GaAs which has equal numbers of gallium and arsenic atoms, the relative probability that a given photon is absorbed by a gallium or an arsenic atom is proportional to the relative magnitudes of

their linear absorption coefficients at that energy. The interaction is with the whole atom and cannot occur with free electrons. The energy of the photoelectron is equal to the energy of the photon minus the binding energy with which the electron was held in its shell.

$$E_e = h\nu - E_b \qquad (2\text{-}46)$$

The steps, or edges in the photo-electric absorption versus energy curve, indicate the binding energies of the K and L shell electrons and the size of each step indicates the jump ratio, or the relative probability that the ejected electron will be from the K, L or M shell.

As well as a photoelectron, the interaction also leaves an ionised absorber atom with a vacancy in one of its bound shells. This vacancy will be filled through the capture of a free electron or by the rearrangement of electrons from other shells with the consequent emission of one or more characteristic X-ray photon. These 'fluorescence' X-rays have well defined energies, and although they are largely reabsorbed near to their point of origin, some fraction will escape from the crystal altogether. The total energy deposited within the detector after a fluorescence X-ray escapes will be less than that deposited if the fluorescence X-ray is reabsorbed, giving rise to the characteristic "escape" peaks in an X-ray spectrum. Some fraction of fluorescence X-rays are reabsorbed within the atom that produced them, resulting in the ejection of a fast 'Auger' electron from an outer shell. The relative probability of de-excitation by fluorescence or auger emission is given by the fluorescence yield.
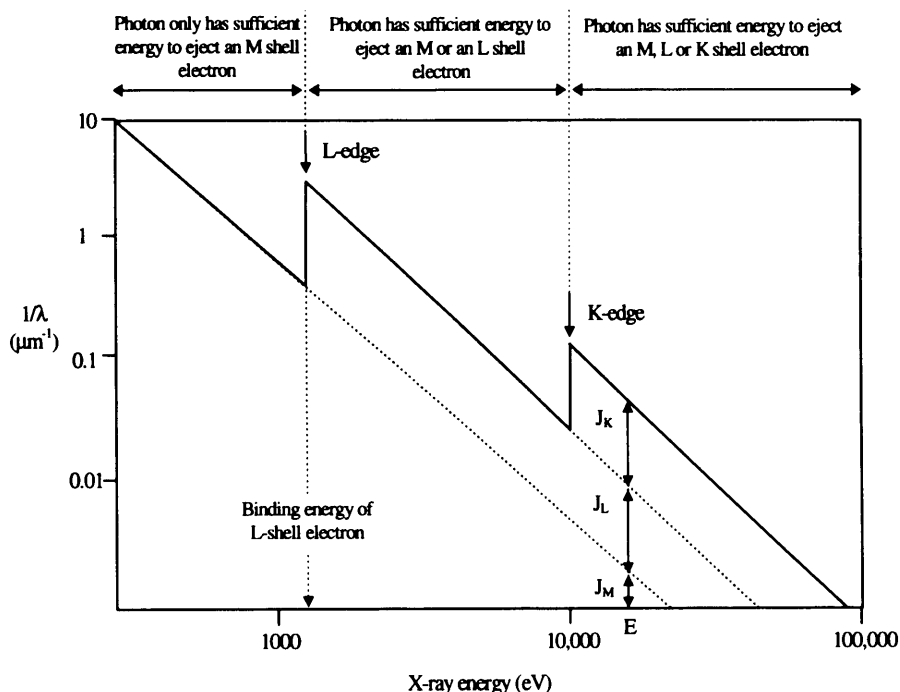
Figure 2-7 Schematic indicating how the steps in the linear attenuation coefficient give the relative contributions to the total absorption by K, L and M shell electrons (jump ratios, J).

$$\text{Probability that a k shell de-excites by fluorescence} = \frac{Z^4}{32^4 + Z^4} \qquad (2\text{-}47)$$

36

$$\text{Probability that an l shell de-excites by fluorescence} \ = \ \frac{Z^4}{89^4 \ + \ Z^4}$$

Table 2-1 K and L shell fluorescent yields for silicon, gallium, arsenic, cadmium and tellurium.

Atom	Z	K-shell fluorescent yield (%)	L-shell fluorescent yield (%)
silicon	14	3.5	0.1
gallium	31	46.8	1.5
arsenic	33	53.1	1.9
cadmium	48	83.5	7.8
tellurium	52	87.5	10.4

2.2.2 Compton scattering

Compton scattering takes place between an incident photon and an electron in the absorbing material. The electron is assumed to be initially at rest and the photon is deflected through an angle θ, with a resultant transfer of energy to the electron. Since all scattering angles are possible, the amount of energy transferred can vary from zero to a large fraction of the photons energy. An equation relating energy transferred to scattering angle can be derived simply from the conservation of energy and momentum.

$$hv' \ = \ \frac{hv}{1 \ + \ \dfrac{hv}{m_o c^2} \ (1 \ - \ \cos \ \theta)} \tag{2-48}$$

where hv is the energy of the photon before the interaction, hv' is the energy of the photon after the interaction and $m_o c^2$ is the rest mass energy of an electron. The probability of Compton scattering per atom of the absorber depends on the number of electrons available as scattering targets and therefore increases linearly with Z. The angular distribution of the scattered photons is given by the Klein-Nishina formula for the differential scattering cross section $d\sigma/d\Omega$ [Knoll, G.F.,1989].

$$\frac{d\sigma}{d\Omega} \ = \ Zr_o^2 \left(\frac{1}{1+\alpha(1-\cos\theta)} \right)^2 \left(\frac{1+\cos^2\theta}{2} \right) \left(1+ \frac{\alpha^2(1-\cos\theta)^2}{(1+\cos^2\theta)(1+\alpha(1-\cos\theta))} \right) \tag{2-49}$$

r_o is the classical electron radius and $\alpha = hv/m_o c^2$.

The maximum energy transfer from photon to electron occurs when the X-ray is scattered through 180°. This gives a well defined upper limit to the energy that may be deposited by Compton interactions (the Compton edge observed in X-ray spectra). From equation 2-48 we have, for a 180° scatter,

$$hv' \ = \ \frac{hv}{1 \ + \ 2 \ \dfrac{hv}{m_o c^2}} \tag{2-50}$$

and the energy of the Compton edge is simply,

37

$$hv - hv' = hv - \frac{hv}{1 + 2\frac{hv}{m_o c^2}}$$

(2-51)

The rest mass energy of an electron ($m_o c^2$) is 511 keV. Hence, for a 59.5 keV Am-241 X-ray the Compton edge is at 11.2 keV, and for a 122 keV Co-57 X-ray the Compton edge is at 39.5 keV.

2.3 The depletion region in a Schottky diode

In order to measure the charge or current due to carrier generation in a semiconductor when a photon is absorbed, it is necessary first to ensure that some volume of the detector is 'active'. That is that carriers generated within this region will give rise to a signal in the output circuit. This is invariably achieved (regardless of detector geometry) by application of a suitable bias potential which will cause the electrons and holes to migrate. Rather than simply applying ohmic electrodes, a diode structure is usually employed so that under reverse bias, the active volume of the detector is depleted of majority carriers, eliminating a major source of noise.

The formation of a rectifying junction (a diode) by the application of a suitable metal to form a Schottky barrier, and the extent of the resulting depletion region which forms in the detector under bias, will be outlined in the following sections. The depletion region width is particularly important when considering the detection of high energy photons since it defines the active thickness and hence the efficiency of the detector.

2.3.1 The Schottky barrier

The formation of a rectifying junction by the application of a metal to an n-type semiconductor with a smaller work function will be described. Theoretically, other configurations will also produce a rectifying barrier, such as applying metal to a p-type semiconductor with a larger work function, but this has not been demonstrated successfully on GaAs material.

If the surface of an n-type semiconductor is brought into intimate contact with a metal which has a larger work function ϕ_m (the amount of energy required to lift an electron from the Fermi level to the vacuum level), so that electrons are free to move between them, then this constitutes a new system. The Fermi level cannot remain different for two regions of the same system so there will be a flow of electrons from the semiconductor into the metal, until the Fermi level is constant across the system. Close to the junction, the metal has an increased negative charge due to the influx of electrons and this will be balanced by a positively charged region in the semiconductor, formed as electrons retreat from the increased negativity of the metal. The region is said to be depleted and is analogous to the depletion region at a pn junction.

Because there is no shortage of allowed states in a metal's 'electron sea', the negatively charged region due to extra conduction electrons is confined to about 0.5 Å (the Thomas-Fermi screening distance) and in detector configuration may be considered negligible. In the semiconductor on the other hand, the carrier density is far lower, and a significantly wide region must be depleted to balance the negative charge. The change in potential or band bending due to the migration of carriers produces the characteristic step or Schottky barrier. An important reference point in determining the barrier height is the electron affinity, χ_s, of the semiconductor which is a measure of the bottom of the conduction band from the vacuum level just inside the surface of the semiconductor. For an ideal junction, the electron affinity, unlike the Fermi level ϕ_s in the semiconductor does not change when the bands bend.
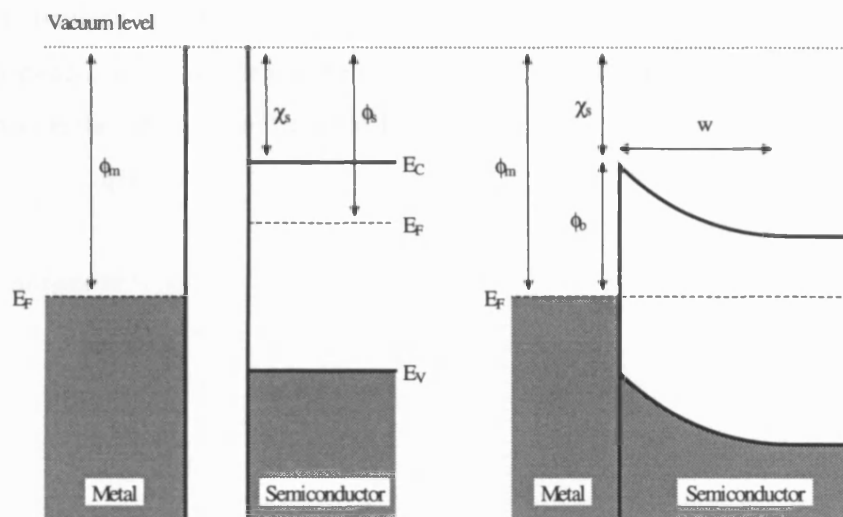
Figure 2-8 The formation of a Schottky barrier. The barrier height $\phi_b = \phi_m - \chi_s$

2.3.2 Depletion

The barrier height for GaAs Schottky diodes is approximately 0.8V and is largely independent of the choice of metal (a consequence of Fermi level pinning due to surface states). Applying forward bias lowers the barrier and causes electrons to flow from the semiconductor into the metal but applying reverse bias increases the barrier height and causes the depletion region to extend further into the semiconductor. The extent of this region w, (and the magnitude of the electric field across it) can be increased until the device breaks down. The most significant source of current that can flow under reverse bias is due to carriers generated within the depletion region itself. This generation may be thermal which gives rise to leakage (or dark) current, or may be due to the absorption of a photon or particle. Schottky diodes therefore have I-V characteristics broadly similar to pn diodes. The I-V curves of bulk GaAs devices have a characteristic slope under forward bias. This is a feature of relaxation material in which a significant proportion of carriers are lost to recombination in traversing the semiconductor. This loss is proportional to the time taken and thus inversely proportional to the

velocity of the carriers and the current measured therefore increases gradually with applied bias rather than 'switching on' suddenly.

In order to predict the active depth and model charge transport within a semiconductor detector, it is necessary to know how the potential and electric fields vary as a function of position, bias voltage and impurity concentration. The charge density and electric field are related via Poisson's equation,

$$\frac{dE}{dx} = \frac{d^2\psi}{dx^2} = -\frac{\rho}{\varepsilon_s} \qquad (2\text{-}52)$$

It is frequently possible to calculate or assume a charge distribution under bias, and hence to calculate the electric field across a device, one common example being the depletion approximation. Here the active region is assumed to end abruptly a distance w into the semiconductor, and to have a uniform charge density $\rho=qN_D$ across it. Clearly the electric field varies linearly (since ρ is constant), from a value of qN_Dw/ε_s at the interface, to 0 at x=w. Hence,

$$E(x) = -\frac{qN_D(w - x)}{\varepsilon_s} \qquad (2\text{-}53)$$

which may be integrated to give the potential,

$$\psi_{(x)} = -\int_x^w \frac{qN_D(w - x)}{\varepsilon_s} \, dx \qquad (2\text{-}54)$$

$$= -\frac{qN_D}{2\varepsilon_s} (w - x)^2 \qquad (2\text{-}55)$$

The value of the potential at the junction, or the total potential across the device is referred to as the diffusion potential V_d and is simply the value of equation 2-55 for x=0.

$$V_d = \frac{qN_D w^2}{2\varepsilon_s} \qquad (2\text{-}56)$$

Since the barrier height is generally less than a volt, and detectors are typically operated with an applied bias V_b of hundreds or even thousands of volts, $V_d \approx V_b$ and re-arranging equation 2-56,

$$w \approx \sqrt{\frac{2\varepsilon_s V_b}{qN_D}} \qquad (2\text{-}57)$$

This depletion or active width dependence on $V^{1/2}$ is well known and may be applied to any semiconductor device in which the space charge density ρ may be assumed constant across the depletion region. This includes silicon and epitaxial GaAs devices.

The electric field in bulk GaAs devices is heavily influenced by the contribution to the space charge of partially filled deep levels and the depletion approximation cannot be applied. Figure 2-9 shows measurements made using a simple probe [Berwick, K., 1993]. These indicate an electric field comprising two regions, one similar to that predicted by the depletion approximation, the other (closest to the interface) having zero net space charge and a constant electric field. This shape is

40

analogous to the Mott barrier, first proposed as an alternative to the Schottky barrier in 1938 [Mott N.F., 1938].
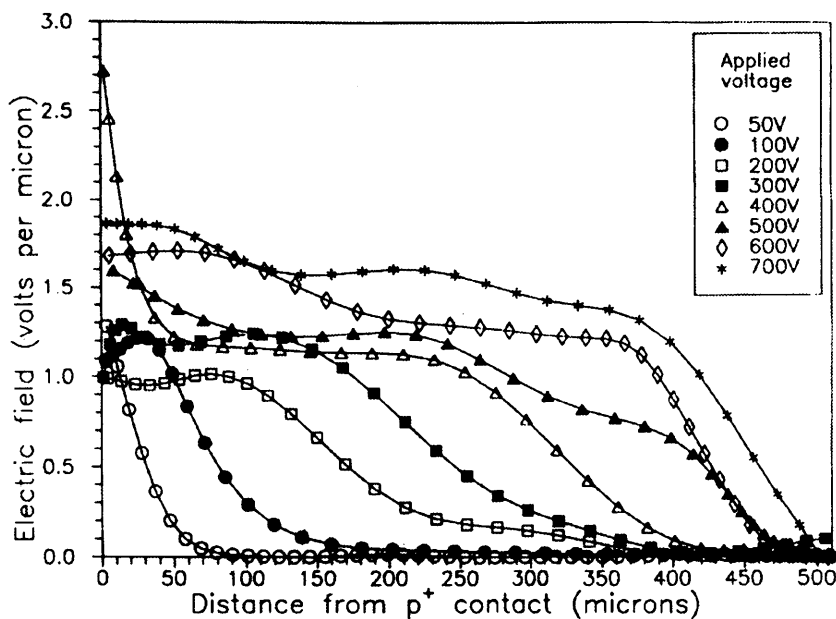
Figure 2-9 The electric field in a bulk GaAs diode measured using a simple probe [Berwick, K., 1993]. The flat portion adjacent to the interface indicates that at a limiting value of the electric field, the net space charge becomes zero and the field can rise no further.

In order to calculate correctly the electric and potential fields across the depletion region, it is necessary to calculate the space charge as a function of position $\rho(x)$. This means that as well as the densities of electrons, holes, ionised shallow donors and ionised shallow acceptors, the density of ionised deep levels is fundamentally important in bulk GaAs. This density is critically dependent upon the trap energy level relative to E_F and hence on the band bending or local potential. Iterative numerical techniques must therefore be used to solve equation 2-52 in this case.

An important consequence of the electric field having this form is that the depletion width will vary linearly with bias voltage rather than as $V^{1/2}$. This electric field shape and the linear variation of w with V_b have been points of some contention in recent years, but the work contained in this thesis provides evidence in support of both.

2.3.3 Electric field models (after McGregor)

Un-doped semi-insulating (SI) LEC bulk GaAs material can be produced with a very low free carrier concentration (10^6-10^7cm^{-3}), yet bulk GaAs devices behave as extrinsic, rather than intrinsic semiconductor detectors. This is because the low free carrier concentration and high resistivity of such semi-insulating material is achieved by the compensation of residual shallow acceptor impurities (usually carbon) with the native deep donor defect, EL2 [Willardson, R.K., 1984, Bourgoin, J.C., 1988]. Thus, although the net free carrier concentration is very low, the material contains a high

density of energy states between the conduction and valence bands which act as trapping and recombination sites. These sites will have a strong influence on the electric field across the device and hence the depletion region width, since their ionisation state will determine the space charge density [McGregor, D.S., 1992, DiLorenzo, J.V., 1982]. A simple model was put to good effect by D.S. McGregor in 1993 [McGregor, D.S., 1994] in which one type of shallow acceptor, deep acceptor, shallow donor, and deep donor are present in the band gap, giving, according to Poisson's equation,

$$\frac{\partial E}{\partial x} = \frac{q}{\varepsilon_s} \left(N_d^+(x) - N_a^- + N_{DD}^+ - N_{AA}^- - n(x) + p(x) \right) \qquad (2\text{-M1})$$

where N_{DD} is the deep donor concentration, N_{AA} is the deep acceptor concentration, N_d is the shallow donor concentration, N_a is the shallow acceptor concentration (+ and - indicating ionisation), n is the electron concentration, p is the hole concentration, q is the charge of an electron, and ε_s is the dielectric constant of the material. McGregor et. al. assumed typical values of between 10^{14}cm^{-3} and 10^{15}cm^{-3} for shallow acceptor concentrations and $\sim 10^{16} \text{cm}^{-3}$ for the deep donor EL2 concentration. They assumed the shallow dopants to be fully ionised and developed a number of electric field models for a Schottky barrier diode under various conditions of deep acceptor concentration, and deep level ionisation by solving equation (2-M1).

In the case where the material is intrinsic or the case where the impurities are perfectly balanced, the net space charge in the detector volume is zero and equation (2-M1) indicates that the electric field in this case will have zero gradient and will therefore be a constant across the full width of the depletion region under reverse bias. This is never observed, and the intrinsic model fails to account for the experimentally observed pulse height characteristics of bulk GaAs diodes under front and back irradiation with photons and charged particles.

In the case where a high density of shallow acceptors (e.g. Carbon), and a high density of deep donors (Eg. EL2) entirely dominate the material, equation (2-M1) predicts an electric field with two distinct regions. The measured energy level of the deep donor EL2 is approximately 0.8 eV below the conduction band edge [Willardson, R.K., 1984, Bourgoin, J.C., 1988] and assuming the Fermi level to be near mid-gap, these deep donors are not fully ionised. The ionised concentration of donors is

$$N_{DD}^+ = N_{DD} \left\{ 1 - \frac{1}{1 + \frac{1}{2} \exp\left(\dfrac{E_{DD} - E_{fn}}{kT} \right)} \right\} \qquad (2\text{-M2})$$

where E_{DD} is the energy level of the deep donor, and E_{fn} is the n quasi-Fermi energy [McKelvey, J.P., 1986]. Adjacent to a Schottky barrier, where the bands are bent upwards, the energy difference between the deep donor level and the quasi-Fermi level increases and hence, so does the degree of ionisation. This band bending and ionisation increases with the application of reverse bias. The result

(shown in figure 2-M1) is two regions, one of fully ionised deep donors extending from the Schottky contact into the device, with a correspondingly high space charge and hence electric field gradient, and the other containing only partially ionised deep donors, with a much lower space charge and a much more gradual drop in electric field. In this case the application of voltage causes the active region to extend further across the detector, and the electric field will fall to zero before reaching the rear contact. This two zone electric field distribution is a more promising representation of the depletion region in bulk GaAs, however, the solution of Poisson's equation for the high space charge in the fully ionised region, predicts that the active depth would be only a few microns with the application of several hundred volts. Again, this is not supported by any experimental evidence.
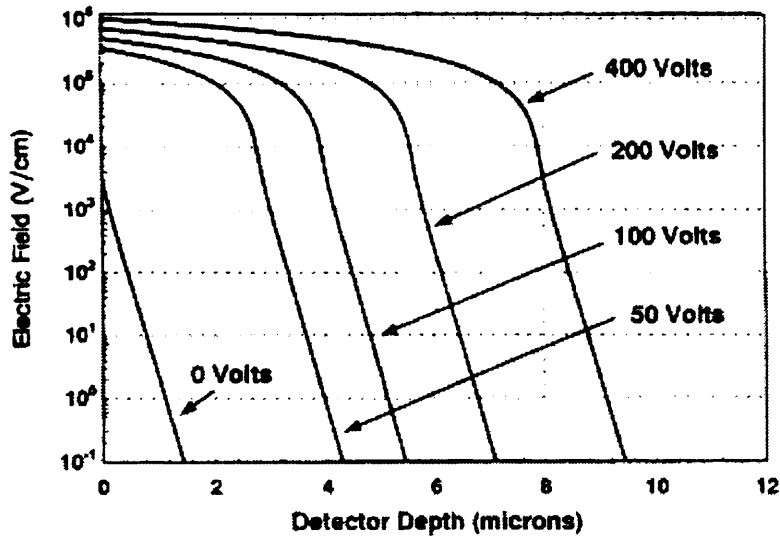
Fig 2-M1 Calculated electric field distribution for high density of deep donors, reproduced from [McGregor et. al., 1994].

It has often been demonstrated however, that the deep donor level EL2 is accompanied by a deep acceptor level 0.2 eV above the valence band edge [Elliot, K.R., 1982, Figielski, T, 1984]. This deep acceptor is thought to be associated with the Ga anti-site (Ga_{As}) and if present in a concentration which is significantly large by comparison with the ~0.8eV EL2 level concentration, then the space charge in the active region will reflect the net concentration of ionised deep donors minus ionised deep acceptors. The concentration of ionised deep acceptors is given by

$$N_{AA}^- = N_{AA} \left\{ 1 - \frac{1}{1 + \frac{1}{4} \exp\left(\frac{E_{fp} - E_{AA}}{kT}\right)} \right\}$$

(2-M3)

where E_{AA} is the deep acceptor energy and E_{fp} is the p quasi-Fermi energy. A lower net charge density in the active region causes the electric field to extend further into the detector bulk. The extent of the depletion region into the device at a given value of reverse bias, will then depend upon the net space charge or the relative concentrations of ionised donors and acceptors. This case is shown for typical deep level densities, in figure 2-M2.

43

In reference [McGregor, D.S., 1994], McGregor et. al. go on to consider the case in which $N_{DD} = N_{AA}$ i.e., the total concentration of deep acceptors is equal to the total concentration of deep donors which they describe as 'highly improbable'. In this case, the solution of Poisson's equation, and hence the expected electric field distribution would depend entirely on the concentration of shallow dopants.
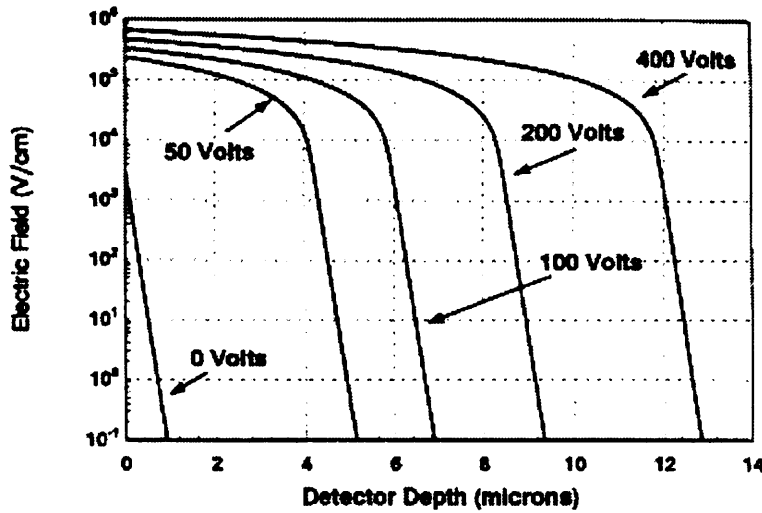
Fig 2-M2 Calculated electric field distribution for high density of deep donors and deep acceptors, reproduced from [McGregor et. al., 1994].

The space charge across the depletion region could be considered to be constant since the shallow impurities will all be ionised, and the solution to Poisson's equation could be obtained using the depletion approximation, as for an intrinsic silicon device. Assuming that the concentration of shallow dopants is far less than that of EL2, the electric field would then extend much further into the detector bulk (figure 2-M3).
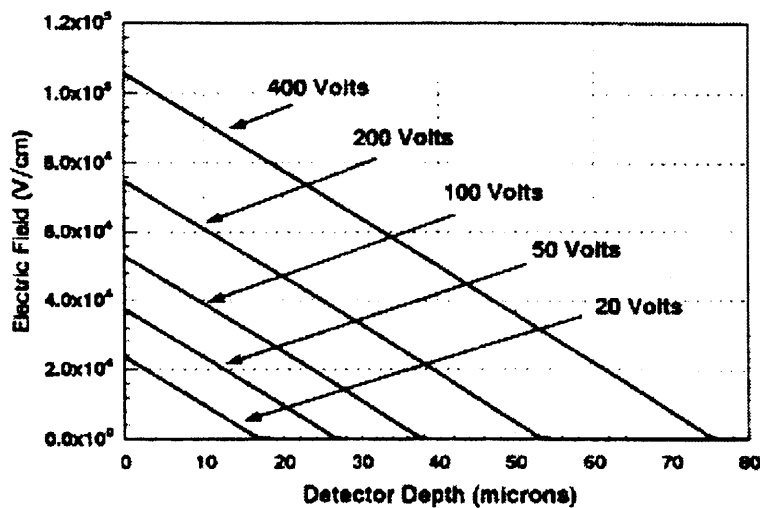

Fig 2-M3 Calculated electric field distribution for density of deep donors equal to density of deep acceptors, reproduced from [McGregor et. al., 1994].

It is of course highly unlikely that $N_{DD} \equiv N_{AA}$, and in any case, this model would indicate that the electric field should demonstrate a growing active region depth that is proportional to $\sqrt{V}$, and real

44

devices consistently show a linear relationship. It is possible however, that for the case of the E_c-0.8eV donor and the E_v+0.2eV acceptor in GaAs, the concentrations could be very similar, if as has been suggested recently, they are related to the same trap complex (possibly a Ga_{As} anti-site and a gallium vacancy).

This then is a simple model which may go some way towards explaining the electric field distribution in bulk GaAs. Measurements of electric field profiles made by Berwick and Brozel (figure 2-9) have indicated however that there appears to be a limiting value in any given sample, above which the electric field will not rise, forming a plateau. The extent of the depletion region then varies linearly with bias as indicated by numerous experimental results (see chapter 4). A more complex model proposed by McGregor et. al., perhaps explains rather better this limiting electric field.

Summarising an extract from reference [McGregor, D.S., 1994]. The EL2 trap has been shown to undergo dramatic changes in carrier capture cross section and emission rate with increasing electric field strength [Prinz, V.Ya., 1980,1982]. The electron emission rate approaches a minimum at an electric field of around $10^5 Vcm^{-1}$. Beyond this the emission rate increases by several orders of magnitude which may be attributed to impact ionisation of the deep levels from injected electrons. Also, the measured EL2 concentration appears to decrease with the free electron density and with increased leakage current [Pantelides, S.T., 1992]. The electron and hole capture rates for EL2 have been reported to increase several orders of magnitude near a critical electric field, E_c of about 10^4 Vcm^{-1} [Prinz, V.Ya., 1980]. If the electron capture rate is higher than the electron emission rate near E_c, then the leakage current through a reverse biased Schottky contact may therefore create a quasi-neutral region. The steady state ionised deep donor concentration in this case can be approximated by [Look D.C., 1989]

$$N_{DD}^+ = \frac{N_{DD}}{1 + \frac{n\sigma_n v_e}{e_n}} \tag{2-M4}$$

where σ_n is the deep donor electron capture cross section in cm^2 and e_n is the deep donor electron emission rate per second. If the thermionic leakage current through the Schottky contact is substantial, then the deep donors will no longer be fully ionised which may account for the reported reduction in the measured EL2 concentration with increased leakage current [Pantelides S.T., 1992]. The room temperature electron capture cross section for EL2 reportedly increases from approximately $10^{-15}cm^2$ at low electric fields to $10^{-13}cm^2$ at electric fields near 10^4 Vcm^{-1} [Prinz, V.Ya., 1983]. The room temperature emission rate for EL2 is approximately $0.1s^{-1}$ at electric fields below 10^5 Vcm^{-1} [Look, D.C., 1981]. A common leakage current of 100nA for a 4mm diameter device results in an electron density (n) approximately equal to $5 \times 10^5 cm^{-3}$ flowing through the depletion region. Assuming saturated carrier velocities (10^7 cms^{-1}), equation (2-M4) gives an ionised fraction for EL2 of 0.95 at low electric fields. However, at high electric fields where the electron

capture cross section increases to $10^{-13}cm^2$, the ionised fraction reduces to 0.17. Therefore, the ionised concentration of EL2 deep donors is reduced to the same order of magnitude as the ionised shallow carbon acceptor concentration. This condition supports the interesting possibility that the electric field enhanced capture of electrons can produce a quasi-neutral region in the device depletion region (or active region). The effect may be modelled by altering equation (2-M2) such that the ionisation of the deep levels decreases dramatically at electric fields approaching E_c i.e.

$$N_{DD}^+ = N_{DD}\left\{ 1 - \frac{1}{1 + \frac{1}{2}\exp\left(\frac{E_{DD} - E_{fn}}{kT}\right)} \right\} - f(N_{DD}, E) \qquad (2\text{-}M5)$$

where $f(N_{DD}, E)$ is a filling function that strongly increases the number of filled EL2 traps as the electric field approaches E_c. Since the actual filling function is unknown, McGregor et. al. selected an arbitrary function to represent the rapid filling of the deep donor centres at fields approaching E_c. The modelled result was a depletion region width which varied linearly with reverse bias, and an electric field (figure 2-M4) comprising two distinct regions. In the first region, the electric field remains almost constant up to an extended distance into the detector bulk. In the second region, the electric field drops abruptly due to the high concentration of ionised deep donors in this lower field region. The modelled pulse height characteristics for ionising radiation indicate a behaviour that closely resembles measured results.
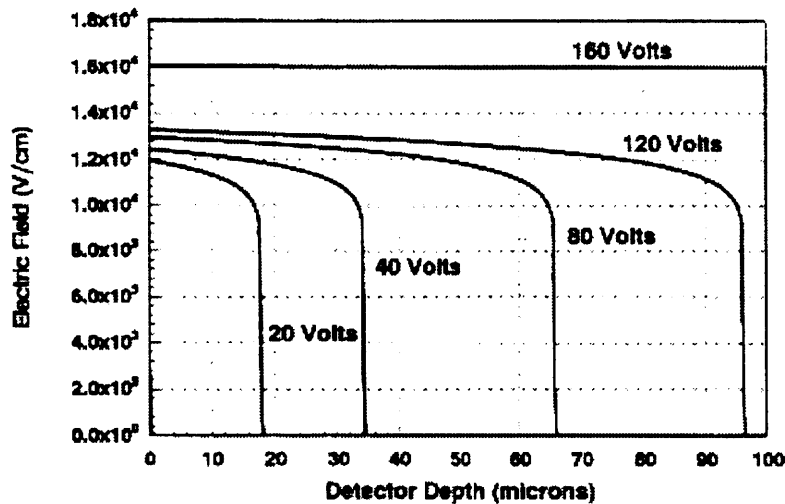
Fig 2-M4 Calculated electric field distribution for case of deep levels which refill at high values of electric field, reproduced from [McGregor et. al., 1994].

McGregor et. al. therefore proposed that the field enhancement of the EL2 capture cross section coupled with a low emission rate promotes the formation of a quasi-neutral region at high electric fields and that the EL2 centres do not remain filled, but that the time averaged effect of the EL2 centres filling and emptying produces a quasi-neutral region at sufficiently high fields.

46

2.4 Charge transport, trapping and recombination

Under a potential gradient (non zero electric field), charge carriers, generated for example, by an X-ray interaction in the depletion region, will migrate through a crystal lattice with a net 'drift' velocity (v_d). The work done by the output circuit in moving the carriers through the potential difference may be measured since all of the electrons in the circuit must move correspondingly, building up a charge on the plates of a parallel capacitor with a magnitude proportional to the work done. In order to maximise the signal to noise ratio, and to prevent depth dependent variations in the signal measured for a given quantity of generated charge, it is important that all of the charge carriers generated within the depletion region are moved to the zero and maximum potentials (for holes and electrons respectively). Bulk GaAs contains a high density of traps (energy levels deep within the band gap), which seriously degrade spectral resolution by trapping carriers and making the charge collection efficiency a function of interaction depth in the depletion region.

In order to quantify charge loss due to trapping, it is necessary to know the carrier drift velocities and the trapping or recombination rate. The drift velocity of electrons and holes in an electric field is often expressed in terms of a mobility, but this assumes a linear relationship which is only reasonable in GaAs at very low electric field strengths. Measured electron and hole $v_d(E)$ relationships are often preferable and these are shown in figure 2-10 [Sze, S.M., 1981].
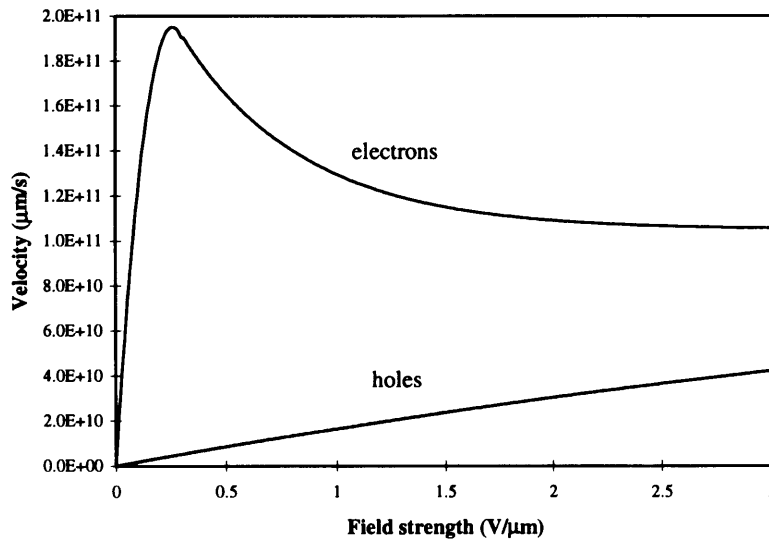
Figure 2-10 Carrier velocities in GaAs

The recombination rate R in $cm^{-3}s^{-1}$ of charge carriers due to a single allowed energy level in the band gap, is given by

$$R = \frac{\sigma_p \sigma_n v_{th}(pn - n_i^2)N_t}{\sigma_n\left(n + n_i \exp\left(\dfrac{E_t - E_i}{kT}\right)\right) + \sigma_p\left(p + n_i \exp\left(-\dfrac{E_t - E_i}{kT}\right)\right)} \qquad (2\text{-}58)$$

where σ_n and σ_p are the electron and hole trap cross sections, v_{th} is the carrier <u>thermal</u> velocity, n_i is the intrinsic carrier density, N_t is the trap density, E_t is the trap energy level and E_i is the intrinsic Fermi level. Although written in terms of a single trap energy, this equation may also be used to characterise multiple energy levels or trap complexes in terms of <u>effective</u> trap cross sections, densities and energy levels. Equation 2-58 can generally be simplified for conditions of low injection into an n or a p type semiconductor etc. In the depletion region of a wide band gap semiconductor detector we may assume that n_i, n_o and p_o are small in relation to the injected n and p. If we further assume that the loss of electrons is largely independent of the injected hole density, but depends primarily on the density of unoccupied energy states in the band gap (direct band to band recombination, whilst allowed, is a somewhat slower process than the charge loss observed), then we may consider an independent electron trap of density N_{tn}. Similarly we may consider holes to be captured principally by the emptying of initially occupied energy levels in the band gap and may characterise these states occupied at equilibrium as hole traps of density N_{tp}. In this way we may consider the electron and hole trapping separately and write,

$$R_n = \sigma_n v_{thn} N_{tn}(n - n_o) \qquad (2\text{-}59)$$

$$R_p = \sigma_p v_{thp} N_{tp}(p - p_o) \qquad (2\text{-}60)$$

the independent recombination rates R_n and R_p for electrons and holes, when n & p $\gg n_i$. Generally, one may express carrier loss in terms of a time constant τ such that,

$$R_n = \frac{(n - n_o)}{\tau_n} \qquad (2\text{-}61)$$

$$R_p = \frac{(p - p_o)}{\tau_p} \qquad (2\text{-}62)$$

where $(n-n_o)$ and $(p-p_o)$ represent the excess carrier densities (due to the absorption of an X-ray for instance). Combining equations 2-59 and 2-60 with equations 2-61 and 2-62, we have

$$\tau_n = \frac{1}{\sigma_n v_{thn} N_{tn}} \qquad (2\text{-}63)$$

$$\tau_p = \frac{1}{\sigma_p v_{thp} N_{tp}} \qquad (2\text{-}64)$$

the electron and hole lifetimes which may be used to calculate the fraction of carriers which remain un-trapped after time t as,

$$\textit{fraction not trapped} = \exp\left(-\frac{t}{\tau}\right) \qquad (2\text{-}65)$$

The thermal velocity is given by, [Blakemore, J.S., 1982]

$$v_{thn} = 4.4x10^5 \sqrt{\frac{T}{300}} \tag{2-66}$$

$$v_{thp} = 1.77x10^5 \sqrt{\frac{T}{300}}$$

Any local imbalances in the numbers of holes and electrons trapped will leave the material in a state other than equilibrium, and this will be corrected by subsequent de-trapping which also has an associated time constant. This de-trapping time constant may be measured as an increase in the charge collection efficiency with increasing integration time and may be expressed very simply in terms of temperature and trap activation energy as,

$$\tau_{re} = C_e \exp\left(-\frac{E_{ae}}{kT}\right) \tag{2-67}$$

$$\tau_{rh} = C_h \exp\left(-\frac{E_{ah}}{kT}\right) \tag{2-68}$$

where E_{ae} and E_{ah} are electron and hole trap activation energies respectively, and C_e and C_h are constants.

2.5 Pulse formation

A pulse is formed in the circuit connected to a detector, because work is done by the circuit to move the charge carriers through the applied potential difference and **not** because the carriers are actually collected at the electrodes. Thus to obtain a pulse which is truly proportional to the energy of the absorbed photon, all of the holes must be moved from the interaction point to the zero potential, and all of the electrons to the maximum potential. The contribution to the measured pulse height of any given charge carrier is proportional to the fraction of the potential difference through which it is moved before it is trapped. In order to calculate the fractional pulse height or charge collection efficiency (CCE) as a function of interaction depth, one must therefore first consider the fractions of charge carriers which are **not** trapped in moving a distance Δx at a point x within a detector.

$$f_e(x \rightarrow x+\Delta x) = \exp[-\Delta x / (v_{de}\tau_n)] \tag{2-69}$$

$$f_h(x \rightarrow x-\Delta x) = \exp[-\Delta x / (v_{dh}\tau_p)] \tag{2-70}$$

which are identical to equation 2-65 with t= $\Delta x/v_d$. τ is the trapping time constant at x from equations 2-63 and 2-64, and v_d is the drift velocity at x which may be taken directly from the data in figure 2-10 if the electric field strength at x is known or can be approximated. Equations 2-69 and 2-70 give the fraction of carriers which are not trapped in traversing Δx, typically within nanoseconds of generation by X-ray absorption. The integration time associated with pulse formation in the readout

circuit is generally of the order of microseconds however, and depending on the trap release time constants given by equations 2-67 and 2-68, it is often the case that a significant fraction of the initially trapped charge will be released within the integration time and contribute to the measured pulse height. The fraction of charge carriers traversing Δx, which is un-trapped after a pulse integration time t is therefore,

$$f_e(x \rightarrow x+\Delta x) = 1 - (1 - \exp[-1/(v_{de}\tau_n)]).\exp(-t/\tau_{re}) \qquad (2\text{-}71)$$

$$f_h(x \rightarrow x-\Delta x) = 1 - (1 - \exp[-1/(v_{dh}\tau_p)]).\exp(-t/\tau_{rh}) \qquad (2\text{-}72)$$

where τ_{re} is the electron trap release time constant and τ_{rh} is the hole trap release time constant.

Assuming that the numbers of carriers which are trapped more than once within the integration time are negligible, equations 2-71 and 2-72 accurately describe the trapping within an interval Δx. The fraction of electrons or holes remaining un-trapped in moving from an initial depth, z to some other depth, y is therefore simply the product of the intervening values of $f(x \rightarrow x+\Delta x)$ or $f(x \rightarrow x-\Delta x)$, depending on carrier type. For the case $f(x \rightarrow x+\Delta x)$, assuming a step size of Δx, this may be expressed as,

$$fraction\ untrapped\ z\ to\ y \ = \ \prod_{x=z,z+\Delta x...}^{x=y} f(x \ \rightarrow \ x \ + \ \Delta x) \qquad (2\text{-}73)$$

and the fractional contribution to the signal measured in moving the un-trapped charge carriers through Δx at y, is simply the work done, or the potential through which they must be moved as a fraction of the total potential across the detector. If the electric field at y is E(y) then the contribution to the signal is,

$$contribution\ to\ signal\ at\ y \ = \ \frac{\Delta x E(y)}{V_b} \prod_{x=z,z+\Delta x...}^{x=y} f(x \ \rightarrow \ x \ + \ \Delta x) \qquad (2\text{-}74)$$

where Vb is the applied bias. In order to calculate the fractional pulse height or charge collection efficiency for an interaction depth z, it is necessary to sum all of the signal contributions for electrons moving from z towards the maximum potential and holes moving from z towards the minimum potential. Thus

$$CCE(z) \ = \ \sum_{y=z,z-\Delta x...}^{y=0} \left\{ \frac{\Delta x E(y)}{V_b} \prod_{x=z,z-\Delta x...}^{x=y} f_h(x \ \rightarrow \ x \ - \ \Delta x) \right\}$$
$$+ \ \sum_{y=z,z+\Delta x...}^{y=thick} \left\{ \frac{\Delta x E(y)}{V_b} \prod_{x=z,z+\Delta x...}^{x=y} f_e(x \ \rightarrow \ x \ + \ \Delta x) \right\} \qquad (2\text{-}75)$$

where the minimum potential is at z=0 and the maximum potential is at z=*thick*, the depletion region thickness. Equation 2-75 may be solved once E(x), fe(x) and fh(x) (equations 2-71 and 2-72) have been calculated, to give the Charge Collection Efficiency as a function of X-ray interaction depth.

If a photon is absorbed near to the positive electrode, the pulse will be formed principally by the movement of holes, and similarly, a photon absorbed near to the negative electrode will form a pulse principally by the movement of electrons. Hence, in a material where electrons and holes are subject to different degrees of trapping, the size of the pulse generated will depend not only on the energy of the incident photon, but on the depth within the detector at which the absorption took place. At higher bias, the carriers move faster and trapping is significantly reduced.

2.6 Detector characteristics

2.6.1 Energy resolution

The energy resolution of a spectroscopic detector is its ability to distinguish between photons with similar but different energies. In order to do this it is important that all sources of noise are minimised to give the narrowest possible spectral peak and resolution is therefore commonly expressed in terms of the full width of a peak at half its amplitude. This is equal to 2.36σ where σ is the total noise or the standard deviation of the measured signal at the point of binning.

Since the energy associated with the generation of an electron hole pair is ω, the number of charge carriers generated by the absorption of an X-ray of energy E is simply,

$$N = \frac{E}{\omega} \qquad (2\text{-}76)$$

If carrier generation were a truly random process, then the standard deviation in this number would be,

$$\sigma = \sqrt{N} = \sqrt{\frac{E}{\omega}} \qquad (2\text{-}77)$$

but since charge carriers are not completely independent at the point of generation, the process is not entirely random and the standard deviation is somewhat less. This is quantified by the introduction of the Fano factor such that,

$$\sigma = \sqrt{FN} = \sqrt{\frac{FE}{\omega}} \qquad F < 1 \qquad (2\text{-}78)$$

The energy required to generate an electron hole pair (ω) in a semiconductor detector is typically about 4eV and the Fano factor (F) is typically about 0.1 which means that the best possible or 'Fano limited' energy resolution for a typical semiconductor detector is about 0.6% at 10keV. This sort of resolution can only be approached however, if all other sources of peak broadening can be minimised. These fall into two categories: broadening due to charge trapping and loss within the depletion region (σ_t) which was discussed in the previous section, and broadening due to noise in the

readout electronics and particularly in the pre-amplifier FET (σ_e). The total standard deviation is given by the quadratic sum of all three sources of noise,

$$\sigma = \sqrt{\frac{FE}{\omega} + \sigma_t^2 + \sigma_e^2} \qquad \text{electrons} \qquad (2\text{-}79)$$

and the full width at half maximum (FWHM) of a spectral peak is therefore given by,

$$FWHM = 2.36\omega\sqrt{\frac{FE}{\omega} + \sigma_t^2 + \sigma_e^2} \qquad \text{eV} \qquad (2\text{-}80)$$

The electronic noise may include significant contributions due to FET characteristics and leakage current, but is invariably a linear function of detector capacitance which places restrictions upon detector area.

2.6.2 Quantum Efficiency (QE)

Another important characteristic of any detector, (particularly in applications where measured fluxes are likely to be low), is its quantum efficiency, or the fraction of incident X-rays which are actually detected. In an ideal detector with negligibly thin electrodes (a reasonable approximation only at high X-ray energies), the quantum efficiency is roughly equal to the linear absorption,

$$QE = 1 - \frac{I}{I_o} = 1 - \exp(-\mu_s d) \qquad (2\text{-}81)$$

where μ_s is the linear attenuation coefficient of the semiconductor at the relevant X-ray energy and d is the depletion region width. To calculate the effect of any number of absorbing layers in front of the depletion region (electrode structure, dead layer etc.) one must multiply equation 2-81 by the product of the transmissions through them. Thus [Fraser, G.W., 1989[1]],

$$QE = \left(\Pi_m \exp(-\mu_m t_m)\right)\left(1 - \exp(-\mu_s d)\right) \qquad (2\text{-}82)$$

where μ_m is the linear attenuation coefficient of the mth absorbing layer and t_m is its thickness.

The depletion region width, d is the most difficult parameter to determine in equation 2-82, since the edge of the depletion region is rarely well defined (except perhaps in a 'fully depleted' detector) and those X-rays which are absorbed in partially depleted regions where the electric fields are weak, may be subject to trapping and spreading which distorts the measured pulse.

The theory which has been presented in this chapter will be referred to throughout the rest of the thesis, most specifically in chapter 4 (Bulk Material Devices), chapter 5 (Modelling Spectral Response) and appendix A (Modelling A Small Pixel CCD X-ray Polarimeter). Epitaxial growth theory is specific to chapter 6 (Epitaxial Material), and is therefore covered separately in that chapter. Similarly, theory relating to the analysis of epitaxial samples by Hall, Deep Level Transient

Spectroscopy (DLTS) and Capacitance Voltage (CV) measurements which are standard techniques, is covered in chapter 3 (Experimental Techniques).

3. EXPERIMENTAL TECHNIQUES

In this chapter, the basic techniques, equipment and facilities used to perform the measurements reported in this thesis, will be presented. These include fabrication of the basic detector test structures, measurement of diode characteristics and measurement of spectral response to X-rays and protons. GaAs grown by Liquid Phase Epitaxy (LPE) in conjunction with EEV Ltd (see chapter 6), was analysed using a four point Hall probe at EEV to establish carrier mobility and density. Samples were sent to ANSTO (the Australian Nuclear Science and Technology Organisation) and Sheffield University to investigate traps by Deep Level Transient Spectroscopy (DLTS) and Capacitance Voltage (CV) measurements and to Loughborough University, to analyse chemical composition by Glow Discharge Mass Spectroscopy (GDMS). Surface morphology was studied using a Scanning Electron Microscope (SEM) at Leicester University.

3.1 The Schottky diode test structure
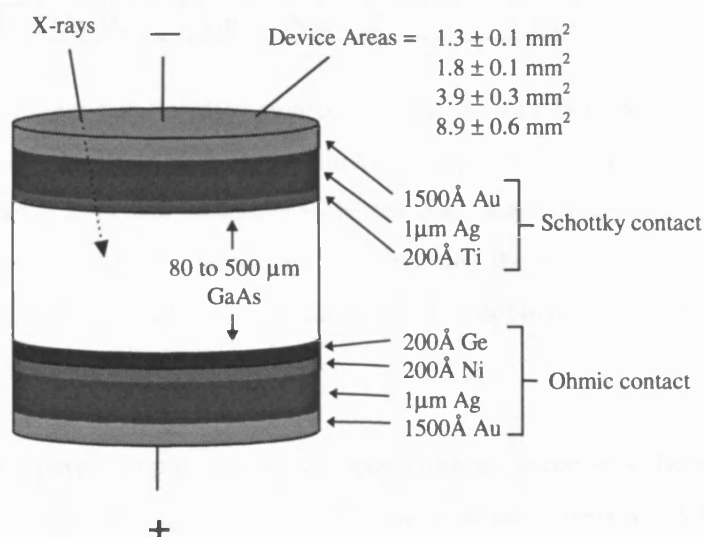
Figure 3-1 Cross section of the diode structure employed.

In order to evaluate bulk and epitaxial GaAs in the laboratory, in terms of both its intrinsic properties, and X-ray detection, a simple diode structure was employed (figure 3-1). Bulk material was procured from MCP Wafertech, Showa Denko K.K. and Outokumpu Semitronic. Table 3-1 gives the specifications for a wafer supplied by Showa Denko K.K. which is typical of the material used for detector fabrication. These wafers were 300 and 500μm thick but selective back thinning was used to increase the range of device thickness available for evaluation. The material from all three sources was grown by the Liquid Encapsulated Czochralski (LEC) method, was semi-insulating and had a <100> orientation. Several of the bulk devices used were fabricated by the University of Glasgow and were 80μm thick with Schottky-Schottky rather than Schottky-Ohmic contacts.

Table 3-1 LEC bulk GaAs material specifications.

	SPECIFICATION	ACTUAL
Growth Method	LEC	LEC
Conductivity Type	Semi-insulating	Semi-insulating
Dopant	None	None
Orientation	$(100)\pm0.5°$	(100) $|0.02°{\sim}0.04°|$
Resistivity (top)	$> 3\times10^7$ Ωcm	$4.7{\sim}5.3\times10^7$ Ωcm
Resistivity (bottom)	$> 3\times10^7$ Ωcm	$3.5{\sim}4.0\times10^7$ Ωcm
Mobility (top)	>7000 cm^2/Vs	$7.1{\sim}7.2\times10^3$ cm^2/Vs
Mobility (bottom)	>7000 cm^2/Vs	$7.2{\sim}7.3\times10^3$ cm^2/Vs
EPD (top)	<50000 cm^{-2}	3.6×10^4 cm^{-2}
EPD (bottom)	<50000 cm^{-2}	4.2×10^4 cm^{-2}
Carbon Concentration		1.8×10^{15} cm^{-3}
Diameter	50.8 ± 0.2 mmϕ	$50.80{\sim}50.81$ mmϕ
Primary Flat Position	$(0\underline{11})\pm0.5°$	$(0\underline{11})\pm0.5°$
Primary Flat Length	$14.23{\sim}17.52$ mm	16 mm
Secondary Flat Position	$(0\underline{1}1)\pm0.5°$	$(0\underline{1}1)\pm0.5°$
Secondary Flat Length	$6.35{\sim}9.65$ mm	8 mm
Thickness	300 ± 20 μm	$307{\sim}311$ μm
Front Surface Finish	Mirror Polished	Mirror Polished
Back Surface Finish	Mirror Polished	Mirror Polished

The metal chosen to form the Schottky contact for the devices fabricated by Leicester/EEV was titanium since work conducted at EEV during their development of solar cells has demonstrated that the adhesion between GaAs and titanium is better than that between GaAs and gold (gold is commonly used by non-industrial researchers). Electrically, the two junctions are almost identical, since the barrier height between GaAs and many metals is approximately 0.8V due to the effect of Fermi level pinning (chapter 2).

Similarly, the ohmic contact employed for the basic diode structure was the standard EEV contact formed by applying germanium and annealing. The external gold layers aid wire bonding, the silver layers are buffers, and the nickel ensures good adhesion between the silver and the germanium. The Glasgow fabricated devices also employed titanium Schottky contacts on the front and back.

Epitaxial GaAs was grown (see chapter 6) to a thickness of 5 to 100μm on n-type bulk GaAs substrates (300μm thick). No back thinning of the substrate was necessary, since the applied potential would be dropped principally across the high resistivity epitaxial layer. After growth and initial cleaning (by chemical etch), test structures identical to those employed on the bulk wafers were fabricated on the epitaxial layers.

3.2 Device fabrication

Fabrication of the Leicester University test structures was carried out at EEV Solar Power Systems. A custom mask (figure 3-2) was designed at Leicester to define very simple circular pads. Device areas ranged from 1.3 to 8.9mm^2 (figure 3-1), and in addition to this some pads also incorporated guard rings which were intended to prevent excessive leakage or dark current due to surface conduction. In the event, the fabrication process included a surface passivation with silicon nitride which eliminates surface currents by 'tying up' the dangling bonds and the guard rings were found to make no observable difference.
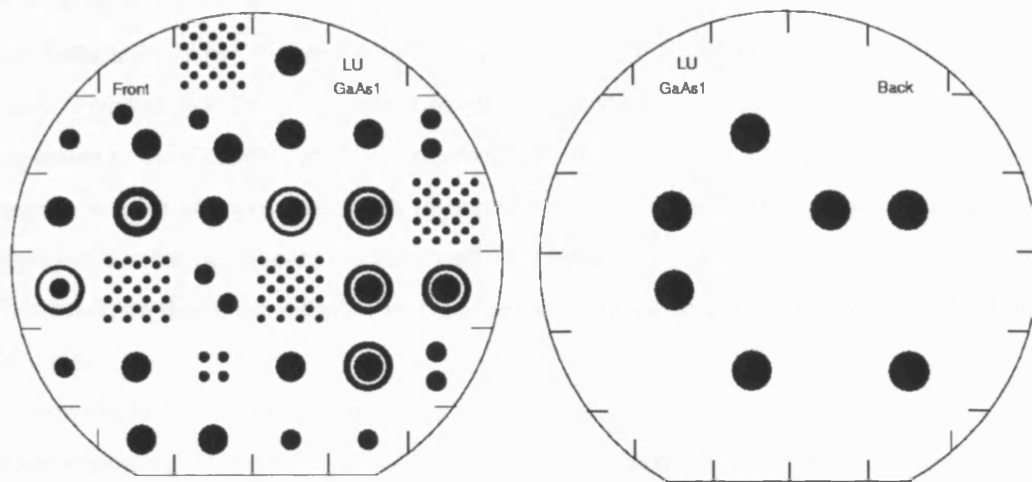
Figure 3-2 The front and back positive masks.

Much of the fabrication process employed is identical to the standard EEV solar cell procedure, a principal exception being the need to selectively back etch some of the bulk devices. The whole process consists of a number of process steps and these are set out below. For clarity, the fabrication procedures for bulk and epitaxial GaAs have been separated, but it will be seen that they are essentially the same with the exception of some cleaning and etching steps.

3.2.1 The fabrication process - bulk material

1. **Chemical clean** in a solution of 7.6g Superstrip 100 (a commercial gold stripping agent), 10g potassium cyanide and 20g EDTA in 1 litre H$_2$O. Wafers are immersed in an ultrasonic bath of the solution at 35°C for ~10 minutes.

2. **Apply silicon nitride passivation layer** to front surface. A Plasma Enhanced Chemical Vapour Deposition (PECVD) technique is used. The wafer is heated to 250°C under silane (SiH$_4$) and ammonia (NH$_3$). An RF field is then applied and silicon nitride is deposited on the wafer. The EEV process gives a layer approximately 750 to 800Å thick in 15 minutes.

3. **Apply black wax** to the whole front surface.

4. **Etch whole of rear surface** using 2 part citric acid (50g/litre) to 1 part hydrogen peroxide solution. This gives an etch rate of ~0.5μm/minute. A short etch simply removes any surface doping contamination. Longer etches (1 hour) used to thin the whole wafer.

5. **Chemical clean.** As 1.

6. **Pre-bake.** The wafer is dried at 115°C for 30 minutes to remove wet chemical residues and water absorbed from the atmosphere.

7. **Spin on photolith.** Rear surface. The wafer is placed on a turn-table and ELIR (Ethyl Lactate Image Reversal) photolith is liberally applied at its centre. Held in place by a vacuum, it is then spun at 3000rpm for 30 seconds. The viscosity of the photolith (38%) is such that this results in a uniform layer ~5μm thick.

8. **Soft bake** at 95°C for 30 minutes to dry the photolith which shrinks to a thickness of 4 to 4.5μm. It also begins to develop so care must be taken not to bake too hot or for too long.

9. **Exposure** to 3.4±0.2mW/cm^2 UV radiation for 8 seconds under a positive mask. This is the first stage in a three part process which chemically alters the photolith making the exposed regions impervious to the developer. The pads defined by the mask correspond to some of the pads on the front mask, so that after selective etching, some of the devices will be considerably thinner than the wafer.

10. **Reversal bake** for 30 minutes at 115°C.

11. **Flood expose** to 3.4±0.2mW/cm^2 UV radiation for 5 minutes to complete the exposure process.

12. **Develop** by immersion in AZ-326 (brand name) for 2 minutes, which simply dissolves the photolith from those regions that were masked during the first UV exposure.

13. **De-scum.** Photolith residues (mostly hydrocarbons) are removed from the GaAs surfaces by a 1 minute exposure to oxygen plasma which reacts with them to form CO, CO_2 etc.

14. **Selectively etch** through the holes in the photolith for ~2 hours, using the same etch as in step 4 to remove ~60μm of GaAs.

15. **Remove photolith** by immersion in acetone for ~2 hours.

16. **De-scum.** As 13.

17. **Rinse in H$_2$O.**

18. **Chrome etch** for 1 minute to ensure that the exposed GaAs surfaces are as clean as possible.

19. **Rinse in H$_2$O.**

20. **Evaporate rear contact.** 200Å Ge, 200Å Ni, 1μm Ag and 1500Å Au are deposited in one run in a Leybold electron beam evaporator. This combination of metals is similar to the standard EEV solar cell rear contact which has been developed to give good adhesion and electrical integrity. The standard EEV contact, however, has a thicker Ag layer and a second Ni layer which acts as a buffer during ultrasonic welding.

21. **Alloy rear contact** for 15 seconds at 400°C under forming gas (95%N + 5%H) to drive Ge atoms into the GaAs surface, break down the metal-semiconductor interface and ensure that the contact is ohmic rather than rectifying.

22. **Pre-bake.** The wafer is dried at 115°C for 30 minutes to remove wet chemical residues and water absorbed from the atmosphere.

23. **Spin on photolith.** Front surface. As 7.

24. **Soft bake** at 95°C for 30 minutes to dry the photolith which shrinks to a thickness of 4 to 4.5μm. It also begins to develop so care must be taken not to bake too hot or for too long.

25. **Exposure** to 3.4±0.2mW/cm^2 UV radiation for 8 seconds under a positive mask. This is the first stage in a three part process which chemically alters the photolith making the exposed regions impervious to the developer.

26. **Reversal bake** for 30 minutes at 115°C.

27. **Flood expose** to 3.4±0.2mW/cm^2 UV radiation for 5 minutes to complete the exposure process.

28. **Develop** by immersion in AZ-326 (brand name) for 2 minutes, which simply dissolves the photolith from those regions that were masked during the first UV exposure.

29. **De-scum.** Photolith residues (mostly hydrocarbons) are removed from the silicon nitride surfaces by a 1 minute exposure to oxygen plasma which reacts with them to form CO, CO_2 etc. This is done prior to the removal of the silicon nitride layer itself in order to prevent the hydrocarbons coming into contact with the GaAs during that removal.

30. **Silicon nitride removed** from the exposed regions of the wafer by 2.5 minutes immersion in a mixture of ammonium fluoride (80 parts) and hydrogen fluoride (1 part).

31. **Rinse in H₂O.**

32. **Chrome etch** for 1 minute to ensure that the exposed GaAs surfaces are as clean as possible.

33. **Rinse in H₂O.**

34. **Evaporate front contact.** 200Å Ti, 1μm Ag and 1500Å Au are deposited in one run in a Leybold electron beam evaporator. This combination of metals is similar to the standard EEV solar cell front contact. The standard EEV contact, however, has a thicker Ag layer and a 300Å layer of Pd between the Ti and the Ag which prevents migration and blistering, making the contact more stable in the very long term.

35. **Lift off.** The remaining photolith is dissolved in acetone so that the metal coating is removed from those parts of the wafer where it is not required. Using an image reversal photolith and a positive mask gives the edges of the holes in the photolith an over-hanging profile so that the acetone can get under the metal. The lift off process takes a couple of hours but the timing is not crucial.

36. **Rinse in H2O.**

37. **The wafer is sawn up.**

38. **Some devices are annealed** for 15 seconds at 400°C under forming gas (95%N + 5%H) to drive Ti atoms into the GaAs surface, forming a p-type layer and giving a PiN rather than a Schottky junction. All devices are now ready to be mounted on PCBs for evaluation.

3.2.2 The fabrication process - epitaxial material

1. **Swab with warm ($\approx$30°C) IPA** to remove residual gallium from the surface. Bulk wafers do not require this swabbing stage since they are bought in as epi-ready and are therefore already clean.

2. **Chemical clean** in a solution of 7.6g Superstrip 100 (a commercial gold stripping agent), 10g potassium cyanide and 20g EDTA in 1 litre H_2O. Wafers are immersed in an ultrasonic bath of the solution at 35°C for 10 to 40 minutes until clean.

3. **More severe clean** is required if any traces of gallium remain (seen as small spheres under a microscope). Usually 10 minutes in an ultrasonic bath of 5% HCl solution at 35°C is sufficient.

4. **Evaporate rear contact.** 200Å Ge, 200Å Ni, 1μm Ag and 1500Å Au are deposited in one run in a Leybold electron beam evaporator. This combination of metals is similar to the standard EEV solar cell rear contact which has been developed to give good adhesion and electrical integrity. The standard EEV contact, however, has a thicker Ag layer and a second Ni layer which acts as a buffer during ultrasonic welding.

5. **Alloy rear contact** for 15 seconds at 400°C under forming gas (95%N + 5%H) to drive Ge atoms into the GaAs surface, break down the metal-semiconductor interface and ensure that the contact is ohmic rather than rectifying.

6. **Apply silicon nitride passivation layer** to front surface. A Plasma Enhanced Chemical Vapour Deposition (PECVD) technique is used. The wafer is heated to 250°C under silane (SiH_4) and ammonia (NH_3). An RF field is then applied and silicon nitride is deposited on the wafer. The EEV process gives a layer approximately 750 to 800Å thick in 15 minutes.

7. **Pre-bake.** The wafer is dried at 115°C for 30 minutes. Note that this step may be omitted if the wafer can be transferred directly from 'passivation' to 'spin on', otherwise it is necessary to remove wet chemical residues and water absorbed from the atmosphere.

8. **Spin on photolith.** The wafer is placed on a turn-table and ELIR (Ethyl Lactate Image Reversal) photolith is liberally applied at its centre. Held in place by a vacuum, it is then spun at 3000rpm for 30 seconds. The viscosity of the photolith (38%) is such that this results in a uniform layer ~5μm thick.

9. **Soft bake** at 95°C for 30 minutes to dry the photolith which shrinks to a thickness of 4 to 4.5μm. It also begins to develop so care must be taken not to bake too hot or for too long.

10. **Exposure** to 3.4±0.2mW/cm^2 UV radiation for 8 seconds under a positive mask. This is the first stage in a three part process which chemically alters the photolith making the exposed regions impervious to the developer.

11. **Reversal bake** for 30 minutes at 115°C.

12. **Flood expose** to 3.4±0.2mW/cm^2 UV radiation for 5 minutes to complete the exposure process.

13. **Develop** by immersion in AZ-326 (brand name) for 2 minutes, which simply dissolves the photolith from those regions that were masked during the first UV exposure.

14. **De-scum.** Photolith residues (mostly hydrocarbons) are removed from the silicon nitride surfaces by a 1 minute exposure to oxygen plasma which reacts with them to form CO, CO_2 etc. This is done prior to the removal of the silicon nitride layer itself in order to prevent the hydrocarbons coming into contact with the GaAs during that removal.

15. **Silicon nitride removed** from the exposed regions of the wafer by 2.5 minutes immersion in a mixture of ammonium fluoride (80 parts) and hydrogen fluoride (1 part).

16. **Rinse in H_2O.**

17. **Chrome etch** for 1 minute to ensure that the exposed GaAs surfaces are as clean as possible.

18. **Rinse in H_2O.**

19. **Evaporate front contact.** 200Å Ti, 1μm Ag and 1500Å Au are deposited in one run in a Leybold electron beam evaporator. This combination of metals is similar to the standard EEV solar cell front contact. The standard EEV contact, however, has a thicker Ag layer and a 300Å layer of Pd between the Ti and the Ag which prevents migration and blistering, making the contact more stable in the very long term.

20. **Lift off.** The remaining photolith is dissolved in acetone so that the metal coating is removed from those parts of the wafer where it is not required. Using an image reversal photolith and a positive mask gives the edges of the holes in the photolith an over-hanging profile so that the acetone can get under the metal. The lift off process takes a couple of hours but the timing is not crucial.

21. **Rinse in H_2O.**

22. **The wafer is sawn up** and the devices are ready to be mounted and evaluated.
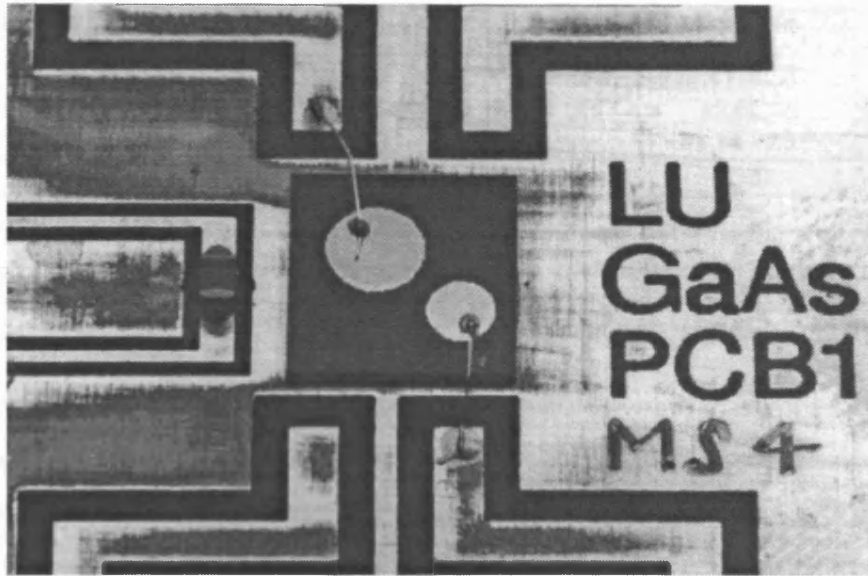
Figure 3-3 A device mounted on a PCB for evaluation.

Figure 3-3 shows a completed detector mounted on a PCB ready for evaluation. The thermistor can be seen to the left, attached to its tracks by silver loaded thermoplastic. In this case, the gold wire bonds are also connected (by hand) with conductive thermoplastic, although a commercial wire bonder was available for later samples. The numbering (MS4) indicates that the material is from MCP Wafertech, the device is a Schottky, rather than a PN diode, and it is the forth from its wafer.

3.3 Leakage current measurement

Current-Voltage characteristics have been measured throughout this work using a Tektronix 577 curve tracer. This has an inherent reading error in both voltage and current of approximately 3% due to the CRT display, grid and spot size. At very low values of current, the absolute error was ±1 nA determined by trace hysteresis. Offset errors were eliminated by zeroing prior to measurement, and other systematic errors were not observed. More accurate measurements, when required, were made using a DC supply and a pico-ammeter.

3.4 Equipment for measuring spectral response to X-rays

Spectral measurements were made using a Tennelec TC 170 charge sensitive pre amplifier and a TC 243 gaussian shaping amplifier giving peaking times of 1,2,4,8,16 and 24 µs. Detector bias was provided by a Tennelec HT power supply and a Tennelec pulse generator was used to evaluate system noise and for energy calibration.

Table 3-2 Tennelec TC 170 pre-amplifier specifications reproduced from manual.

Detector capacitance (pF)	Typical FWHM (keV) ts=2.0μs	Typical FWHM (keV) ts=0.5μs	Maximum FWHM (keV) ts=2.0μs	Typical risetime (ns 10 - 20%)	Maximum risetime (ns 10 - 20%)
0	0.95	1.2	1.4	3.5	5.0
10	1.1	1.5		3.5	
20	1.3	1.9		4.2	
50	1.8	3.1		5.2	
100	2.8	5.1	3.3	6.5	10.0

The pre-amplifier specifications quoted by Tennelec are given in table 3-2. The values of Full Width Half Maximum (FWHM) are for a silicon detector i.e. assuming a mean carrier generation energy of ω=3.65 eV per electron hole pair. Since ω=4.27 eV per electron hole pair in GaAs [Kobayashi, T., 1972/1976], the values of FWHM will be a factor of 4.27/3.65≈1.17 times greater. 'ts' refers to shaping time in μs and the values of risetime given in table 3-2 are based on a 10MeV equivalent input.

In order to reduce dark current and hence noise, and to investigate the effects of trap occupancy upon spectral form, two methods of cooling the detectors were employed. The first used a Peltier cooler mounted on a water cooled copper heat sink, and the second was a vacuum cryostat with a liquid nitrogen cooled cold finger and temperature control circuit. In conjunction with the Tektronix 577 curve tracer already discussed, these cooling systems also allowed reverse current to be measured as a function of temperature in order to obtain trap activation energy.

3.4.1 Peltier cooled system (-30 to +30 °C)
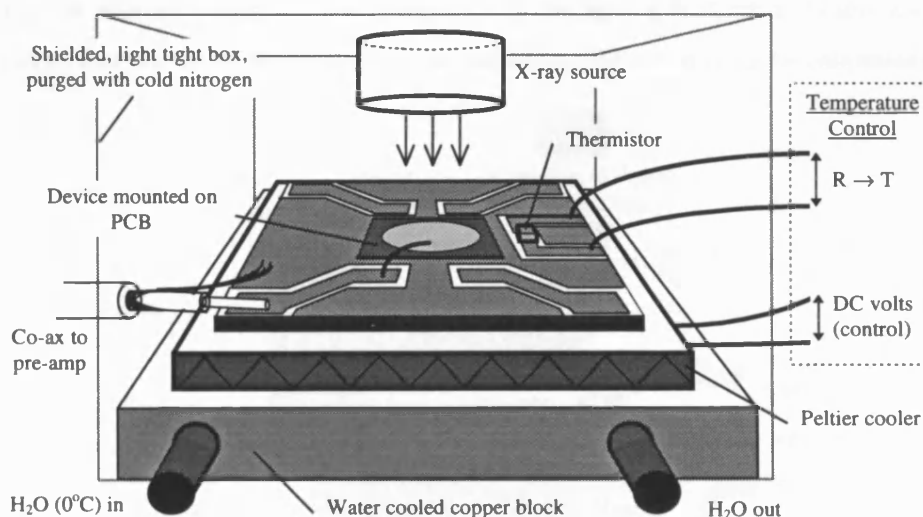
Figure 3-4 Schematic of the early, Peltier cooled system.

From initial spectral measurements made close to room temperature using a Peltier cooler and a simple heat sink, it quickly became clear that further cooling would be advantageous in order to

reduce leakage current and therefore noise. This was achieved by mounting the Peltier cooler on a hollow copper block, water cooled to 0°C (with the aid of anti-freeze) by a closed cycle water chiller (figure 3-4). A Peltier current of 4 amps then gave a minimum attainable temperature of -35 ± 2°C. The whole assembly was mounted in a shielded di-cast box which was purged with a continuous flow of cold (boil off) nitrogen to expel air and thus prevent condensation. Device temperatures were monitored by means of surface mount thermistors placed on each PCB close to the detectors. The thermistors and the diodes themselves were bonded to the PCB using silver loaded thermoplastic. The pre amplifier was outside the nitrogen filled chamber but the length of the co-axial cable running from the detector to the amplifiers FET was still kept to ~ 4cm so that no more capacitance was added than was absolutely necessary. The capacitance of the coaxial cable and un-depleted detector mounted on a PCB was measured, and for bulk devices was typically <10 pF. The capacitance of the cable alone was <3 pF. This was considered to be satisfactory, since the detector capacitance would decrease on application of bias. The noise of the pre-amplifier as a function of detector capacitance is given in figure 3-7, later in this chapter. X-ray sources were positioned according to device thickness, source flux and source emission energy, to give reasonable count rates without causing pileup.

3.4.2 Liquid nitrogen cooled system (-130 to +30 °C)

In order to cool the devices further, a liquid nitrogen cryostat was employed. The devices were mounted on a liquid nitrogen cooled cold finger in a vacuum chamber to prevent condensation of water vapour. The cold finger temperature was controlled to within ~1°C by a feedback control unit connected to a platinum resistance thermometer (PRT) and a number of heaters (resistors). Since the control PRT was attached to the cold finger some distance from the detector, the device temperature was still monitored independently using the PCB mounted thermistors. The pre amplifier was placed inside the cryostat with the signal, HT and test pulse fed through the back plate. In this way the length of the co-axial connection from the detector to the amplifier FET could again be minimised.
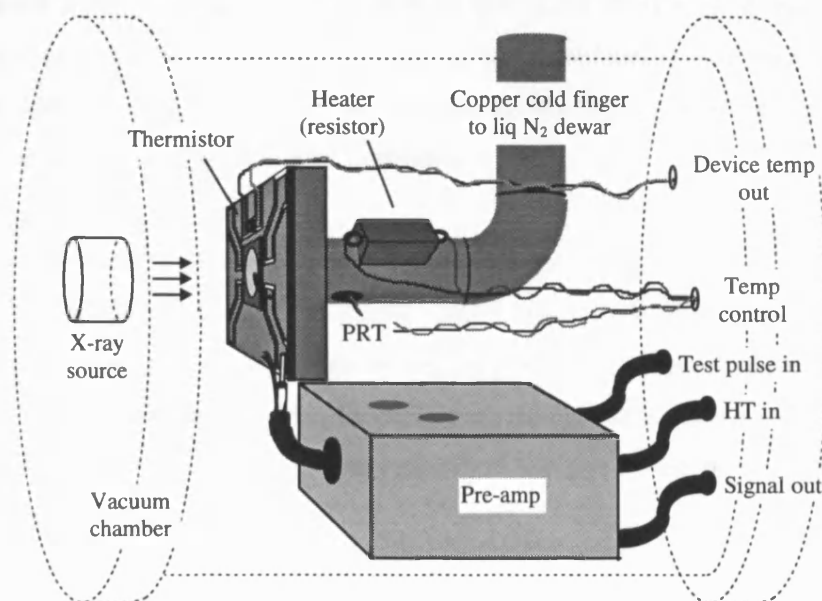

Figure 3-5 Schematic of the liquid nitrogen cooled system.

63

3.4.3 Energy calibration

In forming a spectrum, a multi-channel analyser (MCA), in this case a PC based system, forms a histogram by binning the shaping amplifier output according to pulse height. Initially the horizontal scale, or bins are expressed simply as channels, but it is generally more useful to express them in terms of a physical property of the pre-amplifier input, or more commonly in detector applications, a property of the detector input such as the energy of an incident photon required to give a count in a given channel. In an ideal detector and amplification chain, the pulse height due to a photon of a given energy will be independent of the location within the active volume of the detector at which it is absorbed, and the conversion from incident photon energy to MCA channel will be linear across the full range of the detector response. In this case the energy scale may be calibrated by detecting photons of a known energy. Of course no detector system can be truly ideal, but the response of silicon charge couple devices (CCDs) and other silicon detectors is sufficiently linear and free from charge loss above ~2keV that they may reasonably be calibrated using titanium $K\alpha$ X-rays (4510eV) for instance.

Since charge loss mechanisms dominate the spectral response of GaAs detectors, it is not possible to calibrate the spectral energy scale using X-rays detected in the GaAs directly. An indirect approach must therefore be adopted to calibrate correctly the energy scale and thus to quantify and investigate the effects of charge loss.

The TC 170 pre amplifier has a (nominally) 1pF test capacitor connected directly to the FET. The average X-ray energy required to generate an electron hole pair in GaAs is ω=4.27eV. A 60 keV X-ray therefore generates on average, 14052 electron hole pairs. Multiplying by the electronic charge, this gives a total charge on the amplifier's FET of 2.28×10^{-15} Coulombs. Since the charge on a capacitor is related to the potential across it simply by Q=CV, the 60 keV X-ray may be simulated by applying 2.28mV to a 1pF capacitor. The tolerance of 1pF capacitors is very poor however, and the test input may only be used to measure the linearity of the energy scale unless an independent calibration can be used to measure the test capacitance.

Figure 3-6 shows a typical spectrum used for establishing the energy calibration. The detector is a 125 μm-thick lithium drifted silicon diode giving ~100% CCE across the energy range of interest (5 to 130 keV). By multiplying the energy scale by $\omega_{GaAs}/\omega_{Si}$ (4.27/3.65), spectra such as figure 3-6 may be used directly to calibrate for GaAs i.e. by calibrating the 122 keV line as 142.7 keV and the 14 keV line as 16.38 keV. However, a separate calibration spectrum must be used for each value of shaping/peaking time and gain.

From the position of a pulse generator peak of a given voltage on the energy scale of the silicon spectra, the true value of the test capacitance can be measured and all subsequent spectra can be calibrated using the pulser directly. The TC-170 pre amplifier used throughout this work was found to have a 1.24 pF test capacitor so that a 10.6 mV test input simulates 351 keV in GaAs, and 5.3 mV simulates 175.5 keV.
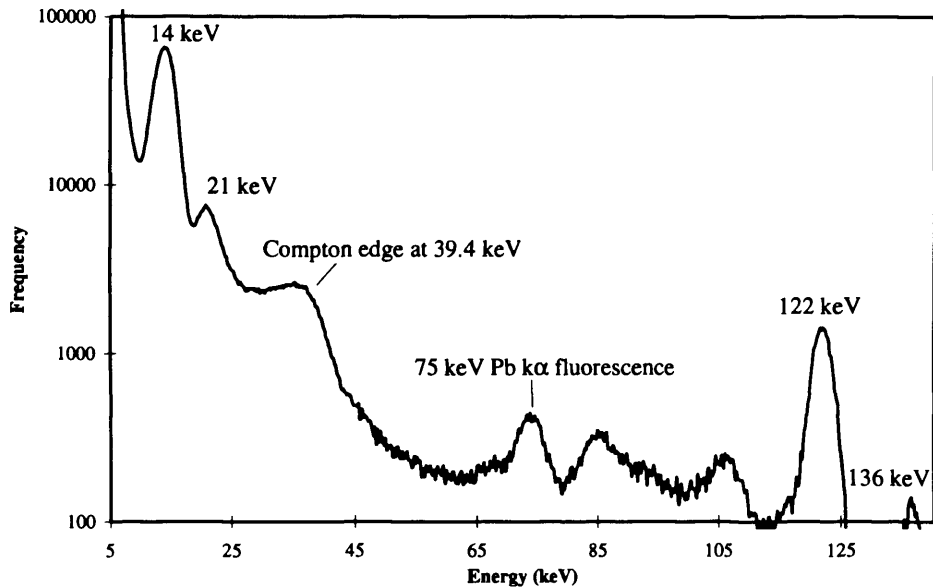
Figure 3-6 Cobalt 57 spectrum from 125μm-thick planar lithium drifted silicon detector.

3.4.4 Electronic noise
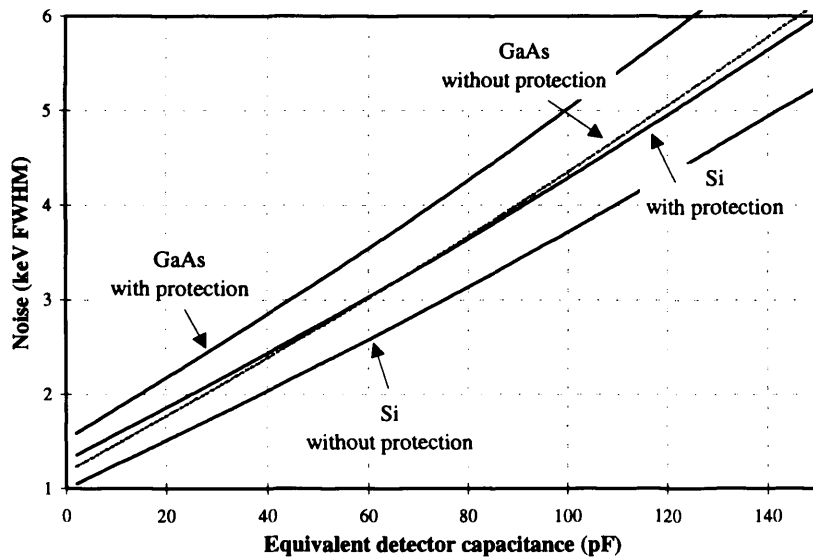
Figure 3-7 TC-170 Pre amplifier noise as a function of detector capacitance (1μs shaping time)

Figure 3-7 shows the electronic noise of the TC-170 pre amplifier as a function of detector capacitance. The values referred to a silicon detector are taken from the pre amp manual and those relative to GaAs are obtained by multiplying by $\omega_{GaAs}/\omega_{Si}$ (4.27/3.65). The capacitance of a planar detector may be approximated using the equation for an ideal parallel plate capacitor,

$$C = \frac{A\varepsilon_o\varepsilon_r}{d} \qquad (3\text{-}1)$$

where A is the area of the device, ε_o is the permittivity in vacuum, ε_r is the relative permittivity of the dielectric medium (13.1 for GaAs) and d is the distance between the capacitor plates or the depletion width of the detector. Figure 3-8 shows the capacitance per unit area according to equation 3-1 for a GaAs device.
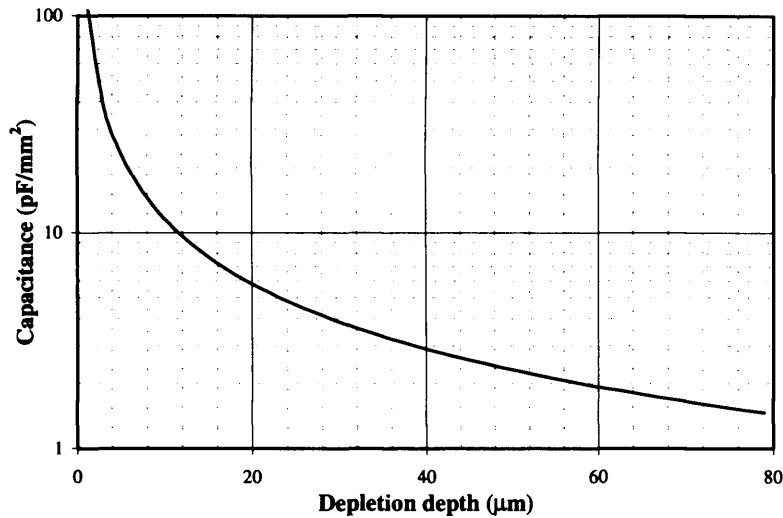
Figure 3-8 GaAs device capacitance/mm^2 as a function of depletion depth.

Combining the results of figures 3-7 and 3-8 one may predict (figure 3-9) the electronic contribution to the spectral noise for real devices as a function of depletion width. In this case the FWHM in keV is shown for several device areas, with the pre amp protection structure in and a 1μs shaping time (2μs peaking time).
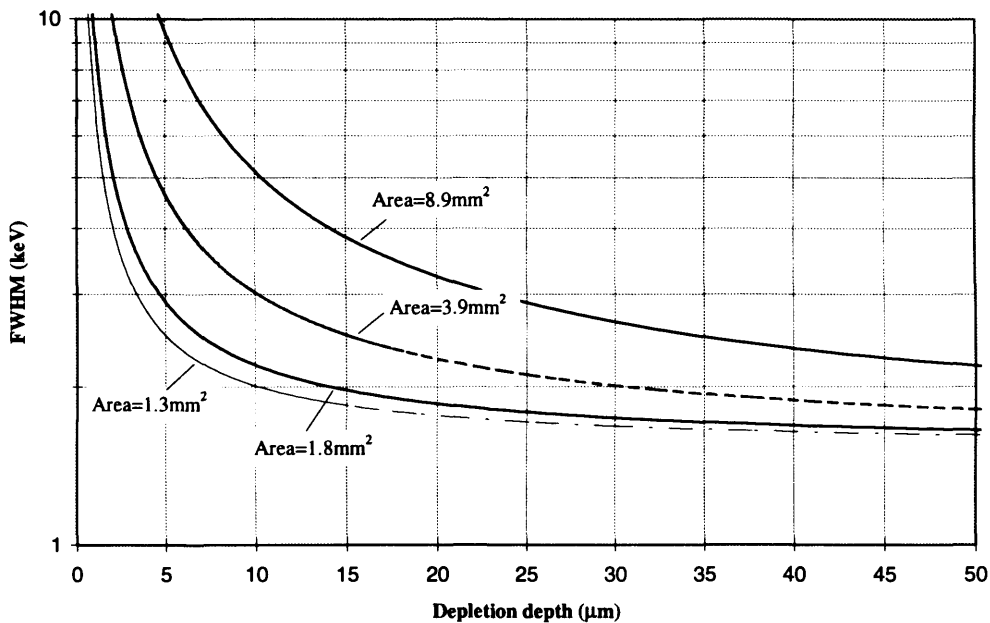
Figure 3-9 Theoretical electronic noise for GaAs devices connected to TC-170 pre-amplifier with protection structure (1μs shaping).

3.5 Measuring spectral response (protons)

In order to measure the spectral response of GaAs diodes to protons, the vacuum chamber (figure 3-5) was bolted by means of an adapter to a beam line of the Radial Ridge Cyclotron Facility at Birmingham University. The proton energy was 6.25MeV and the flux (monitored using a silicon diode) was kept below ~4000s^{-1}mm^{-2} to reduce dead time effects due to pile up. All proton measurements were made at room temperature.

3.6 Analysis of epitaxial samples (Hall, CV, DLTS, SEM)

3.6.1 Hall measurements

The majority carrier mobility, as determined by the Hall effect (Hall mobility) in cm^{2}V^{-1}s^{-1}, was measured for all epitaxial layers grown on semi-insulating substrates, using a commercial, four point Hall probe. These measurements, performed at room, and liquid nitrogen temperatures also gave the net carrier concentration if the thickness of the grown layer was known.
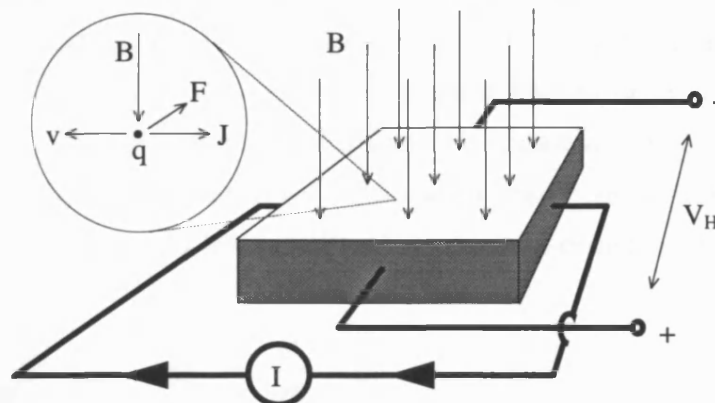
Fig 3-10 The principle behind the Hall effect, shown for an n-type sample.

The Hall effect, discovered in 1874 by E. H. Hall, may be used to measure majority carrier density, and to determine if a sample is n or p type. If the conductivity is also measured, one can calculate the carrier mobility. The effect results from the force F, with which a magnetic field B (Wm^{-2}) acts on a current density J, according to the vector product,

$$F = J \times B \qquad (3-2)$$

If J and B are perpendicular, then F, J and B form a right-handed Cartesian co-ordinate system. The force acts on the charge carriers, which are moving at a drift velocity v, and pushes them towards one side of the sample. Since the force depends on the current J and not on the type of carriers, it will remain in the same direction, pushing the majority carriers towards the same side whether they are holes moving in the direction of conventional current, or electrons moving in the opposite direction. When the mobile carriers are pushed towards one side of a sample, the other becomes depleted and

the semiconductor loses its local neutrality. There is now an excess of the mobile charge carriers on one side, and an excess of ionised impurities on the other. This gives rise to a measurable voltage drop, V_H, called the Hall voltage and hence an electric field E_H. The force acting upon the charge carriers due to this electric field must balance the force due to the magnetic field. Hence, for electrons,

$$JB + nqE_H = 0 \tag{3-3}$$

$$E_H = -\frac{1}{nq} JB \tag{3-4}$$

or,

$$\frac{E_H}{JB} = -\frac{r_H}{nq} = R_H \tag{3-5}$$

where R_H is called the Hall coefficient and r_H is a correction factor between 0.5 and 1.5 called the Hall coefficient factor which must be introduced to account for non-linearities in the relationship between carrier velocity and 'perpendicular' force. Similarly, for holes, the Hall coefficient is,

$$R_H = +\frac{r_H}{pq} \tag{3-6}$$

Measurement of R_H gives the carrier concentration directly. It can be measured at any temperature and, if that is low enough for some of the impurities not to be ionised, it gives an indication of the ionised fraction. In defective crystals however, a sizeable fraction of the impurities may not be ionised because they are located at grain boundaries or dislocations and not at proper lattice sites. The Hall effect yields the active fraction only. Hall measurements can be made, which are sensitive enough to detect concentrations as low as $10^{12} \mathrm{cm}^{-3}$ and, from the definition of the conductivity of an extrinsic semiconductor,

$$\mu_h = \frac{\sigma}{q\bar{p}} \quad \text{and} \quad \mu_e = \frac{\sigma}{q\bar{n}} \tag{3-7}$$

it can be seen that carrier mobilities may be obtained from Hall measurements: i.e. combining (3-5/6) and (3-7),

$$\mu_h = \sigma|R_H|_h \quad \text{and} \quad \mu_e = \sigma|R_H|_e \tag{3-8}$$

Mobility measured in this way is called Hall mobility and differs from the conductivity mobility by the Hall coefficient factor r_H which is approximately equal to one.
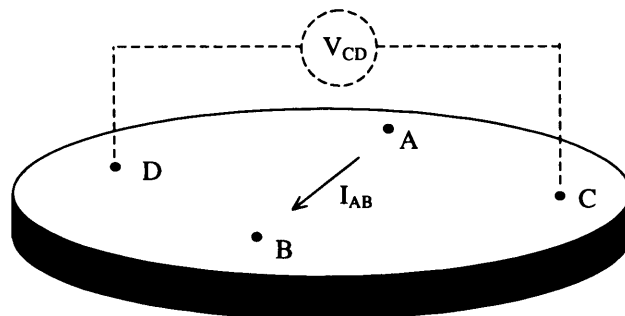

Fig 3-11 Hall analysis by the Van der Pauw method.

68

Samples of arbitrary shape may be used for Hall measurements since, defining the ratio of the voltage V_{CD} between the points C and D, and the current I_{AB} flowing between the points A and B, as R_{ABCD}, then Van der Pauw has demonstrated that the application of a perpendicular magnetic field results in a change in R_{ABCD}, and,

$$\mu_H = \frac{\sigma d}{B} \Delta R_{ABCD} \tag{3-9}$$

The samples analysed using this technique at EEV are etched into a clover leaf shape in order to reduce edge effects.

3.6.2 Capacitance-Voltage (CV) measurements

Capacitance-Voltage measurements can reveal deep trap energy levels and densities. The depletion region capacitance per unit area, C, of a metal-semiconductor contact may be expressed as a function of voltage, V,

$$C = \frac{|\partial Q|}{\partial V} = \sqrt{\frac{q \varepsilon_s N_D}{2(V_{bi} - V - kT/q)}} = \frac{\varepsilon_s}{W} \tag{3-10}$$

where Q is the space charge, V_{bi} is the built in potential and W is the depletion region width. Rearranging,

$$\frac{1}{C^2} = \frac{2(V_{bi} - V - kT/q)}{q \varepsilon_s N_D} \tag{3-11}$$

Differentiating with respect to potential and again rearranging,

$$N_D = \frac{2}{q \varepsilon_s} \left[- \frac{1}{d(1/C^2)/dV} \right] \tag{3-12}$$

By superimposing a small AC voltage onto the DC bias, the capacitance of the depletion region can be measured. For a uniform doping profile, and in the absence of deep levels, a plot of $1/C^2$ versus applied bias, V will be a straight line the intercept with the x axis of which will give the barrier height, Φ according to [Crowell, C.R., 1965, Goodman, A.M., 1963]

$$\Phi = V_i + V_n + \frac{kT}{q} - \Delta\Phi \tag{3-13}$$

where V_i is the intercept and V_n is the depth of the Fermi level below the conduction band edge. Furthermore it can be seen from equation 3-4 that the slope of this straight line will give the doping, or impurity concentration.

If the plot of $1/C^2$ versus V is not a straight line, then this indicates that the doping profile is not uniform or that deep levels are present. Any deep donor above the Fermi level will be ionised, increasing the doping concentration. When the small AC voltage is applied these ionised donors will give an additional contribution to the capacitance measured, which like the fraction of ionised levels, will vary with applied bias, producing steps in the plot. Deep traps may be investigated in this way, but it is essential to use sufficiently low AC frequencies since at higher frequencies the traps cannot respond quickly enough to follow the signal.

The CV measurements of epitaxial samples were carried out at Sheffield University as part of a GaAs detector collaboration.

3.6.3 Deep Level Transient Spectroscopy (DLTS)

DLTS analysis was carried out on several of the epitaxial samples by Dimitri Alexiev of the Australian Nuclear Science and Technology Organisation (ANSTO). The principle is similar to that of CV measurements, and the following description of the technique is a summary of an appendix by Dr. Alexiev.

The occupancy of energy levels within the band gap, away from the conduction and valence band edges (deep traps), alters the space charge and hence the width of the depletion region at a given bias. The capacitance of the depletion region is, in turn, inversely proportional to its width and may be measured. Thus by determining the time constant associated with the increase in device capacitance after the application of bias, one obtains the thermal emission rate, e, of carriers from the trap. This emission rate has the temperature dependence,

$$e = \frac{\sigma v_t N}{g} \exp\left(-\frac{\Delta E}{kT}\right) \tag{3-14}$$

and hence,

$$\Delta E = -kT \ln \frac{e}{AT^2} \qquad A = \text{a constant} \tag{3-15}$$

where σ is the capture cross section of the level, v_t is the average thermal velocity of the level ($\propto T^{1/2}$), N is the effective density of states in the appropriate band ($\propto T^{3/2}$), g is the degeneracy of the level, ΔE is the activation energy of the level and k is Boltzmann's constant. Thus ΔE may be obtained from the slope of a ln e versus $1/T$ plot, and σ from the intercept. The calculated value of ΔE will, however, need to be corrected for the T^2 dependence of σv_t in equation 3-14 and this may be done simply by subtracting 2kT where T is the average temperature of the data collection [Miller, G.L., 1977].

Trap concentrations may be obtained by measuring the relative change in capacitance produced by a small change in the pulse amplitude, V. The defect concentration, $N_T(x)$ is then related to this small change by, [Lang, D.V., 1974]

$$\delta\left(\frac{\Delta C}{C}\right) = \left(\frac{\varepsilon}{qw^2 n}\right) \frac{N_T(x)}{n(x)} \delta V \tag{3-16}$$

where q is the electronic charge, w is the depletion layer width, ε is the dielectric constant, $n(x)$ is the free carrier density at depth x and n is the free carrier density at the edge of the depletion region. If a plot of ΔC against pulse amplitude is linear, then the trap concentration profile is the same as the free carrier density profile. In the case of a one sided abrupt junction, and $\Delta C/C \ll 1$, equation 3-16 gives,

$$N_T \approx 2n \frac{\Delta C}{C} \tag{3-17}$$

where C is the capacitance at constant reverse bias and ΔC is the change in capacitance produced by pulsing to zero bias.

DLTS is now a standard technique for measuring deep level defects in semiconductors. Its advantages over other techniques are,

High sensitivity, typically 10^{-4} of background doping density.

Observes both majority and minority traps.

Gives absolute values of trap density.

Allows direct measurement of capture cross sections.

Non destructive.

Samples can be working devices (FETs, diodes etc.)

Its disadvantages are,

Defect states must be electrically active and not very shallow.

Capacitance must change with bias, thus some devices are un-measurable.

Some states are un-measurable.

Cannot examine bulk defects.

Gives little insight into the physical nature of the defects.

3.6.4 Scanning Electron Microscope (SEM) analysis

Scanning electron microscopes at EEV and at Leicester University were used to examine the surface features of epitaxial layers. Island growth, terracing, craters and non-adhesion indicated errors in the growth conditions (particularly the temperature profile). After device fabrication similar features

were sought as a possible explanation for poor behaviour under bias. Unexpectedly it was found that the SEM also revealed what appeared to be the bulk-epitaxy interface. This was interesting, but was not considered sufficiently reliable to use as a means of measuring the layer thickness.
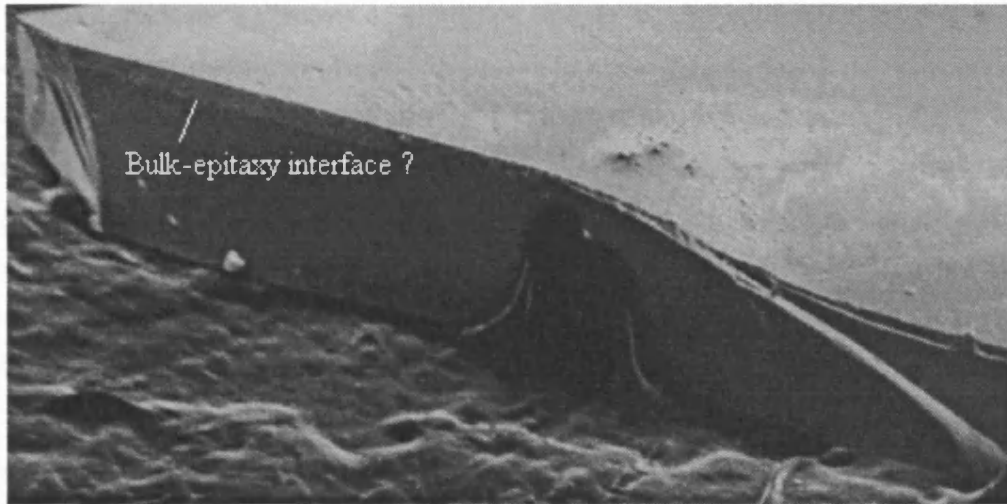

Figure 3-12 S.E.M. image showing possible bulk-epitaxy interface.

4. BULK MATERIAL DEVICES

Results of experiments carried out at Leicester on bulk material devices are presented in this chapter. These include current measurements as a function of voltage, temperature, device area and device thickness, and spectral measurements, principally as a function of applied bias, pulse integration time, temperature and time from application of bias. Evidence is presented in support of EL2 being the most dominant trap in terms of its effects on measured CCE (Charge Collection Efficiency) and hence peak degradation. This trap is sufficiently deep within the band gap that its release time constant at temperatures below approximately -80°C is hours, days or weeks and it is therefore possible to reduce significantly the density of active (empty) traps simply by cooling. In this way a spectral resolution of 2.4keV Full Width Half Maximum at 59.5keV has been achieved.

From measurements made using protons rather than X-rays, it is possible to measure the value and variation of the depletion region width which is shown to increase linearly with detector bias at room temperature. This is in agreement with the measurements of Berwick and Brozel [Berwick, K., 1993] and is also consistent with the existence of a quasi-neutral region as proposed by McGregor [McGregor, D.S., 1994].

4.1 IV characteristics

The IV characteristics of all bulk GaAs diodes used throughout this work were measured to ensure rectifying behaviour. A comparison was made between the simple Schottky devices, and the annealed PiN devices (see chapter 3 for fabrication), and between the 250 to 500μm thick Leicester/EEV devices, and the 80μm thick Glasgow University devices. Current density (J nA/mm^2) has been established simply by dividing the measured current by the contact area. This introduces a small error since, as will be shown in the next section, there is evidence for a non-linear variation in current with device area.

Figure 4-1 gives JV (current density-bias) characteristics typical of Leicester/EEV fabricated devices. The PiN diode (SP15 in table 4-1) is 300 μm thick with a pad area of 3.9 ± 0.3 mm^2, and the Schottky diode (SS12) is 300 μm thick with a pad area of 8.9 ± 0.6 mm^2. These devices were produced on the same Showa Denko K.K. bulk GaAs wafer (specifications given in table 3-1) and hence underwent identical fabrication until after the wafer was sawn up (chapter 3). SP15 was then baked at 400 °C for 15 seconds (rapid thermal anneal) to drive Ti atoms into the GaAs surface forming a P-type layer, and is therefore a PiN (P-type intrinsic N-type) diode, rather than a Schottky diode.
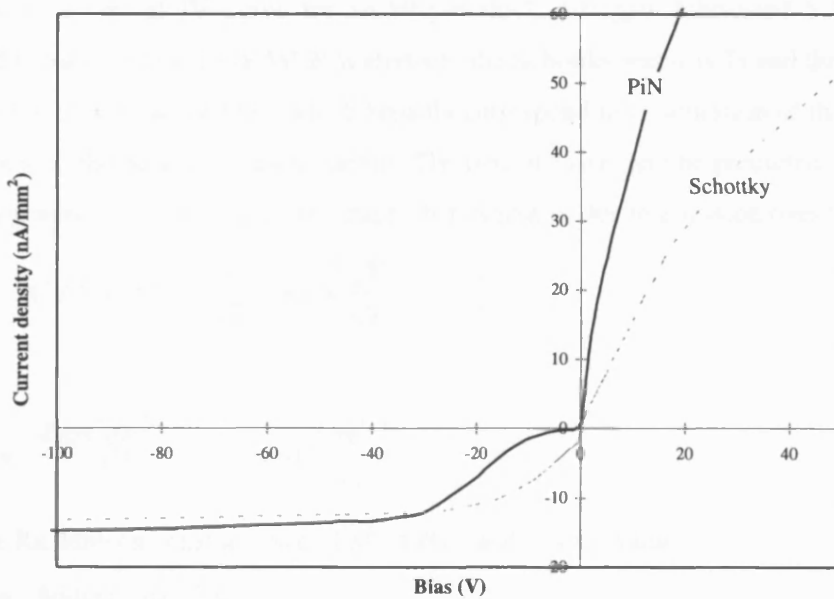
Figure 4-1 Typical JV characteristics for 300 μm, Leicester fabricated devices at 21°C.

Clearly, both devices are rectifying junctions, and the 'soft turn-on', or ohmic forward characteristic is typical of relaxation semiconductor devices, i.e. those in which the minority carrier recombination lifetime is short in comparison with the dielectric relaxation time [Jones, B.K., 1995]. Under reverse bias, the current in both junctions plateaus at approximately 17 $nAmm^{-2}$ which implies that the dominant source of leakage is the same in both devices. This is therefore likely to be thermal generation in the depleted N-type material which is independent of the nature of the junction. However, when the devices are not depleted (i.e. under forward bias and at low values of reverse bias), conduction is dominated by injection through the junction, and it is therefore clear from figure 4-1 that the Schottky and PiN interfaces are very different.
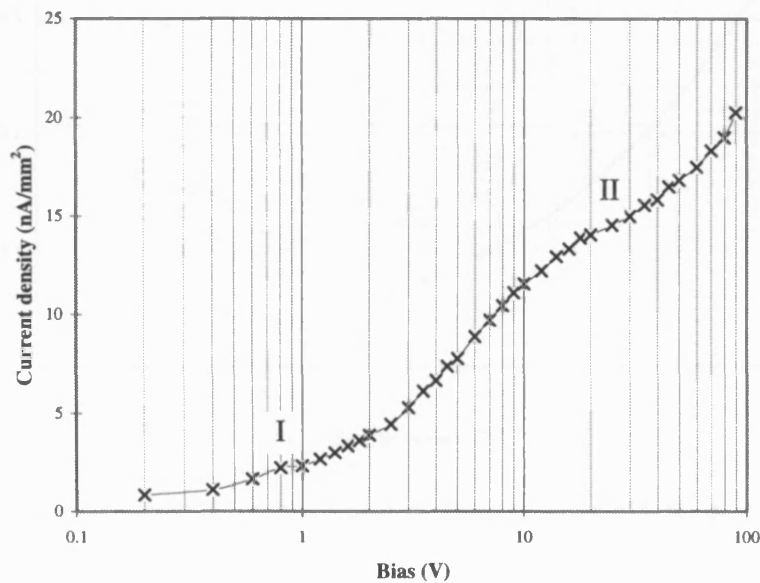
Figure 4-2 JV characteristic of 80μm Glasgow fabricated Schottky-Schottky device at 24°C.

Figure 4-2 shows a typical JV curve for an 80 μm thick, Glasgow fabricated Schottky-Schottky device. The LEC bulk GaAs is from MCP Wafertech, the Schottky metal is Ti and the pad area is 1.8 ± 0.1 mm². Two plateaux can be seen, which broadly correspond to I) saturation of the barrier current and II) saturation of the bulk generation current. The first of these may be predicted from thermionic emission theory, which gives the current/voltage characteristics due to emission over the barrier as,

$$J = A^*T^2 \exp\left(-\frac{q\phi_b}{kT}\right)\left\{\exp\left(\frac{qV}{kT}\right) - 1\right\}$$ (4-1)

where,

$$A^* = \frac{4\pi m^* q k^2}{h^3} = 1.2x10^6\left(\frac{m^*}{m}\right)$$ (4-2)

is the effective Richardson constant [Sze, S.M., 1981], and has the value,

$$A^* \approx 86400 \quad Am^{-2}K^{-2}$$ (4-3)

in GaAs (m*/m ≈ 0.072). Combining 4-1 and 4-3 it can be seen that the thermionic emission current will saturate under reverse bias at,

$$J_s = -86400T^2 \exp\left(-\frac{q\phi_b}{kT}\right)$$ (4-4)

This is shown graphically in figure 4-3 for a barrier height of 0.8 V. The leakage current predicted at 24°C (0.21 nAmm⁻²) is far less than observed in the first plateau of figure 4-2 (~2 nAmm⁻²), but this is not unexpected and indicates that energy levels in the band gap (due to surface states and bulk impurities) are dominating carrier migration through the barrier.
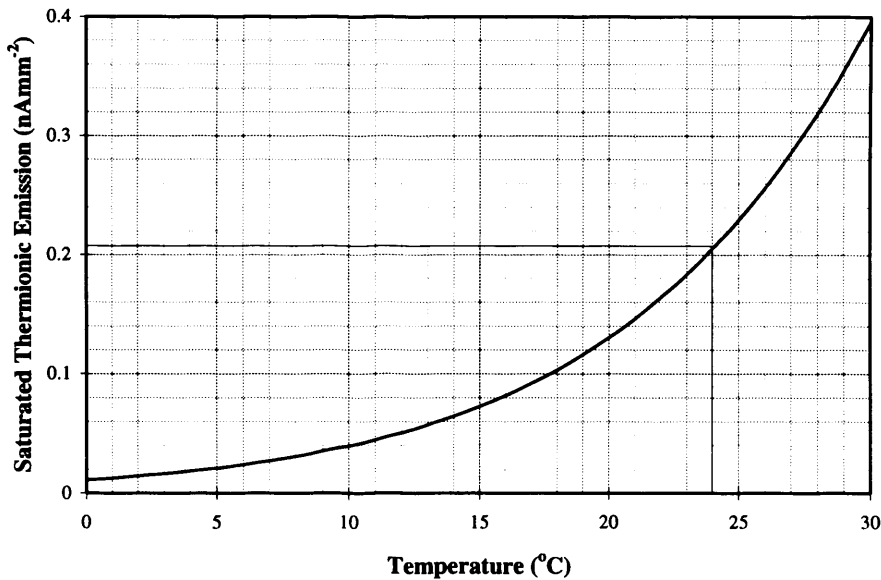
**Figure 4-3** Saturated thermionic emission from equation 4-4, for ϕ_b = 0.8 V.

From the results in this section, it is clear that the measured JV characteristics demonstrate only that the devices are rectifying, that the rapid thermal anneal alters the properties of the junction, but has little effect on the bulk, and that the current flowing is greater than that predicted by thermionic

emission theory. The last of these is an indication that there is a significant contribution to the total current measured due to surface currents and/or generation at defect sites and/or injection through the barrier due to surface states. The presence of generation sites, surface states and dangling bonds (which give rise to surface currents) are all properties of the GaAs material. Attempts have been made to eliminate surface currents however, by the application of a silicon nitride passivation layer during fabrication, and by giving some of the detectors guard rings. These guard rings had no observable effect in practice which may simply indicate that the passivation layer worked completely.

4.2 Leakage current and activation energy

Variation of leakage current with device contact area, can be an indication of the significance of any surface current contribution to the total current measured, and variations with temperature give values of 'activation energy' i.e. the energy associated with carrier generation in the bulk or at the barrier.

Figures 4-4, 4-5 and 4-6 show the room temperature leakage current for 53 diodes at 20, 50 and 100 volts reverse bias. The devices were fabricated on two 3 inch diameter bulk GaAs wafers, one from Showa Denko KK (designated SS.. and SP..) and the other from MCP Wafertech (designated MS.. and MP..). The two wafers were processed together so that all of the contact preparation and metallization should be as similar as possible (see section 3.2). Some of the diodes were then back etched in order to give a wider variety of device thickness.
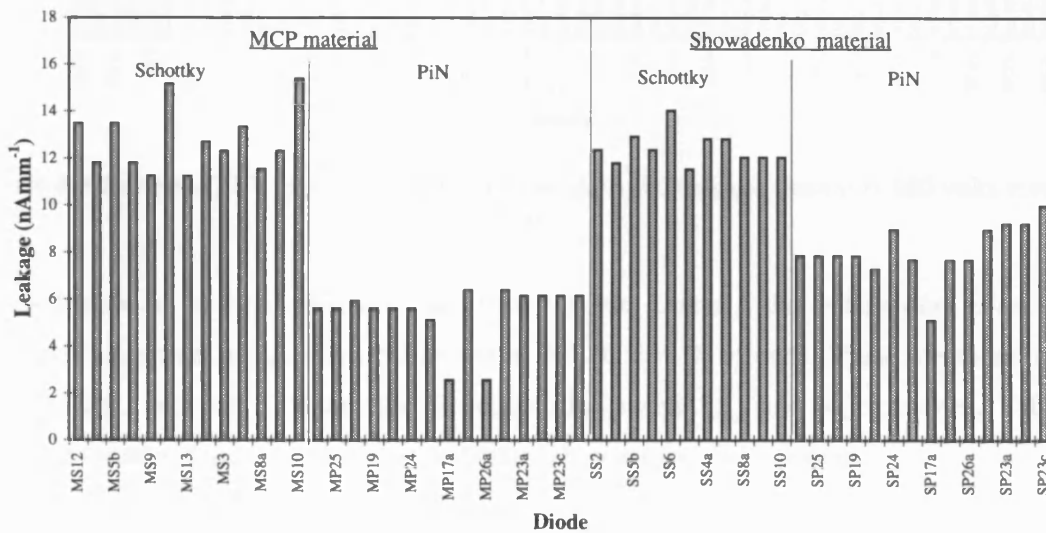
Figure 4-4 Leicester/EEV fabricated bulk GaAs diodes - RT leakage current at 20 volts reverse bias.
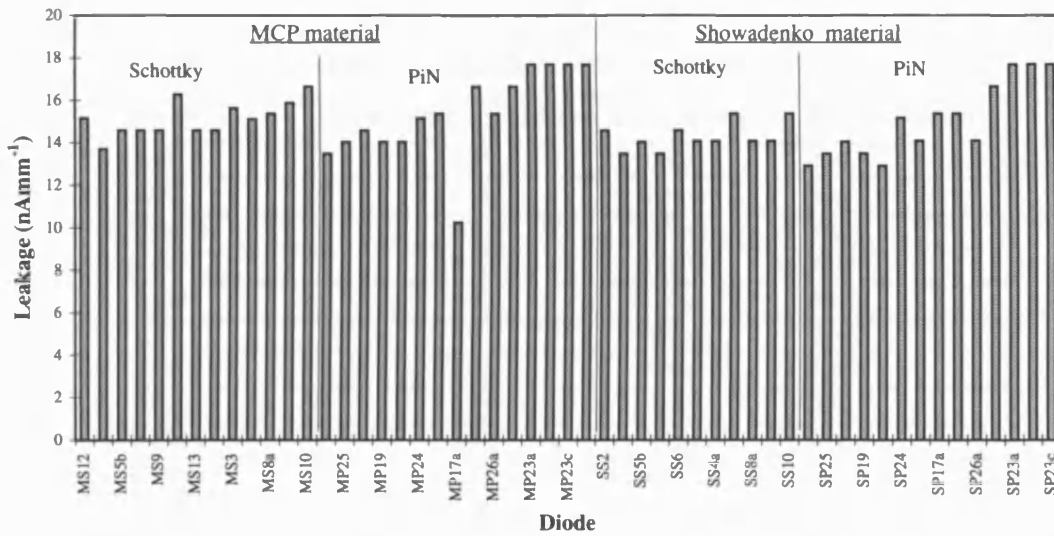
Figure 4-5 Leicester/EEV fabricated bulk GaAs diodes - RT leakage current at 50 volts reverse bias.
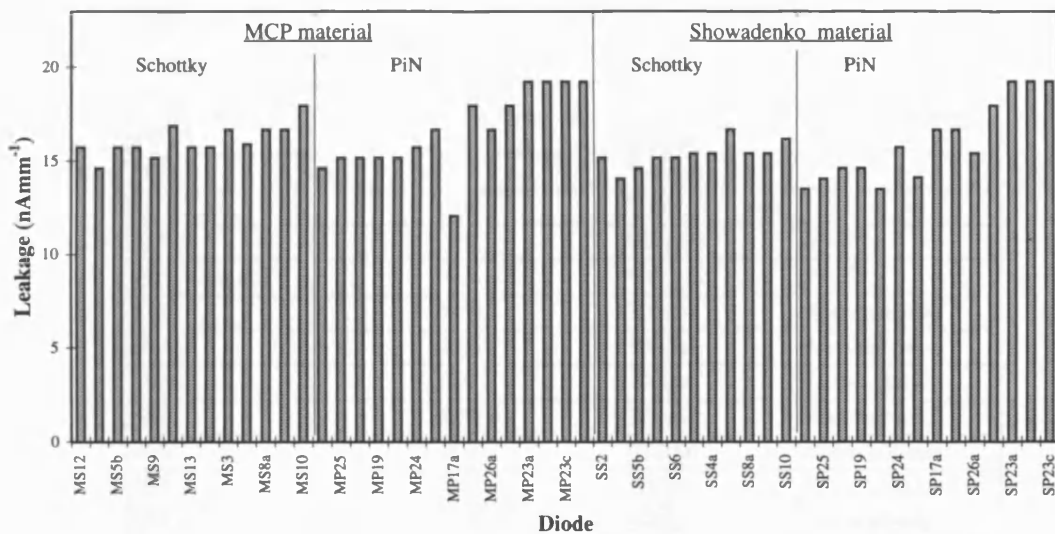
Figure 4-6 Leicester/EEV fabricated bulk GaAs diodes - RT leakage current at 100 volts reverse bias.

After application of the front (Schottky) and back (Ohmic) contacts, the wafers were sawn up and half of each underwent a rapid thermal anneal at 400 °C for 15 seconds. These are therefore PiN (designated SP.. and MP..) rather than Schottky (designated SS.. and MS..) diodes. Table 4-1 summarises the area, thickness, annealing and material source for all 53 devices.

The results of figures 4-4, 4-5 and 4-6 indicate that the leakage current is smaller in all of the PiN devices than the Schottky devices at low bias, but that it converges quickly with increasing bias as previously demonstrated for SS12 and SP15 in figure 4-1. The diodes are further arranged in order of decreasing contact area and it is clear that at higher values of bias, the current density appears to be greater for smaller devices. In the case of annealed Showa Denko material, 1.3mm^2 devices have up to 20% higher current density than 8.9mm^2 devices. This indicates that the active volume of GaAs is greater than that covered by the contact metal and/or that surface currents are significant.

77

Table 4-1. Leicester/EEV fabricated bulk GaAs devices.

Diode	Area (mm^2)	Thickness (μm)	Annealed	Material source
MS12	8.9	500	no	MCP
MS2	8.9	500	no	MCP
MS5 b	8.9	500	no	MCP
MS7	8.9	500	no	MCP
MS9	8.9	500	no	MCP
MS11	8.9	450	no	MCP
MS13	8.9	450	no	MCP
MS6	8.9	450	no	MCP
MS3	3.9	500	no	MCP
MS5 a	3.9	500	no	MCP
MS8 a,b	3.9	500	no	MCP
MS10	3.9	450	no	MCP
MP20	8.9	500	yes	MCP
MP25	8.9	500	yes	MCP
MP28	8.9	500	yes	MCP
MP19	8.9	450	yes	MCP
MP22	8.9	450	yes	MCP
MP24	8.9	450	yes	MCP
MP15	3.9	500	yes	MCP
MP17 a,b,c	3.9	500	yes	MCP
MP29	3.9	500	yes	MCP
MP23 a,b,c,d	1.3	500	yes	MCP
SS2	8.9	300	no	Showadenko
SS4 b	8.9	300	no	Showadenko
SS5 b	8.9	300	no	Showadenko
SS7	8.9	300	no	Showadenko
SS6	8.9	250	no	Showadenko
SS3	3.9	300	no	Showadenko
SS4 a	3.9	300	no	Showadenko
SS5 a	3.9	300	no	Showadenko
SS8 a,b	3.9	300	no	Showadenko
SS10	3.9	250	no	Showadenko
SP20	8.9	300	yes	Showadenko
SP25	8.9	300	yes	Showadenko
SP28	8.9	300	yes	Showadenko
SP19	8.9	250	yes	Showadenko
SP22	8.9	250	yes	Showadenko
SP24	8.9	250	yes	Showadenko
SP15	3.9	300	yes	Showadenko
SP17 a,b	3.9	300	yes	Showadenko
SP26 a	3.9	300	yes	Showadenko
SP29	3.9	300	yes	Showadenko
SP23 a,b,c	1.3	300	yes	Showadenko

Figures 4-7, 4-8 and 4-9 are plots indicating carrier activation energy from leakage current measured as a function of temperature. These assume a temperature relationship for current of the form

$$ J \ \propto \ T^2 \ \exp\left(- \ \frac{qE_a}{kT} \right) \qquad (4\text{-}5) $$

where E_a is the activation energy in eV, regardless of the generation process. Thus, according to thermionic emission-diffusion theory for an ideal Schottky barrier, under saturated reverse bias (equation 4-4), $E_a = \phi_b$, (the barrier height); and under forward bias $E_a = V+\Delta\phi-\phi_b$ where V is the applied bias and $\Delta\phi$ is the Schottky barrier lowering [Sze, S.M., 1981]. If generation in the depletion region is the dominant source of current, then for material with just one dominant state in the band-gap, $E_a = E_t$, the trap energy level. For material with a number of states in the band-gap and particularly near the middle of the gap, $E_a \approx E_g/2$ where Eg is the width of the band gap in eV (≈ 1.424 for GaAs).

Re-arranging equation 4-5 gives,

$$\ln\left(\frac{J}{T^2}\right) = -\frac{qE_a}{k}\frac{1}{T}$$ (4-6)

and a graph of $\ln(J/T^2)$ versus $1/T$ (called an Arrhenius plot) will therefore have a gradient of $-qE_a/k$, giving E_a directly. Figure 4-7 shows Arrhenius plots for an 80μm thick $1.8 \pm 0.1mm^2$ Schottky diode operating at three values of reverse bias. The values of activation energy obtained are close to the mid-band energy of 0.71 eV, suggesting that generation in the depletion region due to multiple traps (or a single trap such as EL2 close to the band gap centre) is the dominant source of current.
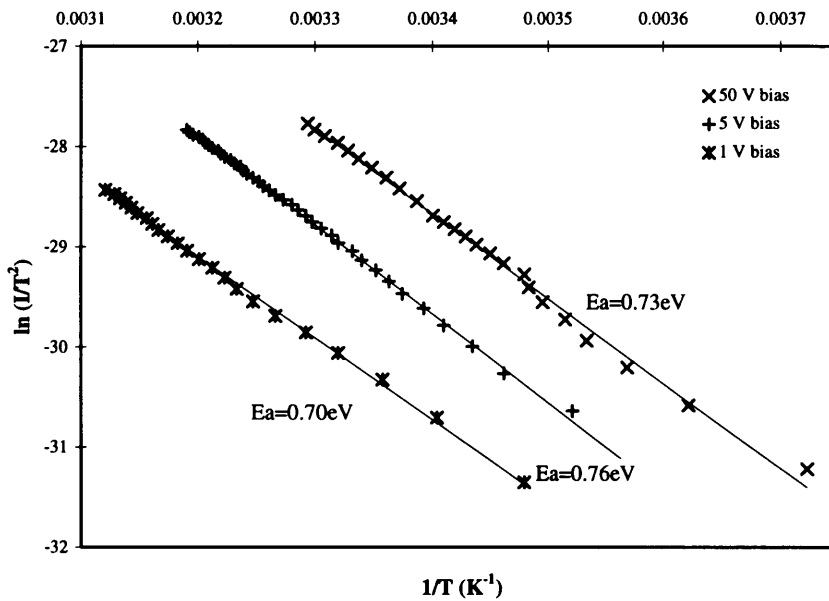
Figure 4-7 Arrhenius plots for 80 μm Schottky-Schottky device, indicating the activation energy at three values of applied bias corresponding to three regions of figure 4-2.
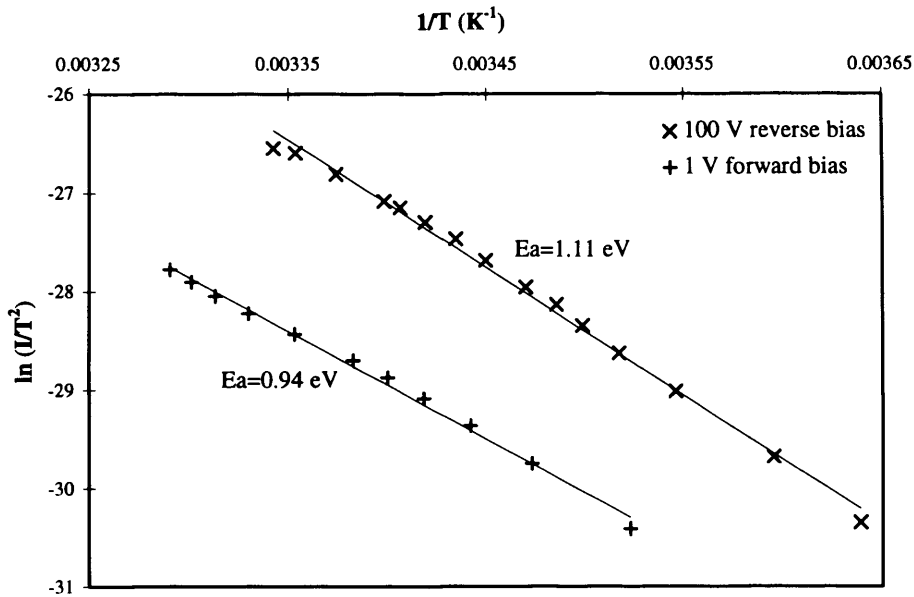
Figure 4-8 Arrhenius plots for Leicester 300 μm Schottky-Ohmic device at 1 volt forward and 100 volts reverse bias, indicating values of activation energy.
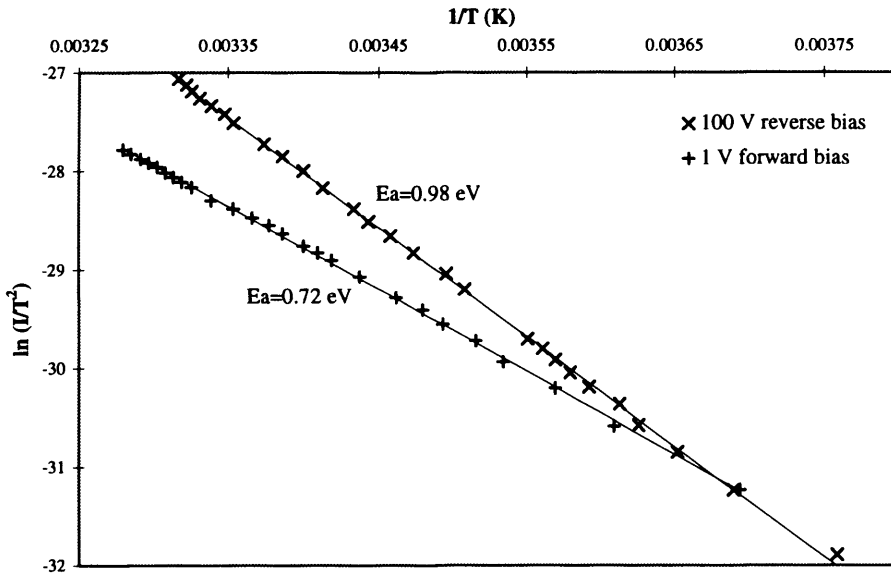
Figure 4-9 Arrhenius plots for Leicester 300 μm PiN-ohmic device at 1 V forward and 100 V reverse bias, indicating values of activation energy.

4.3 Investigation of active depth

X-rays may only be detected in those regions of a semiconductor device across which there is a potential gradient i.e. where there is a non-zero electric field (section 2-5). One of the most important parameters for any detector and especially for high energy X-ray devices, is therefore the depletion depth since, by definition, this is the thickness across which the potential falls from a value equal to approximately the applied bias plus the barrier height, to zero. Since it is sensitive to X-rays, the thickness of the depletion region in a detector is called the active depth. This may be calculated using Poisson's equation,

80

$$\frac{dE}{dx} = \frac{d^2\psi}{dx^2} = -\frac{\rho}{\varepsilon_s} \qquad (4\text{-}7)$$

if the distribution of space charge (ρ) may be modelled or approximated (section 2-3), and it is often adequate to assume that the charge density has a constant value across the depletion region. This is called the depletion approximation and the solution of Poisson's equation in this case predicts that the depletion depth will vary as the square root of the applied bias.

If the active depth stretches across the full thickness of a detector then it is said to be fully depleted and it will give a similar efficiency whether X-rays are incident from the front or the rear (provided the contacts are of similar thickness). If a device is not fully depleted then lower energy X-ray lines may be entirely absent from spectra obtained under back illumination. This is a simple test for full depletion.

Figure 4-10 shows front and back illumination spectra from a 300 μm thick Leicester/EEV fabricated PiN device. The temperature is approximately -130°C and the applied bias is 250 V. The Co-57 source gives a line at 14 keV which is present in the front illumination, but not in the back illumination case.
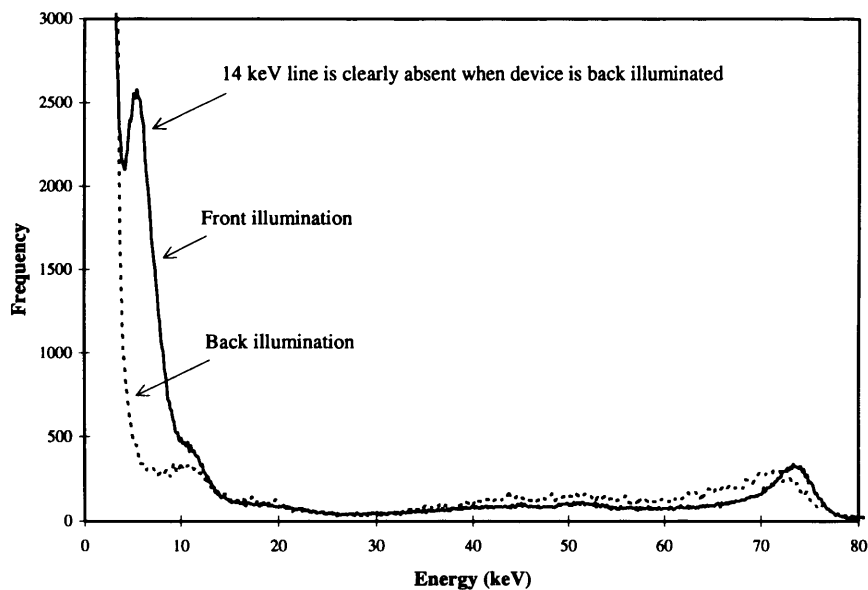
Figure 4-10 Cobalt 57 front and back illumination spectra indicating that the depletion region does not extend across the entire device thickness.

This demonstrates that the diode is not fully depleted and gives an approximate minimum width for the un-depleted region of about 75 μm in accordance with the linear attenuation of 14 keV X-rays shown in figure 4-11.
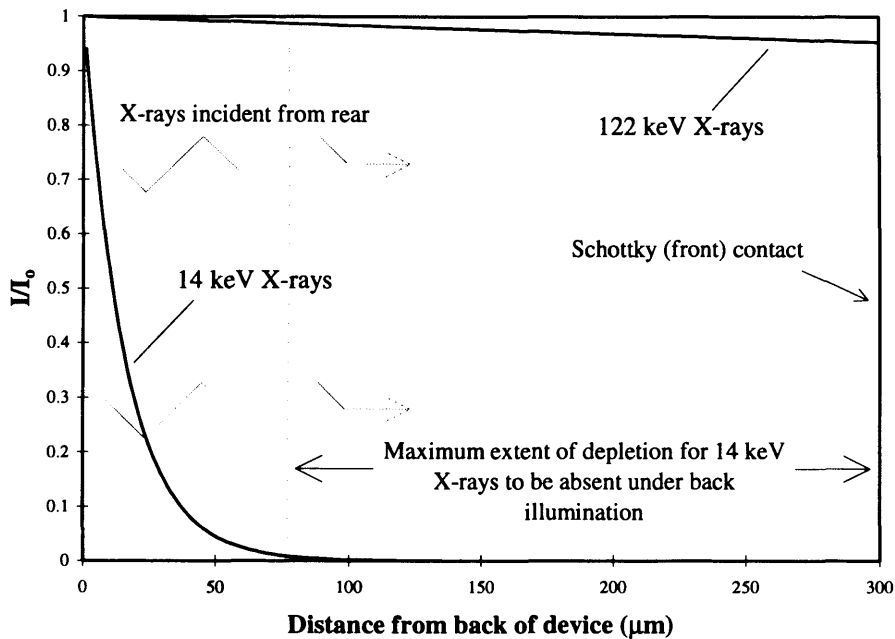
Figure 4-11 Attenuation plots indicate a dead layer at least ~ 75μm thick for the measurements of figure 4-10 since the 14 keV peak is absent when the X-rays are incident from the rear.

4.3.1 Proton measurements

Having demonstrated that the devices are not fully depleted, a simple method may be employed to measure the active width by detecting charged particles and by repeating at a number of different values of applied bias one may determine how the depletion depth varies as a function of voltage. For this purpose protons have been chosen since these deposit their energy along a fairly straight track through the depletion region.

It has been known for many years that the depletion region width in bulk GaAs devices cannot always be calculated using the depletion approximation because of the contribution to the space charge from partially occupied mid band levels or traps. Figure 4-12 shows electric field profiles measured by Berwick and Brozel which clearly indicate that there is a constant field region in which the net space charge must be zero. This prevents further band bending according to Poisson's equation. An obvious consequence of this is that once the constant field region has been established, the depletion region width will increase linearly with bias.
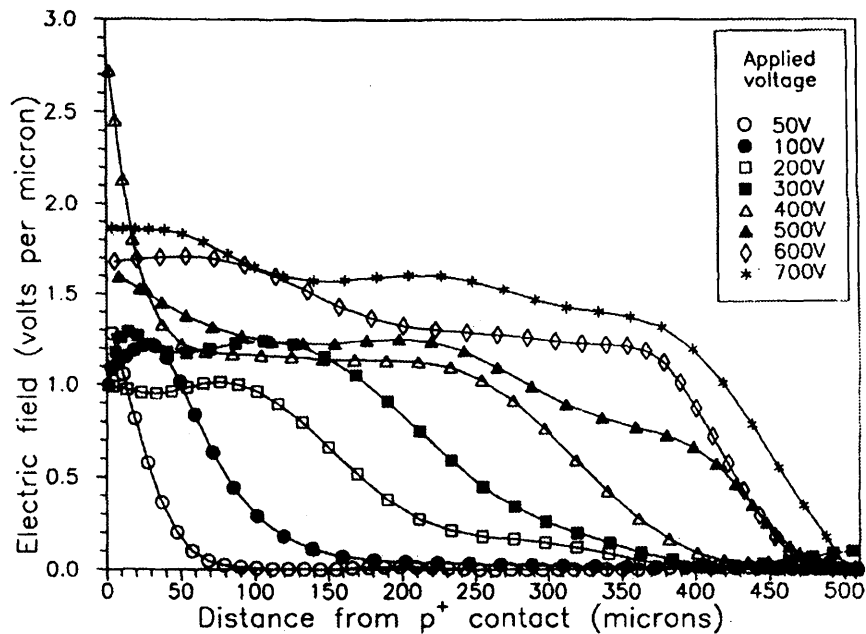
Figure 4-12 The measured electric field in a bulk GaAs diode reproduced from [Berwick, Brozel]

The width of the active region may be calculated from the proportion of a proton's energy which is deposited within it. In order that this may be determined from the energy measured it is first necessary to know the mean charge collection efficiency of the active region, as its width increases i.e. as a function of applied bias. This may be measured using X-rays, and is given for the test device in figure 4-14.
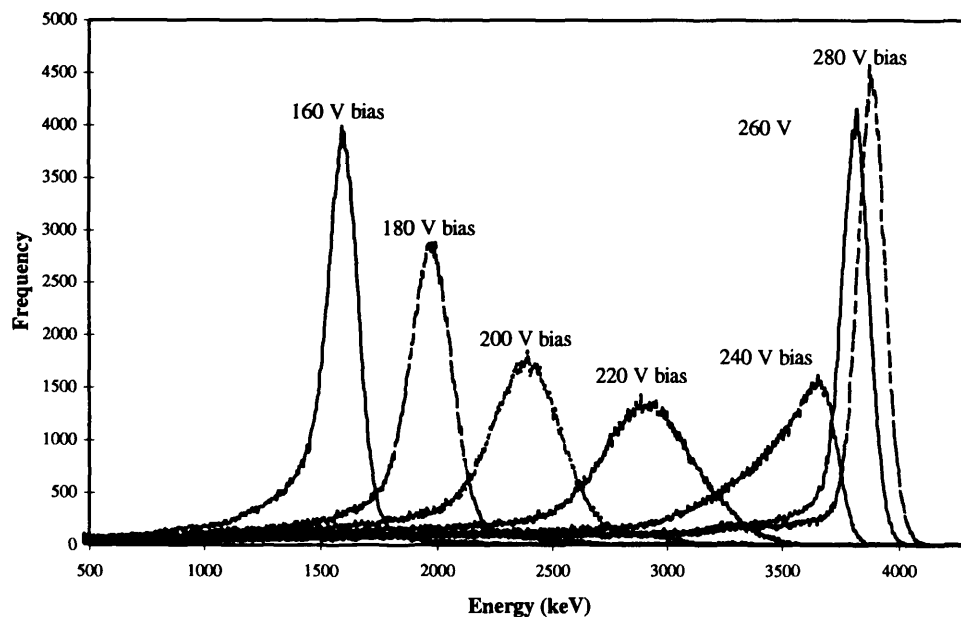
Figure 4-13 Spectra as function of bias for 6.25 MeV protons in 300μm bulk GaAs Schottky diode.

Room temperature proton measurements made at the Radial Ridge Cyclotron at Birmingham University are shown in figure 4-13. The proton energy was 6.25MeV and the device thickness was 300μm. Since the peak position represents the mode energy deposited within the depletion region per proton, it can be seen that as the bias is increased, the depletion region extends further into the device

and encompasses more of the proton's path length. Above 280 volts the peak barely moves any further along the energy scale, indicating that the depletion region width is greater than the mean proton range. The energy measured per proton is still only ~ 4MeV however, due to the poor room temperature CCE.
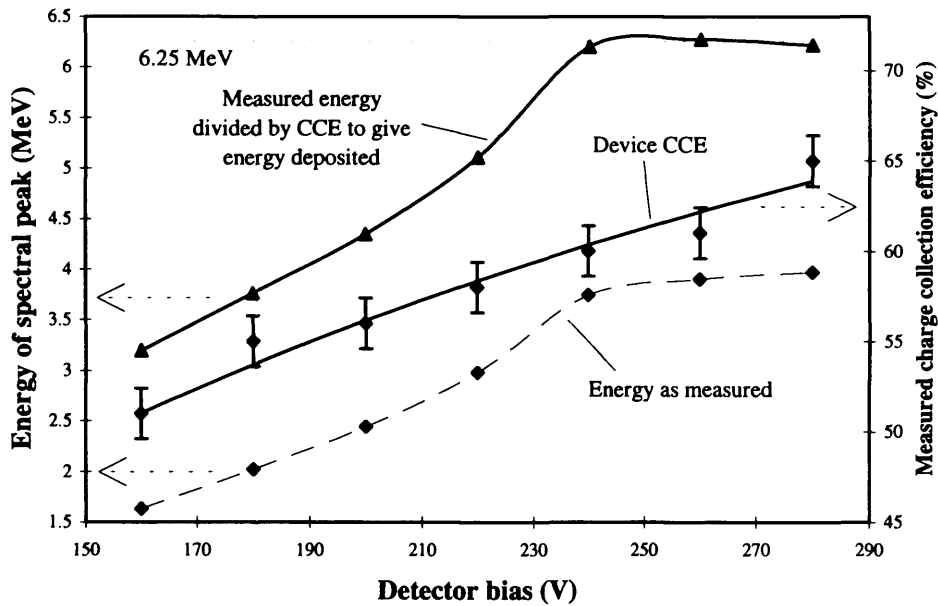
Figure 4-14 Spectral peak position, as measured, and adjusted for the device CCE (also shown).

In figure 4-14, the position of the spectral peak has been plotted as a function of applied bias. Also shown is the position of the peak after compensating for the measured charge collection efficiency of the test device i.e. after dividing by the CCE. The curve then plateaux at 6.25 MeV, indicating that for an applied bias of just ~ 240V the active region extends beyond the proton range so that all of the energy deposited may be accounted for if not measured.
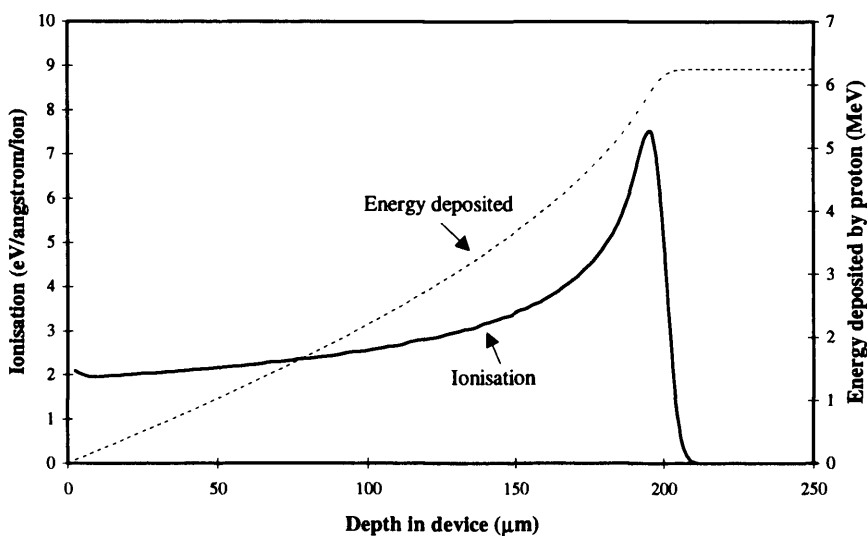
Figure 4-15 Modelled energy deposition by 6.25 MeV protons in bulk GaAs.

The ionisation of GaAs by 6.25 MeV protons may be modelled using a shareware simulation package such as TRIM [Ziegler J.F. and Biersack, J.P., 1985]. The results of this modelling, which includes the effect of the electrode structure, are shown in figure 4-15. Integrating this ionisation gives the modelled energy deposited as a function of depth within the device.
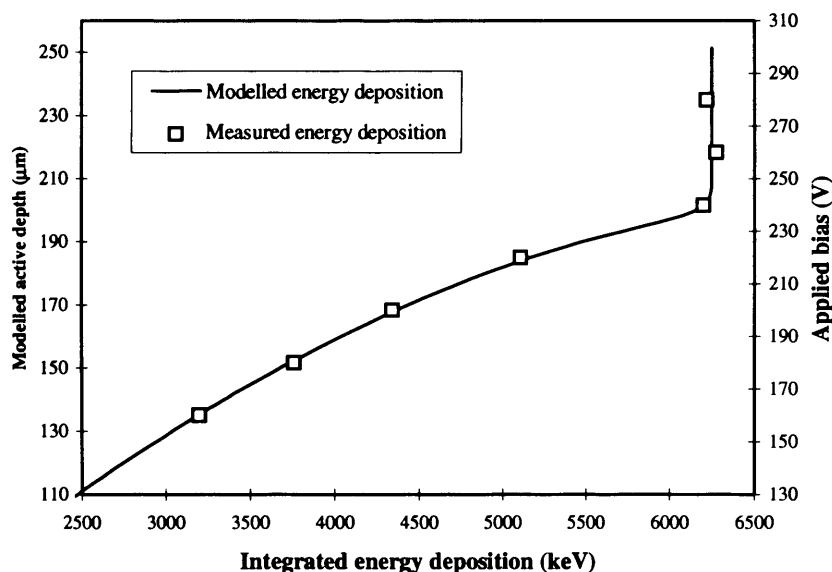
Figure 4-16 Modelled energy-active depth and measured energy-bias data, giving active depth-bias relationship.

Fitting the measured and modelled energy deposition (figure 4-16), it can be seen, by comparing the dual Y axes, that there is a linear relationship between the applied bias and the active region width. For this device, the relationship is,

$$Active \quad thickness \quad = \quad 0.83 \ V_B \quad + \quad 1.6 \qquad \mu m \qquad (4-8)$$

Hence for an applied bias of 250V (as is the case in figure 4-10), the active thickness will be ~ 209μm, and as shown in figure 4-11 the 14keV X-rays are therefore absorbed within the field free region, when incident from the rear.

This experiment was only carried out once and it would be desirable in the future to repeat it with different devices and different proton energies, but most importantly, at a range of temperatures. It will be shown in the following sections that ionised traps in the band gap make a major contribution to the space charge and hence dictate the electric field shape, so that cooling the devices and increasing trap occupation decreases the depletion depth.

4.4 Charge collection efficiency and trap activation energy

The main effect of trap energy levels in the band-gap is to reduce the charge collection efficiency (CCE) of the detector. Since an energy level can only act as a trap when it is not already occupied

(i.e. when it is ionised), the charge collection efficiency is a measure of trap occupation. When a trap is occupied, the energy required to release the trapped charge carrier and thus re-activate the trap is called the activation energy. In the case of an electron trap, the activation energy is simply the energy required for the trapped electron to reach the conduction band and in the case of a hole trap, it is the energy required by an electron from the valence band to reach the trap energy level and liberate the hole. The probability that an electron makes a given transition per unit time is proportional to the probability that it gets enough energy, and since the energy distribution for electrons is simply the Fermi distribution, the time constant associated with the release of charge carriers from traps may be expressed in terms of the activation energy E_a of the trap,

$$\tau = C \exp\left(-\frac{E_a}{kT}\right) \qquad \text{seconds} \qquad (4\text{-}9)$$

where C is a linear constant, k is Boltzmann's constant and T is the temperature in Kelvin. Thus trap activation energy, or the depth of the trap within the band-gap may be calculated if two values of the trap release time constant, τ_1 and τ_2, are measured at temperatures T_1 and T_2.

$$\tau_1 = C \exp\left(-\frac{E_a}{kT_1}\right) \qquad \text{seconds} \qquad (4\text{-}10)$$

$$\tau_2 = C \exp\left(-\frac{E_a}{kT_2}\right) \qquad \text{seconds} \qquad (4\text{-}11)$$

Dividing equation 4-10 by 4-11, and rearranging,

$$E_a = k \frac{\ln\left(\tau_1/\tau_2\right)}{\left(\frac{1}{T_2} - \frac{1}{T_1}\right)} \qquad \text{joules} \qquad (4\text{-}12)$$

$$= \frac{k}{q} \frac{\ln\left(\tau_1/\tau_2\right)}{\left(\frac{1}{T_2} - \frac{1}{T_1}\right)} \qquad \text{eV} \qquad (4\text{-}13)$$

Figure 4-17 is a series of spectra acquired at -79.3 °C (193.7 K) over a six hour period. The temperature was monitored with a platinum resistance thermometer (PRT) mounted on the PCB alongside the detector, and was constant (±0.2°C) throughout this period. The bias was applied at t=0 seconds, when the device was already cold, and was maintained at a constant value of 120 V. The shaping time and X-ray flux were also constant. Clearly the mode value of the charge collection efficiency (position of the spectral peak) decreases with time after the application of bias. This indicates that the density of active traps is increasing as carriers are thermally emitted and are not replaced because the device is under bias and therefore depleted.

Figure 4-17 Spectra acquired at -79.3°C over a six hour period.
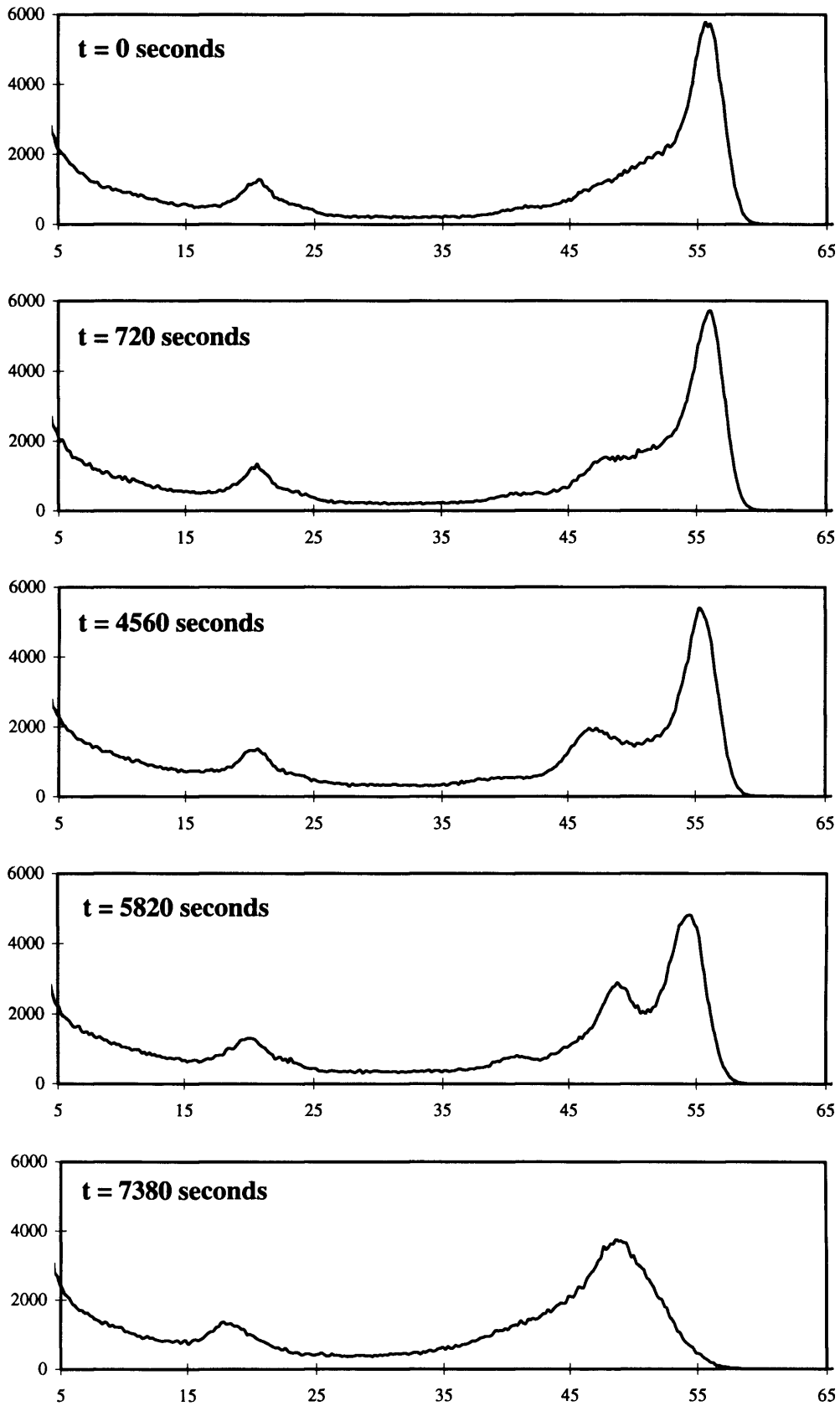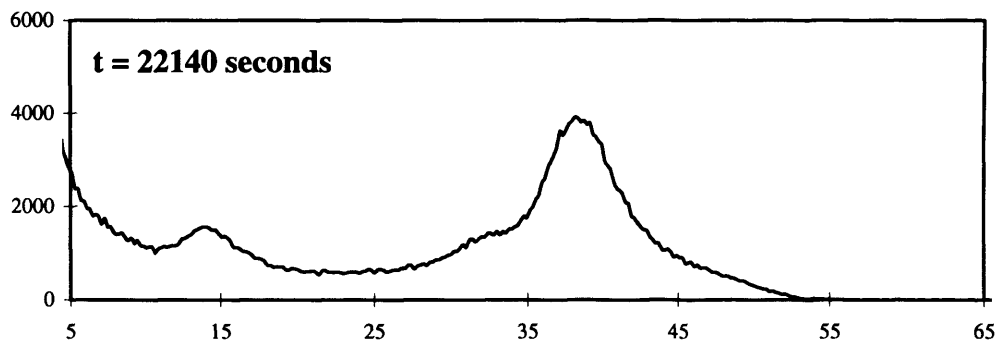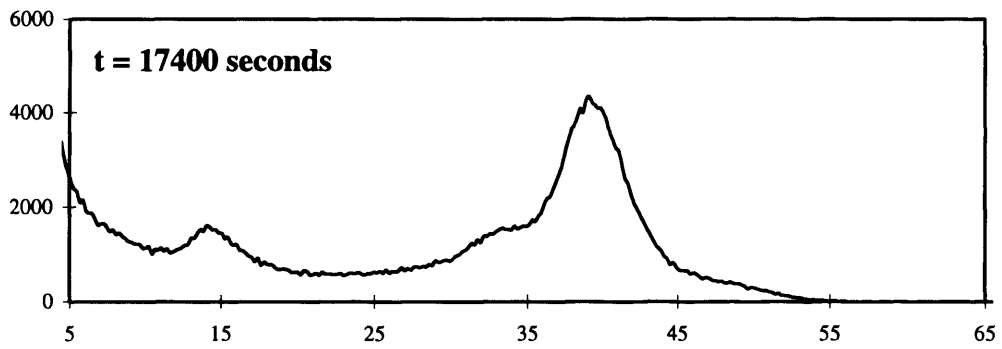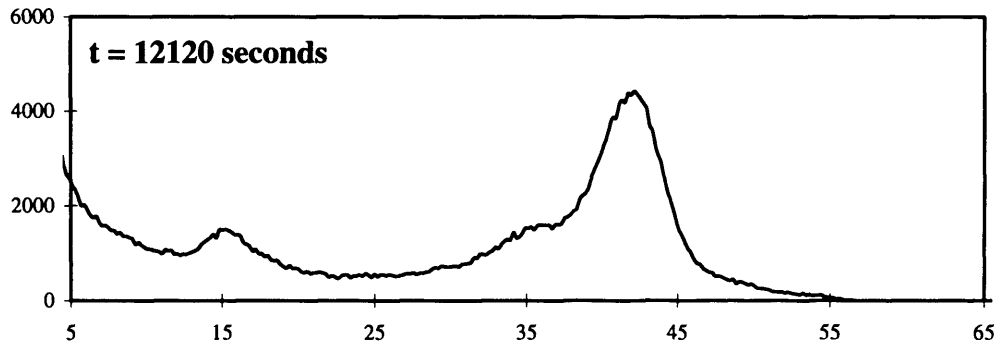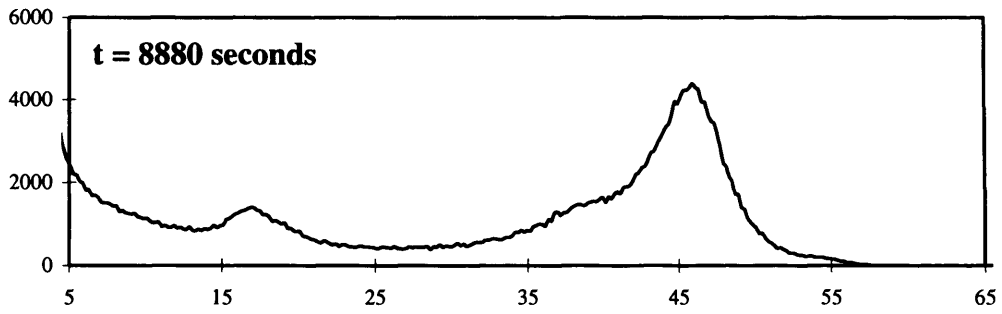
By accurately measuring the modal charge collection efficiency and fitting an exponential function, it may be seen that the time constant associated with the increase in active trap density, and hence with the de-trapping of carriers is 4500 ± 100 seconds at this temperature (figure 4-18). Repeating the measurement at -71.7°C (201.3 K), the time constant is 860 ± 30 seconds (figures 4-19 and 4-20). Using these results in equation 4-12 we find that the activation energy associated with the dominant trapping mechanism at these temperatures is,

$$= \frac{k}{q} \frac{\ln\left(\frac{4500}{860}\right)}{\left(\frac{1}{201.3} - \frac{1}{193.7}\right)} = 0.73 \pm 0.05 \ eV \qquad (4\text{-}14)$$

which is one of the energies associated with the well known EL2 trap complex. Despite being one of the most thoroughly studied traps in any semiconductor, the exact nature of this defect is still unclear, although it is certainly centred upon an As_{Ga} anti-site and is believed to comprise at least three energy levels [Hoon Young cho, 1988]. One of these lies at a depth of ~0.73eV from the conduction band edge or 0.69eV from the valence band edge. Substitution of τ_1, E_a and T_1 into equation 4-10 gives the linear constant, C (= 4.14E-16) and equation 4-9 then gives the de-trapping time constant for this trap as a function of device temperature. This is shown in figure 4-21.

$$CCE = 63.7 + 100\exp(-t/4500)$$
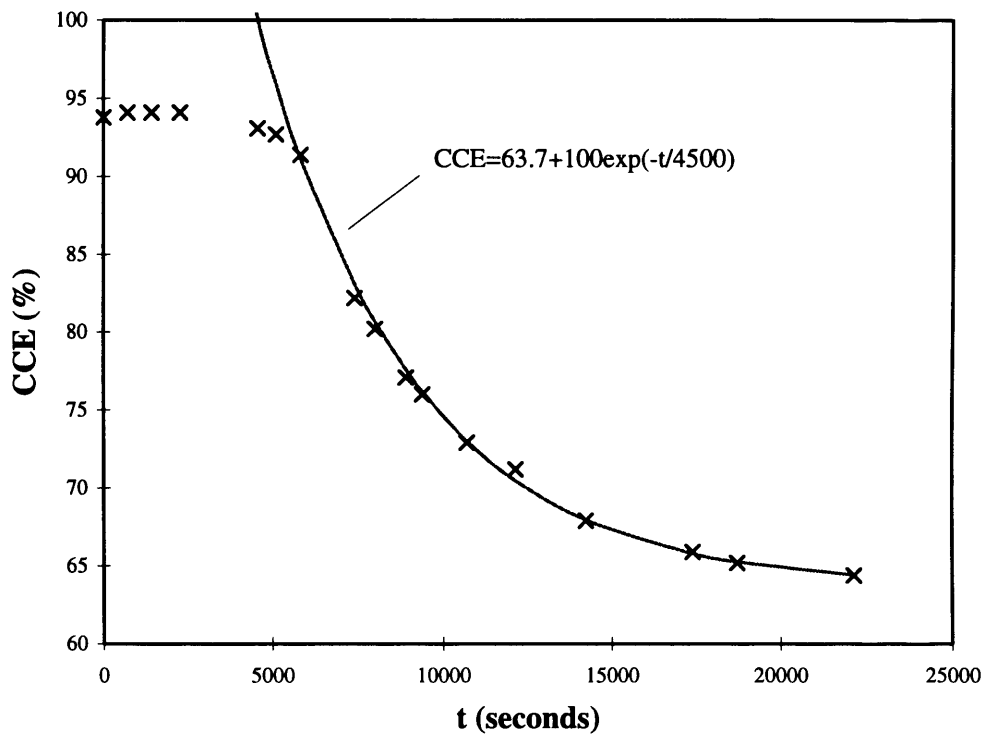
Figure 4-18 Exponential decrease of CCE at -79.3°C, indicating a trap release time constant of ~4500 seconds.

Figure 4-19 Spectra acquired at -71.7°C over a six hour period.
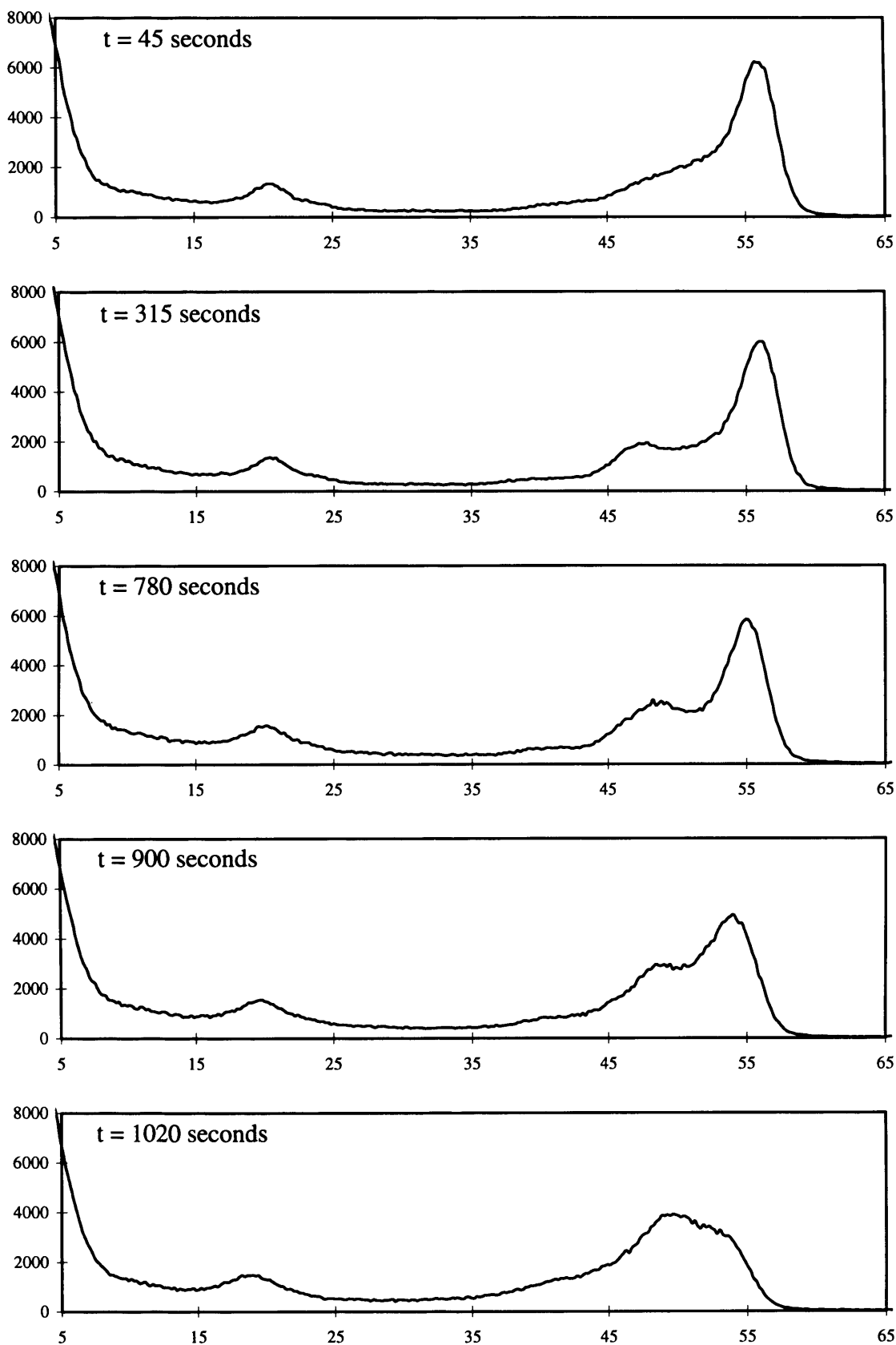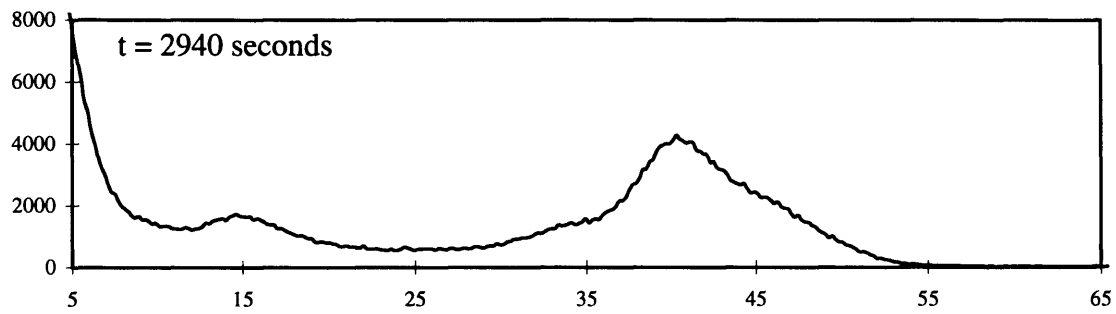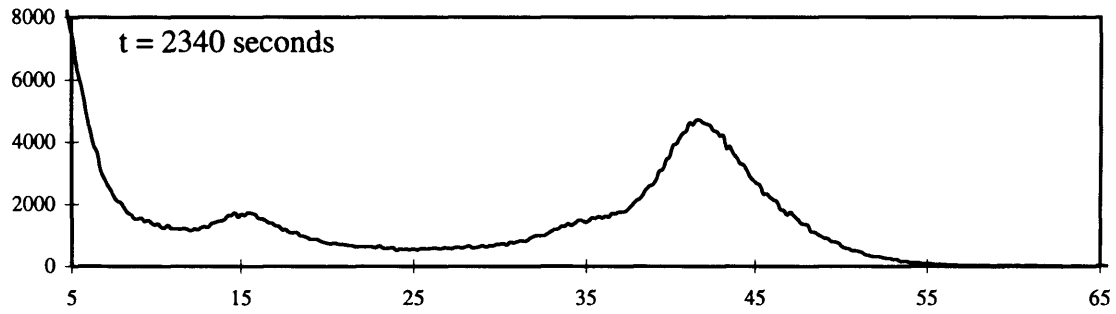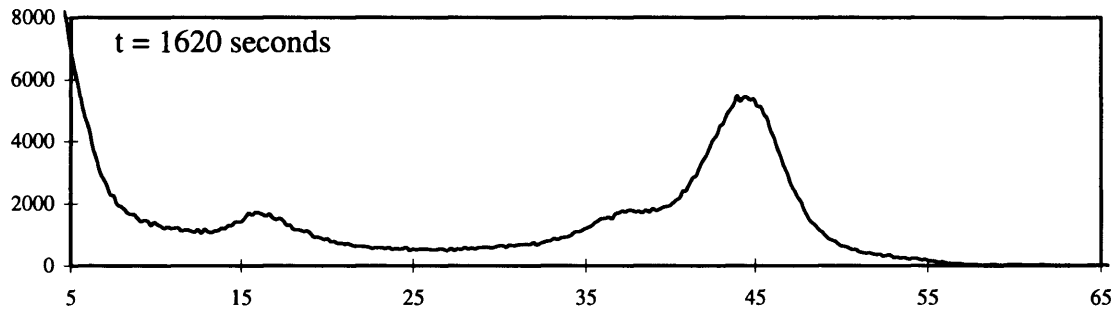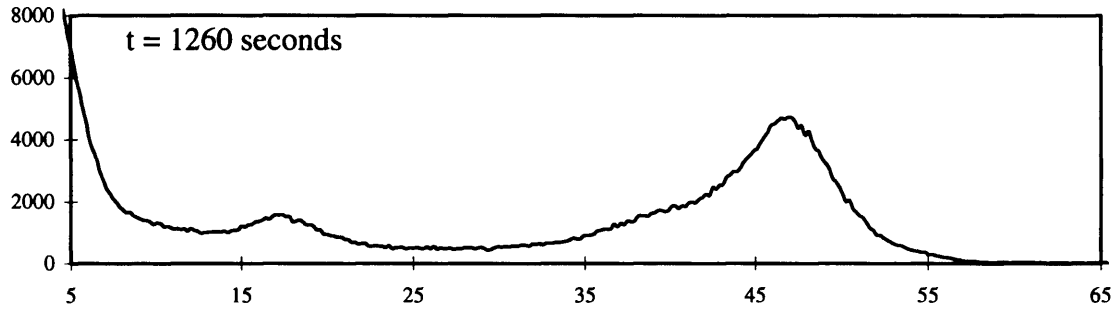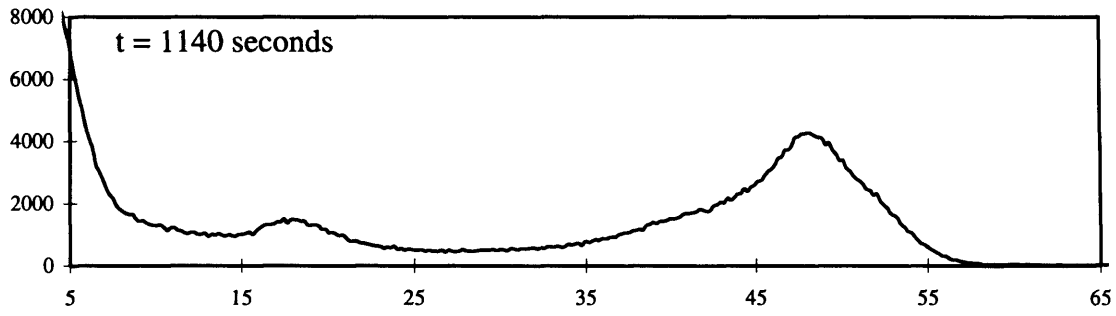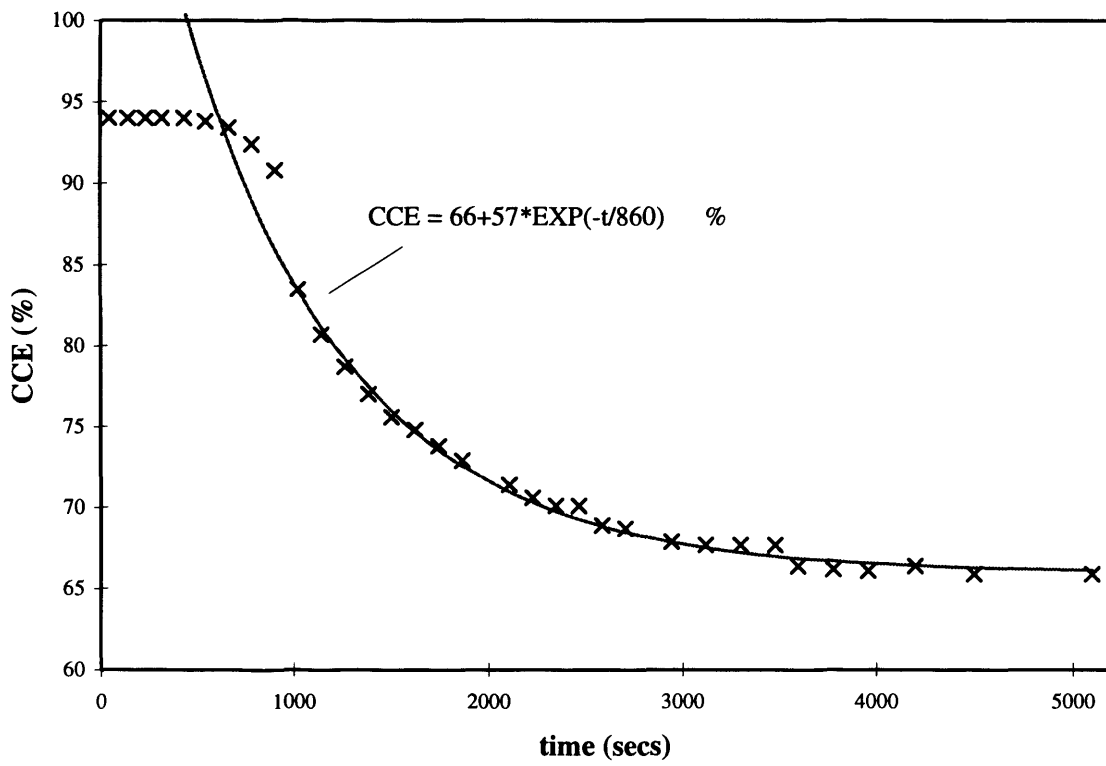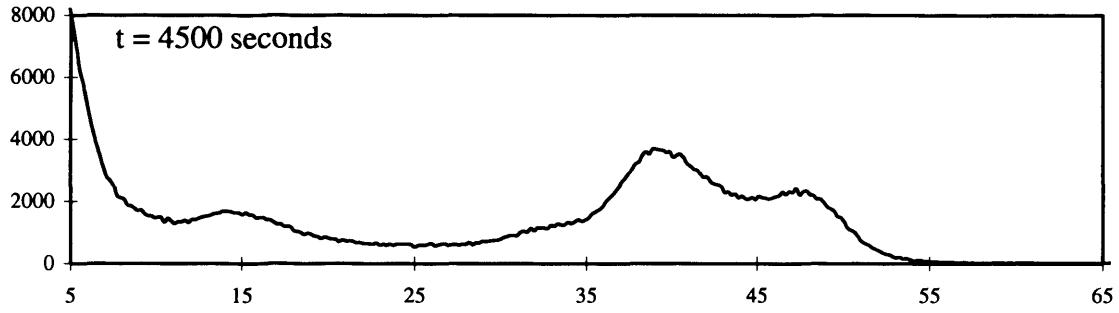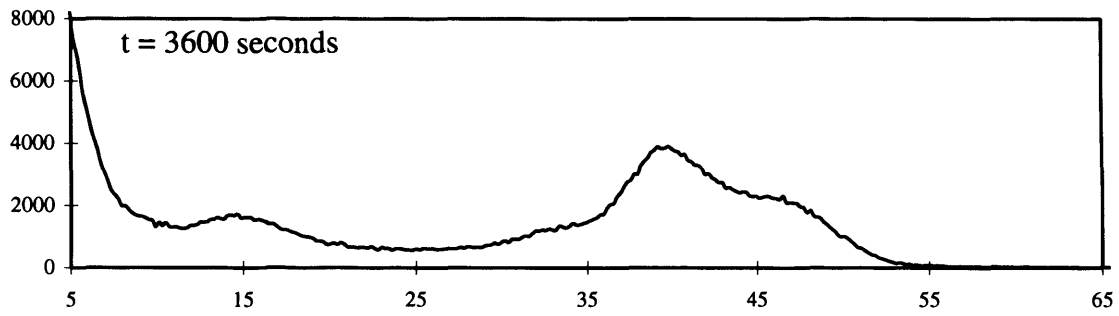
Figure 4-20 Exponential decrease of CCE at -71.7°C, indicating a trap release time constant of ~860 seconds.
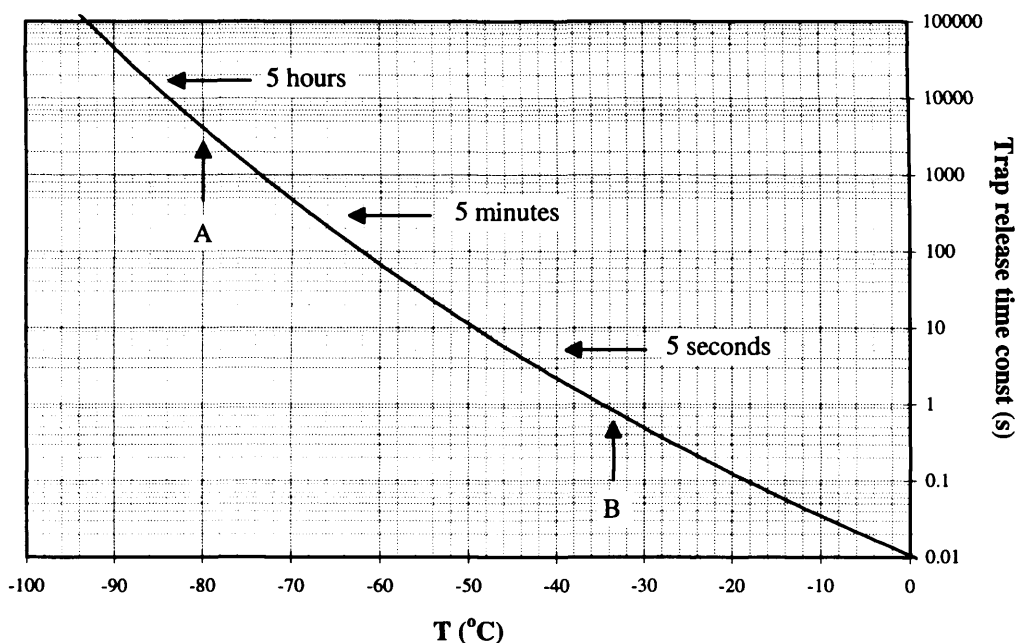
Figure 4-21 Exponential release time constant for a trap (or trap complex) with an activation energy of 0.73eV.

The effect of this trap may be seen as a step in a plot of CCE as a function of temperature (figure 4-22). Point A, where the deviation from a linear increase in CCE is first observed, corresponds to a de-trapping time constant of about 5000 seconds (1.4 hours). By point B, there are no significant numbers of occupied traps remaining. In figure 4-22, this occurs at -33°C which corresponds to a de-trapping time constant of about 1 second for a 0.73eV activation energy, but the location of this turning point will depend upon the time-scale of the experiment.
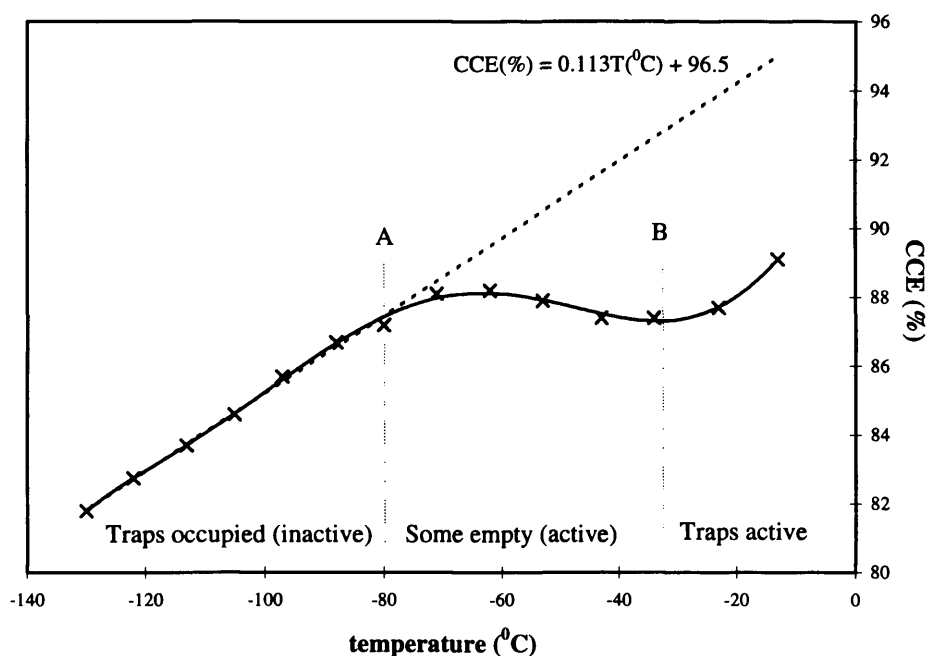
Figure 4-22 Step in CCE is due to the emptying or activation of traps with increasing temperature.

4.5 Offset of breakdown at low temperatures and best spectra
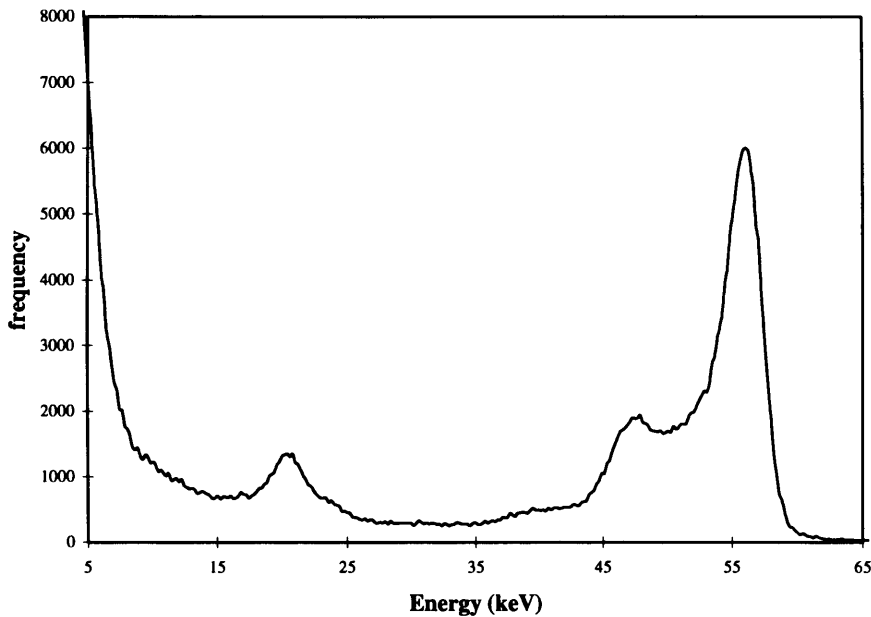
Figure 4-23 Typical Am 241 spectrum at -30°C indicating dominance of carrier trapping.

Figure 4-23 is a typical spectrum from an 80 μm device at -30°C under an applied bias of 130V. The effects of carrier trapping are evident as an extended low energy tail to the photo-peak which is centred on 56 rather than 59.5 keV (a modal charge collection efficiency of 94%).

In the previous section it was demonstrated that by cooling bulk GaAs devices to below -80°C before the application of bias, a large fraction of traps can be left occupied and hence inactive. This not only reduces trapping directly, but also has the effect of deferring device breakdown. At -30°C a maximum field of approximately 1.5 V/μm can be applied, while at -100°C the devices can support in excess of 4 V/μm. This implies that unoccupied (or active) traps acting as generation centres, are causing the devices to breakdown prematurely.

Applying greater bias has the effect of increasing the mean electric field strength and hence carrier velocities, reducing the probability of direct band to band recombination and carrier trapping. It also reduces the width, and hence the significance of the low field, or partially depleted region. This, combined with the direct reduction in trap density, means that spectra obtained under conditions of low temperature and high bias show a substantial decrease in the effects of trapping.

94
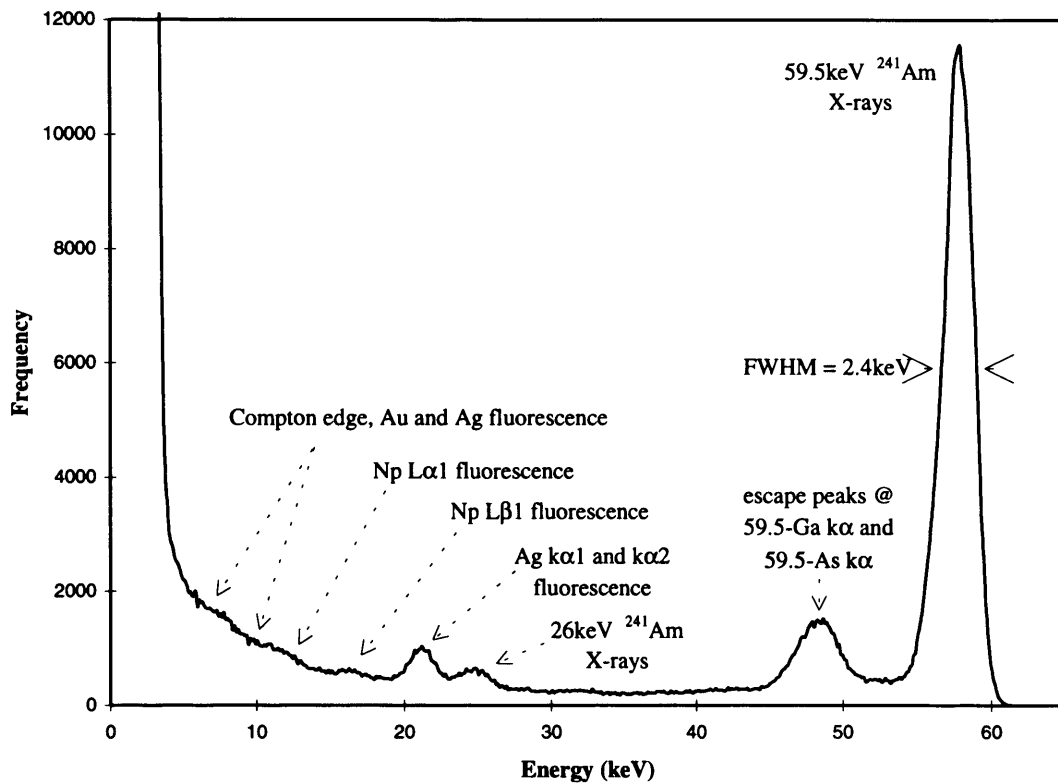
Figure 4-24 Am 241 spectrum indicating reduced trapping at low (-130°C) temperatures.

Figure 4-24 shows a spectrum obtained at -130°C from the same 80μm device as figure 4-23, under an applied bias of 300V. Again the source is [241]Am giving a principal emission line at 59.5keV. The effects of charge trapping are greatly reduced, giving reasonable separation of the photo-peak and the escape peak, as well as the appearance of a number of lower energy features. The resolution is 2.4keV FWHM @ 59.5keV which, with a readout noise of 1.8keV (FWHM of pulser peak), indicates that there is still a 1.6keV component to the measured FWHM, due to the effects of trapping.

Among the features present at lower energies are Neptunium L fluorescence (Neptunium is a decay product of Americium 241), Gold fluorescence from the Schottky contact, and Silver fluorescence from the thermoplastic used for wire bonding. As well as the principal emission at 59.5 keV, the Americium 241 source gives lines at 43, 33 and 26 keV and a significant Compton background which is virtually obscured by a continuum feature due to X-rays being absorbed in low field regions.

By including the Neptunium, Gold and Silver fluorescence in a Monte-Carlo simulation (chapter 6), and fitting the measured and modelled spectra, the energy scale may be calibrated with some accuracy. This then gives the degree of trapping in terms of a σN product for holes and electrons, where σ is the trapping cross section and N is the effective trap density.
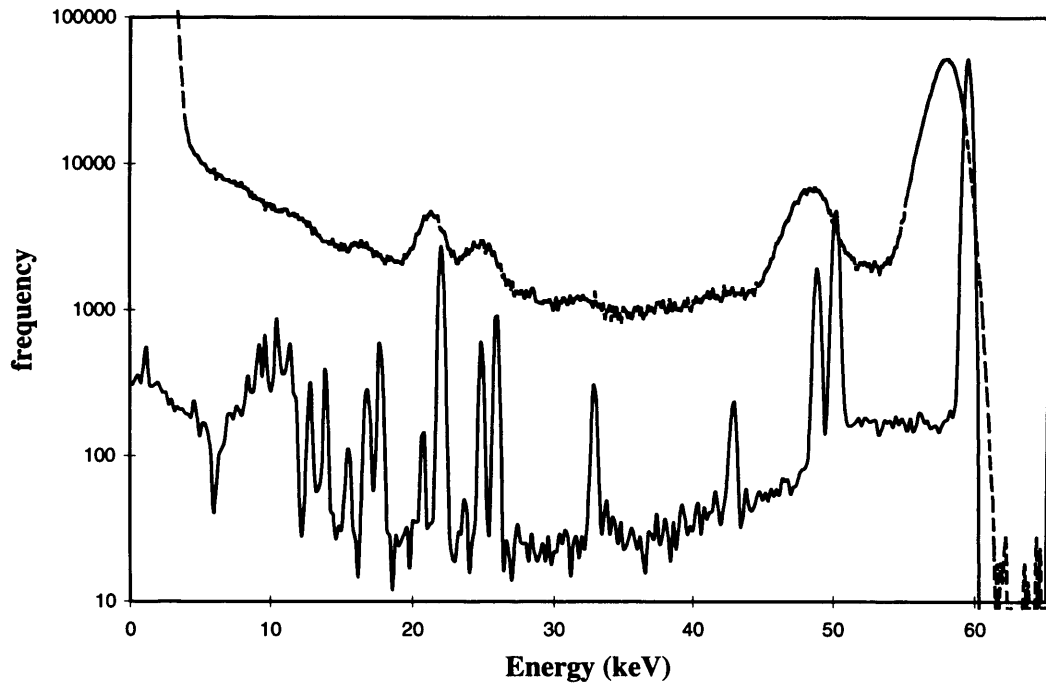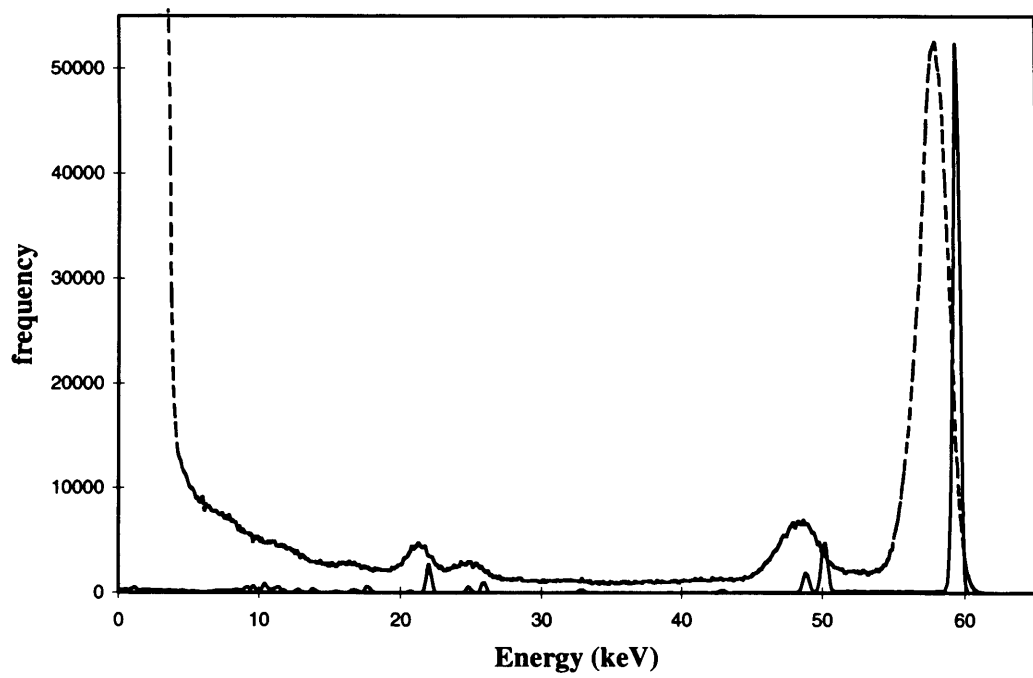
Figure 4-25 Measured spectrum (dotted) and modelled Fano limited, 'trap free' spectrum

Figure 4-25 shows the measured spectrum of figure 4-24 with the results of the Monte-Carlo simulation in the absence of trapping or readout noise (Fano limited). The numerous lines due to Np, Au and Ag fluorescence can be seen in the modelled spectrum when plotted logarithmically, as well as the Compton distribution and well separated escape peaks.
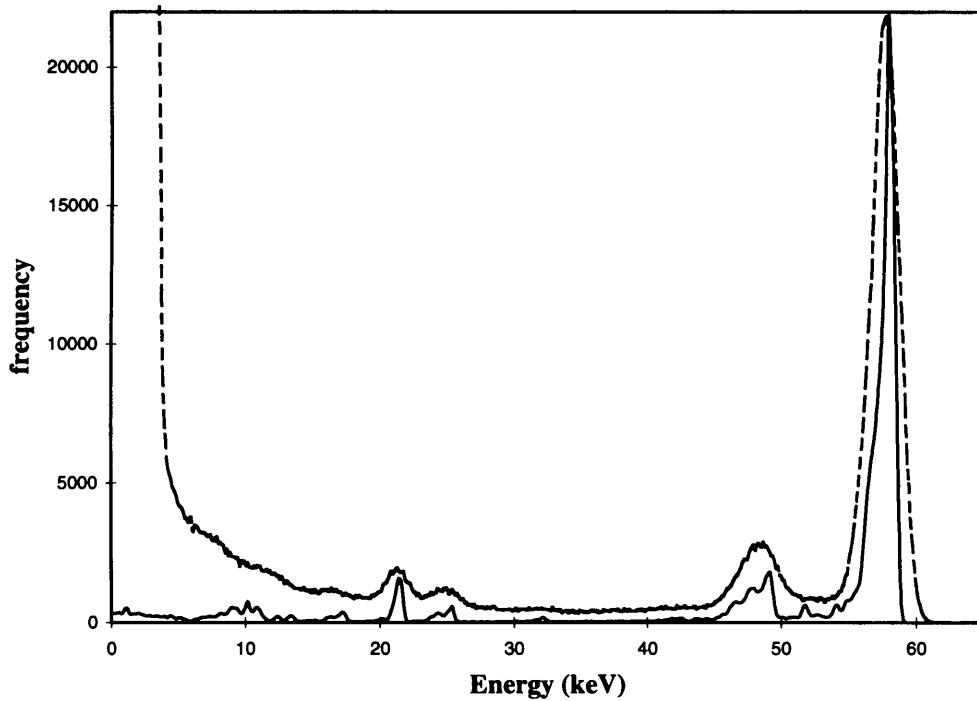
Figure 4-26 Measured spectrum (dotted) and modelled spectrum including trapping but no noise

In figure 4-26, the effects of carrier trapping have been added to the simulation, but the simulated readout noise is still zero.
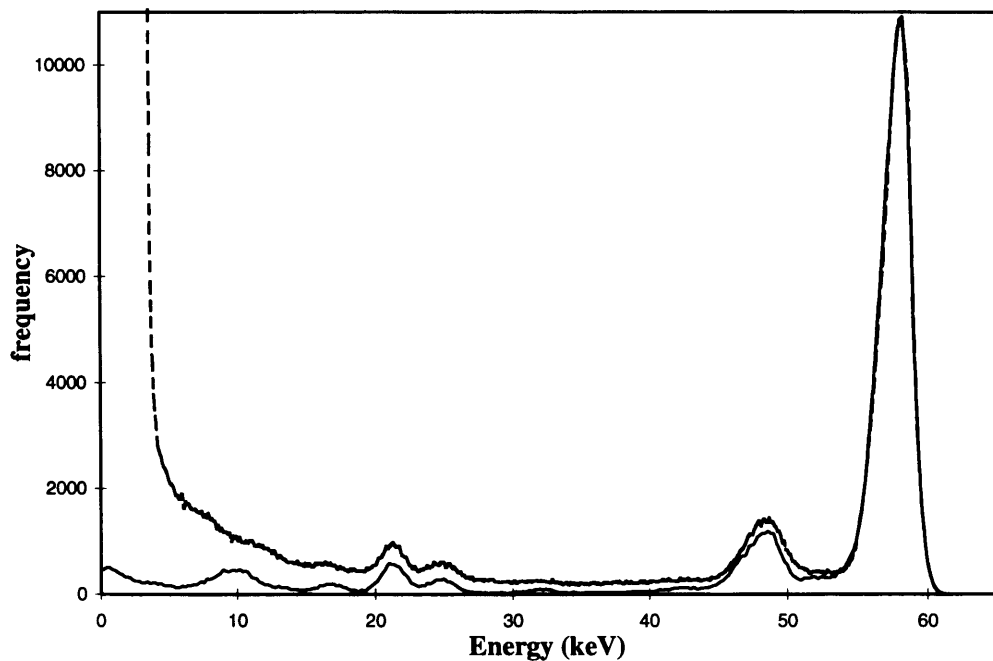
Figure 4-27 Measured spectrum (dotted) and modelled spectrum including trapping and readout noise

Figure 4-27 shows the measured spectrum and the results of the Monte-Carlo simulation including carrier trapping and readout noise. The significant background level across much of the measured spectrum is due to X-rays being detected in an extended low field region around the device perimeter

and/or in a partially depleted (almost field free) region between the depletion region and the rear contact. These weak field regions are not included in the model.

The values of the cross section and density product (σN) giving this best fit are 7.5cm^{-1} for electrons and 3cm^{-1} for holes. Typical values at approximately -30°C (well above -80°C) are 37cm^{-1} and 5.5cm^{-1} for electrons and holes respectively. By cooling the device before applying bias we have therefore achieved a reduction in active trap density by a factor of ~5 for electrons and ~2 for holes.
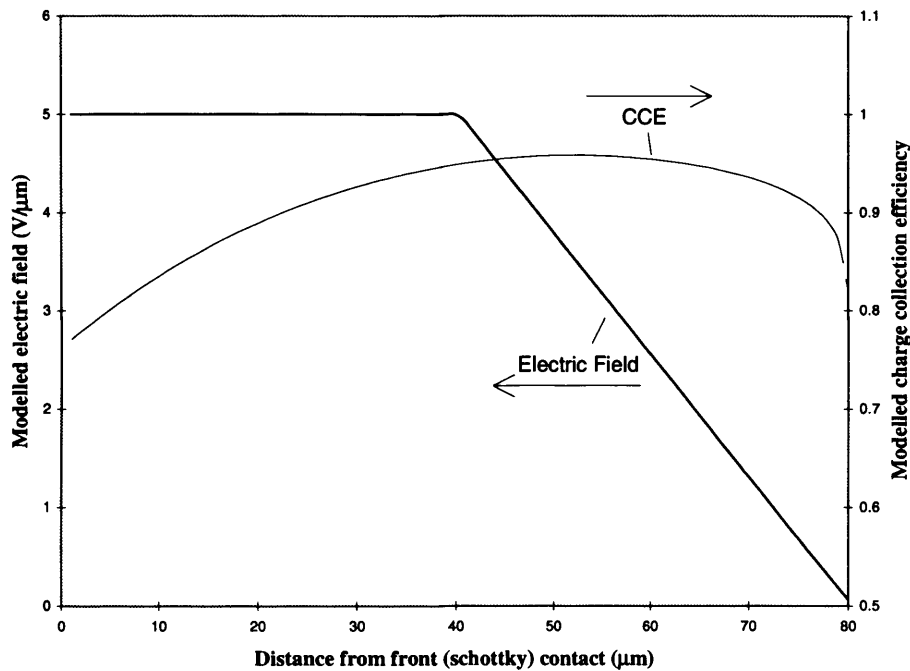
Figure 4-28 Electric field profile found to give the best fit to measured spectrum at -30°C

Figure 4-28 shows the form of the electric field profile found to give the best fit to measured spectra above approximately -80°C. It includes a zero space charge (constant E-field) region and a constant space charge (linearly decreasing E-field) region. The inclusion of a zero space charge region was first suggested by the results of figure 4-12 (electric field profiles measured by Berwick and Brozel), and its extent was quickly found to be an important parameter in spectral fitting.
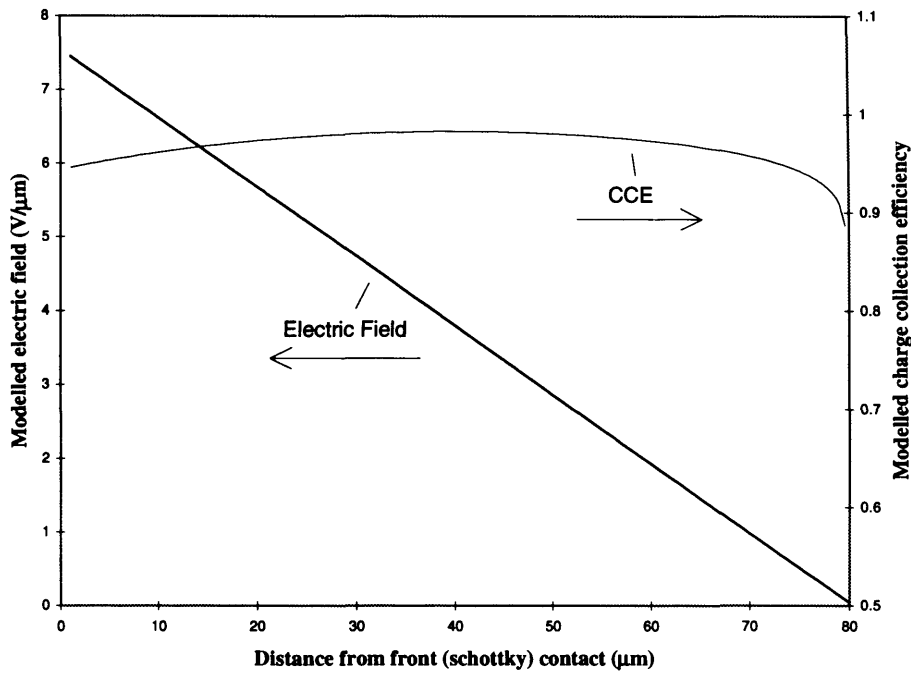
Figure 4-29 Electric field profile found to give the best fit to measured spectrum at -130°C

The electric field profile required to give the best fit in the case of reduced trapping (figure 4-27), is shown in figure 4-29. In this case a linearly decreasing electric field is found to give the best fit, with no region of zero net space charge. An electric field of this form (dE/dx = constant) indicates that the net charge density is constant throughout the depletion region, and may be modelled using the depletion approximation (section 2.3).
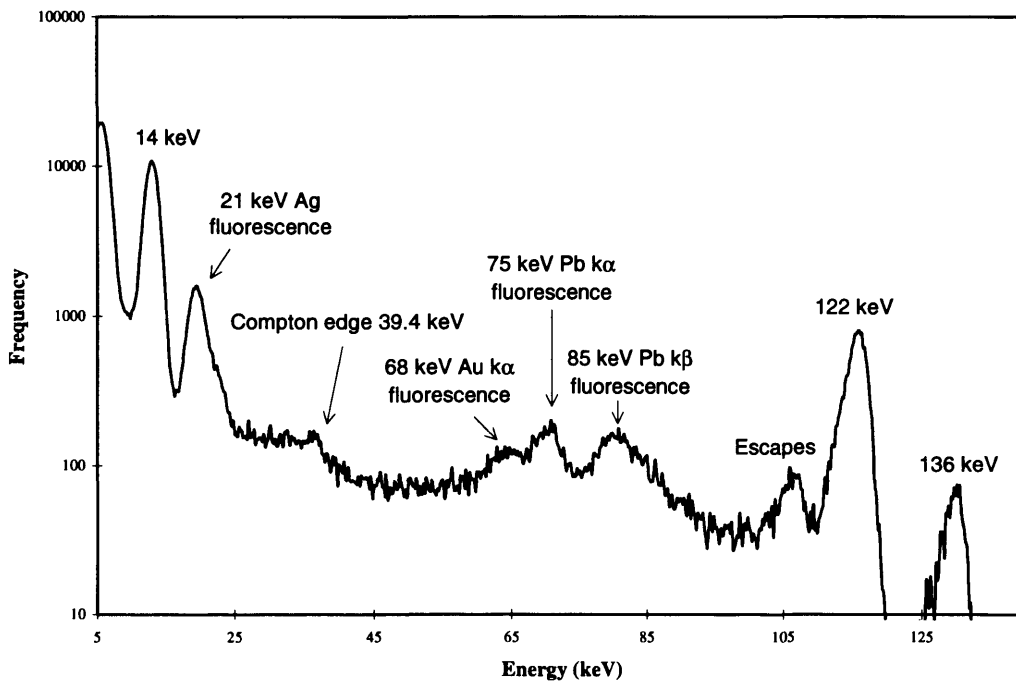
Figure 4-30 Co 57 spectrum obtained from 80μm device at -130°C with 300V bias.

Figure 4-30 shows a Cobalt 57 spectrum obtained under optimum conditions of temperature and bias. The source gives decay lines at 136, 122 and 14 keV. Gold, silver and lead fluorescence lines from

the contact, the wire bond and the shielding are also present and the Compton edge is particularly clear. The charge collection efficiency at 122 keV is approximately 95%.

From the results presented in this chapter it can be seen that the presence of a significant density of charge trapping and recombination centres degrades spectral resolution both by the direct removal of signal charge, and by altering the space charge which reduces the electric field and hence carrier velocities. Although there are probably several trap species present, the energy level which dominates the trapping as evaluated by measuring release time constants, lies 0.73eV below the conduction band edge. This energy level is one of several commonly associated with the EL2 native defect which is thought to be a crystalline point defect comprising a gallium vacancy and a Ga_{As} anti-site.

The effect of 'freezing in' the dominant trap species has been demonstrated as a dramatic improvement in spectral resolution, and the influence of the trap on space charge has been shown to give a linear variation of the depletion depth with applied bias.

5. MODELLING SPECTRAL RESPONSE

X-ray spectra obtained using bulk GaAs detectors are generally dominated by features resulting from the high density of traps, or energy levels deep within the band gap. As shown in the previous chapter, the energy level associated with a dominant trap species may be calculated by measuring the trap release time constant at several temperatures, and the effects of trapping can be reduced by simply cooling the detector to fill traps and reduce the active trap density. Traps have also been shown to be responsible for altering the form and extent of the depletion region by virtue of their inherent space charge.

In order to understand better the relationship between trap parameters (such as cross section-density product and energy level), experimental parameters (such as temperature, applied bias and peaking time), and spectral features, a Monte-Carlo model has been developed to simulate the response of GaAs planar Schottky diode detectors to X-rays. The model has been used to fit measured spectra and hence to quantify trapping in terms of electrons and holes independently. It has also proved an aid to predicting trends with temperature, bias etc. and has been successfully used to fit spectra measured with different shaping times, giving trap release time constants and hence a value for trap activation energy.

5.1 Introduction

All of the devices tested throughout this work have been planar, with large (>1mm^2) circular electrodes covering front and back. They have therefore been modelled using a simple one dimensional array, depth being the only positional parameter.

Before simulating the absorption of any X-rays, the model first calculates the Charge Collection Efficiency (CCE) of the detector as a function of X-ray interaction depth. This is the proportion of an electron and hole cloud that will be detected in the circuit connected to the device as a fraction of the charge generated at the interaction point. All of the trap parameters which are responsible for the characteristic GaAs peak shape (cross section, density and energy level), are incorporated into the calculation of the CCE which is also a sensitive function of carrier velocity and hence applied bias and electric field shape.

Once the charge collection efficiency has been established as a one dimensional array (CCE(depth)), a number (usually several hundred thousand) of incident X-rays are simulated. An interaction depth is randomised according to the linear attenuation coefficient of GaAs at this photon energy, and a series of randomisations is used to determine whether the interaction is by Compton scattering or by

photoelectric absorption with a gallium or an arsenic atom. In the case of photoelectric events, the means of de-excitation is randomised according to the fluorescence yield and electron shell jump ratios, and for all types of interaction, the energy and direction of the scattered or emitted photon is fed back into the X-ray interaction loop, and the energy deposited is multiplied by the CCE at the interaction depth, and added to the total for this event.

The charge deposited at the interaction depth is adjusted according to the Fano noise, and the charge measured in the external circuit (after multiplying by the CCE) is adjusted according to the noise of the readout circuit. The total energy for the event is then used to increment a spectral array. In this way a spectrum is built up which contains photo-peaks, escape peaks and a Compton distribution, all of which are deformed by the effects of trapping, through the depth dependent CCE.

The model does not include the effect of weak field regions which are believed to surround the area defined by the contact metallisation, and which are probably responsible for the extended background observed in all bulk GaAs spectra. Too little is known about these regions to make physically reasonable assumptions about their shape and extent. Edge effects due to the long photoelectron range at high X-ray energies are included however, since energy losses here may be randomised according to simple geometrical considerations.

5.2 User defined parameters

The input required by the model is device thickness, applied bias, temperature, integration time (peaking time), the number of X-ray detections to be simulated, the electronic noise of the detection circuit, measured as the FWHM of a pulse generator peak, and the energy of the incident X-rays. This may be a single energy, or for some laboratory sources, a range of energies with associated probabilities. X-rays are generally incident upon, and perpendicular to, the negative Schottky contact, as in the lab, although back illumination may also be readily simulated.

The electron and hole trap 'cross section-density products' ($\sigma_n N_{tn}$ and $\sigma_p N_{tp}$) may be set to trial values or may be evaluated by looping the model in an attempt to find the best fit to a measured spectrum. By modelling several spectra with different integration times, or by observing the decrease in the measured CCE with time at certain temperatures, values for the trap release time constants may be ascertained which are related to the trap energy levels. These levels may then be incorporated into the model, to demonstrate much of the spectral variation observed with integration time and temperature.

5.3 Calculation of depth dependent Charge Collection Efficiency

The model first calculates the electron and hole trapping time constants τ_n and τ_p in seconds according to (see section 2.4 for derivation)

$$\tau_n = \frac{1}{\sigma_n v_{thn} N_{tn}}$$ (2-63)

$$\tau_p = \frac{1}{\sigma_p v_{thp} N_{tp}}$$ (2-64)

where σ is the trap cross section, N is the trap density, and the thermal velocity is given by [Blakemore, J.S., 1982]

$$v_{thn} = 4.4x10^5 \sqrt{\frac{T}{300}}$$ (5-1)

$$v_{thp} = 1.77x10^5 \sqrt{\frac{T}{300}}$$

The electric field is then determined across the device in 1μm steps according to the thickness, the applied bias and the profiles measured by Berwick and Brozel [Berwick, K., 1993] i.e. with a constant field region adjacent to the Schottky contact (zero net space charge). From the electric field strength, the drift velocities v_{de} and v_{dh} may be calculated in μms^{-1}. Values of mobility quoted for GaAs ($8500cm^2/V$-s and $400cm^2/V$-s for electrons and holes respectively) are only applicable over small ranges of electric field strength because the velocity-field relationships are clearly non-linear (figure 5-1). Measured values of carrier velocity have therefore been used.
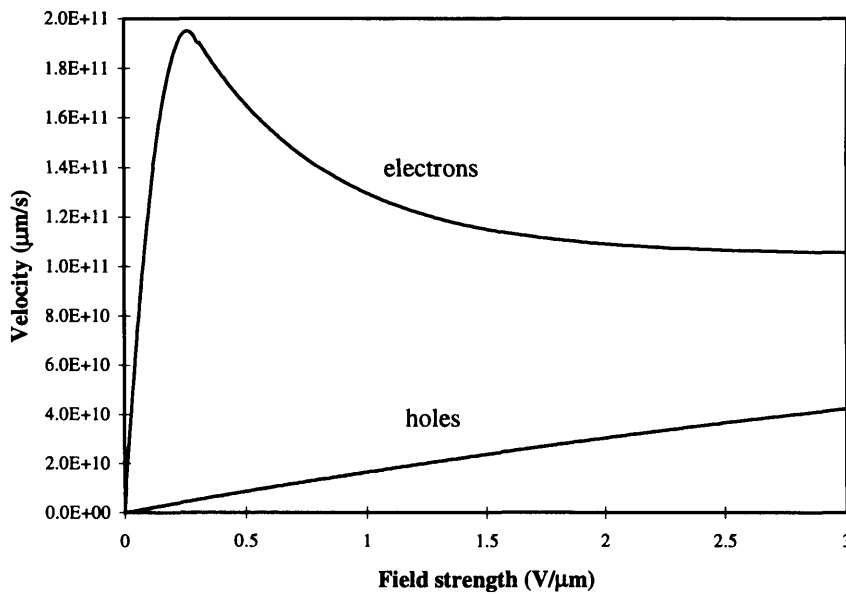
Figure 5-1 Carrier velocities in GaAs

The reciprocal of the carrier velocity in μm/s is the time, (in seconds), taken to traverse one micron. Using the trapping time constants already calculated in equations 2-63 and 2-64, the fractions of carriers that are not trapped during this time are therefore given by the exponentials

$$f_e(x) = \exp[-1/(v_{de}\tau_n)] \qquad (5\text{-}2)$$

$$f_h(x) = \exp[-1/(v_{dh}\tau_p)] \qquad (5\text{-}3)$$

These equations give the fraction of carriers which are not trapped in traversing a given one micron step within the device as a function of the electric field strength, but they do not allow for those carriers which are trapped but then subsequently de-trap within the integration time and contribute to the pulse height. They may be used as they stand to fit measured spectra, but the resulting values of σN will be too small, since one would then be equating these values of f(x) to the fraction of charge carriers never trapped plus that fraction released within the pulse integration time. These fractions must therefore be adjusted exponentially once again, according to the trap release time constants and the integration time.

$$f_e(x) = 1 - (1- \exp[-1/(v_{de}\tau_n)]).\exp(-t/\tau_{re}) \qquad (5\text{-}4)$$

$$f_h(x) = 1 - (1- \exp[-1/(v_{dh}\tau_p)]).\exp(-t/\tau_{rh}) \qquad (5\text{-}5)$$

where t is the integration time, τ_{re} is the electron trap release time constant and τ_{rh} is the hole trap release time constant. The fractions of charge that escape trapping, given by equations 5-4 and 5-5, now quantify the net trapping and will increase with pulse integration time. Values of cross section-density product obtained using these equations rather than equations 5-2 and 5-3 will be independent of integration time (as they should be), and trap release time constants have now been introduced as fitting parameters. These release time constants are related to trap energy levels by

$$\tau_{re} = C_e \exp\left(- \frac{E_{ae}}{kT}\right) \qquad (5\text{-}6)$$

$$\tau_{rh} = C_h \exp\left(- \frac{E_{ah}}{kT}\right) \qquad (5\text{-}7)$$

where E_{ae} and E_{ah} are electron and hole trap activation energies respectively, and C_e and C_h are constants.

The elements of arrays $f_e(x)$ and $f_h(x)$ (each representing one micron of device thickness) are now numbers between 0 and 1, which is the fraction of any number of electrons ($f_e(x)$) or holes ($f_h(x)$) which, passing through, will **not** be trapped within this micron. The fraction of electrons or holes remaining un-trapped in moving from an initial depth, z to some other depth, y is therefore simply the product of the intervening values of f(x),

$$fraction\ untrapped\ z\ to\ y\ =\ \prod_{x=z}^{x=y} f(x) \tag{5-8}$$

and the fractional contribution to the signal measured in moving the un-trapped charge carriers across a one micron step at y, is simply the work done, or the potential through which they must be moved as a fraction of the total potential across the detector. If the electric field at y is E(y) $V\mu m^{-1}$ then the contribution to the signal is,

$$contribution\ to\ signal\ at\ y\ =\ \frac{E(y)}{V_b} \prod_{x=z}^{x=y} f(x) \tag{5-9}$$

where Vb is the applied bias. In order to calculate the charge collection efficiency for an interaction depth z, it is necessary to sum all of the signal contributions for electrons moving from z towards the maximum potential and holes moving from z towards the minimum potential. Thus

$$CCE(z)\ =\ \sum_{y=z}^{y=0} \left\{ \frac{E(y)}{V_b} \prod_{x=z}^{x=y} f_h(x) \right\} + \sum_{y=z}^{y=thick} \left\{ \frac{E(y)}{V_b} \prod_{x=z}^{x=y} f_e(x) \right\} \tag{5-10}$$

where the minimum potential is at z=0 and the maximum potential is at z=*thick*, the depletion depth thickness. Equation 5-10 may be solved once arrays for E(x), fe(x) and fh(x) (equations 5-4 and 5-5) have been established, to give the Charge Collection Efficiency as a function of X-ray interaction depth. This array may then be used as a response matrix to adjust the energy deposited in the following Monte Carlo simulation according to interaction depth.

5.4 Monte Carlo simulation of X-ray detection

Having established the charge collection efficiency of the detector as a function of depth, the required number of X-ray detections must be simulated. The initial photon energy is set according to the source being simulated and the angle (θ) of the photon from normal incidence is set to zero. The total linear absorption coefficient for photons of this energy in GaAs is calculated by fitting the data in figure 5-2.
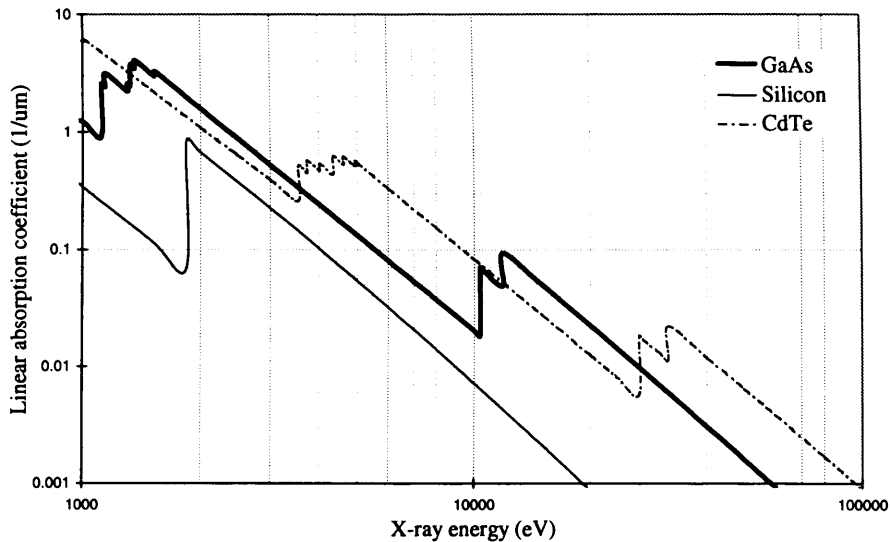
Figure 5-2 The total linear absorption coefficients of GaAs, Silicon and CdTe

X-ray attenuation may be expressed in terms of the linear absorption coefficient and intensity, as (from section 2.2)

$$I = I_o \exp(-\mu t) \qquad (5\text{-}11)$$

and re-arranging for thickness, t, (using a random number, R, between 0 and 1 for I/I_o), gives a random path length (p).

$$p = -\frac{1}{\mu} \ln(R) \qquad (5\text{-}12)$$

The depth of the interaction in the device is given by pcos θ. If this depth lies within the detector thickness then a detection is registered and a second randomisation weighted by the linear absorption coefficients for photoelectric and Compton events at this energy, is used to determine which interaction has occurred. The photon's energy and direction, θ, are then passed to the appropriate charge deposition function (described in the following sections), which returns the energy deposited by this interaction along with the photon's new direction and energy.

The energy deposited is multiplied by the CCE at this depth and the total energy for this event (initially 0) is incremented accordingly. The scattered or emitted photon in all cases other than Auger emission is fed back into the start of the loop with its new direction and energy. This process is repeated until the photon falls outside the device (an escape) or until its energy falls below a threshold when its range is assumed to be negligible.

Figure 5-3 shows the main program loop which is repeated for the required number of X-ray events to build up an energy spectrum.
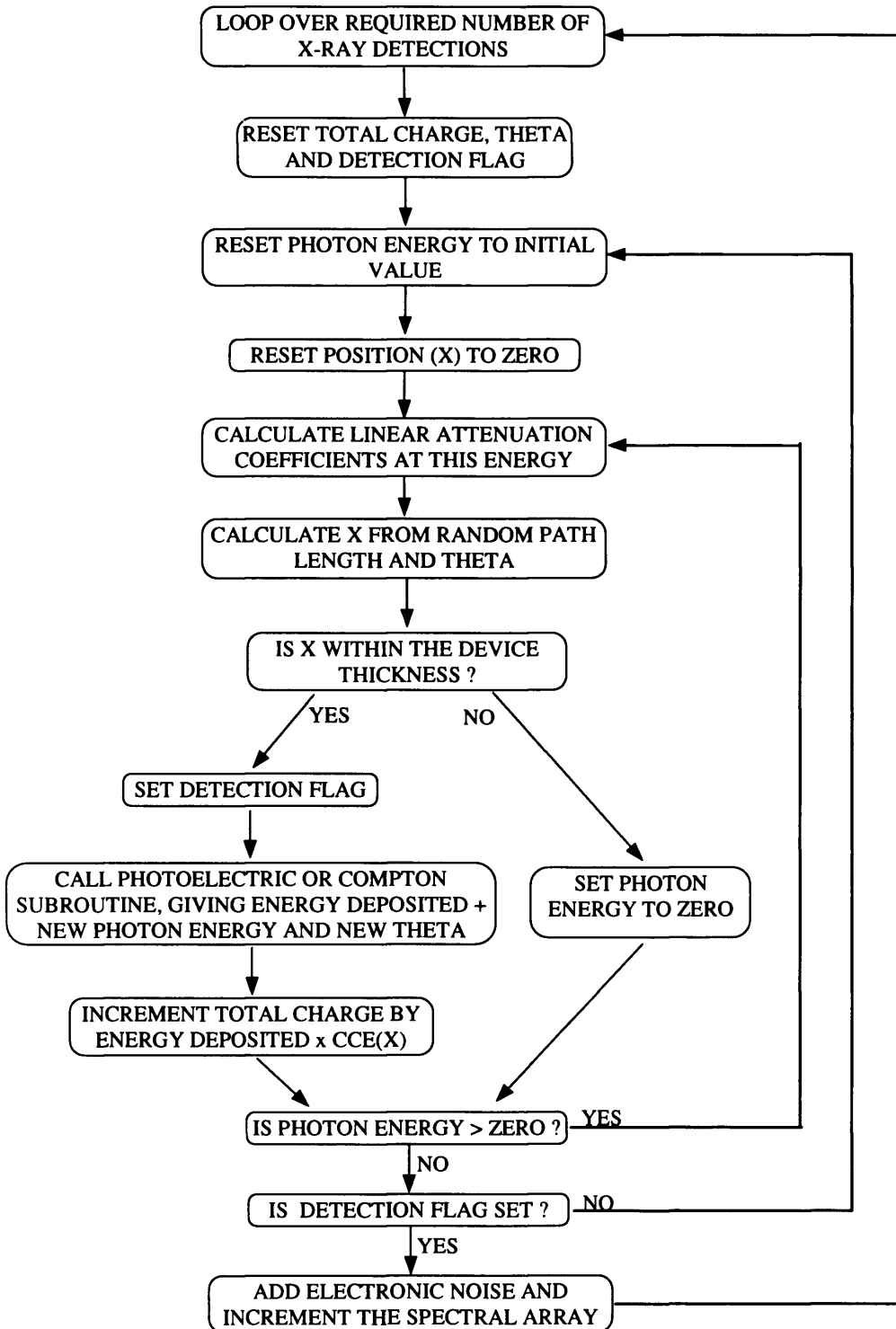
Figure 5-3 Flowchart indicating the X-ray simulation process

5.4.1 The photoelectric absorption subroutine

The photoelectric interaction subroutine carries out a series of weighted randomisation's to establish whether the photon interacts with a gallium or an arsenic atom, whether a K,L or M shell electron is ejected and whether the atom de-excites by $K\alpha$ or $L\alpha$ photo-emission or by the ejection of an Auger electron. In the case of photo-emission, the new photon energy and direction (random*2π) are

returned as well as the energy that has been deposited. In the case of Auger emission, all of the photon's energy is assumed to have been deposited locally.

In a diatomic crystal such as GaAs which has equal numbers of gallium and arsenic atoms, the relative probability that a given photon is absorbed by a gallium or an arsenic atom is proportional to the relative magnitudes of their linear absorption coefficients at that energy and may be readily randomised. The energy of the photoelectron is equal to the energy of the photon minus the binding energy with which the electron was held in its shell.

$$E_e = h\nu - E_b \tag{5-13}$$

It is therefore necessary to know from which shell the photoelectron was ejected. For the purposes of the simulation this is simple to randomise, since the steps, or edges in the photo-electric absorption versus energy curve, indicate the binding energies of the K and L shell electrons and the size of each step indicates the jump ratio, or the relative probability that the ejected electron will be from the K, L or M shell. This is shown schematically in figure 5-4.

Photon only has sufficient energy to eject an M shell electron | Photon has sufficient energy to eject an M or an L shell electron | Photon has sufficient energy to eject an M, L or K shell electron

L-edge

K-edge

J_K

J_L

J_M

Binding energy of L-shell electron

$1/\lambda$ (μm^{-1})

10

1

0.1

0.01

1000   10,000   100,000

E

X-ray energy (eV)
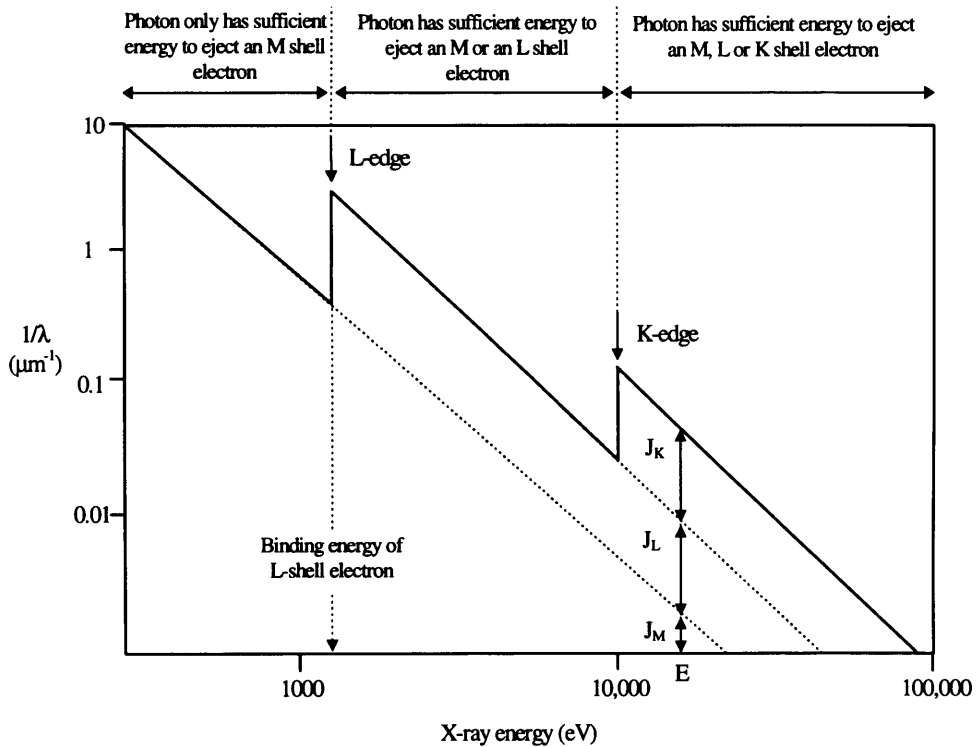
Figure 5-4 Schematic indicating how the steps in the linear attenuation coefficient give the relative contributions to the total absorption by K, L and M shell electrons (jump ratios, J).

If the modelled detector dimensions are very large compared with the photoelectron range, then all of the electron's energy may be considered to be deposited at the X-ray interaction point. It is necessary to consider edge losses in smaller detectors however, and this will be covered in a subsequent section.

As well as ejecting a photoelectron, the interaction also leaves an ionised absorber atom with a vacancy in one of its bound shells. This vacancy will be filled through the capture of a free electron or by the rearrangement (or transition) of electrons from other shells with the consequent emission of one or more characteristic X-ray photons. If the vacancy lies in the atom's K-shell, then Kα is by far the most likely transition, and if the vacancy lies in the L-shell, then it will likewise most commonly de-excite by an Lα transition. The characteristic 'fluorescence' X-rays associated with these transitions have very well defined energies, and although they are largely reabsorbed within the detector, some fraction will escape. The total energy deposited within the detector after a fluorescence X-ray escapes will be less than that deposited if the fluorescence X-ray is reabsorbed, giving rise to the characteristic "escape" peaks in an X-ray spectrum. Since the photoelectric interaction subroutine simply returns the emission depth, energy and direction of fluorescence X-rays to the beginning of the main program loop which treats them just like any other X-ray, 'escapes' occur in the model quite naturally. Even in the majority of cases where the fluorescence X-ray is reabsorbed within the detector, this may occur at a depth where the CCE is quite different from that at the original interaction point.

Some fraction of fluorescence X-rays are reabsorbed within the atom that produced them, resulting in the ejection of a fast 'Auger' electron from an outer shell. The relative probability of de-excitation by fluorescence or Auger emission is given by the fluorescence yield.

$$\text{Probability that a K shell de-excites by fluorescence} \quad = \quad \frac{Z^4}{32^4 + Z^4} \qquad \text{(5-14)}$$

$$\text{Probability that an L shell de-excites by fluorescence} \quad = \quad \frac{Z^4}{89^4 + Z^4}$$

Auger electrons are significantly slower than photoelectrons, and may invariably be considered to deposit all of their energy in the vicinity of the absorber atom.

5.4.2 The Compton scattering subroutine

Compton scattering takes place between an incident photon and an electron in the absorbing material. The electron is assumed to be initially at rest and the photon is deflected through an angle θ, with a resultant transfer of energy to the electron. Since all scattering angles are possible, the amount of energy transferred can vary from zero to a large fraction of the photon's energy. An equation relating energy transferred to scattering angle can be derived simply from the conservation of energy and momentum.

$$hv' = \frac{hv}{1 + \dfrac{hv}{m_oc^2}\,(1 - \cos\theta)} \qquad (2\text{-}48)$$

where hv is the energy of the photon before the interaction, hv' is the energy of the photon after the interaction and m_oc^2 is the rest mass energy of an electron. The probability of Compton scattering per atom of the absorber depends on the number of electrons available as scattering targets and therefore increases linearly with Z. The angular distribution of the scattered photons is given by the Klein-Nishina formula for the differential scattering cross section $d\sigma/d\Omega$.

$$\frac{d\sigma}{d\Omega} = Zr_o^2\left(\frac{1}{1+\alpha(1-\cos\theta)}\right)^2\left(\frac{1+\cos^2\theta}{2}\right)\left(1+\frac{\alpha^2(1-\cos\theta)^2}{(1+\cos^2\theta)(1+\alpha(1-\cos\theta))}\right) \qquad (2\text{-}49)$$

r_o is the classical electron radius and $\alpha = hv/m_oc^2$.

The Compton simulation uses Kahn's method (figure 5-5) to select the cosine of the polar scattering angle from the Klein-Nishina angular distribution formula. The scattered photon's energy then satisfies the general Compton equation (2-48). The function returns the scattered photon's direction as well as its energy and the amount of charge deposited locally.
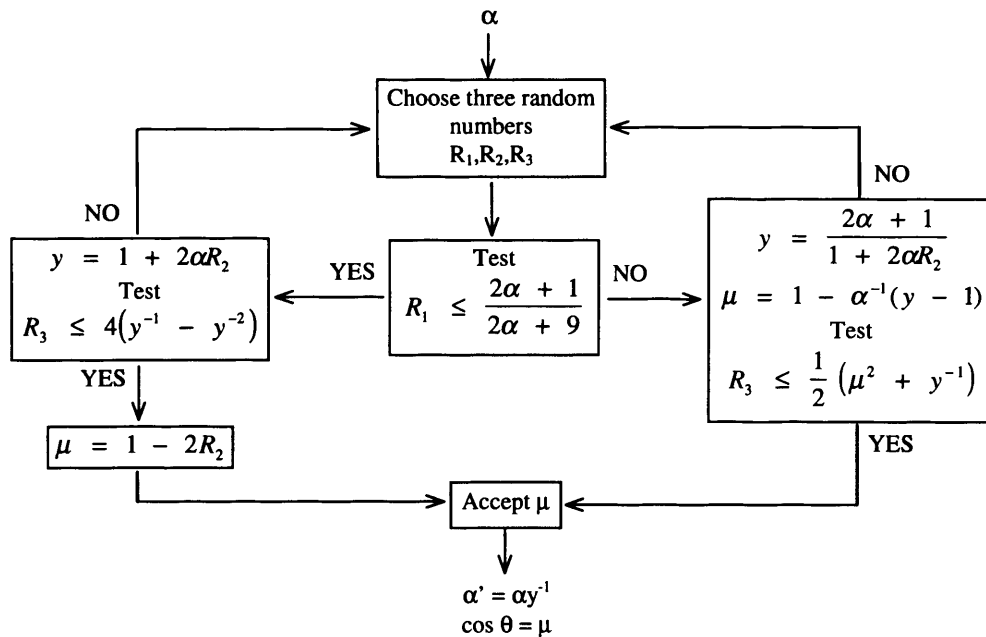
Figure 5-5 Kahn's method for selecting the polar scattering angle, θ from the Klein-Nishina angular distribution (equation 2-48), $\alpha = E_{in}/m_oc^2$, $\alpha' = E_{out}/m_oc^2$.

5.4.3 The edge loss function

The edge loss function adjusts the charge collected to allow for losses that occur around the device perimeter. It may be called by the photoelectric absorption subroutine when X-ray energies and hence photo-electron ranges are high and/or when the detector dimensions are small making edge effects

more significant. Contributions to the collected charge from X-rays absorbed outside the pad area are also included.
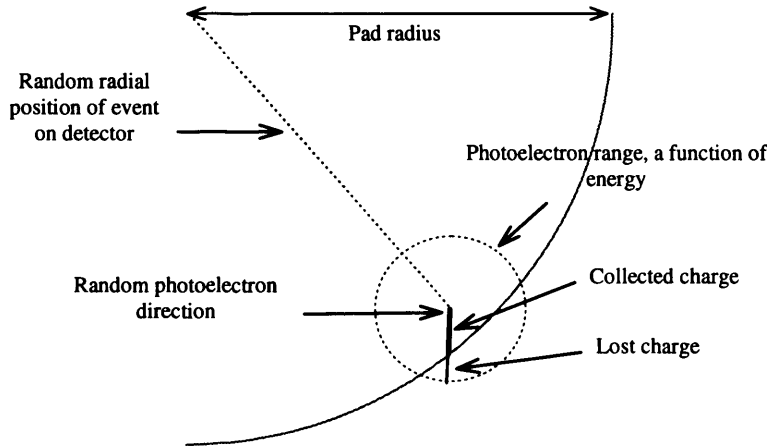
Figure 5-6 Loss of charge due to photoelectron range at detector perimeter

The function first calculates the range of the photoelectron according to its energy and assigns it a random radial position on the pad. For the majority of X-rays this will be sufficiently far within the pad perimeter that the function has no effect and simply returns the energy unaltered. If the event occurs within the photoelectron's range of the pad perimeter however, then the electron is given a random photo-ejection direction (valid even if the X-rays were polarised thanks to the pad symmetry) and that fraction of the X-ray's energy which is actually collected is calculated and returned.

The photoelectron range is calculated using Burke's equation [Burke E.A., 1977],

$$range = k(E + b)^n \qquad (5\text{-}15)$$

$$n = 1.715 - 1.698 \times 10^{-3} Z$$

$$b = 0.6868 - \frac{0.7121}{\rho} (2.659 \times 10^{-2} Z + 1)$$

in which the constant, k is calculated by setting E=10keV, and equating with,

$$range_{10} = 6.824 \times 10^{-6} Z + 2.566 \times 10^{-4} \qquad (5\text{-}16)$$

Evaluating n, b and k for GaAs (Z=32, ρ =5.32 gcm^{-3}) gives,

$$range = 0.018(E + 0.439)^{1.661} \quad \mu m \qquad (5\text{-}17)$$

for E, the photoelectron energy, in keV. This is shown graphically in figure 5-7.
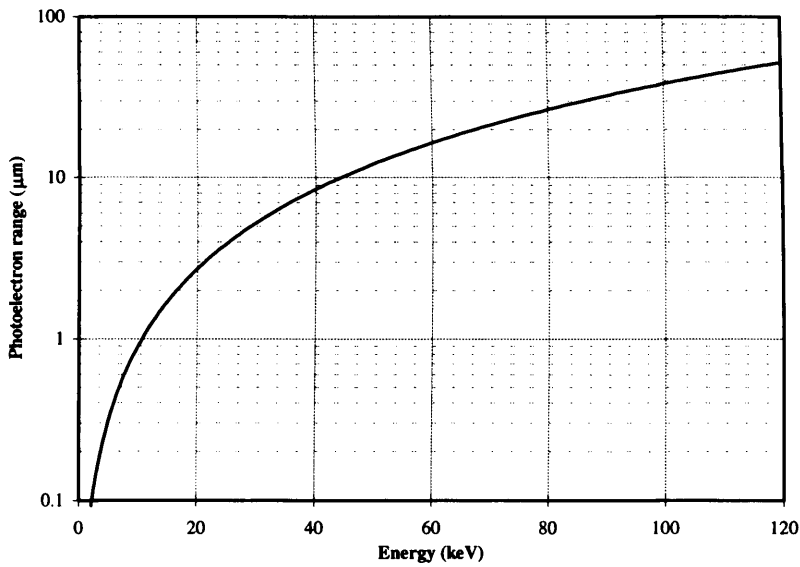
Figure 5-7 Photoelectron range in GaAs from Burke's equation

5.5 Results

5.5.1 Source of spectral features

The charge collection efficiency in bulk GaAs detectors is a complex function of depth (equation 5-10), but when modelled, the sources of prominent spectral features become apparent.
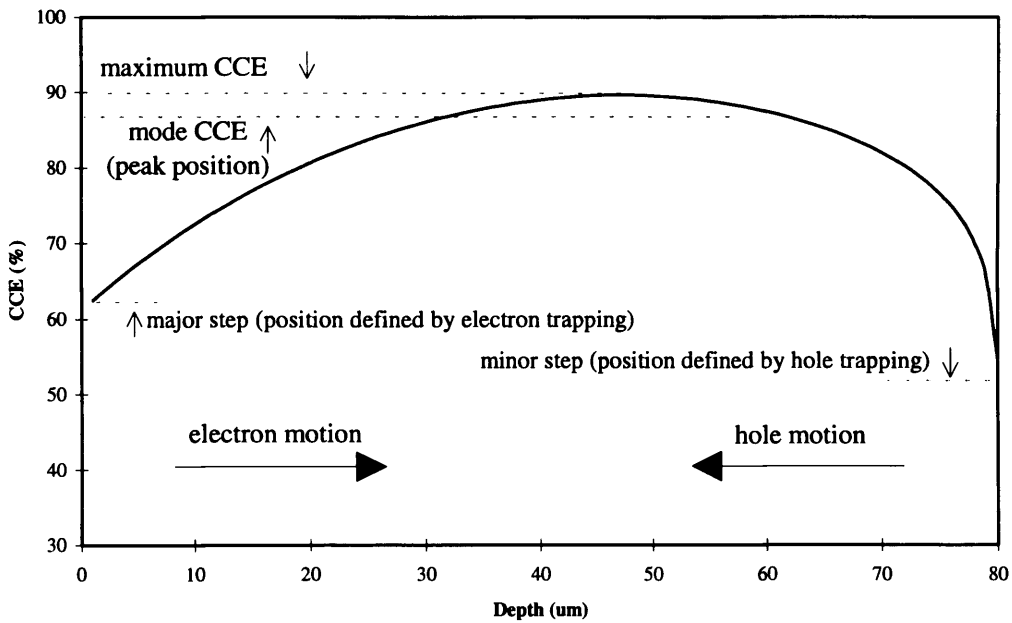
Figure 5-8a Typical charge collection efficiency, as calculated by the simulation.

112
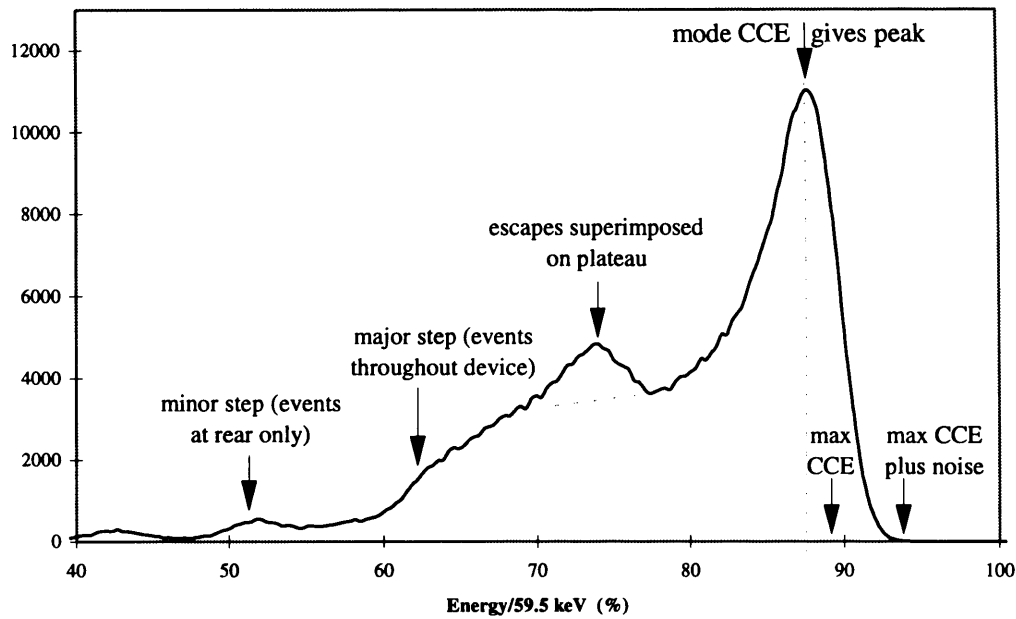
Figure 5-8b Features of the 59.5 keV spectral peak obtained using the CCE shown in figure 5-6a

Figure 5-8 shows the relationship between (a) the charge collection efficiency as calculated by the model as a function of depth through the device and (b) the features observed in the resultant spectral peak. A relatively high trapping case ($Vb=200V,T=173K,\sigma N_{te}=67,\sigma N_{th}=10$) has been used to emphasise these features. The abscissa of (b) has been expressed as a percentage of 59.5 keV, the mono-energetic input, so that it may be compared directly with the ordinate of (a).

Since the pulse is formed in the circuit connected to a detector, by the motion of charge carriers through an applied potential difference (equation 5-9), the signal generated when an X-ray is absorbed close to the negative electrode will be entirely due to electron motion across the full width of the depletion region and similarly an X-ray absorbed close to the negative electrode will give a signal entirely dependent upon hole motion. Thus the charge collection efficiency close to the negative electrode depends only on electron trapping and vice versa. Two steps in the resultant X-ray spectrum indicate the charge collection efficiency at the edges of the depletion region, the larger being from the front of the device where the X-ray flux is higher. Since the X-rays are incident upon the negative Schottky contact, the position of this larger step is determined by electron trapping.

5.5.2 Modelled variations with trap densities and electric field shape

Figures 5-9 to 5-11 show the variation in modelled spectral shape produced by altering the degree of electron and hole trapping (σN_e and σN_h). Three different widths of the zero space charge region are considered since this has a pronounced effect on the distribution of carrier velocities and hence the

113

degree of trapping and the peak shape. In all cases the bias is 200 V, the temperature is -100°C and the energy of the incident X-rays is 59.5 keV (Americium 241).

The effect of the electron trap density can be seen quite clearly as the appearance and position of a step in the spectra, although it is often confused by the location of the escape peaks. These escapes, resulting as they do from X-rays absorbed close to the front (negative) contact, are themselves subject to distortion primarily due to electron trapping.

5.5.3 Variation with bias

Figure 5-12 shows the modelled spectra for a range of values of applied bias, from 1 volt to 1024 volts. The device is 80 μm thick and the zero net space charge region extends 40 μm from the front (Schottky) contact. The temperature is set to -13 °C and the system noise to 1800 eV FWHM. A relatively high trap density (σN_e=46 and σN_h=10.4) has been used in order to emphasise the associated spectral features.

When the modelled bias is low ($\leq$ 32V), giving a weak electric field, the resultant spectra contain flat, continuum features which extend from the spectral peak, down the energy scale towards the zero channel, where the frequency increases. This is analogous to a feature which is missing from the modelled results when fitting real spectra, which indicates that the source of the continuum feature in the real spectra is likely to be a low field region. This is probably located behind the depletion region and/or around the contact perimeter.

5.5.4 Variation with temperature

Figure 5-13 shows the modelled variation in spectral shape with temperature. The device is 80 μm thick with a 60 μm zero space charge region. The applied bias is 100 volts and the system noise is 2800 eV FWHM. The trap parameters used here have been deduced by fitting real spectra. They are,

Electron trap activation energy	= 0.677 eV
Hole trap activation energy	= 0.21 eV
Electron linear de-trapping constant	= 1.08×10^{-14}
Hole linear de-trapping constant	= 1.66×10^{-9}
Electron trap density x trap cross section	= 41
Hole trap density x trap cross section	= 6.7

114

It can be seen from these results that the modelled charge collection efficiency initially worsens with increasing temperature, i.e. the trapping increases. This has nothing to do with any increase in active trap density (which gives steps in a CCE(T) plot at particular temperatures if the traps are initially occupied) as was demonstrated for a real device in chapter 4. The increase in trapping observed here is due to the increasing thermal velocity of the charge carriers which causes them to interact with a larger number of traps. From equations 2-63 and 2-64, the exponential trapping time constant varies inversely and linearly with thermal velocity, trapping cross section and trap density,

$$\tau = \frac{1}{\sigma v N} \qquad (5\text{-}19)$$

Assuming that the cross section and the trap density do not generally vary appreciably with temperature, this leaves just the temperature dependence of v, the thermal velocity, (from equation 5-1),

$$v \propto \sqrt{T} \qquad (5\text{-}20)$$

and hence,

$$\tau \propto \frac{1}{\sigma N \sqrt{T}} \qquad (5\text{-}21)$$

Thus the time constant associated with carrier trapping will decrease as the square root of the temperature, and the trapping will increase as modelled in figure 5-13. At 240K (-33°C), the charge collection efficiency has stopped decreasing. This is because the release time constant associated with the trap being modelled is of the same order as the amplifier integration time, so that carriers which are initially trapped may now be re-released, and contribute to the measured charge.

Figure 5-9 Modelled spectral variation with trap parameters for an 80μm device for which the zero net space charge region is assumed to extend 10μm from the Schottky contact
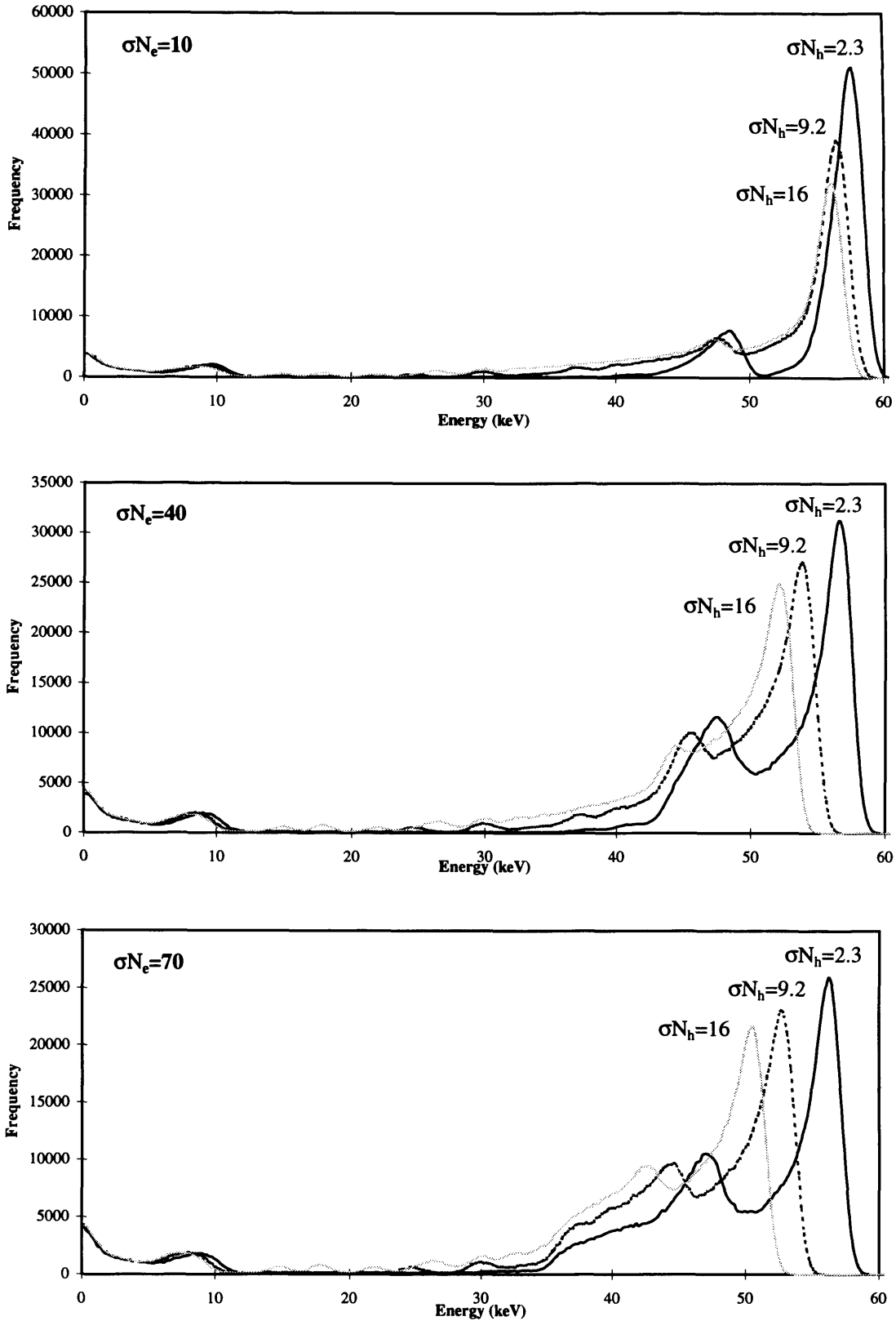
Figure 5-10 Modelled spectral variation with trap parameters for an 80μm device for which the zero net space charge region is assumed to extend 40μm from the Schottky contact
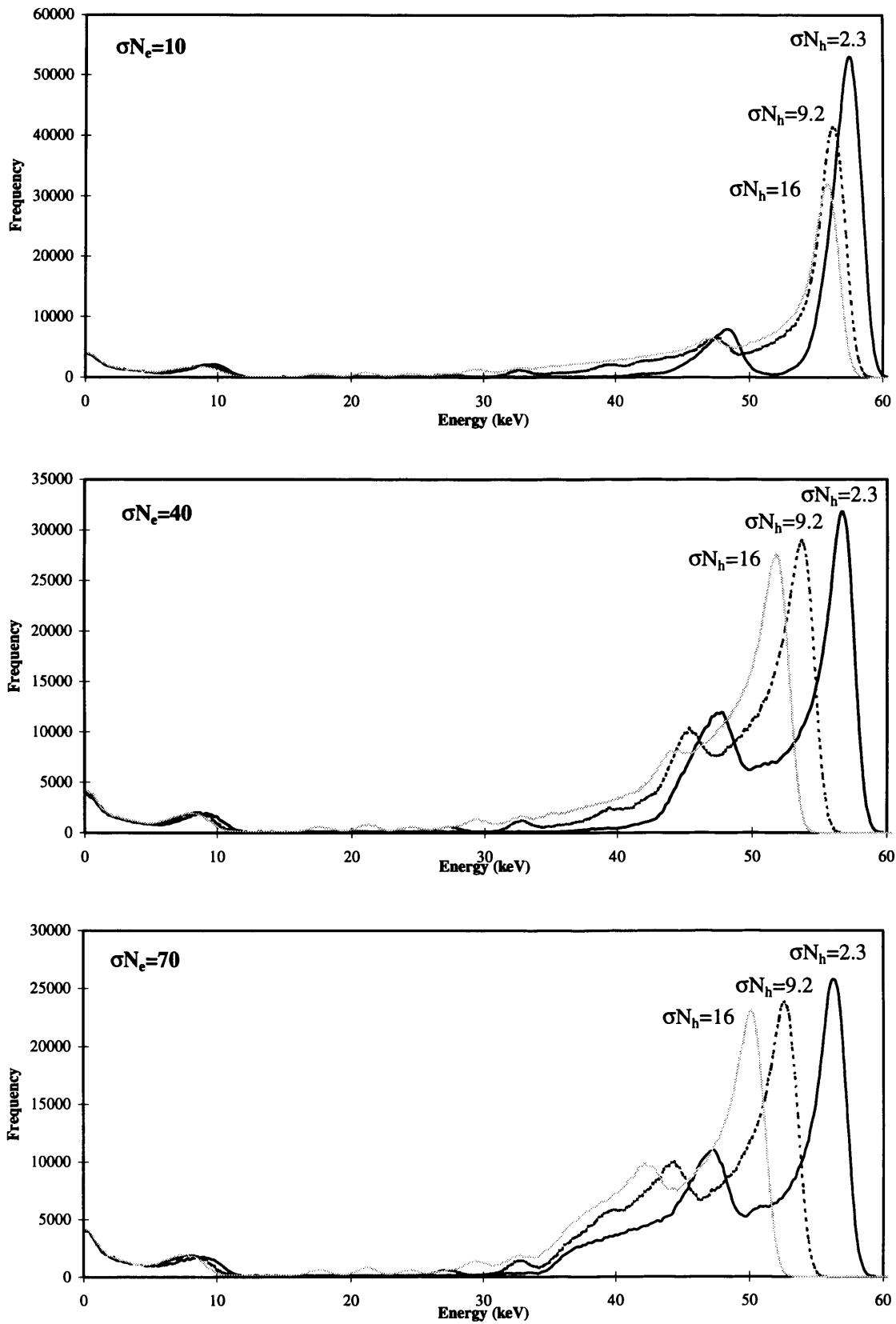
Figure 5-11 Modelled spectral variation with trap parameters for an 80μm device for which the zero net space charge region is assumed to extend 70μm from the Schottky contact
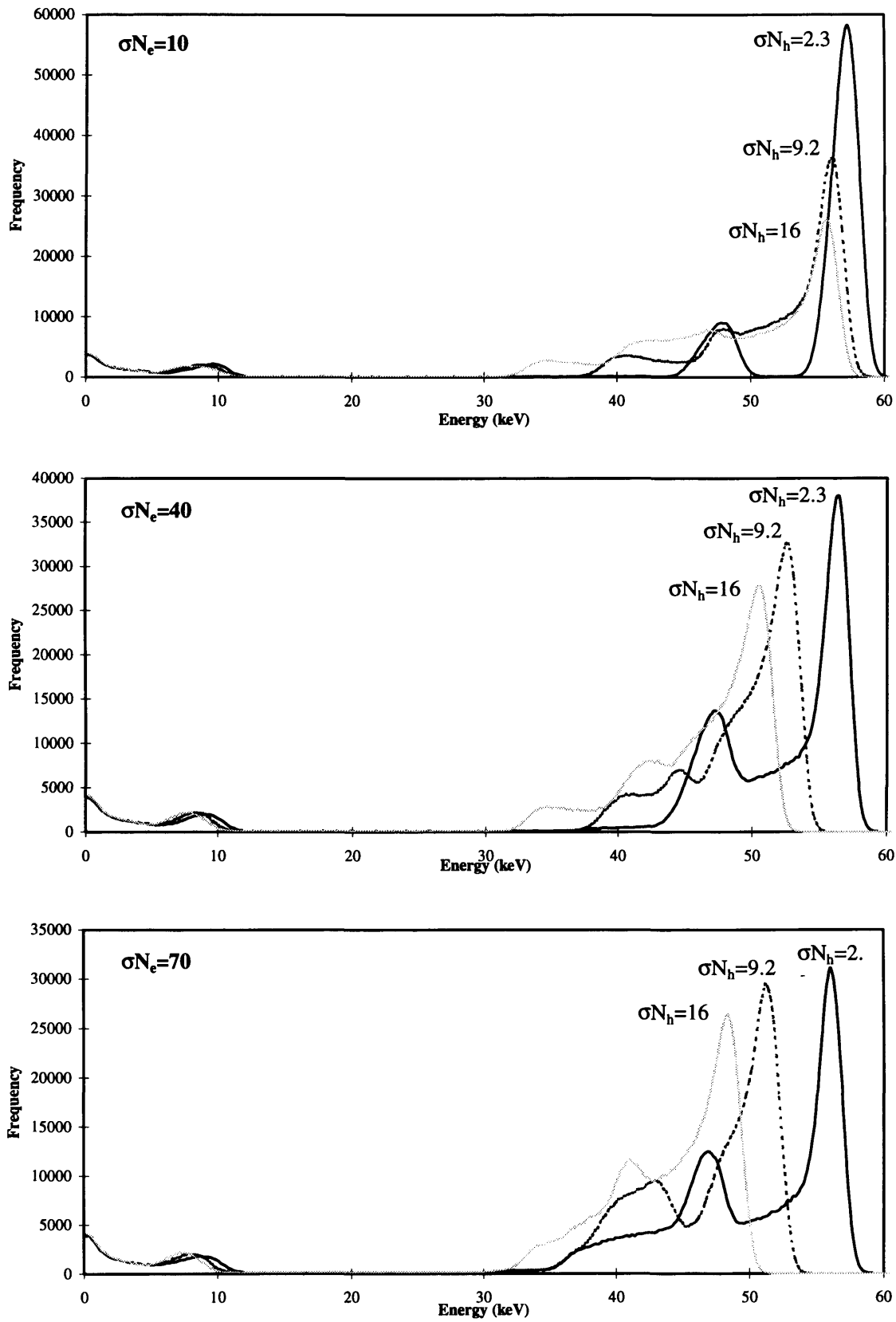
Figure 5-12 Modelled spectral variation with applied bias
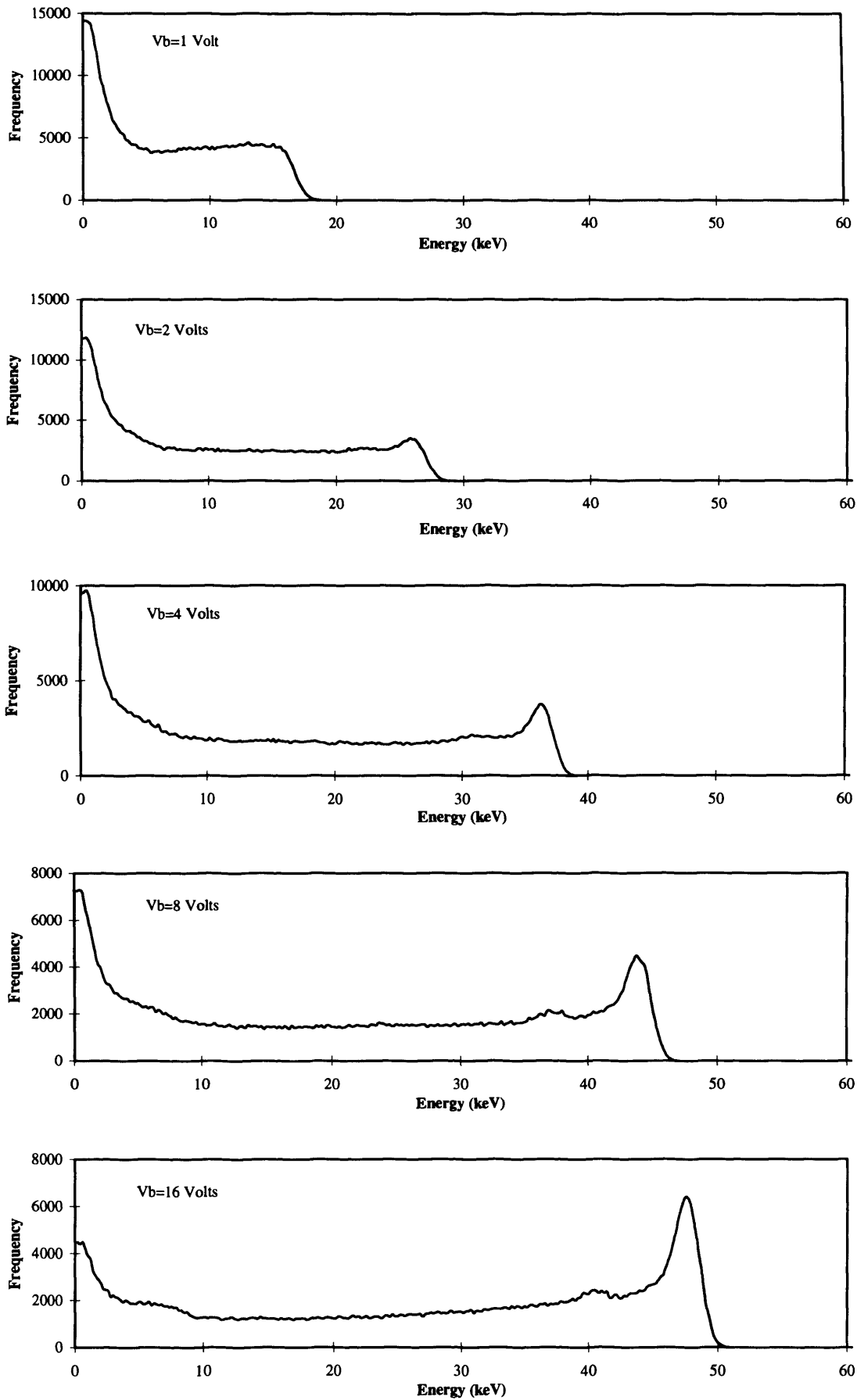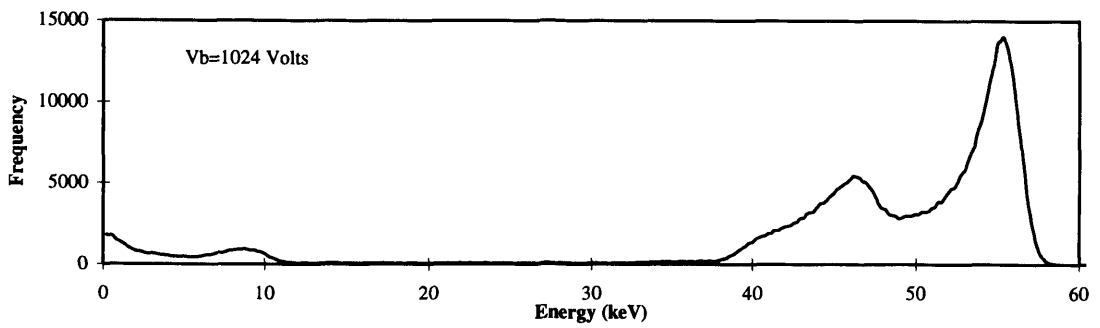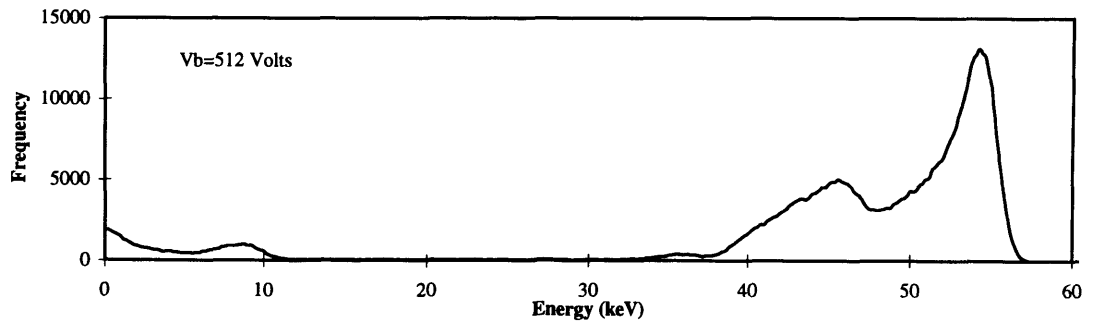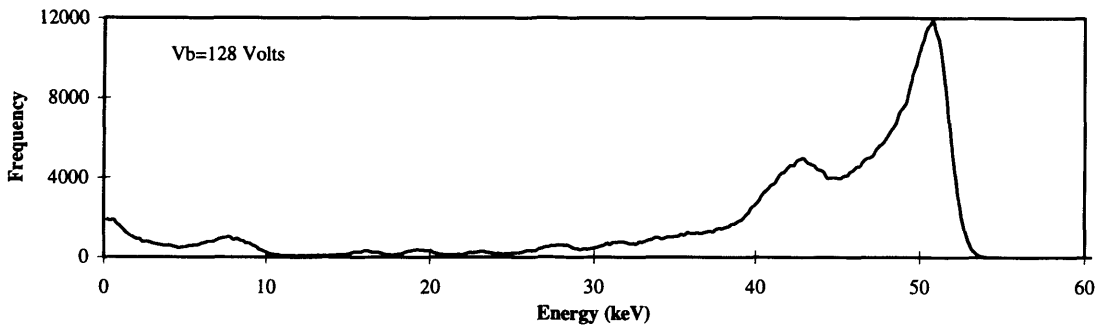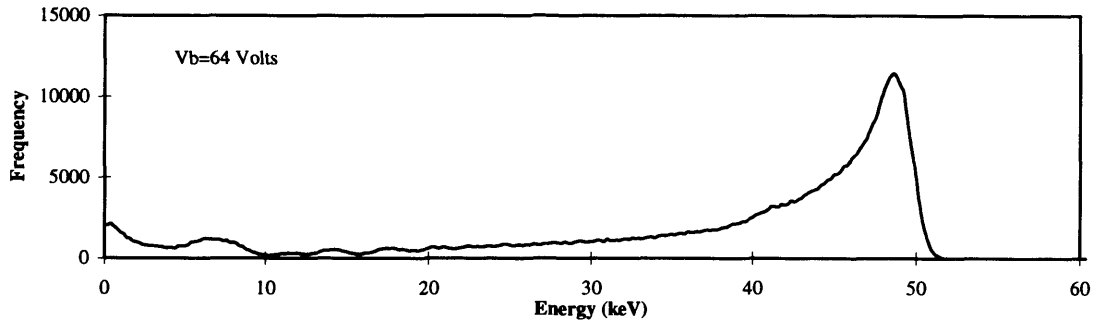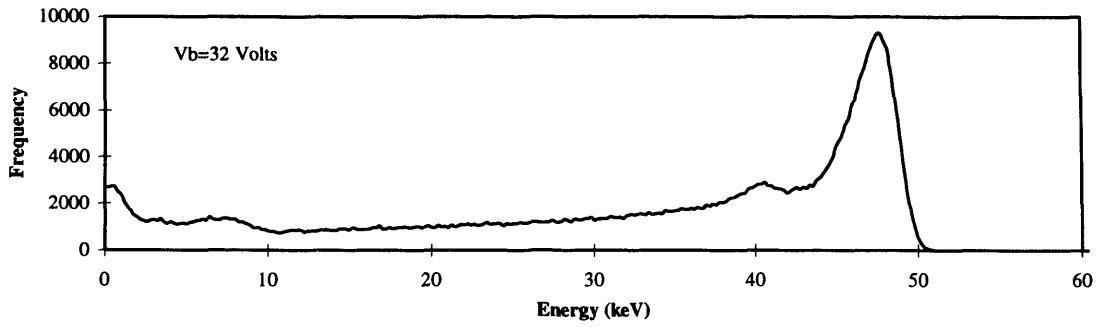
Figure 5-13 Modelled spectra, variation with temperature
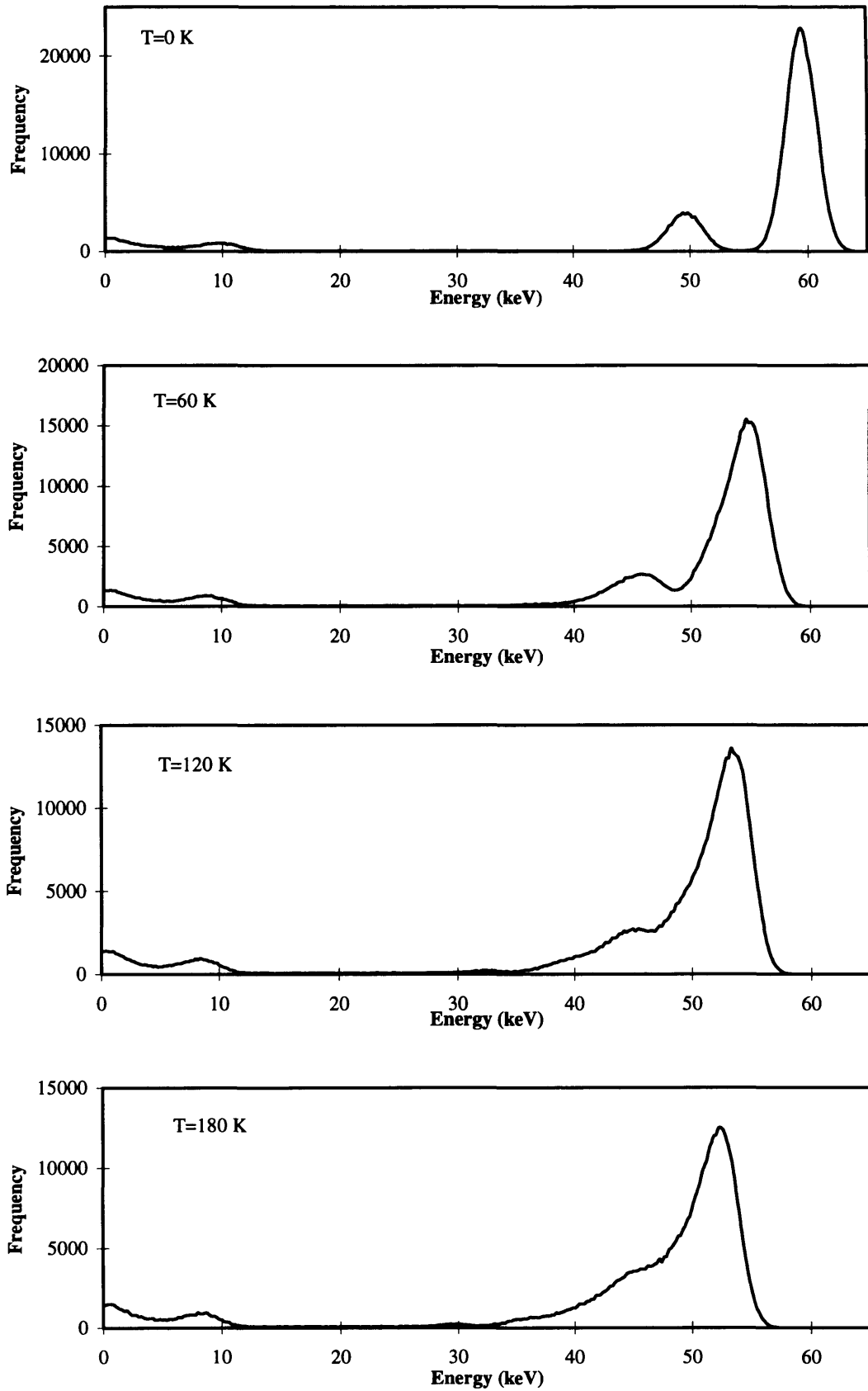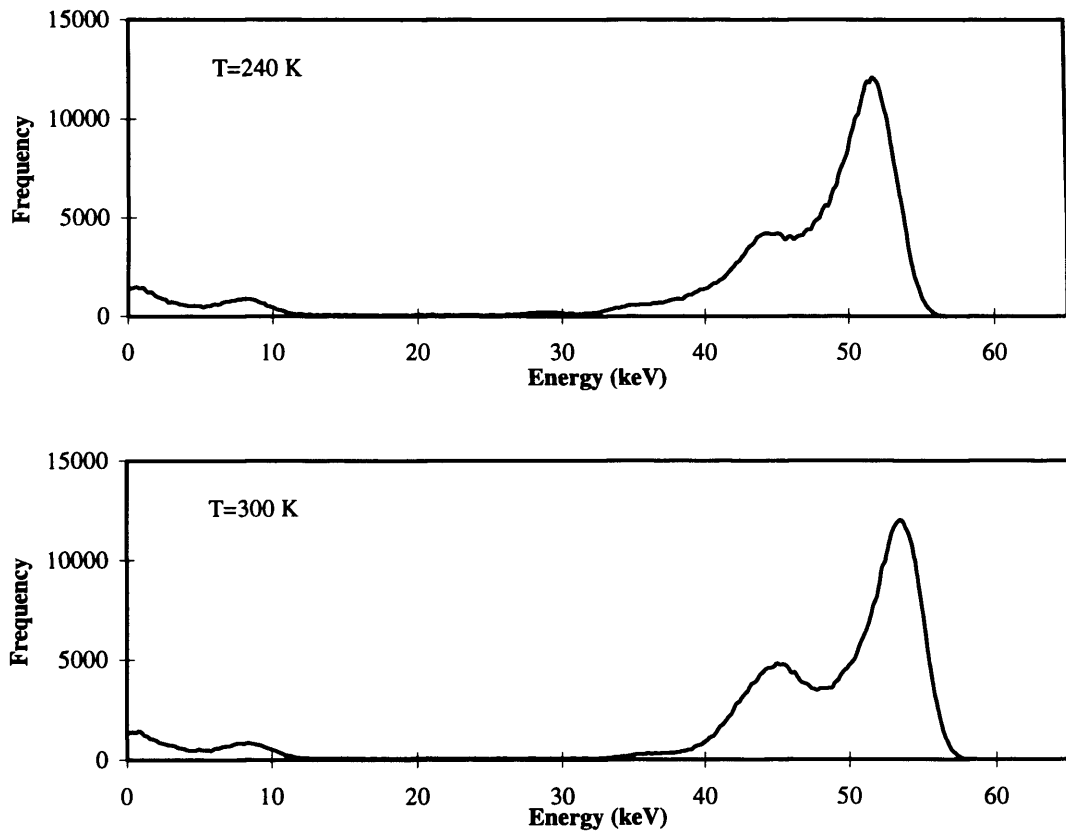
5.5.5 Fitting measured spectra

Developing a model proved to be a useful method of understanding the effects of carrier trapping and the source of spectral features. In order to verify that the results given by the model are reasonable, and to distinguish with some accuracy between the trapping observed in different spectra, it is necessary to compare the modelled results with those measured in the lab.
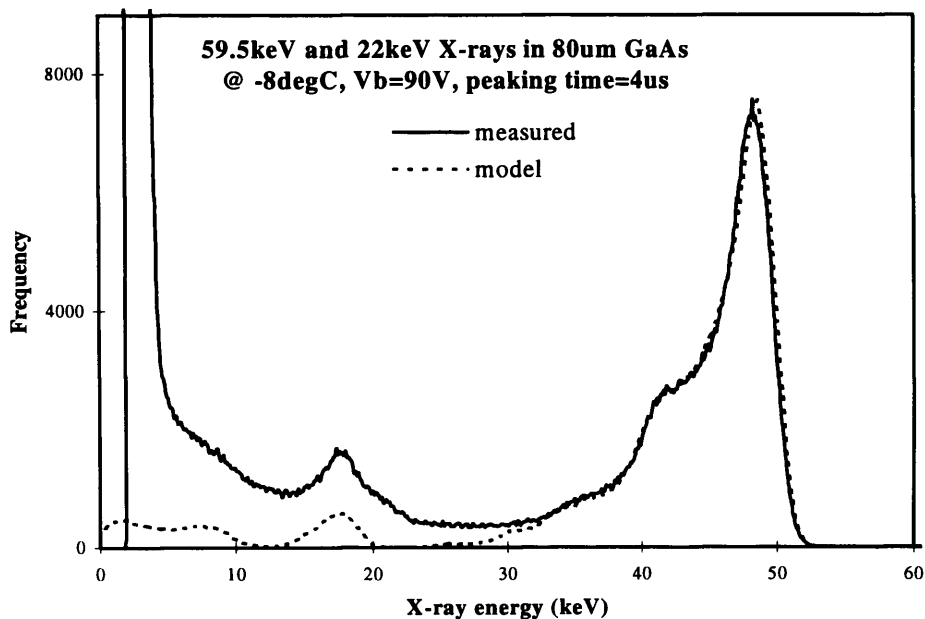
Figure 5-14 Example of measured and 'best fit' modelled X-ray spectra.
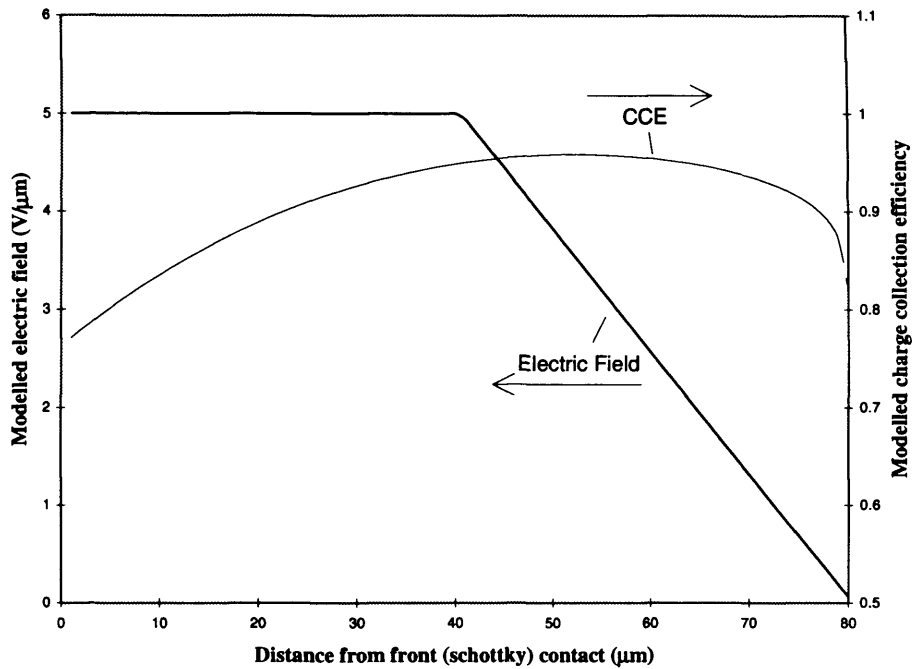
Figure 5-15 Simplified electric field profile found to give best fit to measured spectrum (figure 5-14) and resultant modelled CCE profile.

Figure 5-14 is an early comparison of a measured X-ray spectrum with the best fit achieved by the model. Two X-ray energies were simulated, the principal ^{241}Am emission at 59.5 keV and a significant fluorescence (Ag Kα) line at 22 keV. The experimental parameters employed in the model were

T	= -8	°C
V_b	= 90	V
device thickness	= 80	μm
peaking time	= 0	μs *

*Note that in early simulations, re-release of carriers from traps was not calculated. The experimental peaking time was 4μs, so in this case, the results describe the net trapping after 4μs and not the full trapping which occurred. The best fit was obtained manually by varying the electric field shape, and the trapping cross section-density products for holes and electrons, and then observing the fit of the modelled to the measured spectrum. The model results for the net electron and hole trapping were

$\sigma_e N_e$	= 39 cm^{-1}
$\sigma_h N_h$	= 17.7 cm^{-1}

and the electric field shape in the best fit case is given in figure 5-15. The charge collection efficiency (CCE) as a function of position in the device, calculated during this simulation, is also shown and the quantum efficiency was calculated to be 7.1% at 59.5 keV.

With the improvement to spectral resolution achieved by cooling the detectors to below approximately -80°C before the application of bias (see chapter 4), a number of additional X-ray lines

had to be added to the model input. When modelling Americium 241 for instance, these included Neptunium L fluorescence (Neptunium is a decay product of Americium 241), Gold fluorescence from the Schottky contact, and Silver fluorescence from the thermoplastic used for wire bonding. Weak 43, 33 and 26 keV lines from the Am241 itself, were also added.
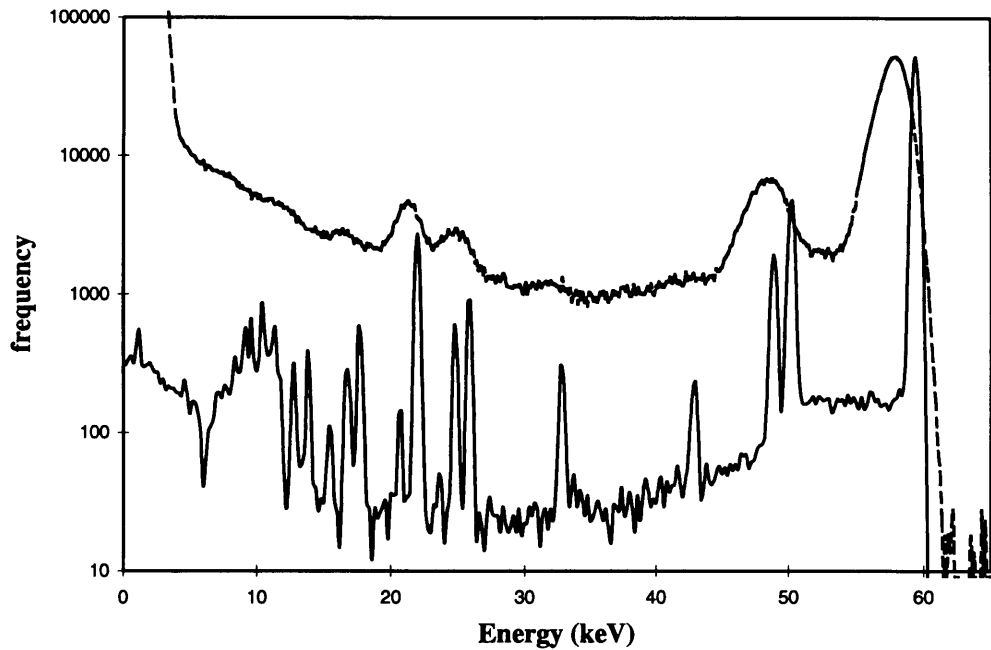
Figure 5-16 Measured spectrum (dotted) and modelled Fano limited, 'trap free' spectrum

Figure 5-16 indicates the number of X-ray lines which now appear in the modelled spectra when simulating an Americium 241 source. A hypothetical case of zero trapping and zero electronic noise has been assumed for clarity. Also shown is a measured 'best' spectrum acquired using an 80μm device at -130°C and 300V bias (annotated and discussed in chapter 4). Since the energy scale has been accurately calibrated using a silicon lithium detector (chapter 3), the figure indicates the degree of offset in all peaks due to the effect of trapping.
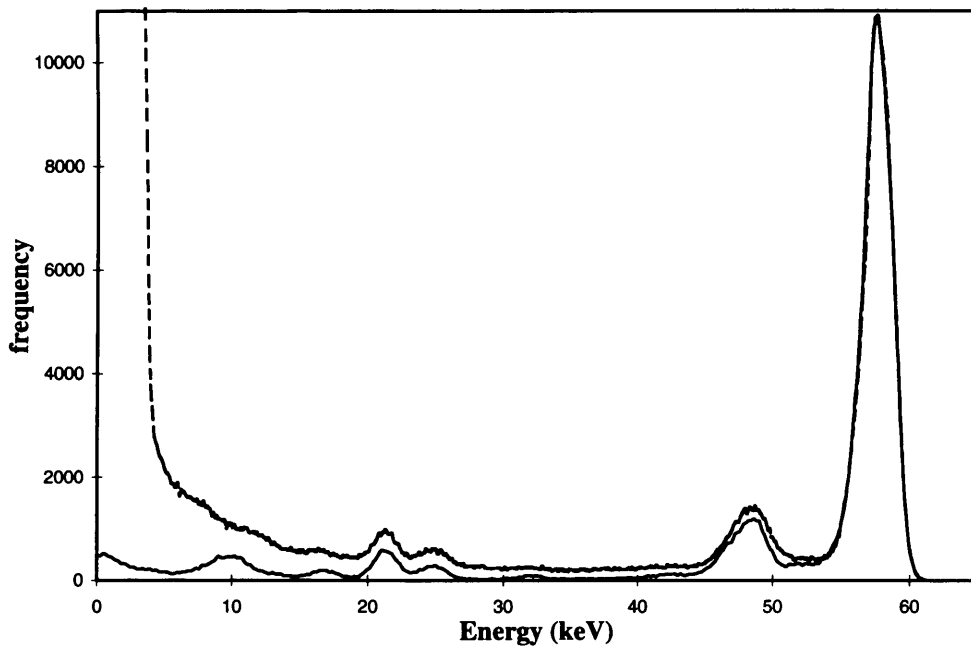
Figure 5-17 Measured spectrum (dotted) and modelled spectrum including trapping and readout noise

Figure 5-17 shows the same measured spectrum and the results of the Monte-Carlo simulation including carrier trapping and readout noise. The background level across much of the measured spectrum is due to X-rays being detected in an extended low field region around the device perimeter and/or in a partially depleted (almost field free) region between the depletion region and the rear contact. These weak field regions are not included in the model. The values of the cross section and density product (σN) giving this best fit are 7.5cm^{-1} for electrons and 3cm^{-1} for holes.
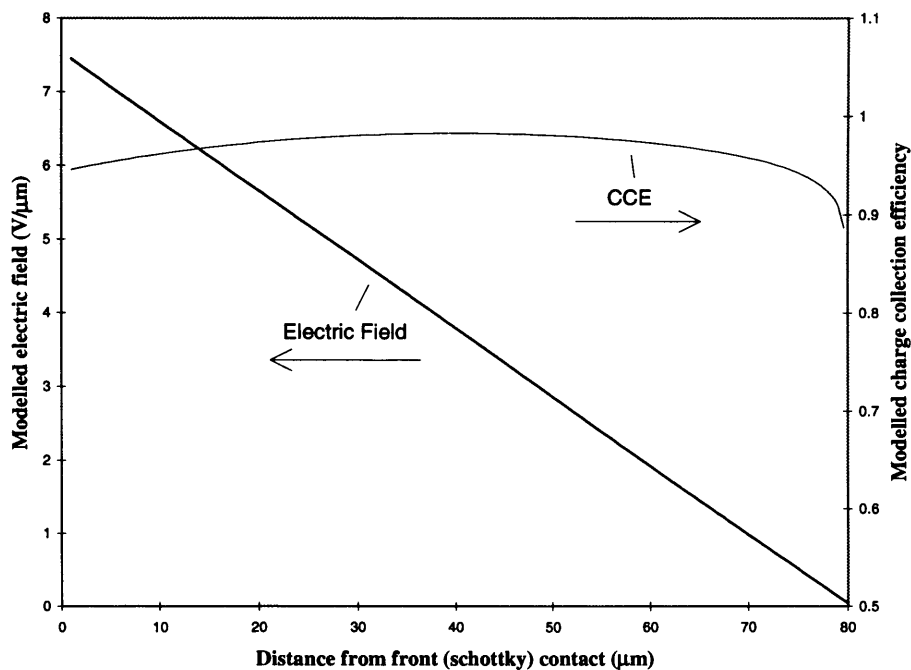
Figure 5-18 Electric field profile found to give the best fit to measured spectrum at -130°C

The electric field profile required to give the best fit in the case of reduced trapping (figure 5-17), is shown in figure 5-18. In this case a linearly decreasing electric field is found to give the best fit, with no region of zero net space charge. An electric field of this form (dE/dx = constant) indicates that the net charge density is constant throughout the depletion region, and may be modelled using the depletion approximation (section 2.3).

5.5.6 Trap release time constants from fitting different integration times

When trap release time constants are of the order of tens of minutes, or hours, they can be measured by observing a reduction in charge collection efficiency in a series of spectra (see chapter 4). If a difference in CCE is observed in spectra acquired using different pulse integration times however, then this indicates that the time constant associated with the release of carriers from traps is of the order of the pulse integration time (generally μs). This may be the case for a shallow trap at low temperatures, or for a deeper trap when operated at higher temperatures. With a release time constant of microseconds, the traps may essentially be considered all active, and the effect which may be measured here is an increase in CCE with pulse integration time as charge carriers generated by an X-ray interaction which are initially trapped, are then subsequently released to contribute to the measured pulse height.

Spectra may be acquired in the lab using pulse integration times of 1, 2, 4 and 8 μs, but it is not possible to fit the resulting charge collection efficiency plots using an exponential with any accuracy. The model has therefore been employed, since it may be used to fit the peak shape as well as the peak position and hence to improve confidence in the fit, to distinguish if the change in CCE is due to electron or hole trapping, and to express the decay in terms of trapping variables σN_e and σN_h directly, rather than CCE.
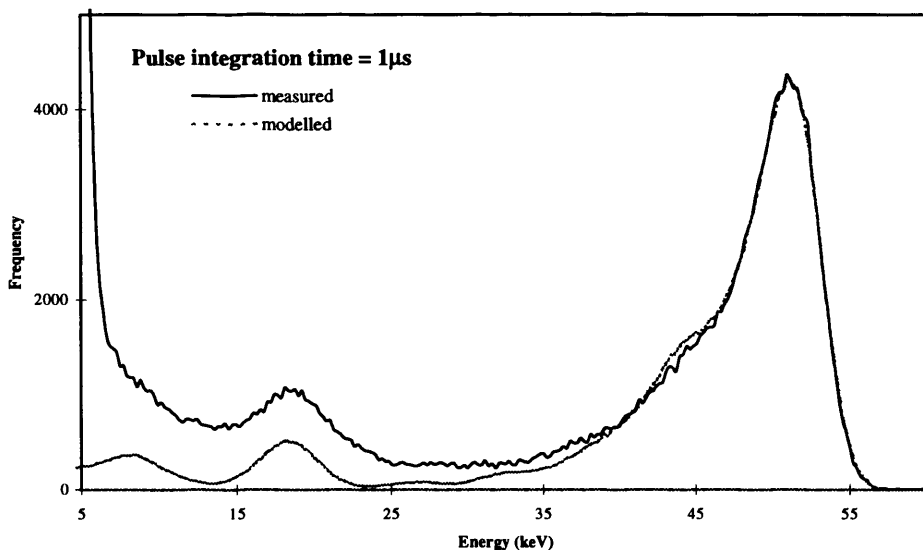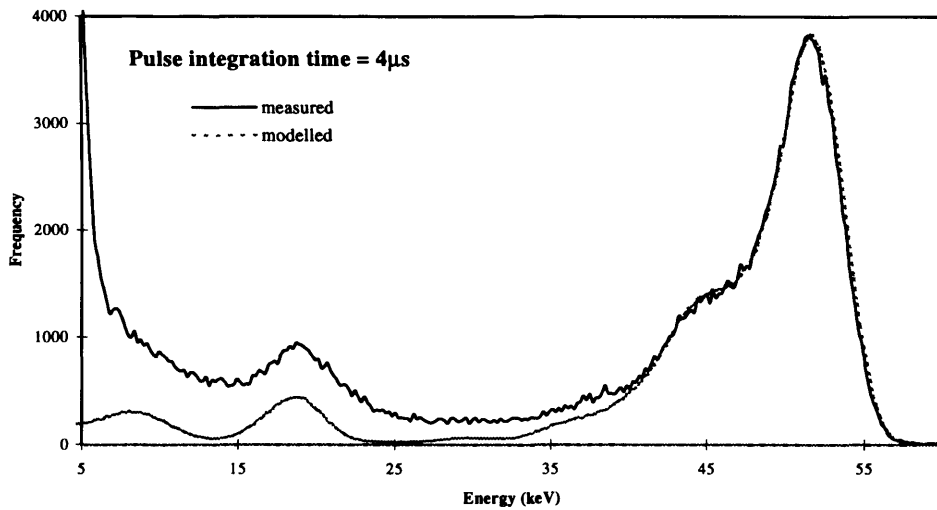
Figure 5-19 Variation of spectra with pulse integration time (measured and modelled).

Figure 5-19 shows measured and modelled spectra for two values of peaking time, at -13°C and 100V bias. The differences between the spectra are attributable to the additional de-trapping which occurs during the longer integration time. In order to obtain the best fit, a looped version of the model is employed twice, with the simulated pulse integration time set to zero. This gives two sets of trap parameters. Table 5-1 shows these parameters for the spectra in figure 5-19,

Table 5-1 results of fitting shown in figure 5-19

Integration time	1 μs	4 μs
Zero space charge region width	60 μm	60 μm
σN$_e$	38	38
σN$_h$	6.7	5.5

According to table 5-1, the differences between these two spectra are principally due to a hole trap whose occupation must be decreasing with a time constant of the order of microseconds at this temperature. From equations 2-63, 5-1 and 5-4, the net trapping after an integration time t may be expressed in terms of the un-trapped fraction, as,

$$f = 1 - (1 - \exp(-A\sigma N)) \exp\left(- \frac{t}{\tau_r}\right) \qquad (5\text{-}22)$$

where σN is the real trap 'cross section-density product', τ_r is the trap release time constant (equation 5-6) and,

$$A = \frac{100}{v_d} \sqrt{\frac{kT}{m^*}} \qquad (5\text{-}23)$$

By fitting spectra without regard for trap release, i.e. for t=0, one essentially models the un-trapped fraction as,

$$f = \exp(-A\sigma N_m) \qquad (5\text{-}24)$$

127

Equating (5-9) and (5-11) and re-arranging,

$$\tau_r = \frac{t}{\ln\left\{\frac{1 - \exp(-A\sigma N)}{1 - \exp(-A\sigma N_m)}\right\}} \qquad (5\text{-}25)$$

Which contains two unknowns, the real trap 'cross section-density product' (σN) and the trap release time constant (τ) and may be solved if two values of σN_m may be determined at two different pulse integration times i.e. (more simply)

$$\sigma N_{m1} = \sigma N \exp\left(-\frac{t_1}{\tau_r}\right) \qquad (5\text{-}26)$$

$$\sigma N_{m2} = \sigma N \exp\left(-\frac{t_2}{\tau_r}\right) \qquad (5\text{-}27)$$

Re-arranging equations 5-13 and 5-14 for σN, equating and again re-arranging,

$$\tau_r = \frac{t_2 - t_1}{\ln\left(\frac{\sigma N_{m1}}{\sigma N_{m2}}\right)} \qquad (5\text{-}28)$$

By fitting pairs of spectra, equation 5-15 can thus give values for the electron and hole trap release time constants, which can be fed back into equation 5-13 or 5-14 to give values of the σN products which describe the gross rather than net trapping. In the case of the example shown in figure 5-14, this gives, for T = -13°C,

$\sigma_e N_e$	$\approx 38 \text{ cm}^{-1}$
$\sigma_h N_h$	$\approx 6.9 \text{ cm}^{-1}$
electron release τ	$\approx$ very large
hole release τ	$\approx 16 \ \mu s$

Repeating the whole process for this device at -7°C, one obtains a hole trap release time constant of $\approx 13 \ \mu s$ and hence from equations 5-6 and 5-7,

$$16x10^{-6} = C_h \exp\left(-\frac{E_{ah}}{260k}\right) \qquad (5\text{-}29)$$

$$13x10^{-6} = C_h \exp\left(-\frac{E_{ah}}{266k}\right) \qquad (5\text{-}30)$$

Solving simultaneously, these give a hole trap activation energy of $\sim 3.3x10^{-20}$ joules or ~ 0.21 eV.

In this way the model may be used as an aid to identifying dominant trap energy levels, and determining (where the cross section is known), the density of these traps which are active under given conditions. Once a trap energy level is known, it may be used in the model which can then

calculate the release time constant, and hence simulate the spectral changes with temperature and pulse integration time.

5.6 Discussion

GaAs trap parameters, including energy level, density and capture cross section have been experimentally determined, typically by deep level transient spectroscopy (DLTS). Although there is a great deal of variation in the values measured from one experiment to another, and from sample to sample, table 5-2 gives some typical results. Several different traps and trap complexes are detected, more than one of which may play a significant role in trapping charge.

Table 5-2. Measured trap parameters. (*DLTS measurements made at Lancaster University.)

Label	σ_n	σ_p	N_t	$\sigma_n N_t$	$\sigma_p N_t$	Reference
EL2	6.7E-16	2E-18	2E16	13.4	0.04	[Brozel, 1990]
Cr	3E-20	3E-17				[Brozel, 1990]
EL2	1.2E-14		9E15	108		*
EL9 ?	7E-16		9E14	0.63		*
EL2	1.6E-14		1.9E16	304		*
EL6	4.2E-15		1.2E15	5.04		*
EL2	4E-16	2E-18	~E16	~4	~0.02	[Haegel, 1991]

The probability that carriers escape capture by a particular trap type (1) is exponentially proportional to $-\sigma_1 N_1$ i.e.

$$P_1 \, \alpha \, \exp(-\sigma_1 N_1) \tag{5-31}$$

Similarly for a second trap type with cross section/density product $\sigma_2 N_2$, the probability of escaping capture is,

$$P_2 \, \alpha \, \exp(-\sigma_2 N_2) \tag{5-32}$$

The combined probability P of escaping capture by either trap type is simply $P_1 P_2$ so from equations 5-31 and 5-32,

$$P \, \alpha \exp(-\sigma_1 N_1) \times \exp(-\sigma_2 N_2) \; = \; \exp[-(\sigma_1 N_1 + \sigma_2 N_2)] \tag{5-33}$$

The model calculates a σN value describing the combined trapping due to all traps present and from 5-20,

$$\sigma N = \Sigma_n \, \sigma_n N_n \tag{5-34}$$

Unless the trapping is entirely dominated by just one trap type, the values of the cross section/density products measured by DLTS for individual levels should thus tend to be rather smaller than the combined value given by the model. To date, this appears to be the case.

5.7 Conclusions

The work so far has demonstrated that the poor CCE and the characteristic photo-peak shape observed in spectra from bulk GaAs X-ray detectors may be modelled in terms of a uniform distribution of electron and hole trapping centres. These traps have been characterised in terms of density, cross section and release time constants. From trap release time constants determined at different temperatures, activation energies may also be deduced.

The density of active traps is a function of temperature, time, applied bias, material and also device history (i.e. At what temperature and time the bias was applied). With so many interrelated parameters it has not proved possible to use the model to predict trapping and spectral form, but only to quantify the trapping in individual spectra.

Measurements have been made to determine trap energy levels by looking for steps in the charge collection efficiency and by measuring the trap release time constants at low temperatures when they are minutes or hours (see chapter 4). These measurements have indicated that the EL2 centre with an activation energy of 0.73eV is the most dominant electron trap. This activation energy has therefore been used subsequently to calculate the modelled electron de-trapping time.

6. EPITAXIAL MATERIAL

It has been demonstrated in previous chapters, that the degradation of spectra obtained from bulk GaAs devices may be attributed directly and indirectly to the presence of traps (chemical impurities and crystalline defects). In order to maximise spectral resolution over a wide range of measurement conditions, it is therefore necessary to fabricate detectors using GaAs with the lowest obtainable defect/impurity density. All of the devices considered so far, have been fabricated using bulk grown GaAs crystals which places a fundamental restriction on material purity. This chapter describes the epitaxial growth technique which offers the possibility of far greater purity and crystallinity but which is generally restricted to the growth of thin layers. A number of attempts were made between 1994 and 1996, to grow thick (up to 100μm) epitaxial layers. This work was conducted using facilities at EEV Ltd. as part of a PPARC CASE award and although some of the growth trials were successful, the resulting detectors all exhibited premature breakdown. This was possibly due to poor surface uniformity or contamination disrupting the Schottky interface.

6.1 Introduction

Epitaxial growth trials were conducted using a large scale liquid phase epitaxial dipping facility owned and operated by EEV Ltd. This facility was previously used for the production of GaAs solar cells which is now predominantly carried out using MOCVD (Metal Oxide Chemical Vapour Deposition), another form of epitaxy. The cost of material procurement and of running the LPE dipping facility for this study was funded in part by PPARC CASE and PIPSS grants.

The term epitaxy, derived from the Greek words 'epi' meaning on, and 'taxis' meaning arrangement, describes the growth, by chemical reaction, of thin crystal layers on a substrate of the same crystal lattice structure. This chemical deposition commonly takes the form of LPE (Liquid Phase Epitaxy), VPE (Vapour Phase Epitaxy) and MBE (Molecular Beam Epitaxy) all of which are used in the growth of GaAs, which is an example of binary III-V heteroepitaxy. LPE has an advantage over the other techniques, that thick layers may be grown relatively quickly, and the large scale dipping facility at EEV also offers the potential for dipping multiple wafers, and achieving a high degree of material uniformity between consecutive batches (since the melt is baked over a long period of time, re-used and only replenished infrequently).

In 1971 Eberhardt, Ryan and Tavendale of the Australian Atomic Energy Commission, published work [Eberhardt, J.E., 1971] in which they presented X-ray spectra from detectors fabricated using epitaxial layers 60 to 80μm thick with a residual free carrier concentration of $\sim10^{13}$cm^{-3}. The epitaxial layers were grown at STL, Harlow, U.K. Their substrates were 400μm-thick tin-doped n+ ($\sim10^{17}$cm^{-3}) <100> oriented bulk GaAs wafers and although liquid and vapour phase techniques were both

available, LPE was favoured because the low distribution coefficients of most impurities between the liquid and solid phases means that most impurity atoms remain in the gallium. The Schottky junctions were formed by depositing 200Å of gold through a mask which defined circular detectors of 1.5 to 2 mm diameter.
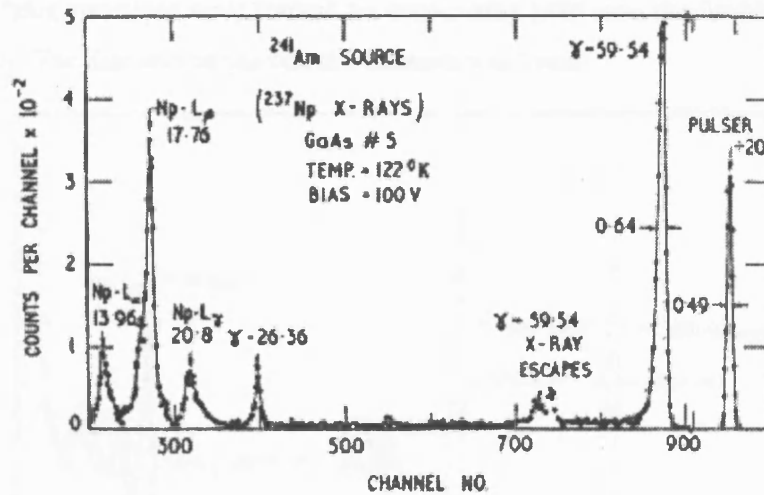
Fig 6-1 Spectrum measured by Eberhardt et. al. Reproduced from [Eberhardt, J.E., 1971].

With these detectors, the group measured a best spectral resolution of 0.64keV FWHM at 59.5keV, operating at 122K (-151°C), with an applied bias of 100V. At room temperature they achieved resolutions of 2.6keV and 2.5keV FWHM at 122 and 59.5keV respectively, (with an applied bias of 84V). They also confirmed that direct band to band recombination of excess carriers, even in the very dense charge clouds generated by alpha particles, did not significantly degrade the spectral performance. They thus demonstrated the potential of epitaxial GaAs as an efficient detector at energies above 10keV, and at room temperature, and cited a number of applications in medical and nuclear physics. However, the area of these devices was very small and the yield seems to have been poor. Quoting from [Eberhardt, J.E., 1971], "Four satisfactory detectors were made from one wafer and one other from a second wafer. Devices made in the same way from a third high resistivity wafer were unsatisfactory".

Subsequent effort by workers in the field was therefore aimed at producing larger area devices with a degree of consistency, but in the event it proved very difficult even to reproduce the results of Eberhardt, Ryan and Tavendale. Apart from a few early studies (Eg. [Gibbons and Howes, 1972], [Kobayaski et al., 1972]), work on GaAs as an X-ray and particle detector largely dwindled in favour of CdTe which offered an easier though still not ideal alternative. More recently however, with high purity semi-insulating bulk GaAs under consideration for potential detector applications (notably for the Atlas detectors in the LHC at CERN), interest in the material generally has received a boost. A new, annual, international workshop on 'Gallium Arsenide and Related Compounds' [Pelfer, P.G., 1995] was begun in 1993, and the potential of LPE GaAs has again been motivating investigators.

In 1992 D. Alexiev and K. Butcher of the Australian Nuclear Science and Technology Organisation (ANSTO) published results [Alexiev, D., 1992] reporting LPE grown layers up to 220μm-thick with a free carrier concentration of ~2×10^{13}cm^{-3}. For detector fabrication the substrates were n+ GaAs and once again rectifying junctions were formed by evaporating gold onto the freshly etched surface of the epitaxial layer. The diameter of the circular contacts was 2mm.
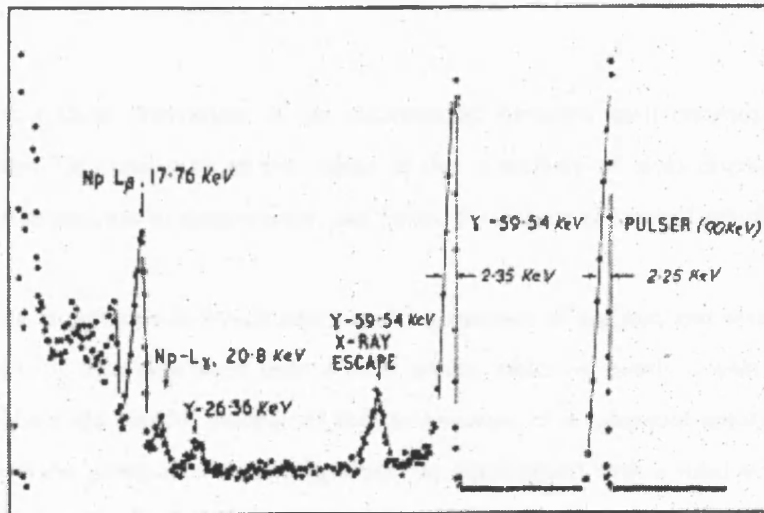
Fig 6-2 Spectrum measured by Alexiev and Butcher, reproduced from [Alexiev, D., 1992].

The devices were electrically and spectroscopically evaluated, and it was noted that those in which the least dark current was measured were also in general, the best in terms of X-ray resolution. Their best results were obtained from a 120μm-thick detector which gave a room temperature resolution of 2.3keV FWHM at 59.5keV and had a corresponding dark current of just 4×10^{-10}A (~0.13nAmm^{-2}). By investigating the variation of diode current with temperature they concluded that it could be explained as a combination of both bulk generated currents and surface leakage currents, and that "surface passivation must therefore be an important sequence in (detector) fabrication". Subsequently, similar devices fabricated at ANSTO and elsewhere have been evaluated, giving similar results (e.g. [Bencivelli, W., 1994, Bauser, E., 1992/1995])

A common factor in nearly all of these trials of epitaxial GaAs for detector applications has been the use of layers grown from very small volumes of melt with consequent difficulties in achieving uniformity and reproducing good material. With the use of GaAs for solar cells however, large scale (~3kg of gallium) growth facilities have been developed such as that used by EEV Ltd. which can handle ten wafers at a time, and in which the temperature control and mechanical mixing are automated to provide a high yield of similar layers. The aim of this study was therefore not simply to investigate the purity of GaAs grown in a large liquid phase epitaxy facility and the performance of the resulting X-ray detectors, but to evaluate the potential advantages of growing from a semi-infinite melt, in terms of uniformity and consistency between wafers and batches.

There are two fundamental differences between growing epitaxial layers for solar cells and for X-ray detectors. Firstly, solar cells require only very thin epitaxial layers since the optimum junction depth for maximum solar cell efficiency is just 0.5µm, and secondly the epitaxial layers which comprise a solar cell are doped to form a pn junction whereas an X-ray detector should ideally comprise a thick layer of high resistivity (un-doped) material.

6.2 Theory

Presented here, is a short derivation of the relationship between melt composition and epitaxial growth temperature. This will give an indication of the sensitivity of layer deposition from a dilute solution of arsenic in gallium to temperature, and hence the degree of control which may be achieved.

Unlike bulk growth techniques in which equal molal quantities of gallium and arsenic are melted and mixed so that GaAs is then deposited onto a seed crystal which is slowly drawn from the melt, the LPE process involves the careful control of the temperature of a saturated solution of the group V element (arsenic) in the group III element (gallium), in equilibrium with a solid state GaAs substrate. A small degree of cooling will then cause the solution to be over saturated so that a very thin layer of GaAs is formed on the substrate, reducing the concentration of the solution and returning the system to equilibrium. Further cooling will continue the deposition and in this way thicker layers may be built up.

The gradual nature of the growth process facilitates the correct positioning of alternate gallium and arsenic atoms, drastically reducing the density of anti-sites and other crystal defects, as well as helping to preclude or 'segregate' residual impurity atoms.

Figure 6-3 is a general representation of the solidus-liquidus curve for a binary III-V compound reproduced from [Casey, H.R., Panish, M.B.]. A is the group III element (gallium), C is the group V element (arsenic), and AC is the compound (gallium arsenide). The melting temperature of AC is TF and two further points on the curve indicate the compositions $X_C(T_1)$ and $X_C(T_2)$ at temperatures T_1 and T_2 respectively.
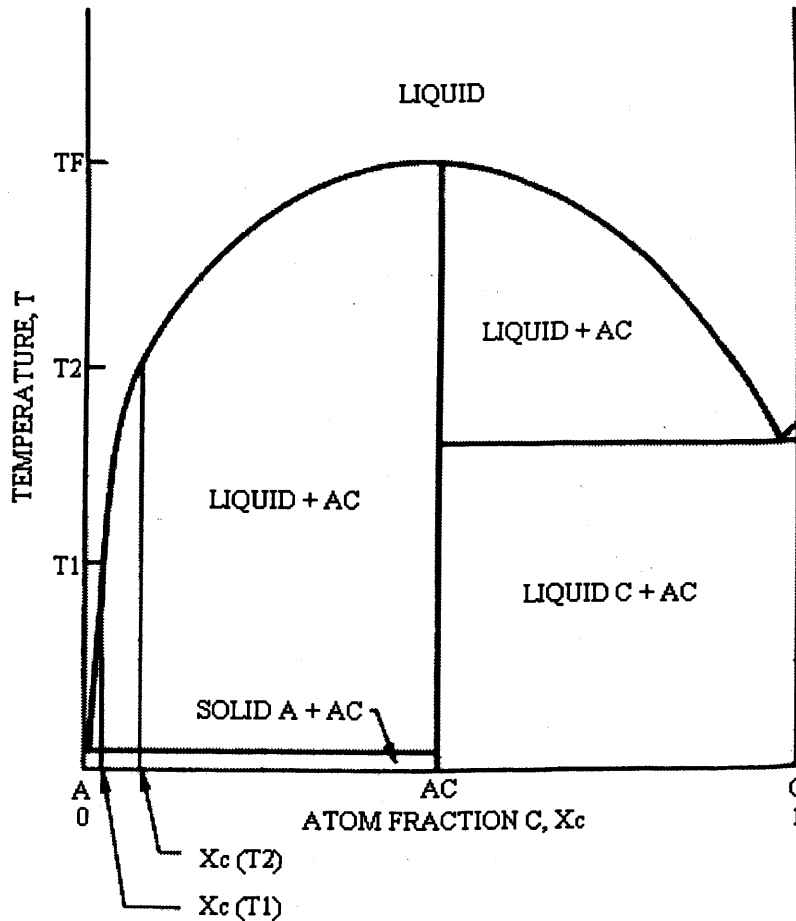
Fig 6-3 A representation of the liquidus-solidus phase diagram for the general case of a binary III-V compound. Reproduced from [Casey, H.R., Panish, M.B.].

At temperatures T_1 and T_2, the III-V compound AC is clearly in equilibrium with liquid solutions that are extremely dilute in the group V element, C. The equilibrium between A, C and AC is simply,

$$A(l) + C(l) \Leftrightarrow AC(s) \tag{6-1}$$

which implies a zero net change in chemical potential μ. i.e.

$$\mu_A(T) + \mu_C(T) - \mu_{AC}(T) = 0 \tag{6-2}$$

Chemical potential may be expressed in terms of chemical activity, a, mole fraction, X, and activity coefficient, γ,

$$\mu = \mu^o + RT \ln a = \mu^o + RT \ln \gamma X \tag{6-3}$$

where μ^o is the value for a pure component (not in solution). The activity a_{AC} for the pure solid AC is unity. Substituting from equation 6-3, equation 6-2 may be re-written as,

$$\mu_A^o(T) + RT \ln[\gamma_A(T)X_A(T)] + \mu_C^o(T) + RT \ln[\gamma_C(T)X_C(T)] - \mu_{AC}^o(T) = 0 \tag{6-4}$$

and the change in chemical potential between temperatures T1 and T2 (T2>T1) is given by the difference in equation 6-4 at each, or,

135

$$\Delta\mu^o \equiv \mu_A^o(T_2) - \mu_A^o(T_1) + \mu_C^o(T_2) - \mu_C^o(T_1) - \mu_{AC}^o(T_2) + \mu_{AC}^o(T_1)$$

$$= -RT_2 \ln[\gamma_A(T_2)\gamma_C(T_2)X_A(T_2)X_C(T_2)] \tag{6-5}$$

$$+ RT_1 \ln[\gamma_A(T_1)\gamma_C(T_1)X_A(T_1)X_C(T_1)]$$

In order to express the left hand side of this equation in terms of thermodynamic quantities that may be evaluated, the relationship between chemical potential and partial molal entropy is used,

$$\overline{S} = -\frac{\partial\mu}{\partial T} \tag{6-6}$$

For a pure component, μ is a function of temperature only, and between the two temperatures, T_2 and T_1,

$$\mu^o(T_2) - \mu^o(T_1) = -\int_{T_1}^{T_2} S^o(T)dT \tag{6-7}$$

where S^o is the entropy of the pure component. For a reversible process, entropy is related to the heat capacity at constant pressure, C_p, by

$$dS = \frac{C_p}{T} dT \tag{6-8}$$

and hence for a pure component and no phase change between temperatures T_2 and T,

$$S^o(T) = S^o(T_2) + \int_{T_2}^{T} \frac{C_p^o}{T} dT \tag{6-9}$$

Combining equation 6-7 and equation 6-9,

$$\mu^o(T_2) - \mu^o(T_1) = S^o(T_2)(T_1 - T_2) - \int_{T_1}^{T_2}\int_{T_2}^{T} \frac{C_p^o}{T'} dT' dT \tag{6-10}$$

Hence, the left side of equation 6-5 may be written as,

$$\Delta\mu^o = \Delta S^o(T_2)(T_1 - T_2) - \int_{T_1}^{T_2}\int_{T_2}^{T} \frac{\Delta C_p^o}{T'} dT' dT \tag{6-11}$$

Setting T_2 equal to TF and recalling that $X_A=X_C=0.5$ at TF, the right side of equation 6-5 may be equated to the right side of equation 6-11 to give,

$$RT_1 \ln[\gamma_A(T_1)\gamma_C(T_1)X_A(T_1)X_C(T_1)] - RT_F \ln[\gamma_A(T_F)\gamma_C(T_F) / 4]$$

$$= -\Delta S^o(T_F)(T_F - T_1) - \int_{T_1}^{T_F}\int_{T_F}^{T} \frac{\Delta C_p^o}{T'} dT' dT \tag{6-12}$$

In fact, ΔC_p^o is relatively very small, and the integral term may be neglected. Activity coefficients cannot be measured directly for III-V systems, but may be represented instead by a quantity called the interaction parameter $\alpha(T)$. The III-V liquid is a 'simple' un-associated solution which means that its excess Gibbs free energy of mixing G^E is given by [Guggenheim, E.A., 1967]

$$G^E = \alpha(T)X(1 - X) \tag{6-13}$$

The excess chemical potential μ_A^E of component A in a two component system, is simply the non ideal part of equation 6-3,

$$\mu_A^E = RT \ln \gamma_A = G^E - X_C \left(\frac{\partial G^E}{\partial X_C} \right) \tag{6-14}$$

Solving the right hand side of equation 6-14 with equation 6-13 then gives,

$$RT \ln \gamma_A = \alpha(T) X_C^2 = \alpha(T)(1 - X_A)^2 \tag{6-15}$$

since $X_A + X_C = 1$, and similarly,

$$RT \ln \gamma_C = \alpha(T) X_A^2 = \alpha(T)(1 - X_C)^2 \tag{6-16}$$

which, substituting into equation 6-12 and adding and subtracting RT ln 4, gives the liquidus equation of a simple liquid solution with a binary compound, as,

$$RT \ln[4X_C(1 - X_C)] + [\Delta S^o(T_F) + R \ln 4](T_F - T)$$
$$+ \alpha(T)[2X_C^2 - 2X_C + 1] - \alpha(T_F) / 2 = 0 \tag{6-17}$$

Now,

$$\Delta S^o(T_F) + R \ln 4 = \Delta S_F^{ID} \qquad = \text{the ideal entropy of fusion} \tag{6-18}$$

and it has been found experimentally that for many III-V binary systems, including GaAs, $\alpha(T)$ has a linear temperature dependence [Panish, M.B., 1972],

$$\alpha(T) = a + bT \tag{6-19}$$

Substitution of equations 6-18 and 6-19 into equation 6-17, gives

$$0.5\{RT \ln[4X_C(1 - X_C)] + (\Delta S_F^{ID} - b/2)(T_F - T)\}$$
$$= -(a + bT)(0.5 - X_C)^2 \tag{6-20}$$

The entropy of fusion, ΔS_F is the ideal entropy plus the excess entropy (-b/2),

$$\Delta S_F = \Delta S_F^{ID} - b / 2 \tag{6-21}$$

and substitution of this, and $\alpha(T) = a + bT$ into equation 6-20, gives,

$$\alpha(T) = -0.5 \frac{RT \ln[4X_C(1 - X_C)] + \Delta S_F(T_F - T)}{(0.5 - X_C)^2} \tag{6-22}$$

an equation relating the equilibrium concentration, X_C, of the liquid at temperature T to the known quantities $\alpha(T)$, the interaction parameter, ΔS_F, the entropy of fusion and T_F, the temperature of fusion. Experimentally determined values of these parameters for GaAs are given in table 6-1.

Table 6-1 - Values of T_F, ΔS_F and $\alpha(T)$ for GaAs.

Quantity	Value	Reference
Temperature of fusion, T_F (K)	1511	[Richman, D., 1963],[Koster, W. et. Al., 1955]
Entropy of fusion, ΔS_F (cal/mole-K)	16.64	[Lichter, B.D. and Sommelet, P., 1969]
Interaction parameter, $\alpha(T)$ (cal/mole)	5160-9.16T	[Panish, M.B., 1974]

Using these values in equation 6-22, and re-arranging for T, we obtain the relationship for GaAs,

$$T = \frac{25143 + 2580(0.5 - X_{As})^2}{4.58(0.5 - X_{As})^2 - R \ln[4X_{As}(1 - X_{As})] + 16.64} \qquad (6\text{-}23)$$

where X_{As} has been substituted for the arbitrary group V atom fraction X_C. This relationship may be used to calculate the dipping temperature and the cooling required to remove a specific quantity of arsenic (and hence an equal molal quantity of gallium) from the melt, which in the ideal case would all be deposited as a uniform layer of GaAs on the substrate. It is shown graphically in figure 6-4.
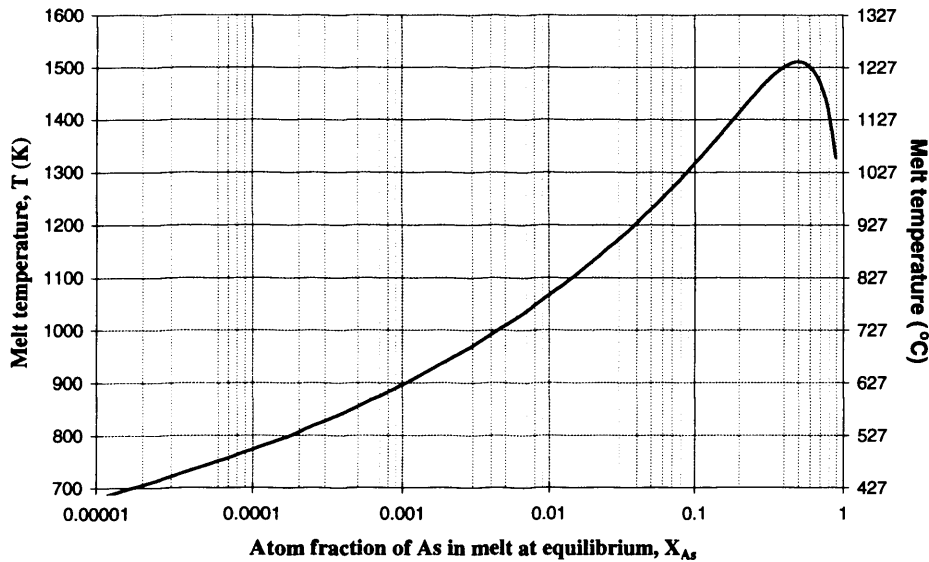
Fig 6-4 The theoretical liquidus curve for GaAs, (a specific case of figure 6-3).

In practice, it is not possible to place a PRT or thermistor very close to the growing surface and the theoretical growth temperature can only serve as a rough guideline when choosing the temperature (as measured at some point outside the melt holder) at which to attempt the first growth. If the temperature at which the substrate is introduced into the melt is too high, then the substrate will begin to etch. A very small degree of etching is desirable to remove potentially contaminated surface layers, but excessive etching is unlikely to be uniform, and will alter the melt composition adjacent to the wafer surface. If the initial temperature is too low then deposition will be rapid and un-controlled with local depletion of the melt giving rise to 'blobs' rather than layers. Furthermore, if the surface of the substrate does not initially melt, then the junction between the substrate and the epitaxial layer is likely to be poor. Determining the correct initial temperature (as measured in a real system), for a given melt composition is therefore an iterative process in which part wafers are commonly dipped and then examined for indications of excessive etching or un-controlled deposition.

Just as the initial dipping temperature must be carefully controlled, so too must the cooling or ramp rate. This must be gradual enough in comparison with the rate at which the melt is mechanically mixed, so that the melt adjacent to the growing surface does not become depleted of arsenic. In order to correctly follow the curve of figure 6-4, the melt composition at the substrate must vary uniformly and gradually. The required cooling rate may be specified in the temperature control loop but there

138

will inevitably be some thermal imbalance as the substrate and holder are introduced into the melt. This is particularly prevalent in a large scale system such as the dipper at EEV, where the graphite holder must be lowered ~15cm into the melt with a corresponding movement of the stainless steel shaft within the five zone furnace.

Wafer orientation and surface preparation are also vitally important to the successful growth of epitaxial layers. Localised, or island growth which may result from dipping at saturation (i.e. with the melt too cool), is also symptomatic of a surface which has insufficient nucleation sites [Casey, H.C., et al.] so that growth occurs preferentially on the newly formed GaAs (which thanks to its purity will have a high density of nucleation sites) rather than on the surrounding substrate. This forms geometrical islands, the facets of which indicate the underlying crystal planes. It has been repeatedly demonstrated that chemical etching [Ilegems, M., 1974], [Guggenheim, E.A., 1967], [Kubaschewski, O., 1967] and the rigorous avoidance of oxidisation [Miller, B.I., 1972], [Peters, R.C., 1973] can reduce or eliminate island growth, indicating that nucleation site density is a sensitive function of even light contamination.

At the time of publication of reference [Casey, H.C., et al.], terraces were the most common surface feature observed on III-V LPE epitaxial layers. These result from small misalignments of the substrate wafer, of the order of ~5°. Today, these features seem less dominant which is probably due to the availability of 'epi ready' wafers with a misalignment specification of <5° (see table 6-2). Within this range, terracing is rarely observed at growth temperatures above ~780°C.

6.3 Experimental set-up and basic procedure

6.3.1 The large scale dipping facility
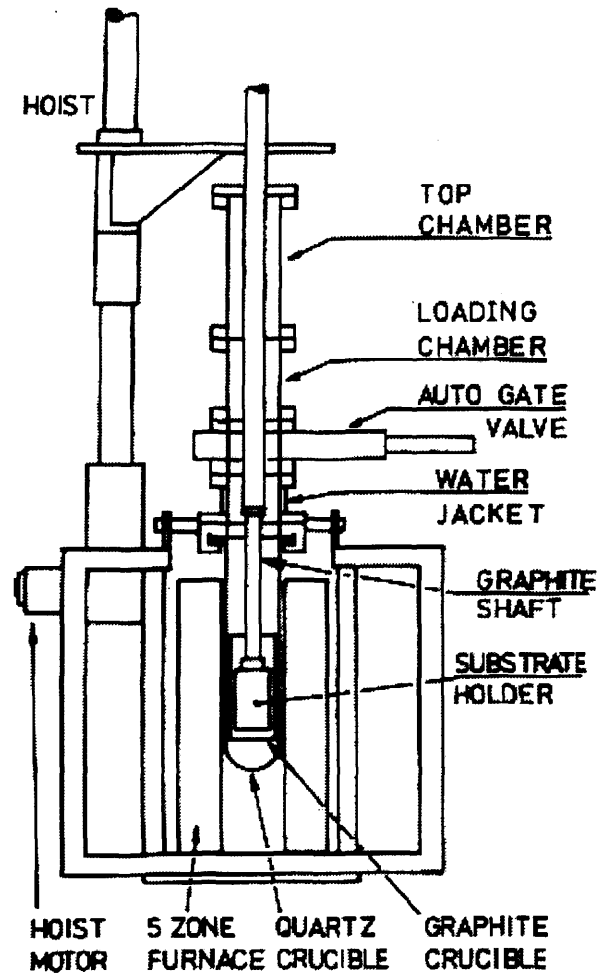
Fig 6-5 The large scale Liquid Phase Epitaxy dipping facility at EEV Ltd, reproduced from [Cross, T.A., 1991]

Figure 6-5 shows the large scale dipping facility operated by EEV Ltd. Three kilograms of liquid gallium (referred to as an infinite melt due to its large volume in comparison with the grown layers) are held in a high purity graphite crucible. This is housed in a quartz crucible within a five zone vertical furnace. The system is fed with high purity palladium diffused hydrogen to keep atmospheric contamination to a minimum and the GaAs substrates are introduced via a loading chamber which is also purged with palladium diffused hydrogen. They are held in a cassette of high purity graphite which is lowered on a graphite shaft to a position just above the surface of the melt where they can be held indefinitely so that the temperatures of the upper melt and the wafer holder assembly can equalise. The slowly rotating wafer holder is then lowered into the melt and shutters are opened, allowing the gallium to flow into the cassette, covering the substrate(s). The purpose of the rotation is to ensure that the melt adjacent to the growing surface is continuously replenished and does not become locally depleted of arsenic. The temperature of the system is then decreased, typically at a

140

rate of less than 0.3°C/min, so that GaAs will be deposited in accordance with figure 6-4. The shutters are closed again, until the holder has been lifted through the melt surface so that 'floating' contamination is avoided, and are then re-opened to empty the cassette which is lifted to a cooling position in the loading chamber. Two graphite holders were used during these trials, a standard EEV cassette which holds multiple wafers vertically, and a custom designed unit which holds whole or part wafers horizontally.

6.3.2 Graphite substrate holder for vertical growth

Initially, all of the epitaxial growth trials were carried out using a wafer holder which had been designed for the growth of solar cell layers. This graphite cassette holds up to ten 2" x 2" wafers vertically, in 'picture frames', and is the result of much development [Cross, T.A., 1991] aimed at ensuring sufficient melt circulation, minimum melt contamination (i.e. by eliminating the use of graphite screws), and most importantly a minimum temperature gradient across the substrates during growth. This holder is shown in figure 6-6. Once it is submerged, the shutter rod is raised within the support shaft, lifting the shutters vertically and allowing the melt to cover the (up to ten) substrate wafers. When the required ramp, or temperature gradient has been completed, the shutters are re-closed until the holder has been lifted through any floating contamination, and are then opened once again to allow the melt to drain away (quickly to avoid meniscus formation). The entire assembly rotates throughout to ensure melt circulation.
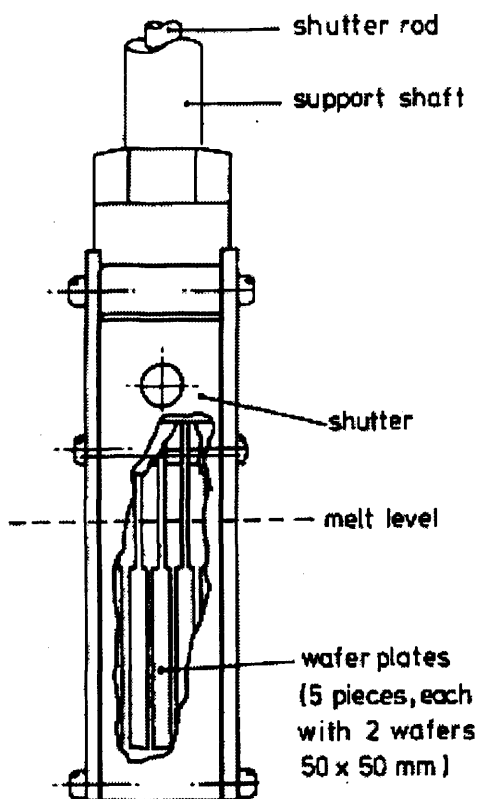
Fig 6-6 Schematic of graphite wafer holder for vertical growth, reproduced from [Cross, T.A., 1991].

141

6.3.3 Graphite substrate holder for horizontal growth

For the second phase of the growth programme, a horizontal substrate holder was designed which would allow a small volume of melt to be entirely removed from the system and cooled to room temperature with the substrate. The design criteria for this holder were [Hardingham, C.M., Ricketts, A., 1995],

1. The holder should be compatible with the use of ϕ 2" round substrates.

2. In this configuration, the holder should include a means of removing excess melt from the wafer after growth, which may be accomplished with a tipping mechanism.

3. The holder should also be compatible with the use of part wafers, in order to minimise the substrate cost during the development phase.

4. In (at least) this configuration, the holder should be compatible with significant cooling and As depletion from the melt.

5. The holder should be designed for ease of manufacture.

6. The holder should be designed for ease of use, with a minimum number of high fragility components.
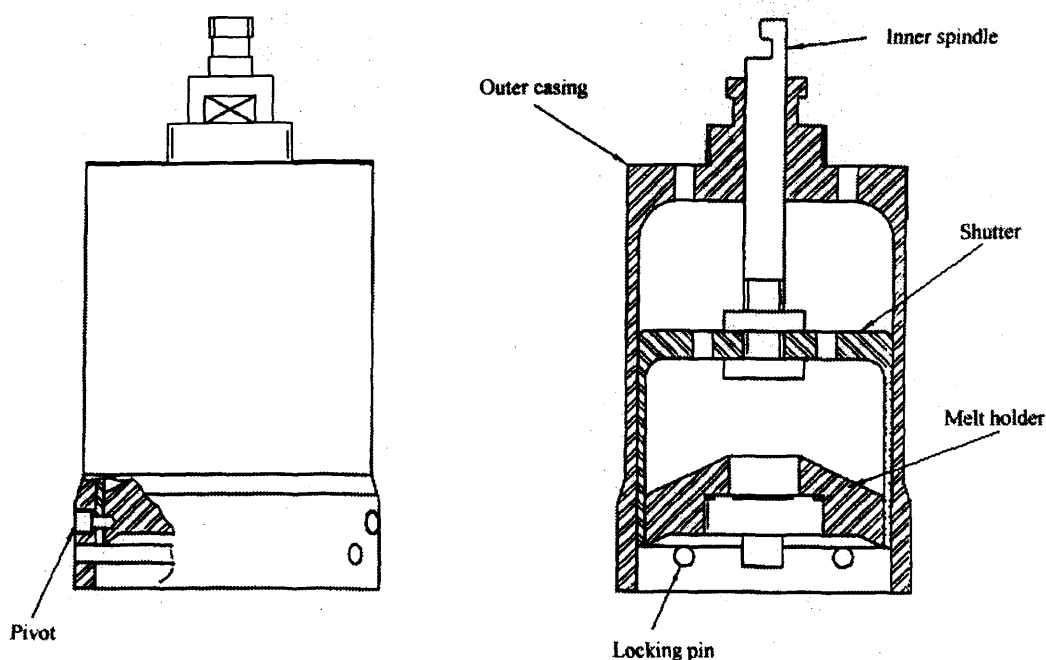
Fig 6-7 Schematic of the custom designed graphite wafer holder for the growth of thick layers

Figure 6-7 shows the resulting wafer holder. It is operated in much the same way as the vertical wafer holder, except that after dipping (which need be only brief) and emptying of the cassette, a small volume of melt remains in the melt holder and cools very gradually with the substrate, to room temperature. This highly experimental arrangement was devised after a previous growth with the vertical wafer holder, in which the shutters were inadvertently left closed after dipping, resulted in very thick, if somewhat wedge shaped epitaxial layers. A new cassette design was required to hold

the substrates horizontally and to remove less melt from the crucible with each dip. A range of melt holders was produced, to accommodate different sized portions of substrate, and a pivot was incorporated so that the melt could be ejected if required. In the event, the pivot was never used. Photographs of the graphite cassette and three of the melt holders are shown in figure 6-8.
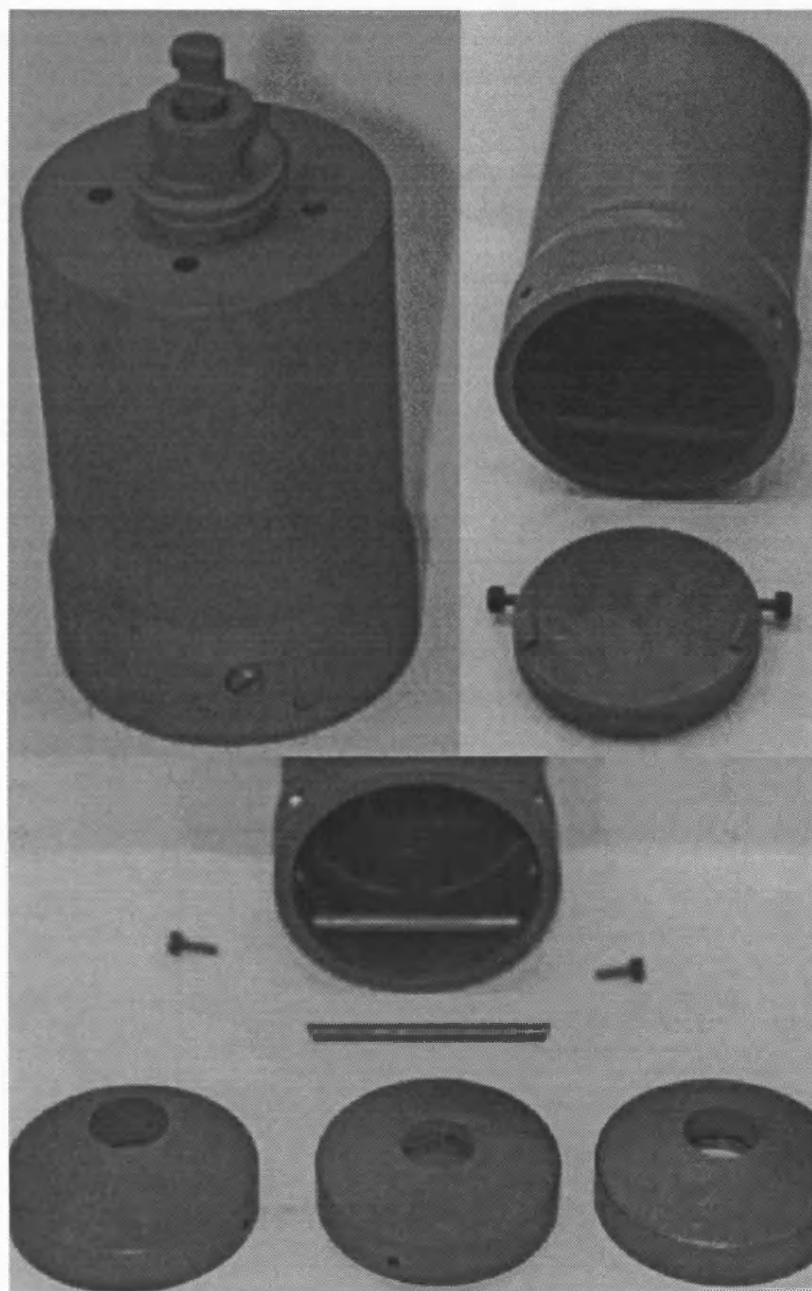
Fig 6-8 The graphite wafer holder for horizontal growth.

6.3.4 System cleanliness

Prior to installation within the furnace, the quartz crucible, graphite crucible and graphite wafer holder were chemically cleaned and baked to remove contamination but once in operation, the system was continuously purged with palladium diffused hydrogen, and only the wafer holder was

subsequently exposed to air. Each time it was re-loaded, it was therefore purged overnight in the hydrogen filled chamber above the growth chamber before being lowered to a position just above the melt surface where it was baked for a further two hours at 800°C prior to dipping. This procedure is shown schematically in figure 6-9.
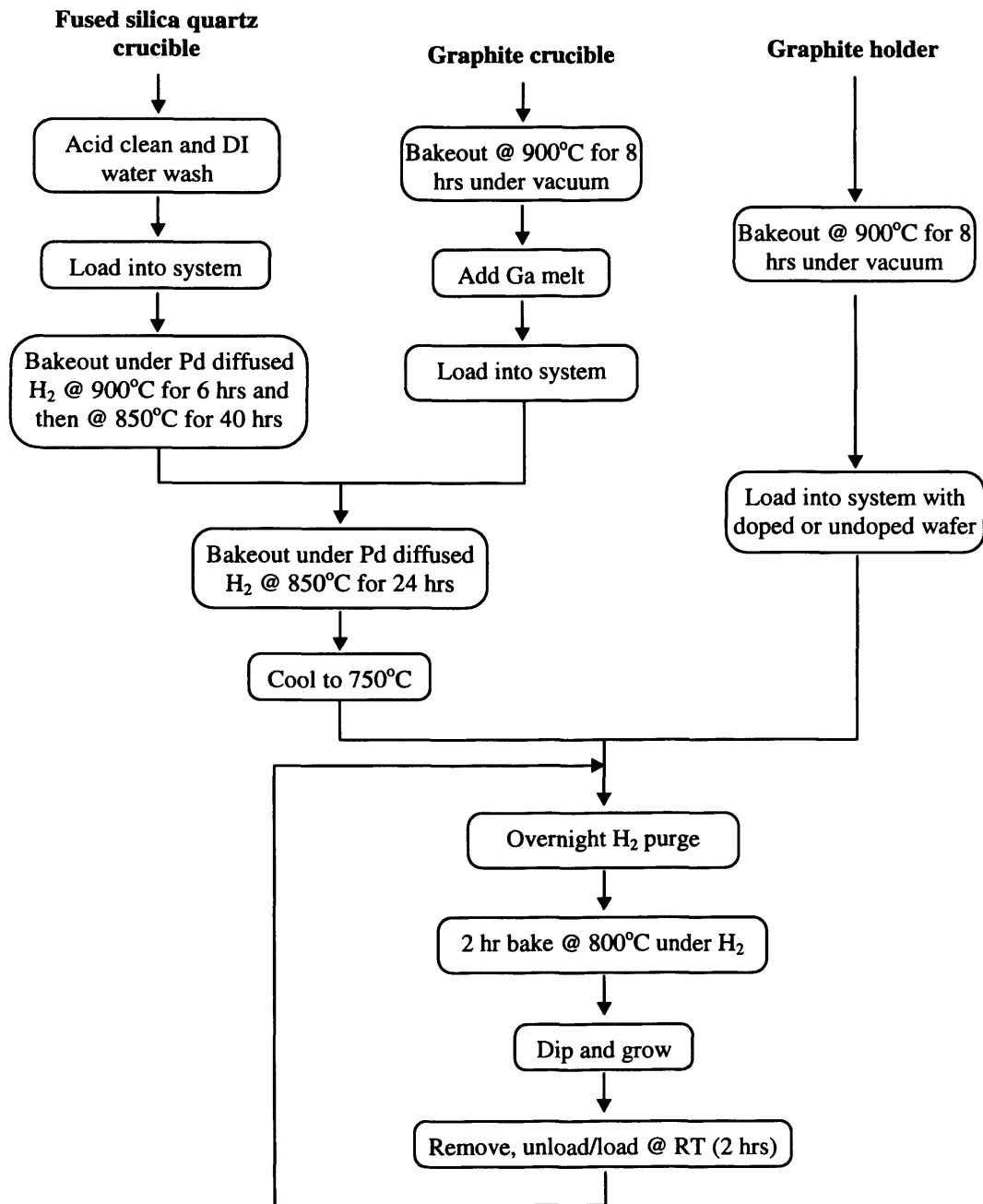
Fig 6-9 Basic procedure for epitaxial growth using EEV LPE facility

6.4 The growth program

In all, twenty nine runs were made using the vertical wafer holder, including a trial without any substrate present, and eight runs were made using the horizontal wafer holder. Bulk GaAs substrate wafers were procured from MCP Wafertech (semi-insulating for material analysis and n-type for

144

detector fabrication). A typical substrate specification is given in table 6-2. Six kilograms (enough for two separate melts) of 6N (6 nines or 99.9999% pure) gallium were also purchased from MCP Wafertech with a test specification as determined by Glow Discharge Mass Spectroscopy (GDMS), given in table 6-3.

Table 6-2 'epi-ready' LEC bulk GaAs wafer specifications.

	SPECIFICATION	ACTUAL
Growth Method	LEC	LEC
Conductivity Type	Semi-insulating	Semi-insulating
Dopant	None	None
Orientation	$(100)\pm0.5°$	(100) $\|0.02°\sim0.04°\|$
Resistivity (top)	$> 3x10^7$ Ωcm	$4.7\sim5.3x10^7$ Ωcm
Resistivity (bottom)	$> 3x10^7$ Ωcm	$3.5\sim4.0x10^7$ Ωcm
Mobility (top)	>7000 cm^2/Vs	$7.1\sim7.2x10^3$ cm^2/Vs
Mobility (bottom)	>7000 cm^2/Vs	$7.2\sim7.3x10^3$ cm^2/Vs
EPD (top)	<50000 cm^{-2}	$3.6x10^4$ cm^{-2}
EPD (bottom)	<50000 cm^{-2}	$4.2x10^4$ cm^{-2}
Carbon Concentration	-	$1.8x10^{15}$ cm^{-3}
Diameter	50.8±0.2 mmϕ	50.80~50.81 mmϕ
Primary Flat Position	$(011)\pm0.5°$	$(011)\pm0.5°$
Primary Flat Length	14.23~17.52 mm	16 mm
Secondary Flat Position	$(011)\pm0.5°$	$(011)\pm0.5°$
Secondary Flat Length	6.35~9.65 mm	8 mm
Thickness	300±20 µm	307~311 µm
Front Surface Finish	Mirror Polished	Mirror Polished
Back Surface Finish	Mirror Polished	Mirror Polished
TTV	<20 µm	1.8~4.2 µm

Table 6-3 GDMS analysis of 6N gallium purity. Figures in Parts Per Billion (PPB).

Element	PPB	Detection limit	Element	PPB	Detection limit	Element	PPB	Detection limit
Li	ND	0.1	Fe	2	0.2	Sn	ND	2
Be	ND	0.1	Co	ND	0.1	Sb	ND	0.5
B	ND	0.2	Ni	0.6	0.2	Te	4	0.5
C	140	50	Cu	ND	0.4	I	ND	1
N	ND	50	Zn	ND	0.6	Cs	ND	0.2
O	100	50	Ge	ND	5	Ba	ND	0.2
F	ND	3	As	ND	0.5	La	ND	0.2
Na	ND	0.2	Se	ND	5	Ce	ND	5
Mg	ND	0.2	Br	ND	5	Hf	ND	0.2
Al	0.4	0.1	Rb	ND	0.2	W	ND	0.2
Si	0.8	0.4	Sr	ND	0.2	Re	ND	0.3
P	0.4	0.2	Y	ND	0.2	Os	ND	1
S	0.5	0.3	Zr	ND	0.2	Ir	ND	1
Cl	ND	0.5	Nb	ND	0.2	Pt	ND	1
K	ND	3	Mo	ND	0.2	Au	ND	1
Ca	ND	3	Ru	ND	1	Hg	ND	3
Sc	ND	0.2	Rh	ND	1	Tl	ND	1
Ti	0.3	0.1	Pd	ND	2	Pb	0.6	0.5
V	ND	0.2	Ag	ND	10	Bi	ND	0.3
Cr	0.3	0.2	Cd	ND	3	Th	ND	0.2
Mn	ND	0.2	In	2	0.2	U	ND	0.2

Arsenic was introduced into the melt by adding carefully weighed pieces of semi-insulating GaAs wafer (table 6-2). The mass of gallium used in the first melt was 2894.5g and to this was added 76.7g of GaAs wafer. Since the atomic masses of gallium and arsenic are 69.7 and 74.9g respectively, the GaAs added comprised,

$$\left(\frac{76.7}{74.9 + 69.7} \right).74.9 = 39.73g \quad \text{of arsenic, and}$$

$$76.7 - 39.73 = 36.97g \quad \text{of gallium.}$$

Hence, the total gallium in the melt was 2894.5 + 36.97g = 42.06 moles, and the total arsenic in the melt was 39.73 g = 0.53 moles. The atom fraction of arsenic in the melt was therefore,

$$X_{As} = \frac{0.53}{42.06 + 0.53} = 0.012$$

According to equation 6-23, this gives an equilibrium (or initial dipping) temperature of 810°C. As already explained however, this figure can only serve as a guideline since a PRT can not be placed close to the growing surface and in the EEV facility, the melt temperature is monitored close to the bottom of the crucible, whilst the growth takes place close to the top. With their experience of the growth facility, Chris Hardingham, Steve Woods and Andy Ricketts of EEV proposed that the initial growth should be attempted with the temperature at the bottom of the crucible set to 755°C, some 55°C lower than the calculated temperature. It was also decided that the first run with a substrate would be reasonably long to give a clear indication of the net growth or etch rate. About 17 minutes at a ramp rate of 0.3 °C per minute was selected to give a drop in temperature of 5°C.

6.5 Results

For the first run (L1), no substrate was placed in the holder. This was simply to check that the system did not leak hydrogen, that the temperature control was sufficiently stable and that the mechanical operations of rotating, lowering and raising the holder assembly, and opening and closing the shutters, worked correctly. The graphite was examined after this run since any GaAs deposition here would indicate that the dipping temperature was too low. There was none.

The first run with a substrate, commencing at 755°C as discussed, was therefore L2. The result (established by the reduction in wafer mass), was a net etch of some 100μm, clearly indicating that the temperature of the melt and substrate at the time of dipping was too high. For the next run, the initial temperature was therefore decreased to 749°C. Since the etching of L1 was so severe it was also decided to reduce the dipping time (and hence ΔT) so that subsequent etching would be reduced and the composition of the melt would not be substantially altered by the addition of GaAs from the substrate. The result was still net etching rather than growth, so the initial temperature was reduced once again, and so on, until, at an initial dipping temperature of 740°C, the first net growth (1μm) was measured, although this was thin and irregular. These, and all subsequent runs are summarised in

table 6-4. Unless otherwise stated, the substrate is semi-insulating to allow Hall analysis on uniform layers. This also avoids the serious melt contamination which would occur if doped wafers were to etch. Once net growth was established however, n-type substrates were used so that detectors could be produced. Runs L1B to L8B were conducted using the horizontal wafer holder.

Table 6-4 Summary of epitaxial growth trials conducted at EEV.

Run	Date	Ramp (°C/mn)	Dip Temp (°C)	End Temp (°C)	Net Growth (μm)	Hall Mobility @ RT ($cm^2V^{-1}s^{-1}$)	Hall Mobility @ 77 K ($cm^2V^{-1}s^{-1}$)	≈ Carrier Conc @ RT (cm^{-3})	
L1	7/94	0.6							Test run (no substrate)
L2	7/94	0.3	755	750	-100				Heavy etching (temp too high)
L3	7/94	0.3	750	749	-16				Still etching
L4	7/94	0.3	745	744	-6				Still etching
L5	7/94	0.3	740	739	1				Thin, irregular growth
L6	8/94	0.3	735	734	5	6344	20248	6.6E15	Even growth
L7	8/94	0.3	735	733	5.7	6416	20505	7.6E15	Mainly even growth but cloudy regions
L8	8/94	0.3	735	733	4.1				Changed temp profile of upper furnace
L9	8/94	0.225	735	734.5	1.7				
L10	8/94	0.225	735	734	3.6				Speckled, uneven growth
L11	8/94	0.225	735	733.5	3.9				Poor (island) growth
L12	8/94								Graphite broke
L13	9/94	0.3	732	731	9				
L14	9/94	0.3	729	728	8				
L15	9/94	0.3	732	730	5				
L16	9/94	0.3	729	728					Very poor, island growth
L17	9/94	0.3	734	728	15				
L18	9/94	0.3	736	726	14	6643	23638	8E15	
L19	9/94	0.3	737	726					N-type substrate
L20	9/94	0.3	738	726	10	7282	38182	4.7E15	
L21	10/94	0.3	738	724	16				N-type substrate
L22	10/94								N-type substrate
L23	10/94	0.5	738	718	20	7564	41947	2.8E15	
L24	10/94	"	"	"	20	6903	30564	6.86E15	Possible leak
L25	11/94	"	"	"	22	7628	46760	1.95E15	
L26	12/94	"	"	"	18	7833	50228	1.63E15	
L27	4/95				3.3	7644	44510	1.75E15	
L28	4/95								N-type Substrate
L29	6/95								N-type Substrate
L1B	10/95	0.35	750	542	-68.5	5366	13751		
L2B	10/95	Free	740		-44	5594	9771		
L3B	10/95	Free	730		-29.5	5419	11079		
L4B	10/95	Free			-20				N-type Substrate
L5B	10/95	Free	740		17	6093	17089		
L6B	10/95	Free	730		23	6035	16740		
L7B	10/95		703	592	36				N-type Substrate
L8B	10/95		693	491	114				N-type Substrate

6.5.1 Epitaxial layer thickness and purity

Samples from all runs using semi-insulating substrate wafers which resulted in growth of sufficient uniformity, were analysed using a commercial four point Hall probe (see chapter 3). This measures the mobility of the majority charge carriers in $cm^2V^{-1}s^{-1}$ using the Hall effect (Hall mobility) which reveals whether the material is n or p-type and gives a good, first indication of the purity. These measurements were conducted at room temperature (~300 K), and with the sample submersed in liquid nitrogen (~77 K). The results are shown in figure 6-10.
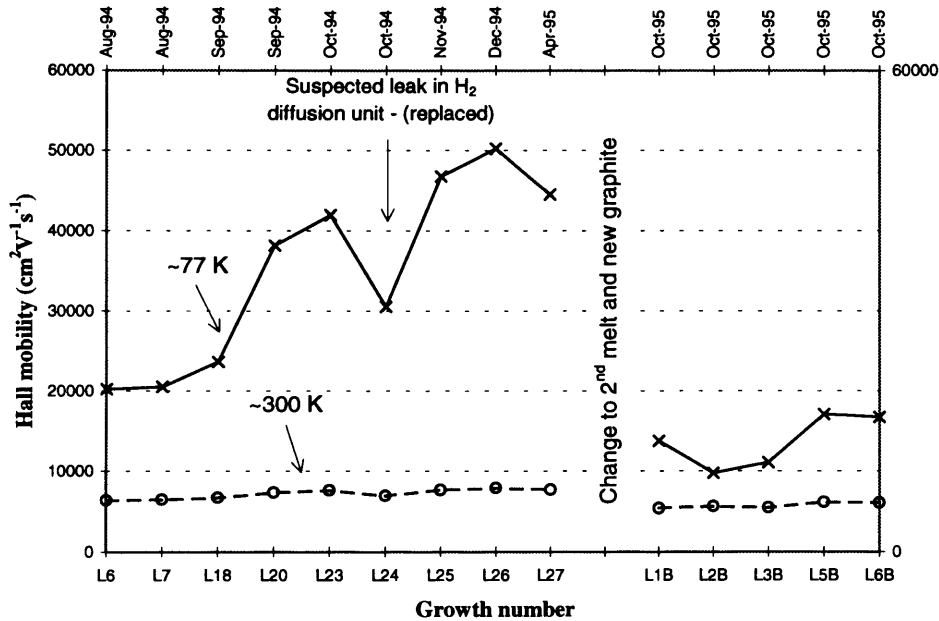
Fig 6-10 Hall mobility at RT and lN_2 temperature for all samples analysed.

The most striking feature of figure 6-10 is that the mobility as measured at 77 K improves as the melt is baked over a period of several months, whereas the mobility as measured at room temperature barely changes. This could indicate that the most dominant defect in the grown layers at room temperature is not due to a chemical impurity in the melt whose concentration decreases with prolonged baking, but is a crystalline defect introduced at growth. The improvement in Hall mobility at 77 K over a number of months, suggests that a different (probably chemical) impurity dominates charge trapping at these temperatures, and hence that the first trap is frozen out. This is extremely similar to the effect observed in bulk material (chapter 4) and tends to suggest that the same trap species (EL2) could be responsible.

The drop in mobility at run L24 corresponds with a suspected leak in the palladium diffusion unit which filters all of the hydrogen entering the system. This was indicated by poor dew points in the upper and lower chambers. The diffuser was replaced and the dew points improved. The purity of the epitaxial layers indicated by the Hall mobility also returned to its original trend but no conclusive link between the suspected leak and the purity of L24 should be implied from one measurement.

Between April and October 1995, the entire facility was overhauled and the detector growth program was moved to a second furnace. During this time the graphite holder for thick horizontal growth was manufactured, and new quartz and graphite crucibles were procured. The original melt was considered likely to have been contaminated and was therefore replaced with the second 3kg, 6N gallium melt. The growth programme recommenced using the new system in October 1995. Referring again to figure 6-10, it can be seen that on replacing the gallium melt, the 77 K Hall mobility dropped from ~45000 $cm^2V^{-1}s^{-1}$ to ~15000 $cm^2V^{-1}s^{-1}$, close to the value measured at the beginning of phase 1. In fact it dropped slightly lower, but it should be noted that the first melt had already been baking in the facility for about a month before layers suitable for Hall analysis could be grown. The two lots of gallium were from the same source and had identical specifications, and it is also worth noting that the room temperature Hall mobility barely changed between the two melts. This then is strong evidence that the increase in 77 K Hall mobility observed during phase 1 of the growth trials was due to the long term baking of the gallium melt. The second melt was only baked for one month before commercial pressures ended the programme. It was therefore not possible to establish whether or not the Hall mobility at 77 K would increase once again.
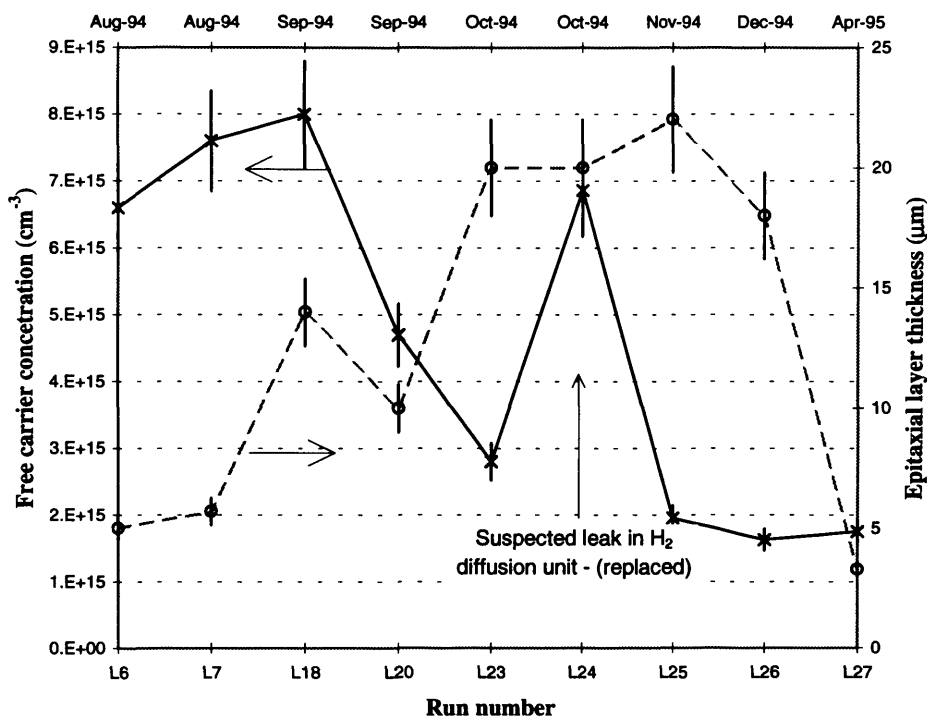
Fig 6-11 Residual carrier concentration for all samples in figure 6-10 for which a reasonable estimate of epitaxial layer thickness (also shown) could be made.

Given the thickness of the epitaxial layer, the commercial four point Hall probe used at EEV can also calculate the free carrier concentration. The results for all samples for which a reasonable estimate of epitaxial layer thickness (also shown) could be made, are given in figure 6-11. Unfortunately, layer thickness was calculated from the increase in mass, and the wafers were rarely free from regions of uneven growth or blobs which clearly made this difficult. Also, figures calculated this way can only

describe the net growth i.e. taking no account of the fact that some unknown thickness of bulk GaAs at the surface of the substrate will have been etched back and replaced with epitaxial material. The values of thickness and hence of free carrier concentration given in figure 6-11 therefore probably carry errors of around ± 10%.

The lowest values of free carrier concentration measured were around $1.7 \times 10^{15} cm^{-3}$ and although this is extremely pure by bulk standards, it is still poor compared with the material produced by Eberhardt [Eberhardt, J.E., 1971], and by Alexiev [Alexiev, D., 1992], who both achieved $\sim 10^{13} cm^{-3}$.

In the case of thick layers using the horizontal holder, several samples showed signs of very severe etching prior to epitaxial growth and it was not therefore possible to make a reasonable estimate of the layer thickness. As shown in table 6-4 however, the net growths achieved in the last four runs using this holder were 17, 23, 36 and 114 μm.

6.5.2 Surface analysis with scanning electron microscope

Several early samples had a speckled appearance after dipping, which on examination with a scanning electron microscope, was revealed to be due to island growth, as shown in figure 6-12. The orientation of the crystal planes can be seen clearly, and the areas in between the islands are remarkable for a complete lack of growth.
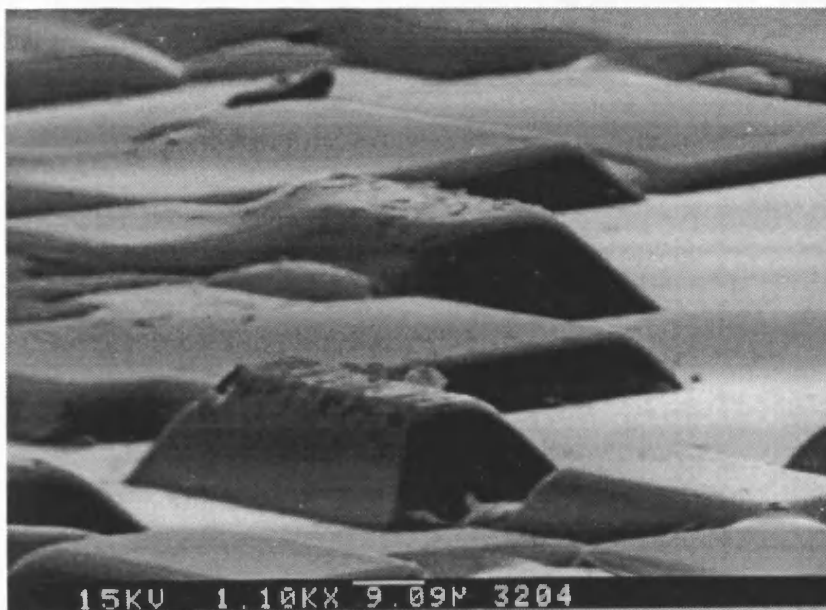
Fig 6-12 Scanning Electron Microscope image of 'speckled' region indicating severe island growth.

In figure 6-13 it can be seen that the growth is highly variable across the wafer, and some regions are completely devoid even of islands. In this image, regions can also be seen in which islands appear to be joining up and eventually disappearing.
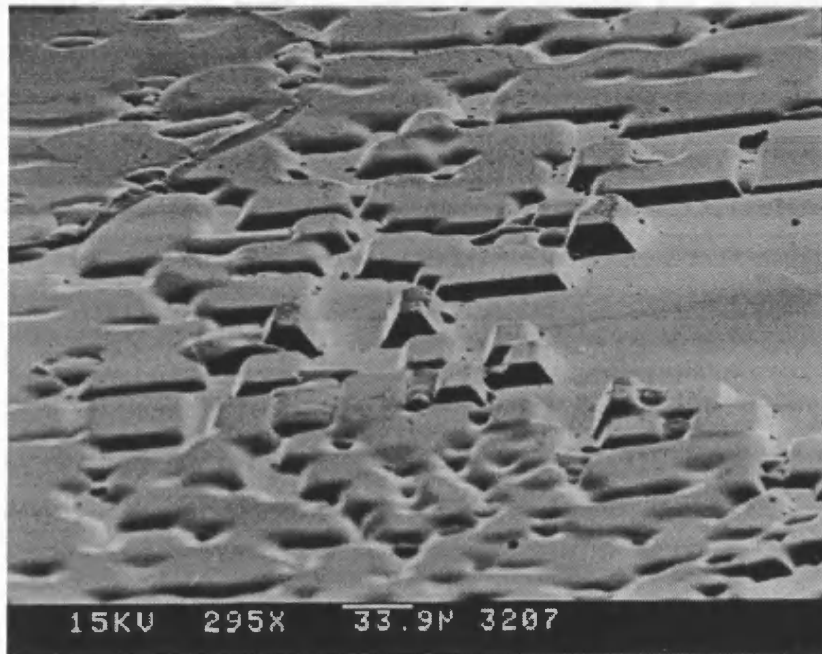
Fig 6-13 Viewing a wider area reveals great variation in different regions of the wafer. It also appears that neighbouring islands have begun to join up in some regions to form a layer.

Figure 6-14 shows a region in which growth has progressed a little further. This is a still clearer indication that a smooth layer is being formed, but that the mechanism, far from being a uniform deposition of monatomic layers, is a connecting of islands, and regions of islands. This raises an important question, since an epitaxial layer formed by the connection of many islands is likely to contain planes of crystalline defects (and hence dangling bonds) joining the substrate to the front contact metal.
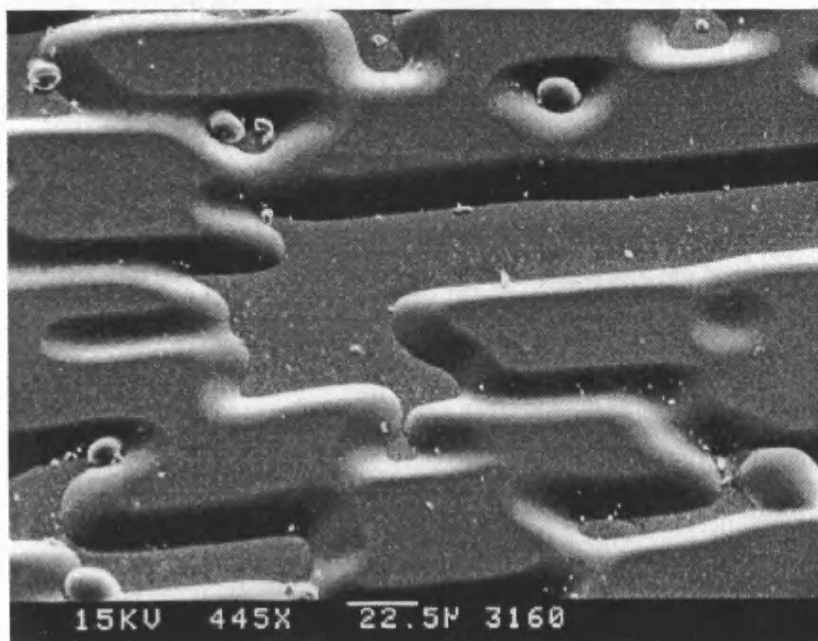
Fig 6-14 Another view which indicates that the epitaxial layers may have been formed by the connection of islands, rather than by the deposition of uniform monatomic layers.

Island growth commonly occurs when the surface of the substrate has an insufficient density of nucleation sites due to the presence of an oxidised layer or other contamination which has not been removed by sufficient chemical etching, or melting of the surface at the time of growth. This is not a satisfactory explanation for the island growth observed here, since standard 'epi-ready' wafers were used throughout and several wafers on which island growth was observed had clearly melted back significantly prior to growth.

A far more likely explanation in this case is that the initial growth rate was far too high. This would have the effect of depleting the melt of arsenic close to the growing surface, faster than it is replaced by diffusion, and mechanical mixing. The initial deposition of GaAs onto the substrate would therefore consist of isolated patches rather than a layer, as arsenic atoms diffuse towards depleted regions in the melt rather than towards the growing surface. As the melt is replenished, growth will tend to occur preferentially on the epitaxial islands.
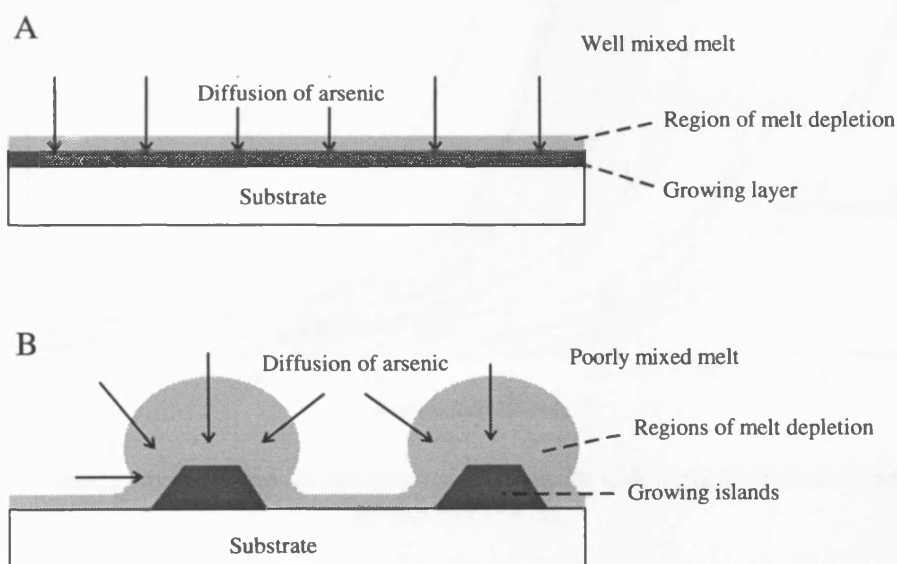
Fig 6-15 Schematic indicating possible mechanism for island growth if initial growth rate is too high with respect to melt circulation.

If growth continues for a sufficient length of time after island formation has begun, it would appear from figures 6-12, 6-13 and 6-14 that the islands join up to form a smooth layer. Since the aim of this growth program was to produce thick layers relatively quickly, the cooling rates were high and the implication now is therefore that the layers produced may consist of merged islands rather than monatomic layers. This would almost certainly produce a very high density of crystalline defects across the grown layer.

6.5.3 Detector evaluation

Schottky barrier diode detectors were fabricated on all N-type substrate wafers on which epitaxial layers of satisfactory uniformity and surface finish had been produced. This selection was simply a visual inspection with an optical microscope, which revealed that runs L22, L28 and L29 from the vertical growth phase, and L8B from the horizontal phase, resulted in smooth, 'mirror like' finishes and were therefore most likely to form satisfactory Schottky junctions. The detector fabrication process (given in chapter 3) was almost identical to that for bulk GaAs devices.
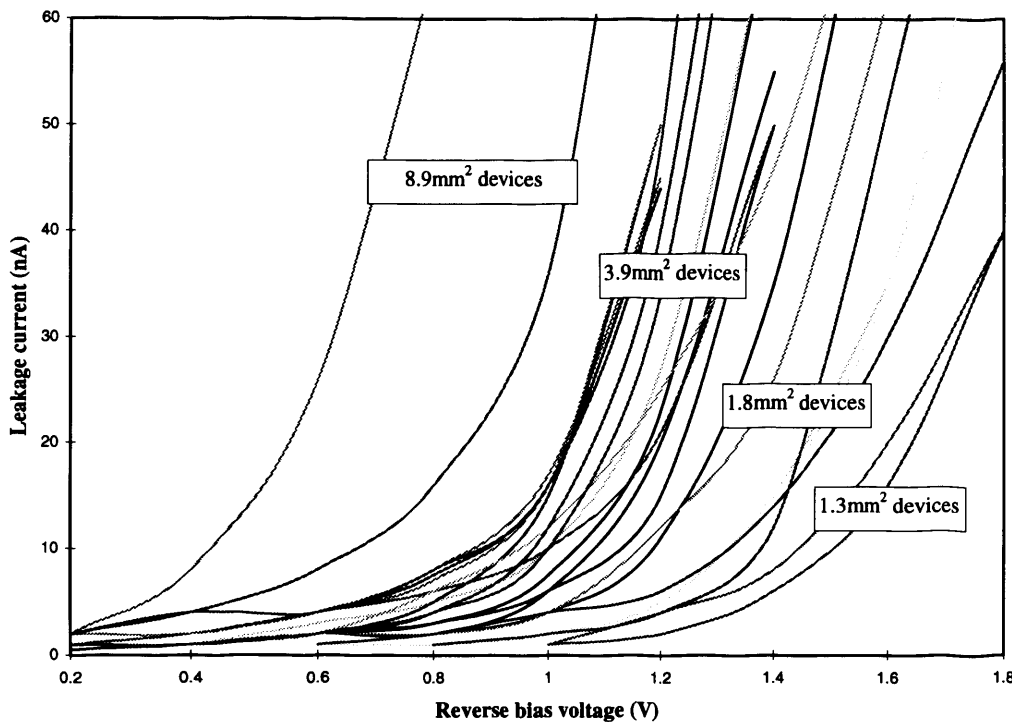
Fig 6-16 Room temperature IV curves for devices from wafer L28, typical of those from all epitaxial devices produced.

Figure 6-16 shows the room temperature reverse IV characteristics of devices produced from wafer L28. These characteristics are typical of those from all the devices produced during the growth program and indicate that there is a rectifying barrier, but that it breaks down at typically just 0.8 to 1 volt. Attempts were made to detect X-rays using these detectors, but at such low values of applied bias, the depletion region is extremely narrow (probably only a couple of microns) and the device capacitance is therefore high, generating noise in the pre-amplifier. The narrow depletion region also means that the detectors are inefficient, and that the charge clouds generated by many of the X-rays absorbed within the epitaxial layer will be only partially detected. The best spectrum which could be obtained was from a 1.8mm^2 device i.e. small enough to reduce capacitance and hence noise, but large enough to give a sensible X-ray detection rate. The measurement was made at -30°C and took five hours due to the small active volume. The applied bias was 1V and the spectrum given in figure 6-17 was recorded shortly before the diode broke down. Attempts to cool the device further, resulted in increased instability and breakdown, and it has not subsequently proved possible to repeat this

measurement. The X-ray source was Am-241 (59.5keV) which was placed behind several thin sheets of molybdenum to give 17.44keV Kα fluorescence, an arrangement which allowed the ratio of 59.5keV and 17.4keV X-ray fluxes to be adjusted by altering the thickness of the molybdenum layer. The 17.44keV fluorescence line can be seen as a peak in the spectrum, but the 59.5keV peek is absent indicating that the depletion region is not sufficiently broad to encompass the charge clouds generated at this energy. Assuming a mean binding energy for K-shell electrons in GaAs, of 10keV, then 17.4keV X-rays generate photoelectrons with an energy of approximately 7keV and 59.5 keV X-rays generate photoelectrons with an energy of approximately 50keV. According to Burke's equation from chapter 5 [Burke E.A., 1977],

$$range \ = \ 0.018(E \ + \ 0.439)^{1.661} \quad \mu m \qquad\qquad (5\text{-}18)$$

which gives ranges of approximately 12μm and 0.5μm for photoelectrons generated by 59.5 and 17.4keV X-rays respectively. That the molybdenum X-rays generate a peak whilst the americium X-rays do not is therefore consistent with a depletion region width of approximately 1 to 4μm.
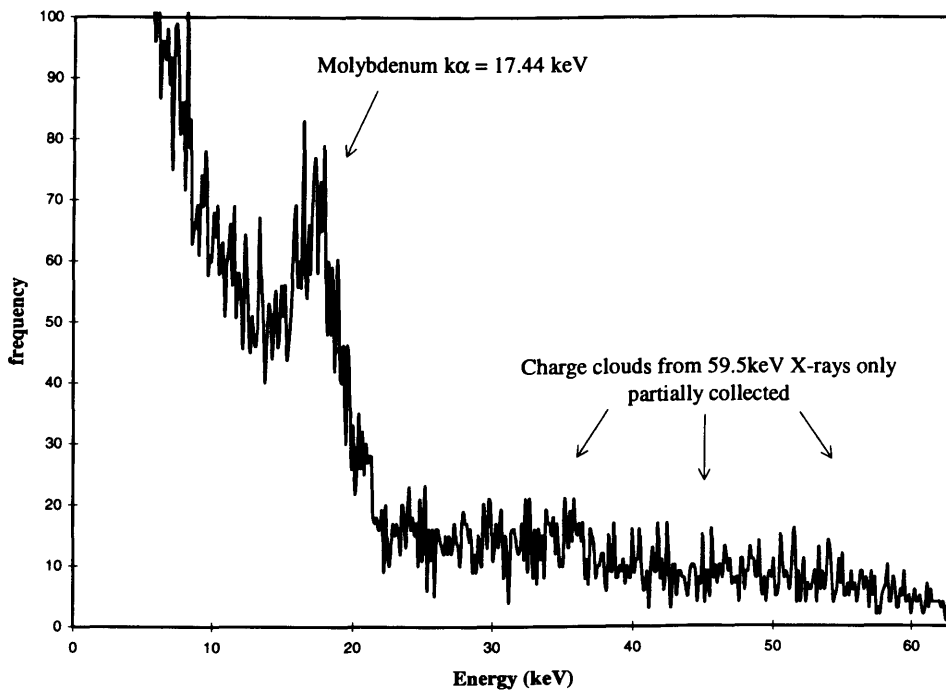
Fig 6-17 Spectrum obtained using 1.8mm^2 epitaxial GaAs device at -30°C.

Another indication of the depletion depth is that the electronic noise given by the FWHM of a pulser peak measured at the same time as the spectrum of figure 6-17, was 3.5keV. Figure 3-9 from chapter 3 combines the equation for a simple parallel plate capacitor with the capacitance/noise specification of the pre-amplifier (both given in chapter 3), to give the approximate electronic noise contribution for a 1.8mm^2 GaAs detector as a function of depletion region width.
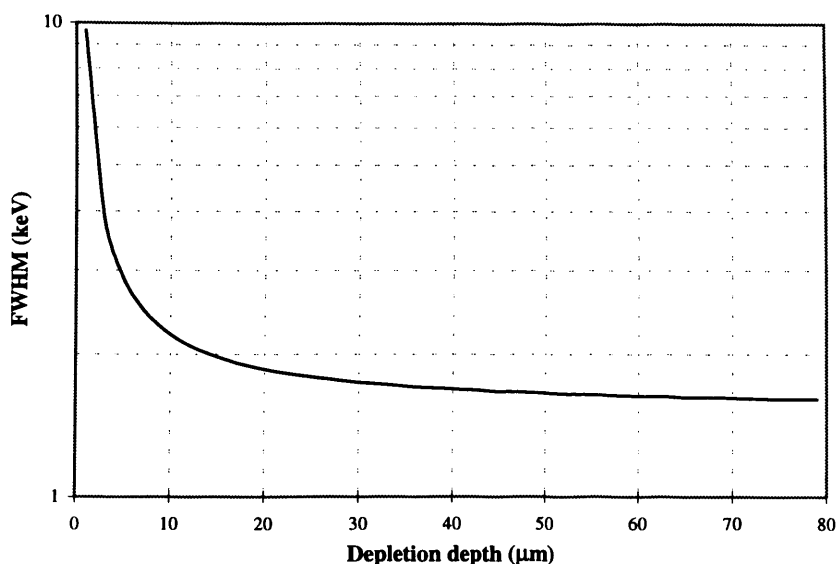
Figure 3-9 Electronic noise for 1.8mm^2 GaAs device with pre amp protection structure (1μs shaping).

These data indicate that the electronic noise contribution of 3.5keV is also consistent with a depletion region width of less than 5μm.

6.5.4 Other analysis

In an attempt to establish whether a chemical impurity had been introduced into the epitaxial material produced during this growth programme which might explain the poor resistivity, junction properties and spectral performance, samples were sent to Craig Buttar at Sheffield University for CV (capacitance voltage) analysis, Dimitri Alexiev at ANSTO for DLTS (deep level transient spectroscopy) analysis and Alison Chew at Loughborough University for GDMS (glow discharge mass spectroscopy) analysis. These methods are discussed in chapter 3 (Experimental Techniques).

The CV and DLTS analysis revealed no detectable deep levels in the band gap, and the GDMS revealed no significant atomic traces other than gallium and arsenic. Dimitri Alexiev did confirm a carrier concentration of approximately 1E16 (n-type) and suggested that the most likely cause for this poor resistivity was oxygen contamination which is a shallow donor. This was not however confirmed by any measurement.

6.6 Conclusions

In the course of this program it has been successfully demonstrated that epitaxial GaAs can be grown to a thickness of more than 100μm in a large scale commercial LPE facility. The purity of the grown layers was shown to improve with prolonged baking of the melt over a period of several months, and

the surface morphology which was dominated by island growth early in the programme, was excellent by the end.

The carrier concentration of the best epitaxial layers grown, was only about $2\times10^{15}cm^{-3}$. Furthermore, diodes fabricated on this material had a breakdown voltage of just ~1V. The reason for this premature breakdown is not clear. The metallization for both the front, Schottky and rear, ohmic contacts was identical to that employed on bulk material, including passivation with silicon nitride to prevent surface currents due to hopping conduction via dangling bonds. Chemical contamination by oxygen is a possibility, although none was revealed by glow discharge mass spectroscopy. Another possible explanation could be a high density of crystalline defects due to the initial growth being too rapid, and examination of early samples with a scanning electron microscope indicated that initial island growth may be hidden in thick epitaxial layers.

7. CONCLUSIONS AND FUTURE WORK

7.1 Conclusions

The work presented in this thesis was initiated in order to assess the characteristics and the potential of GaAs as a suitable semiconductor for the fabrication of X-ray detectors for astronomy. It has been known for some time that many of the electrical properties of bulk GaAs in particular, are determined by the action of energy levels deep within the band gap, although the precise nature of the impurity or defect responsible has been, and still is, a subject of some debate. The X-ray spectra presented here demonstrate, as have others, that the effect of these energy levels is to broaden the spectral peak, with the addition of a low energy tail, by trapping charge carriers and introducing a depth dependence into the charge collection efficiency. This is a characteristic which GaAs has in common with other compound semiconductors such as CdTe.

By means of a Monte-Carlo simulation it is shown in this thesis that the observed spectral peak deformation and incomplete charge collection efficiency may be accurately reproduced by modelling a single electron trap, and a single hole trap. By fitting measured spectra, the trapping is independently quantified for holes and electrons in terms of the product of active trap density and cross section ($\sigma N^{+/-}$). The value of this product required to give the best fit to measured spectra varies as a function of a number of parameters, including temperature. The temperature dependence of carrier trapping is incorporated into the model through thermal velocities, and the predictable variation in 'best fit' values of $\sigma N^{+/-}$ due to the temperature dependence of trap release time, is systematic and does not account for the degree of the variation observed. It is therefore concluded that not all native traps are ionised under reverse bias and that the ionised fraction is not a simple function of temperature. One possible explanation for this is that the depletion region of a reverse biased GaAs diode contains a quasi-neutral region as proposed by McGregor [McGregor, D.S., 1994] in which, at a limiting value of electric field, an equilibrium is achieved between carrier release and carrier capture. The ionised fraction of trap energy levels in this dynamic situation would be a complex function of temperature and applied bias.

Another consequence of a limiting electric field and quasi neutral region is that the active width of a GaAs diode will increase linearly with applied bias, rather than as $V^{1/2}$. Proton measurements given in chapter four demonstrate that this is indeed the case.

Although the precise nature of the dominant native defect in GaAs material has been the subject of much debate for many years, it is known to have one or more associated donor energy levels close to the centre of the band-gap. Values ranging between Ec-0.73eV and Ec-0.87eV [Cho, H.Y., 1989, Nava, F., 1994, Masselink, W.T., 1988] have been widely quoted. Since this places the trap(s) just below the mid band Fermi energy level, their fractional occupancy under equilibrium conditions will be between 0.5 and 1 depending upon temperature. As calculated in chapter four, the time constant associated with the release of electrons from this energy range is of the order of seconds or less at temperatures down to approximately -60°C. Hence upon application of reverse bias close to room temperature, the upward band bending lifts the trap energy level(s) well above the n quasi Fermi-level causing all of the traps to empty (ionise) with a time constant equal to the trap release time constant, and become active. If however, before the application of bias, the device is cooled to a temperature well below -80°C, where the trap release time constant is days or weeks, then not only does the trap occupancy increase to a value close to unity, but upon application of bias, the traps do not empty, but are left full and inactive. The effect of doing this is shown in chapter four to be a dramatic reduction in the effects of charge trapping, with a best measured spectral resolution of 2.4keV FWHM at 59.5keV, close to the limit imposed by the electronic noise contribution.

Once this condition of trap inactivity is established, the applied bias may be increased to far higher values before the onset of breakdown. An 80μm device with a room temperature breakdown voltage of 130V can be operated at up to 350V if first cooled to -100°C. This indicates that the active region width dependency on reverse bias may have reverted to a $V^{1/2}$ relationship in the absence of space charge due to ionised traps. The application of this technique is not simple however, since devices cooled and biased in this way exhibit a tendency to breakdown unpredictably and revert to behaviour analogous to room temperature operation. This is possibly due to an avalanche of impact ionisation triggered by slightly high leakage current, which empties a large fraction of the EL2 levels and re-establishes the quasi-neutral state described above.

In chapter four, by carefully operating a detector at temperatures where the release time constant of the most dominant trap is of the order of hours, and measuring the reduction in modal charge collection efficiency (proportional to active trap density) over a rather longer period, the trap release time constant was determined. Repeating this at several temperatures, the activation energy of the trap has been calculated. This was shown to give an activation energy for the dominant donor level associated with electron capture, of 0.73eV. It is widely believed today that the EL2 centre is a complex, rather than an isolated defect, probably including a Ga_{As} anti-site and a gallium vacancy [Chadi, D.J., 1989]. Several deep donor energy levels are associated with this trap, but one of the

shallowest, and hence most readily ionised lies 0.73eV below the conduction band edge [Cho, Y.H., 1988].

To measure the activation energy of the dominant hole trap, the Monte-Carlo model developed in chapter five, was used to fit spectra acquired at different amplifier shaping times. Again, by repeating at several temperatures, this gives an activation energy for the dominant hole trap of 0.2eV. It has been demonstrated [Elliot, K.R., 1982, Figielski, T., 1984] that the EL2 deep donor level is generally accompanied by a deep acceptor at $\sim E_v + 0.2eV$. This is probably associated with the Ga_{As} anti-site [Chadi, D.J., 1989, McGregor, D.S., 1984]. It is therefore concluded that the crystalline defect EL2 with a dominant deep donor at Ec-0.73eV and a dominant deep acceptor at Ev+0.2eV is responsible for the charge loss observed in X-ray spectra.

The epitaxial growth program conducted in conjunction with EEV Ltd. demonstrated the feasibility of growing thick epitaxial layers in a large scale commercial facility. The resulting devices could not be operated as detectors however, since the application of ~1V reverse bias induced breakdown. Deep Level Transient Spectroscopy and Glow Discharge Mass Spectroscopy revealed no significant chemical impurities and the cause of the failure is therefore most likely to be a high density of crystalline defects. Early evidence indicated a strong tendency towards initial island growth under conditions of rapid deposition. This large scale liquid phase growth technique therefore does not currently offer a cost effective means of producing detectors.

7.2 Future work

Future modelling work is required to combine the Monte-Carlo simulation of GaAs spectral response presented in this work with the electric field model proposed by McGregor et. al., which should help to confirm the validity of both, and lead to a more complete understanding of field dependent carrier capture. Effort should be directed towards the production of semi-insulating, intrinsic (not compensated) GaAs with a drastically reduced density of crystalline point defects (EL2). Only then may the full potential of GaAs for high resolution, room temperature detection of 'hard' X-rays be realised.

The liquid phase epitaxial dipping facility at EEV Ltd is no longer available, and the large scale approach did not in any case yield useful material. It has been demonstrated in the past however, that epitaxial GaAs can be produced of a sufficient purity to fabricate devices with near intrinsic properties and it is therefore hoped that other growth techniques, such as the Metal Oxide Chemical Vapour Deposition now used for solar cell layers, may provide a new source for a future study.

Although the potential of GaAs for X-ray detector applications is good, and improvements in the purity of bulk material have been achieved in recent years (driven by the electronics industry), the density of native crystalline defects is still so high as to hamper effective room temperature operation. Similarly, epitaxial material of sufficient purity is still extremely difficult (and expensive) to grow. Nevertheless, the methods developed and the experience gained through this work have much broader application. A study of cadmium telluride and cadmium zinc telluride by the X-ray Astronomy Group at Leicester University is to begin this year. The scope of the Monte Carlo simulation is being expanded to other high Z materials and new sources of higher purity GaAs are being investigated (e.g. MOCVD solar cell manufacture).

Some more thought must be given to the long term objectives of a GaAs imaging detector development programme. A working detector array of GaAs produced by molecular beam epitaxy was achieved this year [Bertuccio, G., 1997] and one may envisage a Charge Couple Device (CCD) fabricated on material of sufficient purity, however the carrier lifetime even in trap free GaAs is limited to about 0.1ms because of direct band to band recombination. This clearly prevents the storage of charge as in a conventional silicon CCD, and in designing even a simple array it is clearly necessary to extract the charge from the individual GaAs diodes in a time which is short compared with the carrier lifetime. One relatively simple way in which this might be achieved is to bump bond or flip chip bond an array of GaAs diodes to an array of silicon CMOS amplifiers. The PAC5 chip developed by Rutherford Appleton Laboratories (RAL) would be appropriate for this application. It is an array of 16x16 pre-amplifiers designed specifically for bump bonding to a detector array, and each pre-amplifier has a noise performance of 20 electrons rms when connected to a 250fF detector. This amplifier is being developed as part of the Energy Resolving Detector 1 (ERD1) project, which is funded through 'Impact', a 'Technology Foresight' initiative to pursue the development of large area CCD and pixel array detectors. Leicester University is a member of the 'Impact' consortium and will look at the development of GaAs, CdTe or CZT detector arrays for astronomical applications.

8. BIBLIOGRAPHY

Adesida, I., Shimuzu, R., and Everhart, T.E., J. Appl. Phys. 51 (1980) 5962

Alexiev, D., Butcher, K.S.A., "High purity liquid phase epitaxial gallium arsenide nuclear radiation detector", Nuclear Instruments and Methods in Physics Research A317 (1992) 111-115.

Allen L.C., "Interpolation Scheme for Energy Bands in Solids", Phys. Rev. **98**, 993 (1955).

Armantrout, G.A., Swierkowski, S.P., Sherohman, J.W. and Yee, J.H., IEEE Trans. Nucl. Sci. NS-24 (1977) 121.

Austin, R.A., and Ramsey, B.D., Opt.Eng. 32 (1993) 1990

Austin, R.A., Minamitani T. and Ramsey, B.D., Proc. SPIE 2010 (1993) 118

Bar-Lev, A., "Semiconductors and Electronic Devices 2nd edition", Prentice Hall International (1984), **ISBN 0-13-806265-X.**

Bauser, E., et al., Proc 3rd Int. Workshop on GaAs and related compounds (1995) 10-16.

Bauser, E., et al., Nucl. Inst. And Meth. RD8 A322 (1992) 493.

Beaumont, S.P. et. al., Nuclear Instruments and Methods, A321 (1992^2) 172-179.

Beaumont, S.P. et. al., Nuclear Instruments and Methods, A322 (1992^1) 472-482.

Beaumont, S.P. et. al., IEEE Trans. Nucl. Sci. , 40 (1993^1) 1225-1230.

Beaumont, S.P. et. al., Nuclear Instruments and Methods, A326 (1993^2) 313-318.

Bencivelli, W. et al., "Electrical characterization and detector performances of a LPE GaAs detector for X-ray digital radiography", NIM in Phys. Res. A, 346 (1994) 372-378

Bencivelli, W. et al., NIM in Phys. Res. A, 355 (1995) 425-427.

Bertin, R, et. al., Nucl. Inst. And Meth. In Phys. Res A294 (1990) 211-218.

Bertolini, G. and Coche, A., (eds), "Semiconductor Detectors", Elsevier-North Holland, Amsterdam, 1968.

Bertuccio, G., et. al., IEEE Trans. On Nucl. Sci. vol 44, no 1 (1997)

Berwick, K. et al., "Imaging of High Field Regions in SI GaAs Under Bias", Centre for Electronic Materials, UMIST, Manchester, UK, (1993).

Blakemore, J.S., "Semiconducting and other major properties of gallium arsenide", J. Appl. Phys. 53(10), October 1982.

Bourgoin, J.C., von Bardeleben, H.J. and Stievenard, D., J. Appl. Phys. 64 (1988) R65.

Brozel, M.R., "Defect Densities in SI GaAs", from "Properties of GaAs 2nd Ed.", INSPEC Data reviews Series no2. (1990)

Burke E.A., IEEE Trans.Nucl.Sci. NS-24 (1977) 2505.

Buschhorn, G. et al., "X-ray polarimetry using the photoeffect in a CCD-detector", Nuclear Instruments and Methods in Physics Research A, (1993).

Buschhorn, G., and fifteen co-authors, Nucl. Inst. Meth. A346 (1994) 578

Casey, H.C. et al., "Heterostructure Lasers Part B: Materials and Operating Characteristics", Academic Press, **ISBN 0-12-163102-8.**

Cengiz, A., and Ozmutlu, C., Nucl. Inst. Meth. B84 (1994) 310

Chadi, D.J. and Zhang, S.B., "Vacancy complexes in GaAs: Effects on impurity compensation", Physical Review B, Vol. 41, no.8 (1990) 5444-5446

Cho., Hoon Young et. al., Journal of the Korean Physical society, Vol. 22, No. 1, March, (1989)

Cross, T.A., Burrage, J., Hardingham, C.M., Ginige, R., "Further development of GaAs solar cells for application in space phase B", EEV report no. 45/66-7 (1991).

Crowell, C.R., Sarace, J.C., Sze, S.M., "Tungsten-Semiconductor Schottky-barrier Diodes" Trans. Met. Soc. AIME, **233,** 478 (1965).

DiLorenzo J.V. and Khandelwal, D.D., "GaAs FET Principles and Technology (Artech House, Dedham, (1982).

Dolan, J.F., Astron.J. 70 (1965) 137

Eberhardt, J.E., Ryan, R.D., Tavendale, A.J., "Evaluation of Epitaxial n-GaAs for Nuclear Radiation Detection", Nuclear Instruments and Methods 94 (1971) 463-476.

Eisberg, R. and Resnick, R., "Quantum Physics of Atoms, Molecules, Solids, Nuclei and Particles 2nd edition", Wiley (1985), **ISBN 0-471-87373-X.**

Elliot, K.R., Holmes, D.E., Chen, R.T. and Kirkpatrick, C.G., Appl. Phys. Lett. 40 (1982) 898.

Figielski, T., Appl. Phys. A 35 (1984) 255.

Fitting, H.J., Glaefeke, H. and Wild, W., Phys. Status Solidi 43 (1977) 185

Fraser, G.W., "X-ray Detectors in Astronomy", Cambridge Astrophysics Series, Cambridge University Press, **ISBN 0 521 32663 X,** (1989[1]).

Fraser, G.W. et al., "Hard X-ray Telescope (HXT)", A proposal for the ESA M3 mission opportunity, X-ray Astronomy Group, Leicester University, UK, (1993).

Fraser, G.W., Lees J.E., and Pearson, J.F., Nucl.Instr.Meth. A 2X4 (1989[2]) 483

Fraser, G.W., Proc. SPIE 1140 (1989) 50

Fraser, G.W., Brunton, A.N., Lees, J.E., Pearson, J.F., Willingale, R., Emberson, D.L., Feller, W.B., Stedman M. and Haycocks, J., Proc. SPIE 2011 (1993) 215

Fraser, G.W., Abbey, A.F., Holland, A.D., McCarthy, K.J., Owens, A. and Wells, A., "The X-ray energy response of silicon :(A) Theory", Nucl. Inst. Meth A 350 (1994) 368-378.

Giacconi, R., Gursky, H., Paolini, F.R. and Rossi, B., Phys. Rev. Lett. 9 (1962) 439

Gibbons, P.E., Howes, J.H., IEEE Trans. Nucl. Sci., NS-19 (1972) 353.

Goodman, A.M., "Metal-Semiconductor Barrier Height Measurement by the Differential Capacitance Method - One Carrier System", J. Appl. Phys., **34**, 329 (1963).

Guggenheim, E.A., "Thermodynamics", 5th ed. North Holland Publ., Amsterdam, 1967.

Haegel, N.M., and Derhacobian, N., Physical Review B, Vol. 44, no. 23 (1991), 12754-12760

Hall, R.N., Proc. IEE. 106B (Sup. 17), (1959), 923.

Hart, M., Nucl.Instr.Meth. A316 (1992) 416

Hill, J.E., Holland, A.D., Turner, M.J.L.T., "Preliminary polarisation measurements using small pixel CCDs", to be submitted to N.I.M.

Hill, J.E., Holland, A.D., Castelli, C.M.C., Short, A.D.T., Turner, M.J.L., Burt, D., 'Measurement of X-ray Polarisation with Small Pixel CCDs', Proc. SPIE 1997 (in press)

Holland, A.D., Short, A.D.T, Fraser, G.W., Turner, M.J.L., "The X-ray Polarisation Sensitivity of CCDs", Nuclear Instruments and Methods in Physics Research A 355 (1995) 526-531.

Holland, A.D., Lumb, D.H. and Castelli, C.M., Proc. SPIE 1159 (1989) 113~

Holland, A.D., Turner, M.J.L., Wells, A. and Burt, D.J., ESA Publications, SP-356 (1992) 321

Ilegems, M., Panish, M.B. and Arthur, J.R., J. Chem. Thermodyn. 6, 157 (1974)

Jones, B.K., Santana, J., Sloan, T. and Zdansky, K., "Relaxation Semiconductor Devices", Proc. 3rd International workshop on GaAs and related compounds (1995) 73-77

Kaaret, P., and twenty-five co-authors, Proc. SPIE 1548 (1991) 106

Knoll, G.F., "Radiation Detection and Measurement 2nd Ed.", John Wiley and Sons, Inc. (1989), ISBN 0-471-61761-X.

Kobayaski, T. et al., IEEE Trans. Nucl. Sci., NS-19 (1972) 324.

Kobayaski, T. and Sugita, T., Nucl. Inst. And Meth. 98, 179 (1972)

Kobayaski, T. et al., IEEE Trans. Nucl. Sci., NS-23(1), 97 (1976)

Kubaschewski, O., Evans, E.LL. and Alcock, C.B., "Metallurgical Thermochemistry", p. 392, Pergamon, Oxford (1967).

Landecker, P.B., IEEE Trans. Nucl. Sci. NS-19 (1972) 463

Lang, D.V., J. Appl. Phys. 45 (1974) 3023

Lund, J.C., James, R.B., McGregor, D.S. and Olsen, R.W., Proc. 9th International Workshop on Room Temperature Semiconductor detectors, Grenoble (1995)

Look, D.C., "Electrical Characterisation of GaAs Materials and Devices", (Wiley, New York, 1989)

Lumb D.H., "X-ray Imaging and Spectroscopy with Silicon CCDs", PhD thesis, University of Leicester (1988)

Makishima, K. et. al. (editors), "Beyond the milky way with ASCA GIS", Conf. Proc. (1996)

Masselink, W.T., Brasiau, N., LaTulipe, D., Wang, W.I. and Wright, S.L., Inst. Phys. Conf. Ser. No. 91, 665 (1988).

Matsumoto, C., Takahashi, T., Takizawa, K., Ohno, R., Ozaki, T. and Mori, K., "Performance of new CdTe detector for hard X-ray spectroscopy", Proc. IEEE. (1997) (in press).

McCarthy, K.J. and Wells, A., Proc SPIE 1743 (1992) 211

McGregor, D.S., Knoll, G.F., Eisen, Y. and Brake, R., IEEE, Trans. Nucl. Sci. NS-39 (1992) 1226.

McGregor, D.S., Rojeski, R.A., Knoll, G.F., Terry, F.L., East, J. and Eisen, Y., Nucl. Inst. And Meth. In Phys. Res. A 343 (1994) 527-538

McKelvey, J.P., "Solid State and Semiconductor Physics", Kreiger, Malabar, 1986.

Miller, B.I., Pinkas, E., Hayashi, I. and Capik, R.J., J. Appl. Phys. 43, 2817 (1972).

Miller, G.L., Lang, D.V., and Kimerling, L.C., Ann. Rev. Mater. Sci. 7:377 (1977)

Nava, F. et. al., "Influence of electron traps on charge collection efficiency in GaAs radiation detectors", NIM A, 349 (1994) 156-159

Novick, R., Weisskopf, M.C., Berthelsdorf, R., Linke R. and Wolff, R.S., Astrophys.J. 174 (1972) Ll

Palms, J.M., Rao, P.V., Wood, R.E., Nucl. Inst. And Meth., 76, 59, (1969)

Panish, M.B. and Ilegems, M., "Progress in Solid State Chemistry", Vol 7, p39, Pergamon, New York, 1972.

Pantelides, S.T., "Deep Centres in Semiconductors", 2nd ed. (Gordon and Breach, New York 1992)

Peacock, A., Taylor, B.G., Ellwood, J., Adv. In Space Research, 10-2, (1990), 273-285.

Pelfer, P.G., Ludwig, J., Runge, K., Rupprecht, H.S. (ed), Proc 3rd Int. Workshop on GaAs and related compounds (1995).

Peters, R.C., "Gallium Arsenide Related Compounds: 1972 Symp. Proc.", p. 55, Inst. of Phys., London (1973)

Phillips J.C., "Energy-Band Interpolation Scheme Based on a Pseudopotential", Phys. Rev., 112, 685 (1958).

Pounds, K.A., Nadra, K., Stewart, G.C., George, I.M. and Fabian, A.C., Nature 344, (1990), 132.

Prinz, V.Ya. and Bobylev, B.A., Sov. Phys. Semicond. 14 (1980) 1097.

Prinz, V.Ya. and Rechkunov, S.N., Phys. Status. Solidi. B 118 (1983) 159.

Ramsey, B.D., Austin, R.A. and Decher, R., "Instrumentation for X-ray Astronomy", Space Science Reviews 69, 139-204, (1994).

Sakurai, H., Noma, M. and Niizeki, M. Proc. SPIE 1343 (1990) 512

Shimuzu, R. and Ichimura, S., Surface Science 133 (1983) 250

Short, A.D.T., Holland, A.D., 'Measurement and modelling of the X-ray spectral response of bulk GaAs detectors', SPIE Vol 2808 (1996) 583-594.

Shur, M., "GaAs Devices and Circuits" (Plenum, New York, 1987).

Smith R.A., "Semiconductors", 2nd ed., Cambridge University Press, London, (1979).

Sumner, T.J., et. al., Nucl. Inst. In Phys. Res A322 (1992) 514-517.

Swierkowski, S.P. and Armantrout, G.A., IEEE Trans. Nucl. Sci. NS-22 (1975) 205.

Sze S.M., "Physics of Semiconductor Devices", 2nd ed., John Wiley & Sons, Inc., ISBN 0-471-09837-X, (1981).

Trumper, J., "Rontgen Satellite", Observatories in Earth Orbit and Beyond, Y. Kondo (ed.), Kluwer Academic Publishers (1990), 61-62.

Tsunemi, H., Hayashida, K., Tamura, K., Nomoto, S., Wada, M., Hirano A., and Miyata, E., Nucl. Instr. Meth. A321 (1992) 629

Tsunemi, H., Hayashida K., and Tamura, K., Proc. SPIE 2010 (1993) 201

Tung, C.J., Ashley, J.C., and Ritchie, R.H., Surface Science 81 (1979) 427

Turner, M.J.L. and Watson, M.G., (editors) "The next generation of X-ray Observatories", Special Report XRA97/02 (1997)

Weisskopf, M.C., "Astronomy and astrophysics with the Advanced X-ray Astrophysics Facility", Space Science Reviews, **47**, (1988), pp. 47-49.

Weisskopf, M.C., Silver, E.H., Kestenbaum, H.L., Long K.S., and Novick, R., Astrophys.J. 220 (1978) L117

Willardson, R.K. and Beer, A.C., "Semiconductors and Semimetals, vol. 20 (Academic Press, Orlando, 1984)

Ziegler, J.F. and Biersack, J.P., 'The Stopping and Range of Ions in Solids', Pergamon Press, New York (1985), **ISBN-0-08-021603-X**

Zulliger, H.R., Aitken, D.W., IEEE Trans. Nucl. Sci. NS-17(3) 187 (1970)

APPENDIX A - MODELLING A SMALL PIXEL CCD X-RAY POLARIMETER

The regular array of pixels in a silicon Charge Coupled Device (CCD) may be used to measure photoelectron emission directions following the absorption of high energy X-rays (E >15 keV). Since this direction lies within a distribution about the electric field vector of the incident photon, CCDs offer the possibility of combining X-ray imaging and spectroscopy with measurement of the linear polarisation of the incident beam. For this reason, a small pixel CCD was incorporated into the proposed Hard X-ray Telescope and a model of electron transport in CCDs was developed which leads to an estimate of the energy-dependent modulation factor M(E), the parameter determining polarisation sensitivity. The predictions of the model are in good agreement with published measurements. The sensitivity of an optimised CCD "pixel polarimeter" for cosmic X-ray astronomy is assessed.

A.1 Introduction

The linear polarisation of cosmic X-ray sources has long been recognised as an important diagnostic of source geometry and magnetic field strength [Dolan, J.F., 1965]. Two decades after the deployment of the first Bragg crystal Thomson scattering polarimeters on a sounding rocket platform [Novick, R., 1972], the Crab Nebula remains however, the only cosmic source for which a definitive measurement has been made (P =19.2% at 2.6 keV [Weisskopf, E.H., 1978]). While the Stellar X-ray Polarimeter (SXRP) [Kaaret, P., 1991] on the Spectrum X-Gamma satellite should extend this observational range to ~20 of the brighter galactic sources, the search for new analyser techniques of high sensitivity remains a priority [Fraser, G.W., 1989(1), Hart, M., 1992].

A number of authors (e.g. Austin et al. [Austin, R.A., 1993(1+2)], using an optical imaging chamber) have attempted to make use of the spatial correlation between incident electric vector and photoelectron ejection direction to construct gas counters with linear polarisation sensitivity in the hard X-ray (40-60 keV) band. Recently, there has been considerable interest in using the same physical principle in a solid state detection medium - recovering polarisation information from spread pixel events in silicon Charge Coupled Devices (CCDs) (see figure A-1.).

The first account of a solid state "pixel polarimeter" in the literature [Fraser, G.W., 1989(2)] was followed by the 15-37 keV measurements of Tsunemi et al. [Tsunemi, H., 1992 + 1993] using commercial 12x12 μm pixel CCDs. More recently, Buschhorn et al. [Buschhorn, G., 1994] have

reported the successful use of a 6.8x6.8 μm pixel CCD polarimeter with both synchrotron and planar channelling radiation. The CCD polarimeter is a highly attractive concept, in that X-ray polarisation, position and energy estimates are all delivered on a photon-by-photon basis.

A.2 Modelling the Polarimetric Properties of CCDs

A.2.1 Estimation of the Energy Threshold E_{th}
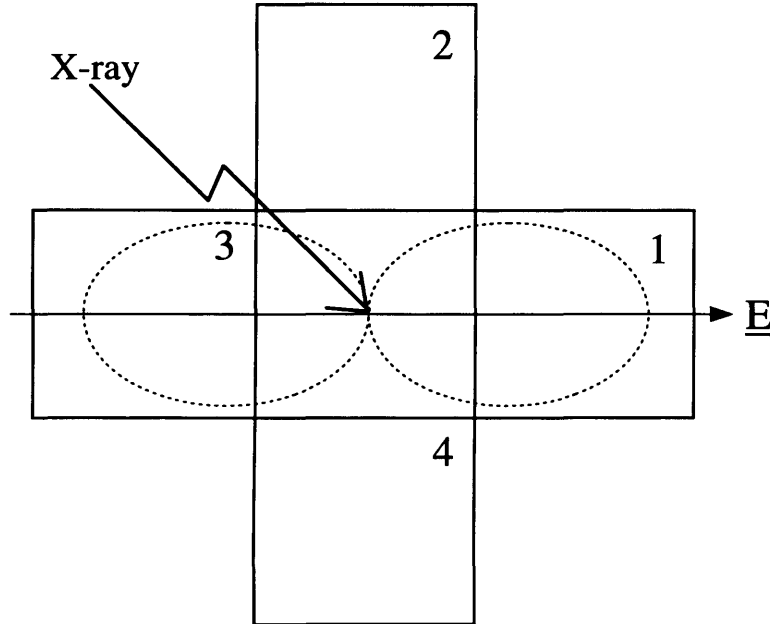
Figure A-1 Operating principle of a CCD pixel polarimeter. Because of the anisotropic distribution of photoelectron emission directions (dashed line) and the finite range of the photoelectron, an excess of events is expected with charge spread between the central pixel and pixels 1 or 3, which lie aligned with the X-ray electric vector.

For a pixellated detector to be capable of polarisation sensitivity, the photoelectron must be capable of crossing adjacent pixel boundaries to create a characteristic "split" event (see figure A-1). For a given pixel size, we may estimate an approximate minimum operating energy, E_{th}, by means of the equation;

$$R(E_{th} - E_b) \geq \frac{l}{4}$$ (A-1)

where R is the electron range, l is the pixel dimension and E_b is the K-shell binding energy of the absorber (E_b=1.839keV in silicon). In silicon, the range, R, of an electron of energy E_e may be approximated by;

$$R(E_e) = \left(\frac{E_e}{10}\right)^{1.75}$$ (A-2)

where E_e is in keV and R is in microns [Tsunemi, H., 1992]. Thus the ranges for 10keV and 30keV electrons in silicon are $\approx$1μm and 6.8μm respectively. Combining equations A-1 & A-2 we obtain E_{th}=20.6, 15.4 and 11.8 keV for 12, 6.8 and 4μm square pixels, respectively, indicating immediately that silicon CCD polarimeters are unlikely ever to be compatible with conventional X-ray telescopes whose bandpass is typically limited to <10keV. The use of CCD polarimeters in X-ray Astronomy will therefore require the parallel development of novel hard X-ray optics [Fraser, G.W., 1993].

Silicon detectors have relatively poor detection efficiency at hard X-ray energies which may be improved through the use of detection materials of higher atomic number. However, from the Bethe-Bloch formula, electron range decreases in proportion to the square of the atomic number of the detector material, while E_b is an increasing function of Z (1.839 keV for Si (Z=14); 11.10 keV for Ge (Z=32); 10.37 keV and 11.87 keV for GaAs (Z=31,33)). Thus a detector fabricated on, for example, GaAs or Ge would require a 2-3μm pixel size in order to possess the same magnitude of polarisation sensitivity as a silicon CCD with 6-12μm pixels. We are therefore constrained to the use of silicon, since the fabrication of such small pixels on exotic materials is impractical at present.

A.2.2 Monte Carlo Model

The model simulates the photoelectric absorption of an X-ray in the central pixel of a five by five pixel array, allowing charge splitting between pixels to be investigated in detail. The CCD depletion depth, dead layer, field free depth, substrate thickness, pixel size and the X-ray energy can all be varied. The CCD lies in the xy plane and the test beam is assumed 100% linearly polarised with the E-vector parallel to the x-axis.

The point at which the X-ray is absorbed within the central pixel is linearly randomised in x,y and z (at energies $E \geq 10$ keV, the X-ray absorption length in silicon is large compared to any realistic depletion depth, so that a uniform probability of absorption over the device thickness is a very good approximation). We further assume that photoelectric absorption dominates over the Compton effect (true in silicon for E<60keV) and that the energy associated with Auger electrons is negligible, since $E>>E_b$.

The initial photoelectron direction is then randomised from a distribution $\sin^2\psi\cos^2\theta$, where ψ is the angle between the incident photon and the ejected photoelectron, and θ is the angle between the electron and E. The initial photoelectron energy is given by $E_e = (E - E_b)$. At the energies of interest here, relativistic effects [Austin, R.A., 1993(1)] are negligible.

It is not simply the range of the photoelectron, but its actual path and hence the locus of secondary electron creation sites that determines a CCD's ability to measure polarisation. A Monte Carlo model of electron-hole pair creation by X-rays in silicon [Fraser, G.W., 1994] has been published recently. For the present analysis, we have represented the individual inelastic processes (valence and core-level ionisation, plasmon and phonon interactions [Fraser, G.W., 1994]) by a collective mean free path λ_{inel} and characteristic energy loss per collision derived from the inverse mean free path and stopping power curves of Tung et al [Tung, C.J., 1979] (see Table A-1). Our treatment of elastic scattering of electrons by silicon is based on that of Cengiz and Ozmutlu [Cengiz, A., 1994].

TABLE A-1. Values for elastic and inelastic scattering mean free paths and inelastic scattering energy loss as a function of electron energy, Ee.

Ee (eV)	100	200	500	1000	2000	5000	10000	20000	50000
ΔE_e (eV)	23	30	29	41	45	49	50	60	64
λ_{inel} (Å)	4	7	11	20	33	70	125	250	500
λ_{el} (Å)	1	2	5	10	20	48	95	190	475

The total elastic scattering mean free path $\lambda_{el}(E_e)$ derived from the screened Rutherford formula (equation 3 of ref. [Cengiz, A., 1994]) with an atomic screening factor, β, scaled by the factor 0.48 in accordance with the results of Adesida et al [Adesida, I., 1980], is tabulated in Table A-1.

Knowing the electron's position, direction and energy after the ith collision, the total mean free path (E_e) is given by

$$\frac{1}{\lambda_t} = \frac{1}{\lambda_e} + \frac{1}{\lambda_{inel}} \tag{A-3}$$

The actual path length, S to the next collision is then given by;

$$S = -\lambda_t \ln(R_1) \tag{A-4}$$

where R_1 is a uniform random number between 0 and 1. Another uniform random number (R_2) is used to determine whether the interaction is elastic or inelastic. If $R_2 < \lambda_t/\lambda_{el}$ then the interaction is elastic, otherwise it is inelastic. The azimuthal scattering angle is independent of the collision type, i.e.

$$\phi = 2\pi R_3 \tag{A-5}$$

where R_3 is a third random number on the interval 0 to 1. If the collision is inelastic then the polar scattering angle is given by [Shimuzu, R., 1983];

$$\sin \theta = \sqrt{\frac{\Delta E_e}{E_e}} \tag{A-6}$$

and at this point the interaction position and the energy deposited in silicon (ΔE_e) are sent to the charge collection sub-routine. If the collision is elastic, however, then the polar scattering angle is given by

$$\cos \theta = \frac{1 + \beta - R_4(1 + 2\beta)}{1 + \beta - R_4}$$

(A-7)

where R_4 is a final, uniform random number and β is the modified screening factor, given, for silicon, by [Cengiz, A., 1994, Adesida, I., 1980]:

$$\beta = \frac{15.14}{E_e}$$

(A-8)

where E_e is in eV. Note that Equation A-7 differs from the version given by Cengiz and Ozmutlu (equation 23 of ref. [Cengiz, A., 1994]), which is not bounded by plus and minus one.

The new energy after the $(i+1)^{th}$ collision, if inelastic, is $(E_e-\Delta E_e)$. These steps are repeated, with full tracking of the electron position within the pixel array, until all of the photoelectron's energy has been deposited. The inclusion of elastic scattering allows for the possibility of large angle deflections. The number of X-rays simulated for a given energy and pixel geometry is 10^5.

A complete description of the CCD charge diffusion and collection model is given in ref. [McCarthy, K.J., 1992]. Only the basic steps are described here. The initial 1σ radius of the secondary electron cloud produced by each inelastic collision (i.e. $n_s = \Delta E_e/\omega$ electrons where $\omega = 3.65\text{eV}$ [Fraser, G.W., 1994]) is taken from [Fitting, H.J., 1977]:

$$r_i = 44E_e^{1.75} \quad \text{Å}$$

(A-9)

This extent is modified by the subsequent spreading of the charge cloud as it is collected. The contribution to the charge cloud radius due to spreading in the depletion region, rd, is given by

$$r_d = \sqrt{\frac{2kT\varepsilon_s}{e^2 N_a} \ln\left(\frac{x_d}{x_d - x}\right)}$$

(A-10)

where x is the interaction depth, x_d the depletion layer depth, N_a the silicon doping concentration, ε_s the silicon permittivity and T the temperature. The contribution to the charge cloud radius due to spreading in the field free region, r_{ff}, is;

$$r_{ff} = \frac{x_{ff}}{2} \sqrt{1 - \left(\frac{x}{x_{ff}}\right)^2}$$

(A-11)

where x_{ff} is the depth of the field free region and x is the interaction depth into the field free region. The contribution to the charge cloud radius due to spreading in the substrate, r_s, is approximately:

$$r_s \approx \frac{L}{2.2} \sqrt{1 - \left(\frac{x}{L}\right)^2} \qquad \text{(A-12)}$$

where $L \approx 5\mu m$ is the diffusion length. The total 1σ radius of the charge cloud on reaching the electrode structure is then given by the quadrature summation of the relevant radii;

$$r = \sqrt{r_i^2 + r_d^2 + r_{ff}^2 + r_s^2} \qquad \text{(A-13)}$$

By adding the small charge clouds generated by each inelastic collision together, the fraction of the total charge from the X-ray event which ends up being collected from each pixel of the test array may be determined. By setting a pixel energy threshold to discriminate signal from noise, as in a real CCD, the X-ray event may be characterised as an event occurring in one, two or three pixels in x or y. For this work, only events which were linearly split between 2 or 3 pixels were counted as polarisation detections, while in the work of ref. [Buschhorn, G., 1994], more complex event morphologies were considered.

If N_x and N_y are the calculated numbers of x- and y-spread events respectively, then the modulation factor [Fraser, G.W., 1989(1)] of the CCD pixel polarimeter is readily seen to be:

$$M = \frac{N_x - N_y}{N_x + N_y} \qquad \text{(A-14)}$$

Previously, Tsunemi et al [Tsunemi, H., 1992 + 1993] have reported measured values of a figure of merit which they refer to as the polarimetric amplitude, here denoted A(E). In fact,

$$A = \frac{1}{2} PM \qquad \text{(A-15)}$$

where P is the degree of linear polarisation of the experimental beam. Buschhorn et al [Buschhorn, G., 1994] have experimentally determined a parameter ("the asymmetry") which is exactly of the theoretical form given in equation A-15. Experimentally, however, this asymmetry must be evaluated from measurements at two orthogonal polarimetric azimuths in order to eliminate the non-zero instrumental polarisation exhibited by any real CCD. That is, $M \neq 0$ for a real CCD illuminated by un-polarised X-rays, because of the intrinsic asymmetry of the device structure - in one direction the pixel is bounded by the fields generated by the implantation and the other, by fields generated by overlying electrodes.

A.3 Results

Table A-2 summarises the results of the model for 15 and 40keV X-rays, giving (i) the typical number of scatter steps for the photoelectron, (ii) the typical distances travelled parallel and perpendicular to the direction of the electric vector and (iii) values of M for three different square pixel sizes.

TABLE A-2. Summary of typical output from the model

X-ray Energy	Steps	Electron travel (μm)		M (%)		
(keV)	(typical no.)	Parallel	Perpendicular	12μm pixel	6.8μm pixel	4μm pixel
15	300	1.2	0.05	2.4	7	9
40	700	5	0.5	12	24	34

Figure A-2 compares measured [Tsunemi, H., 1992 + 1993] and calculated values of A(E) for a device with 12μm pixels. A 20μm thick epitaxial layer and a 3μm thick depletion layer were assumed in the calculations (refs. [Tsunemi, H., 1992 + 1993] state that "the depletion of the chip is about a few microns"). The polarisation fraction assumed in figure A-2 was 60%, at the lower end of the 60-75% range estimated experimentally [Tsunemi, H., 1992 + 1993]. Figure A-2 shows good agreement between model and measurements, with the curve for the "perfect" CCD lying above the results for the real device.
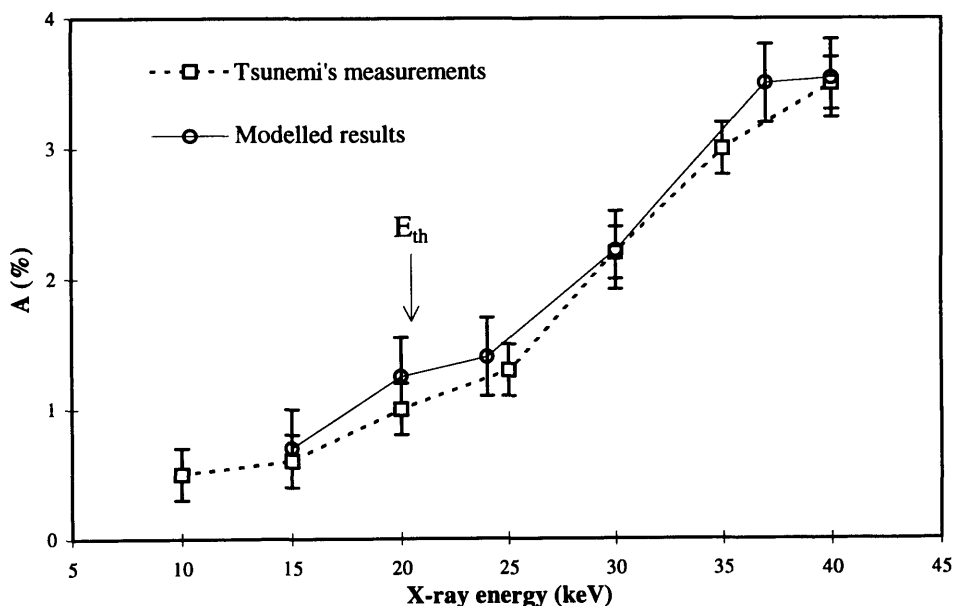
Figure A-2 Modelled results for a 12μm pixel device with P=60% beam polarisation. compared to data from Tsunemi et al [Tsunemi, H., 1992 + 1993]. The appropriate threshold energy (equation A-1,A-2) is indicated by the vertical arrow.
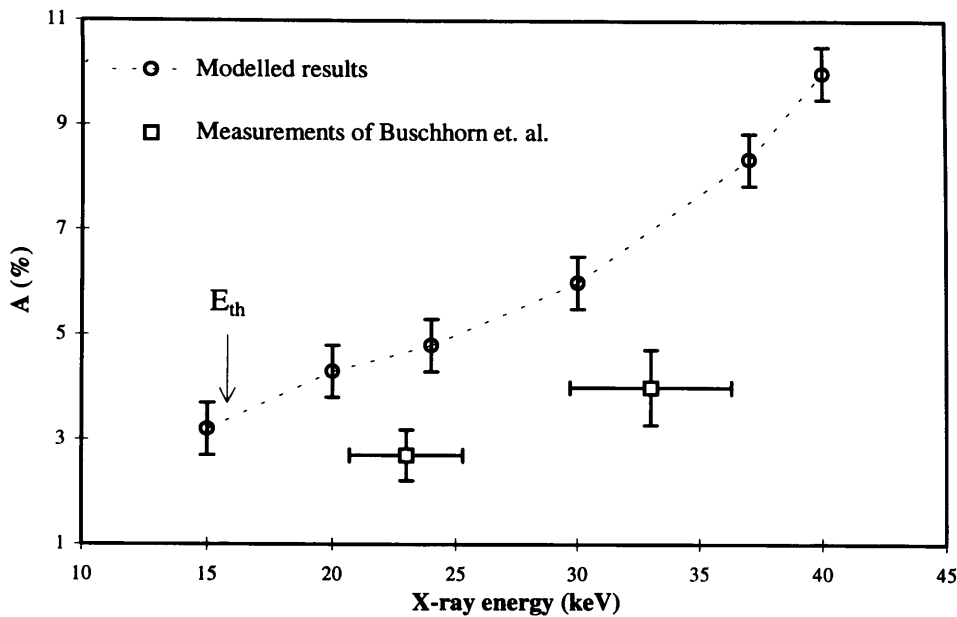
Figure A-3 Modelled results for a 6.8μm pixel device with P=84% polarisation, compared to data from Buschhorn et al [Buschhorn, G., 1994]. The broad-band estimate was obtained from channel radiation, the 33.17keV data point at a synchrotron beam. The appropriate threshold energy (equation A-1,A-2) is indicated by the vertical arrow.

Figure A-3 is the corresponding figure for the 6.8μm pixel CCD of ref. [Buschhorn, G., 1994]. Once again, the silicon epitaxial thickness and depletion depth were chosen to be representative of a commercial video CCD, having values of 20 and 3μm respectively. The 33.17keV synchrotron measurement of Buschhorn et al [Buschhorn, G., 1994] lies some way below the calculated curve A(E) (note that the closer correspondence between our model and this measurement, exhibited in figure 18 of ref. [Buschhorn, G., 1994] was based on an early, incorrect version of the simulation code).

A.4 Discussion

The existing measurements were taken using commercially available CCDs designed for video use and therefore not optimised for X-ray detection. Enhanced X-ray detection may be achieved through a number of techniques [Holland, A.D., 1989]. Increased high energy efficiency may be obtained through the use of high resistivity silicon in the fabrication process. Devices have been successfully constructed with increased depletion depths of up to 80μm [Holland, A.D., 1992]. Deep depletion increases the detection efficiency of events contained within 1-2 pixels, however, an increase in depletion depth in the model was found to not affect M(E). In addition, low noise detectors giving noise values of down to ~3 electrons rms. [Holland, A.D., 1989] enable low level charge splitting to be more accurately determined. An investigation of the effect of system noise on M indicated only a

weak dependence, with a 5% relative increase in M, resulting from a reduction in noise from 50 to 10 electrons rms.
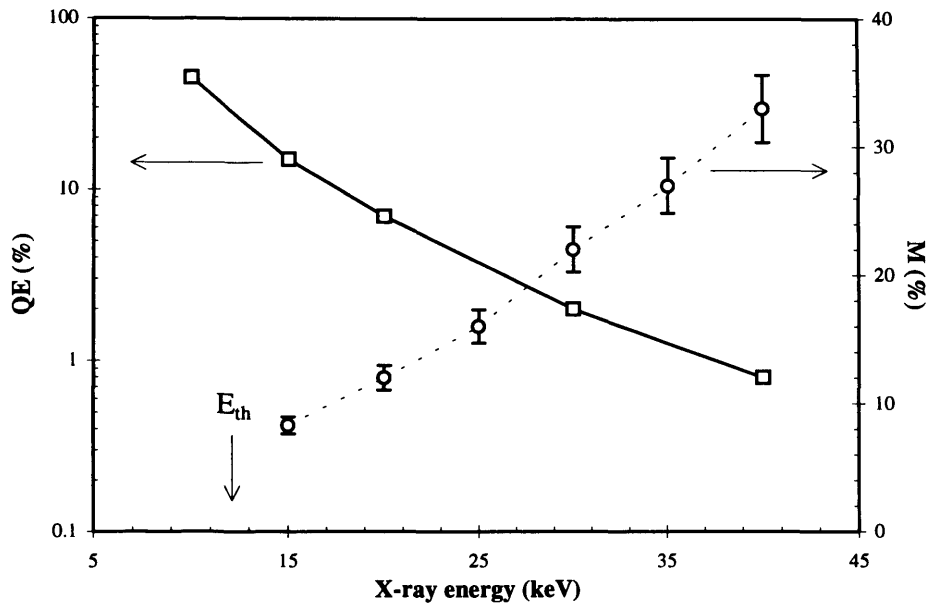
Figure A-4 Modulation factor (right hand scale) and quantum detection efficiency (left hand scale) for a 4μm pixel CCD with 80μm depletion depth on 100μm thick epitaxial silicon.

Figure A-4 shows the variation of the modulation factor, M, with energy for a 4μm square pixel CCD. In addition, the quantum efficiency, Q, is given for a detector with an 80μm depletion depth. The pixel size of 4μm is around the manufacturing limit for standard CCD lithography techniques, while the 80μm active thickness has been demonstrated for X-ray CCDs [Holland, A.D., 1992]. The simulation suggests that a modulation factor in excess of 8% above 15keV should be possible using such a detector; M should be as high as 34% at 40keV. While performing polarisation measurements on a photon-by-photon basis, the CCD would also be able to carry out X-ray spectroscopy with a resolution (full width at half maximum) given by:

$$\Delta E = 2.35\varpi\sqrt{n^2 + \frac{fE}{\varpi}} \quad eV \tag{A-16}$$

where n is the system noise, f=0.12 is the silicon Fano factor and ϖ=3.65eV is the ionisation energy [Fraser, G.W., 1994]. For a typical system with noise, n, of 10 electrons rms, we obtain an energy resolution (FWHM) of 240eV at 20 keV.

For any class of X-ray polarimeter, the minimum detectable polarisation per unit time, per unit collecting area, is determined by a figure of merit:

$$F = \frac{1}{M\sqrt{Q}} \tag{A-17}$$

174

in the strong source limit [Fraser, G.W., 1989(1)]. For an ideal polarimeter, F=1. We may compare real polarimeters by estimating the relevant values of F. For the CCD polarimeter characterised in figure A-4, the function F(E) has a broad minimum (F~30) in the energy range 15-40keV. At lower energies, the modulation factor is un-usably low, while at higher energies, Q becomes impracticably small.

For comparison, the optical imaging chamber of Austin et al [Austin, R.A., 1993(2)] is characterised by F=60 at 60 keV and negligible polarisation sensitivity below 40keV. Improvements proposed in ref. [Austin, R.A., 1993(2)] would, if successful, reduce the figure of merit to ~13 at 60keV. For the non-imaging Thomson scattering X ray polarimeter described by Landecker [Landecker, P.B., 1972], F~7 at 14keV, increasing slowly with energy, while the Compton scattering polarimeter of Sakurai et al [Sakurai, H., 1990] was characterised by F=10 at 60keV.

To summarise, the silicon CCD X-ray polarimeter will possess a moderate, but useful, polarisation sensitivity for X-ray energies between 15 and 40keV, where other detectors using Thomson or Compton scattering or imaging chamber techniques do not perform well. CCD/hard X-ray optics combinations would also provide medium resolution X-ray spectroscopy (E/ΔE(60keV)=83) and high resolution imaging. In addition, the technical implementation of the CCD polarimeter may be more straightforward than the alternative technologies mentioned above.

A.5 Conclusions

A model of X-ray polarisation detection in silicon CCDs has been established and good agreement demonstrated with published results, which indicate that a small pixel CCD manufactured at the limits of current device technology with a 4μm pixel will produce a modulation factor of between 8 and 34% for X-ray energies between 15 and 40keV. Such a detector would be best manufactured on high resistivity silicon, producing depletion depths of around 80μm for increased detection efficiency. As a by-product, such a detector would also provide energy resolution of around 250 eV at 20 keV. This work was carried out in 1993, but polarisation sensitivity using small pixel CCDs continues to be studied at Leicester University through further modelling and measurements using 6.8x6.8 μm and 4x9 μm pixels [Hill, J.E., 1997].

APPENDIX B - PROGRAM LISTINGS

B.1 Simulation of GaAs Detector Spectral Response

```
PROGRAM gaas97

REAL k,CCE(5000),E(5000),fh(5000),fe(5000),linth,XEN(3,40)
INTEGER xnum,count,xcount,spectr(5000)
PARAMETER(PI=3.1416,k=1.3807E-23)
J=9999

*       set variables
        thick=80
        linth=40
        xnum=1000
        Vb=300
        T=273-130
        sigNte=37
        sigNth=5.52
        Eae=-0.677*1.6022E-19
        Eah=-0.21*1.6022E-19
        detcone=1.0808E-14
        detconh=1
        peakt=0*1E-6
        elfwhm=1800
        padrad=757
        atthick=0
        elthick=1


*       calculate carrier lifetimes
        taue=SQRT(300/T)/(sigNte*4.4E7)
        tauh=SQRT(300/T)/(sigNth*1.77E7)
        DO x=1,thick
*         calculate E-field array
          E(x)=2*Vb/(linth+thick)
          IF(x.GT.linth)E(x)=E(x)*(thick+.5-x)/(thick-linth)
*         calculate carrier velocities
          vdh=.9E11*LOG((E(x)/5)+1)
          vde=1.95E11-1.8E11*(((E(x)-0.26)*4)**2)
          IF(E(x).GT.0.3)vde=1.05E11+7E11*EXP(-(E(x)+0.86)*1.8)
*         calculate fractional loss arrays
          f=EXP(-1/(vde*taue))
          fe(x)=1-(1-f)*EXP(-peakt/(detcone*EXP(-Eae/(k*T))))
          f=EXP(-1/(vdh*tauh))
          fh(x)=1-(1-f)*EXP(-peakt/(detconh*EXP(-Eah/(k*T))))
        ENDDO
```

```
*       integrate fractional loss arrays to give cce(x)
        DO depth=1,thick
          CCE(depth)=0
          erem=1
          hrem=1
          DO x=depth,1,-1
            hrem=hrem*fh(x)
            CCE(depth)=CCE(depth)+hrem*2*(thick-x+.5)/(thick*thick)
          ENDDO
          DO x=depth+1,thick
            erem=erem*fe(x)
            CCE(depth)=CCE(depth)+erem*2*(thick-x+.5)/(thick*thick)
          ENDDO
        ENDDO


*       read in line energies and strengths for source
        OPEN(UNIT=1,FILE='Am241.txt',STATUS='unknown')
        READ(1,*) XEN(1,1),XEN(2,1)
        XEN(3,1)=XEN(2,1)
        DO COUNT=2,26
          READ(1,*) XEN(1,COUNT),XEN(2,COUNT)
          XEN(3,COUNT)=XEN(3,COUNT-1)+XEN(2,COUNT)
        ENDDO
        CLOSE(UNIT=1)


*       start of main program loop over the number of detections required
        DO xcount=1,xnum
*       set charge, angle and detection flag to zero
        totch=0
        theta=0
        detection=0
*       loop for X-rays in active region
        DO WHILE (detection.EQ.0)
          x=0
*         optional loop for treating absorption and deposition in electrode
          DO WHILE(x.LT.(atthick+elthick))
*           non-optional part to select the X-ray energy from source data
            sd=RAN(J)
            sd=sd*XEN(3,26)
            phen=XEN(1,1)
            DO COUNT=1,25
              IF(sd.GT.XEN(3,COUNT))phen=XEN(1,COUNT+1)
            ENDDO
*           calculate good approximation to μp(E) for gold electrode
            IF(phen.LT.2300)THEN
              grad=-2.0286
              cons=7.0393
```

177

```
      ELSEIF(phen.GE.2300.AND.phen.LT.12000)THEN
        grad=-2.497
        cons=9.3459
      ELSEIF(phen.GE.12000.AND.phen.LT.80000)THEN
        grad=-2.6038
        cons=10.3813
      ELSEIF(phen.GE.80000)THEN
        grad=-2.486
        cons=10.4287
      ENDIF
      Auph=10**(cons+grad*log10(phen))
      sd=RAN(J)
*     randomise depth in the electrode layer
      x=-LOG(sd)/Auph
      IF(x.LT.(atthick+elthick).AND.x.GT.atthick)THEN
*       if absorbed in electrode, calculate range and randomise direction of photoelectron
        sd=RAN(J)
        alpha=PI*sd
        range=0.0099*(phen/1000.0+0.5725)**1.5809
*       if photoelectron reaches GaAs, calculate the fraction of charge it will deposit there
        IF((x+range*COS(alpha)).GT.(atthick+elthick))THEN
          frac=1-(atthick+elthick-x)/range/COS(alpha)
*         x by cce(1) and add random electronic noise
          endep=phen*frac*CCE(1)+elfwhm*GS(J)/2.35
*         increment spectrum accordingly
          spectr(INT(endep/200))=spectr(INT(endep/200))+1
        ENDIF
      ENDIF
      ENDDO
*     end of loop dealing with electrode, X-ray energy has been set
      x=0
*     loop over this X-ray's treatment in the GaAs
      DO WHILE (phen.GT.0)
*       calculate Compton and photoelectric linear attenuation coefficients
        uco=6.48E-5*EXP(-(LOG10(phen)-4.74)**2/2/.729**2)+phen/2.5E10
        uph=UPHOT(phen)
        sd=RAN(J)
*       randomise depth of interaction in the GaAs
        x=x-COS(theta)*LOG(sd)/(uph+uco)
*       is the X-ray absorbed in the active region of the device
        IF (x.LT.thick.AND.x.GE.0) THEN
*         register a detection
          detection=1
          sd=RAN(J)
*         randomise if photoelectric or Compton interaction and call appropriate subroutine
          IF ((sd*(uph+uco)).GT.uph) THEN
            CALL COMPT(phen,theta,edep,PI,J)
          ELSE
            CALL PHOTO(phen,theta,edep,padrad,PI,J)
          ENDIF
```

```
*          add fano noise to charge deposited and x by the cce at this depth
           totch=totch+(edep+0.877*GS(J)*SQRT(edep))*CCE(INT(x)+1)
           ELSE
*          if interaction not inside device, set X-ray energy=0 to leave loop
           phen=0
           ENDIF
          ENDDO
         ENDDO
         add electronic noise to the signal and increment spectral array
         totch=totch+elfwhm*GS(J)/2.35
         spectr(INT(totch/200))=spectr(INT(totch/200))+1
        ENDDO
*       end of main program loop



*       write out results, simulation parameters first
        OPEN(UNIT=1,FILE='data.out',STATUS='unknown')
        WRITE(1,*)'thick(um)        =',thick
        WRITE(1,*)'linth(um)        =',linth
        WRITE(1,*)'Vb(V)            =',Vb
        WRITE(1,*)'T(K)             =',T
        WRITE(1,*)'sigNte(/cm)       =',sigNte
        WRITE(1,*)'sigNth(/cm)       =',sigNth
        WRITE(1,*)'Eae(eV)          =',Eae/1.6022E-19
        WRITE(1,*)'Eah(eV)          =',Eah/1.6022E-19
        WRITE(1,*)'detcone          =',detcone
        WRITE(1,*)'detconh          =',detconh
        WRITE(1,*)'peakt(us)        =',peakt*1E6
        WRITE(1,*)'elfwhm(eV)            =',elfwhm
        WRITE(1,*)' '
        WRITE(1,*)'el 1/e trapping t (s)   =',taue
        WRITE(1,*)'ho 1/e trapping t (s)   =',tauh
        WRITE(1,*)'el 1/e de-trapping t (s) =',detcone*EXP(-Eae/(k*T))
        WRITE(1,*)'ho 1/e de-trapping t (s) =',detconh*EXP(-Eah/(k*T))
        WRITE(1,*)' '
*       then write out E-field(x) and cce(x) arrays
        WRITE(1,*)'depth      E      CCE'
        DO i = 1,thick
          WRITE(1,*)i,E(i),CCE(i)
        ENDDO
        CLOSE(UNIT=1)

*       finally write out simulated spectrum to a separate file
        OPEN(UNIT=1,FILE='spectr.out',STATUS='unknown')
        DO count = 1,1300
          WRITE(1,*) REAL(count)/5, spectr(count)
        ENDDO
        CLOSE(UNIT=1)
        CLOSE(UNIT=2)
```

END


```
      SUBROUTINE COMPT(phen,theta,edep,PI,J)
*     use Kahn's method to solve Klein-Nishina formula for Compton events
      phe=phen/511000
      accept=0
      DO WHILE (accept.EQ.0)
       r1=RAN(J)
       r2=RAN(J)
       r3=RAN(J)
       IF(r1.LT.((2*phe+1)/(2*phe+9)))THEN
         y=1+2*phe*r2
         u=1-(2*r2)
         IF(r3.LT.(4*(1/y-1/(y*y))))accept=1
       ELSE
         y=(2*phe+1)/(1+2*phe*r2)
         u=1-(y-1)/phe
         IF(r3.LT.(((u*u)+1/y)/2))accept=1
       END IF
      ENDDO
      phe=511000*phe/y
      edep=phen-phe
      phi=ACOS(u)
      sd=RAN(J)
      theta=SQRT(theta**2+phi**2-2*theta*phi*COS(PI*sd))
      phen=phe
      END


      SUBROUTINE PHOTO(phen,theta,edep,padrad,PI,J)
*     approximate attenuation coefficients for Ga and As at this energy
      uga=45E5*phen**(-2.22)
      IF(phen.GE.1110)uga=13E8*phen**(-2.7)
      IF(phen.GE.10350)uga=60E9*phen**(-2.9)
      uas=11E6*phen**(-2.3)
      IF(phen.GE.1327)uas=146E7*phen**(-2.7)
      IF(phen.GE.11892)uas=70E9*phen**(-2.9)
      phenew=0
*     randomise if absorber is a Ga or As atom
      sd=RAN(J)
      IF((sd*(uga+uas)).GT.uas) THEN
*       absorber is Ga atom
        sd=RAN(J)
        IF(phen.GT.10350.AND.sd.LE.0.468)THEN
*         if above k-edge and not an Auger event, set initially for Lα emission
          phenew=1098
          sd=RAN(J)
```

```
*        randomise if Kα emission
         IF(sd.GT.0.134)phenew=9252
       ENDIF
       ELSE
*        absorber is As atom
         sd=RAN(J)
         IF(phen.GT.11892.AND.sd.LE.0.531)THEN
*          if above k-edge and not an Auger event, set initially for Lα emission
           phenew=1282
           sd=RAN(J)
*          randomise if Kα emission
           IF(sd.GT.0.138)phenew=10544
         ENDIF
       ENDIF
*      set energy deposited (calculating edge losses is optional)
       edep=EDGELOSS(phen-phenew,padrad,PI,J)
*      set the new photon energy i.e. fluorescence X-ray (=0 for Auger event)
       phen=phenew
       sd=RAN(J)
*      give the fluorescence X-ray a random direction
       theta=PI*sd
       END




       FUNCTION EDGELOSS(elen,rp,PI,J)
*      calculate range of photoelectron in GaAs
       range=0.0181*(elen/1000.0+0.439)**1.661
       r=rp+range+1
*      randomise a radial position in the circular device
       DO WHILE(r.GE.(rp+range))
         sd=RAN(J)
         td=RAN(J)
         r=(rp+range)*SQRT(sd**2+td**2)
       ENDDO
*      if edge of pad is out of photoelectron range, do nothing to energy deposited
       IF(r.LT.(rp-range))THEN
         EDGELOSS=elen
       ELSE
*        if edge is within range calculate the loss of charge
         EDGELOSS=0
         sd=RAN(J)
*        randomise photoelectron direction
         direct=PI*sd
         DO count=1,100
           r=r+COS(direct)*range/100
*          integrate charge that is not lost
           IF(r.LT.rp)EDGELOSS=EDGELOSS+elen/100
```

181

```
      ENDDO
      ENDIF
      END




      FUNCTION UPHOT(phen)
*     returns very good approximation to μ_p(E)
      UPHOT=35E6*phen**(-2.5)
      IF(phen.GE.1135)UPHOT=135E6*phen**(-2.5)
      IF(phen.GE.1348)UPHOT=13E8*phen**(-2.7)
      IF(phen.GE.10336)UPHOT=49E8*phen**(-2.7)
      IF(phen.GE.11955)UPHOT=60E9*phen**(-2.9)
      END




      FUNCTION GS(J)
*     fast gaussian randomiser
      DOUBLE PRECISION D(30),I,W
      DATA D,U /0.674489750,0.475859630,0.38377116,0.328611323,
     ]0.291142827,0.263684322,0.242508452,0.225567444,0.211634166,
     ]0.199924267,0.189910758,0.181225181,0.173601400,0.166841909,
     ]0.160796729,0.155349717,0.150409384,0.145902577,0.141770033,
     ]0.137963174,0.134441762,0.131172150,0.128125965,0.125279090,
     ]0.122610883,0.120103560,0.117741707,0.115511892,0.113402349,
     ]0.111402720,0.0/
      A=0.0
      I=0
10    U=U+U
      IF(U.LT.1.0) GOTO 20
      U=U-1.0
      I=I+1
      A=A-D(I)
      GOTO10
20    W=D(I+1)*U
      V=W*(0.5*W-A)
30    U=RAN(J)
      IF (V.LE.U)GOTO 40
      V=RAN(J)
      IF(U.GT.V)GOTO 30
      U=(V-U)/(1.0-U)
      GOTO20
40    U=(U-V)/(1.0-V)
      U=U+U
      IF(U.LT.1.0) GOTO 50
      U=U-1.0
```

B.2 Simulation of X-ray Polarisation Measurement Using Small Pixel Silicon CCDs

```
      PROGRAM POLSIM
      REAL NA,L1,LEL,LINEL,LTOT,T(6),DS(6),E(6),PATR(6),
]  NPOL(6,13)
      CHARACTER MASK(13)*25,POL*25
      COMMON ENERGY,NA,DEPTH,DEAD,DEPLN,FF,L1,SUBST,
]  PIXEL,X,Y,FRACT(25)
      DATA MASK /'0000000000000100000000000',
]  '0000000000000100001000000',
]  '0000000000000110000000000','0000000100001000000000000',
]  '0000000000000110000000000','0000000000000010000100000100',
]  '0000000000000111000000000','0010000100001000000000000',
]  '0000000000001110000000000','0000000000000011000110000000',
]  '0000000110001100000000000','0000001100011000000000000',
]  '0000000000000110001100000000'/

*      set variables
      DATA E /15000,20000,25000,30000,35000,40000/
      NOXRAY=30
      FF=20
      DEPLN=80
      SUBST=5
      DEAD=1
      PIXEL=4
      NA=6E20
      THRESH=540
      L1=100


*      clear the npol array
      DO ECOUNT=1,6
       DO COUNT=1,13
        NPOL(ECOUNT,COUNT)=0
       ENDDO
      ENDDO


*      loop over desired energies and no. of xrays
      DO ECOUNT=2,2,1
       DO XCOUNT=1,NOXRAY
*       clear the fract array
        DO COUNT=1,25
         FRACT(COUNT)=0
        ENDDO
*       randomise into an approx. normal distribution
        GS=0
        DO COUNT=1,12
         GS=GS+RAN(99999999)
```

```
        ENDDO
*       add the random photon shot noise
        EX=E(ECOUNT)+3.62*(GS-6)*(.0318*E(ECOUNT))**.5
*       xray energy-binding energy=electron energy
        ELENERGY=EX-1740
*       binding energy will be emitted as cloud of secondary
*       electrons at interaction point. set energy for subroutine
        ENERGY=1740
*       randomise depth, x and y. linear absorption good approx
        DEPTH=(FF+DEPLN+SUBST)*RAN(99999999)+DEAD
        X=PIXEL*RAN(99999999)
        Y=PIXEL*RAN(99999999)
*       call the charge collection subroutine
        IF(((X**2)**.5).LT.(10*PIXEL)) THEN
         IF(((Y**2)**.5).LT.(10*PIXEL)) THEN
            IF(DEPTH.LT.(FF+DEPLN+DEAD+SUBST).AND.DEPTH
]    .GT.DEAD) THEN
                CALL CHARGE
            ENDIF
         ENDIF
        ENDIF
*       randomise initial photoelectron direction, ie direction of
*       E vector which has a cos2 distribution
        DEC=6.283185307*RAN(99999999)
        ALPHA=0
        ASTEP=0.31415926
10      TERM1=ALPHA-DEC
        TERM2=-(SIN(ALPHA)*COS(ALPHA))
        IF(TERM1.GE.TERM2) GOTO 20
        ALPHA=ALPHA+ASTEP
        GOTO 10
20      ASTEP=0.031415926
30      ALPHA=ALPHA-ASTEP
        TERM1=ALPHA-DEC
        TERM2=-(SIN(ALPHA)*COS(ALPHA))
        IF(TERM1.GE.TERM2) GOTO 30
        ALPHA=ALPHA+0.5*ASTEP
*       alpha is angle between electron direction and xy plane.
        DEC=6.283185307*RAN(99999999)
        BETA=0
        ASTEP=0.31415926
40      TERM1=BETA-DEC
        TERM2=-(SIN(BETA)*COS(BETA))
        IF(TERM1.GE.TERM2) GOTO 50
        BETA=BETA+ASTEP
        GOTO 40
50      ASTEP=0.031415926
60      BETA=BETA-ASTEP
        TERM1=BETA-DEC
        TERM2=-(SIN(BETA)*COS(BETA))
```

```
      IF(TERM1.GE.TERM2) GOTO 60
      BETA=BETA+0.5*ASTEP
*     beta is angle between x direction and projection of
*     electron direction onto xy plane.
*     loop over photoelectron journey through silicon until
*     its energy (mean free path) has declined sufficiently
      DO WHILE (ELENERGY.GT.2000)
*       calculate lambda (elastic) at electron energy
        LEL=9.488E-7*(ELENERGY+15.14)
*       calculate lambda (inelastic) at electron energy
        LINEL=(10**(.7749*LOG10(ELENERGY)-.9857))/10000
*       calculate total lambda
        LTOT=1/(1/LEL+1/LINEL)
*       thus choose random path length
70      PLENGTH=-LTOT*LOG(RAN(99999999))
*       find new x,y and depth from direction and pathlength
        X=X+PLENGTH*COS(ALPHA)*COS(BETA)
        Y=Y+PLENGTH*COS(ALPHA)*SIN(BETA)
        DEPTH=DEPTH+PLENGTH*SIN(ALPHA)
*       randomise azimuthal angle into 360 degrees
        GAMMA=6.283185307*RAN(99999999)
        FLAG=RAN(99999999)
*       select elastic or inelastic by weigthed randomisation.
*       if elastic then
        IF((FLAG).LE.(LTOT/LEL)) THEN
*         calculate deflection angle theta and find new alpha
*         and beta but do not touch the energy
          BN=15.14/ELENERGY
          RA=RAN(99999999)
          THETA=ACOS((1+BN-RA*(1+2*BN))/(1+BN-RA))
          ALPHA=ALPHA+THETA*SIN(GAMMA)
          BETA=BETA+THETA*COS(GAMMA)
          GOTO 70
*       else interaction must be inelastic
        ELSE
*         set energy deposited to that lost by electron, ready
*         for charge collection subroutine
          ENERGY=14.945*LOG10(ELENERGY)-6.304
*         calculate deflection angle
          THETA=ASIN((ENERGY/ELENERGY)**.5)
*         decrement electron energy
          ELENERGY=ELENERGY-ENERGY
*         call the charge collection subroutine
          IF(((X**2)**.5).LT.(10*PIXEL)) THEN
           IF(((Y**2)**.5).LT.(10*PIXEL)) THEN
            IF(DEPTH.LT.(FF+DEPLN+DEAD+SUBST).AND.DEPTH
]          .GT.DEAD) THEN
              CALL CHARGE
             ENDIF
            ENDIF
```

186

```
          ENDIF
*         change alpha and beta to new electron direction
          ALPHA=ALPHA+THETA*SIN(GAMMA)
          BETA=BETA+THETA*COS(GAMMA)
          ENDIF
          ENDDO
*         when photoelectron has lost most of its energy, dump the
*         rest at its current position
          ENERGY=ELENERGY
*         call charge collection subroutine
          IF(((X**2)**.5).LT.(10*PIXEL)) THEN
            IF(((Y**2)**.5).LT.(10*PIXEL)) THEN
              IF(DEPTH.LT.(FF+DEPLN+DEAD+SUBST).AND.DEPTH
]    .GT.DEAD) THEN
                CALL CHARGE
              ENDIF
            ENDIF
          ENDIF
*         make a template of 0's for those pixels containing less
*         than threshold energy and 1's for those containing more
          DO COUNT=1,25
            IF (FRACT(COUNT).GT.THRESH) THEN
              POL(COUNT:)='1'
            ELSE
              POL(COUNT:)='0'
            ENDIF
          ENDDO
*         compare the 25 bit template with the patterns stored in
*         mask() to identify 1,2,3 and 4 pixel events. increment
*         npol() the pattern counter accordingly
          DO COUNT=1,13
            IF (MASK(COUNT).EQ.POL) THEN
              NPOL(ECOUNT,COUNT)=NPOL(ECOUNT,COUNT)+1
            ENDIF
          ENDDO
          ENDDO
*         having simulated an xray energy, generate a new output file
          DO EC=1,6
*           sum the x-spread (lnum) and y-spread (snum) events
            LNUM=NPOL(EC,3)+NPOL(EC,5)+NPOL(EC,7)+NPOL(EC,9)
            SNUM=NPOL(EC,2)+NPOL(EC,4)+NPOL(EC,6)+NPOL(EC,8)
*           count the total number of recognised patterns
            TOTR=0
            DO COUNT=1,13
              TOTR=TOTR+NPOL(EC,COUNT)
            ENDDO
*           calculate the polarisation, error and recognition
            T(EC)=((LNUM-SNUM)/(LNUM+SNUM))*50
            DS(EC)=((SQRT(TOTR))/TOTR)*100
            PATR(EC)=(TOTR/NOXRAY)*100
```

187

```fortran
      ENDDO
*     finally open an output file and write the results
      OPEN(UNIT=1,FILE='pol.out',STATUS='unknown')
      WRITE(1,*)'ENERGY(eV)','      POLT(%)','      ',
]    '         RECOG(%)'
      WRITE(1,*)' '
      DO ECO=1,6
        WRITE(1,*) E(ECO),T(ECO),'+/-',DS(ECO),'      ',
]   PATR(ECO)
      ENDDO
      CLOSE(UNIT=1)
      ENDDO
      STOP
      END




      SUBROUTINE CHARGE
      REAL NA,L1,FRACT(25),PX(5),PY(5)
      COMMON ENERGY,NA,DEPTH,DEAD,DEPLN,FF,L1,SUBST,
]   PIXEL,X,Y,FRACT(25)



*     Charge cloud radius on impact 1 SIG radius
      CI=4.936E-3*(ENERGY/1000.)**1.75
*     Charge cloud radius in drifting through depletion layer
      CFR=5465.E6*SQRT(1/NA)*.66
      DEPTH2=DEPTH-DEAD
      DEPTH3=DEPTH-DEAD-DEPLN
      IF (DEPTH2.LT.DEPLN) THEN
*       X-ray absorbed in the depletion layer
*       DEPLN  incremented 0.05 to avoid singularity at boundary
        CF=.66*4130.E6*SQRT(LOG((DEPLN+.2)/(DEPLN+.2-DEPTH2))/NA)
        SIG=SQRT(CI**2+CF**2)
        HH=1.0
      ELSE IF (DEPTH3.LT.FF) THEN
*       X-ray absorbed in the field-free layer
        D=DEPTH-DEAD-DEPLN
        HH=(EXP(FF/L1-D/L1)+EXP(D/L1-FF/L1))/
]       (EXP(FF/L1)+EXP(-FF/L1))*1.0
        CFF=FF*SQRT(1-((FF-D)/FF)**2)
        SIG=SQRT(CI**2+CFR**2+CFF**2)
*       otherwise we are in the substrate with L=10um
      ELSE
        DSUB=DEPTH-DEAD-DEPLN-FF
        HH=SINH((SUBST-DSUB)/10)/SINH(SUBST/10)
        CFSUB=0.5*SUBST*SQRT(1-((SUBST-DSUB)/SUBST)**2)
        SIG=SQRT(CI**2+CFR**2+CFSUB**2+.25*FF*FF)
      ENDIF
```

```
*       Clear the PX and PY arrays
        DO COUNT=1,5
          PX(COUNT)=0
          PY(COUNT)=0
        ENDDO
*       Calculate error functions in x-direction
        COUNT=0
        DO XI=-(2*PIXEL+X),(2*PIXEL-X),PIXEL
          COUNT=COUNT+1
          CASE1=(XI+PIXEL)/1.41/SIG
          CASE2=XI/1.41/SIG
          PX(COUNT)=(S15AEF(CASE1,ISTAT)-S15AEF(CASE2,ISTAT))/2
        ENDDO

*       Calculate error functions in y-direction
        COUNT=0
        DO YI=-(2*PIXEL+Y),(2*PIXEL-Y),PIXEL
          COUNT=COUNT+1
          CASE1=(YI+PIXEL)/1.41/SIG
          CASE2=YI/1.41/SIG
          PY(COUNT)=(S15AEF(CASE1,ISTAT)-S15AEF(CASE2,ISTAT))/2
        ENDDO
*       Combine x & y erf's to map the charge cloud over a grid
        COUNT=0
        DO IY=1,5
          DO IX=1,5
            COUNT=COUNT+1
            FRACT(COUNT)=PX(IX)*PY(IY)*ENERGY*HH+FRACT(COUNT)
          ENDDO
        ENDDO
        RETURN
        END
```